HELLENIC REPUBLIC
National and Kapodistrian University of Athens
School of Health Science
Department of Pharmacy

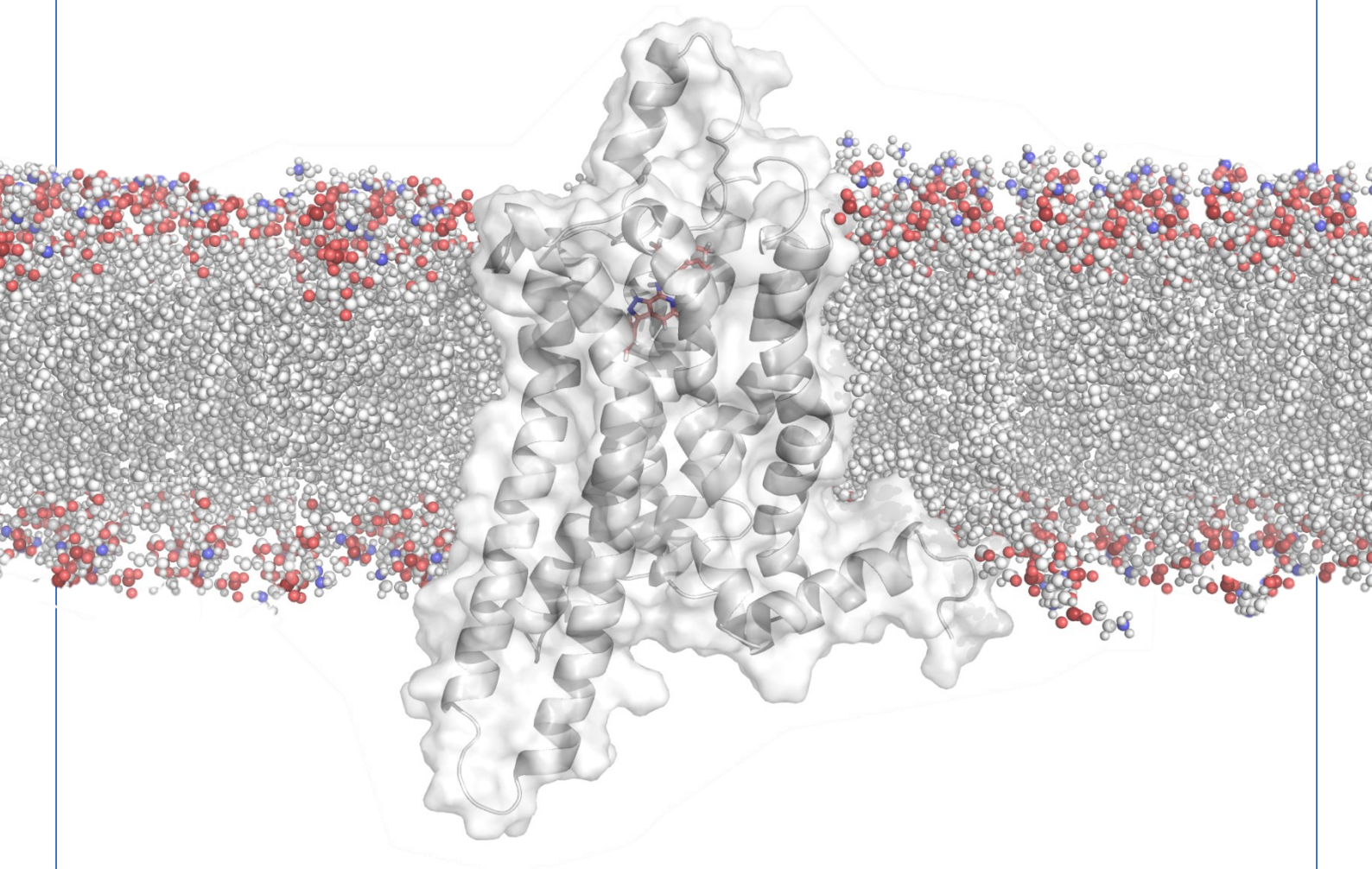

Doctoral Thesis

Structure - based drug design research of antagonists against adenosine receptors A_1 and A_3 using alchemical free energy perturbation and kinetic binding calculations.

Stampelou Margarita Eleni

Athens 2023

HELLENIC REPUBLIC
National and Kapodistrian University of Athens
School of Health Science
Department of Pharmacy

Doctoral Thesis

Structure - based drug design research of antagonists against adenosine receptors A_1 and A_3 using alchemical free energy perturbation and kinetic binding calculations.

Stampelou Margarita Eleni

October 2023

This work has been carried out at Laboratory of Computational Chemistry of the Department of Pharmacy, Section Pharmaceutical Chemistry

Supervisor:
Professor Antonios Kolocouris

The implementation of the doctoral thesis was co-financed by Greece and the European Union (European Social Fund-ESF) through the Operational Programme «Human Resources Development, Education and Lifelong Learning» in the context of the Act "Enhancing Human Resources Research Potential by undertaking a Doctoral Research" Sub-action 2: IKY Scholarship Programme for PhD candidates in the Greek Universities.

Seven-member committee

Antonios Kolocouris (Supervisor)

Professor, Department of Pharmacy, Section of Pharmaceutical Chemistry
National and Kapodistrian University of Athens
Athens, Greece

Emmanuel Mikros *(Consultant Committee)*

Professor, Department of Pharmacy, Section of Pharmaceutical Chemistry
National and Kapodistrian University of Athens
Athens, Greece

Graham Ladds *(Consultant Committee)*

Professor, Department of Pharmacy,
University of Cambridge
Cambridge, UK

Lougiakis Nikolaoas

Assistant Professor, Department of Pharmacy, Section of Pharmaceutical Chemistry
National and Kapodistrian University of Athens
Athens, Greece

Thomas Mavromoustakos

Professor, Department of Chemistry, Laboratory of Organic Chemistry
National and Kapodistrian University of Athens
Athens, Greece

Minos Matsoukas

Assistant Professor, Department of Biomedical Engineering
University of West Attica,
Athens, Greece

Athanasios Papakyriakou

Senior Researcher, Institute of Biosciences & Applications
National Centre for Scientific Research "Demokritos"
Athens, Greece

Abstract

In the pursuit of developing effective therapeutics, structure-based drug design has emerged as a powerful approach, leveraging our understanding of molecular structures to design molecules with enhanced binding and functional properties. The search for effective therapeutics targeting adenosine receptors (ARs), members of the G protein-coupled receptors (GPCRs) family, has gained substantial significance due to their involvement in various pathological conditions.

The aim of this thesis is to explore the field of structure-based drug design, focusing on the development of antagonists targeting adenosine receptors A_1 and A_3. In pursuit of this objective, advanced computational methods like alchemical free energy perturbation and kinetic binding calculations are employed. In Chapter 1, there is an introduction on GPCRs with emphasis on ARs. Agonists, antagonists, and dual antagonists are mentioned that act on the orthosteric and allosteric sites. Chapter 2 describes the principles of the methodologies applied through the present thesis.

In Chapter 3, the synthesized derivatives of 7-aryl or alkylamino-pyrazolo[3,4-*d*]pyridazine provided a novel scaffold for developing ligands against ARs. We have pharmacologically characterized these compounds using functional cAMP assays and fluorescent ligand displacement binding studies, expanding our study to the antiproliferative potential of these agents as well. The introduction of a 3-phenyl group, together with a 7-benzylamino and 1-methyl group at the pyrazolopyridazine scaffold, generated the antagonist compound **10b** which displayed 26 nM affinity and a residence time (RT) 60 min for the human A_1R, 7.4 nM affinity and RT = 73 min for the human A_3R and low μM affinity for the human A_{2B}R while not be toxic against the normal cell line. The site of the N-methyl substitution on the pyrazole ring had a remarkable effect on the bioactivity, since the corresponding 2-methyl-3-phenyl derivative (**15b**) had no significant affinity, while when the 3-phenylgroup of **10b** was replaced by an isopropyl group, the resulting derivative **10a** possessed considerably reduced affinity. We compared the binding interactions of the regio-isomers **10b** and **15b** with molecular dynamics (MD) simulations and the results suggested that the 2-methyl group in **15b** hinders the formation of hydrogen bonding interactions with $N^{6.55}$ which are considered critical for the stabilization inside the orthosteric binding cavity. Mutagenesis experiments for **10b** against A_1R provided results that complement the observations from MD simulations. We showed that $L250^{6.51}A$ mutation resulted in only a slight reduction of binding affinity concerning **10b** while the $Y271^{7.46}A$ mutation caused a 10-fold reduction in binding affinity of this compound. Mutation to alanine of residues

T91$^{3.36}$, H251$^{6.52}$ or S267$^{7.42}$, which are deep in the orthosteric binding affinity, did not affect binding affinity.

In Chapter 4, we report the identification of 7- (phenylamino)-pyrazolo[3,4-c]pyridines L2−L10, A15, and A17 as low-micromolar to low-nanomolar A_1R/A_3R dual antagonists, with 3-phenyl-5-cyano-7-(trimethoxyphenylamino)-pyrazolo[3,4-c]pyridine (**A17**) displaying the highest affinity at both receptors with a long residence time of binding, as determined using a NanoBRET based assay. Two binding orientations of **A17** produce stable complexes inside the orthosteric binding area of A_1R in MD simulations, and we selected the most plausible orientation based on the agreement with alanine mutagenesis supported by affinity experiments. Interestingly, for drug design purposes, the mutation of L250$^{6.51}$ to alanine increased the binding affinity of **A17** at A_1R. We explored the structure−activity relationships against A_1R using alchemical binding free energy calculations with the thermodynamic integration coupled with the MD simulation (TI/MD) method, applied on the whole GPCR−membrane system, which showed a good agreement (r = 0.73) between calculated and experimental relative binding free energies.

In Chapter 5, we sought to develop a computational model of inactive adenosine A_3 receptor (A_3R), not yet resolved experimentally, for drug design purposes. We tested five homology models of inactive human A_3R (hA_3R) that are either publicly available or available from a web-resource. After merging 3 homology models by similarity, we came up with homology Models 1 and 2 and the AlphaFold2-based Model 3. We observed that these models showed good agreement in the orthosteric binding area except in upper region where Models 1, 2 differed from Model 3 in the orientation of side chains of R173$^{5.34}$, M172$^{5.33}$ and M174$^{5.35}$ located in the extracellular loop 2 (EL2). We compared Models 1-3 regarding predictions of the experimentally determined thermodynamic and kinetic stability for the pyrazolo[3,4-*d*]pyridazine antagonists. The protein Models 1-3 in TI/MD calculations performed with good agreement (r = 0.74, 0.62 and 0.67, respectively) between the calculated and experimental relative binding free energies. The τ-Random Acceleration Molecular Dynamics (τRAMD) simulations effectively distinguished between compounds with short and long RT within the receptor only with Models 1, 2, since in Model 3 the orientation of R173$^{5.34}$ located at the top of ligands' exit route affected compound dissociation. By optimizing the orientation of side chains of residues M172$^{5.33}$, R173$^{5.34}$, M174$^{5.35}$ in Model 3 the optimized Model 3 was generated. τRAMD simulations using the optimized model 3 correctly ranked ligands according to their residence time inside binding site. Furthermore, the performance of TI/MD calculations with the optimized Model 3 was improved such as the Pearson correlation coefficient was increased from r = 0.67 to 0.84 while the mean assigned error was reduced from 0.81 kcal mol^{-1} to 0.56 kcal mol^{-1}.

Περίληψη

Στην προσπάθεια ανάπτυξης αποτελεσματικών θεραπειών, ο σχεδιασμός φαρμάκων βασισμένος στη δομή έχει αναδειχθεί ως μια ισχυρή προσέγγιση, εκμεταλλευόμενος την κατανόησή των μοριακών δομών για τον σχεδιασμό μορίων με βελτιωμένες ιδιότητες δεσμευτικότητας και λειτουργίας. Η αναζήτηση αποτελεσματικών θεραπειών που στοχεύουν στους υποδοχείς της αδενοσίνης (ARs), μέλη της οικογένειας των υποδοχέων που συνδέονται με G πρωτείνες (GPCRs), έχει αποκτήσει σημαντική σημασία λόγω της συμμετοχής τους σε διάφορες παθολογικές καταστάσεις.

Σκοπός αυτής της διατριβής είναι η ανάπτυξη ανταγωνιστών που στοχεύουν τους υποδοχείς της αδενοσίνης A1 και A3. Για την επίτευξη αυτού του στόχου, χρησιμοποιούνται προηγμένες υπολογιστικές μέθοδοι, όπως η αλχημική διαταραχή της ελεύθερης ενέργειας και υπολογισμοί κινητικής δεσμευτικότητας. Στο Κεφάλαιο 1, παρέχεται μια εισαγωγή στους GPCRs με έμφαση στους ARs. Αναφέρονται γνωστοί αγωνιστές, ανταγωνιστές και διπλοί ανταγωνιστές που δρουν στα ορθοστερικά και αλλοστηρικά σημεία των ARs. Το Κεφάλαιο 2 περιγράφει τις αρχές των χρησιμοποιούμενων μεθοδολογιών στην παρούσα διατριβή.

Στο Κεφάλαιο 3, τα συνθετικά παράγωγα των 7-αρυλικών ή αλκυλαμινο-πυραζολο[3,4-δ]πυριδαζίνη παρείχαν μια νέα πλατφόρμα για την ανάπτυξη δεσμευτών ενάντια στους ARs. Οι ενώσεις συντέθηκαν στο εργαστήριο της συνθετικής χημείας του ΕΚΠΑ υπό την επίβλεψη των καθηγητών Παναγιώτη Μαράκου, Νικόλ Πουλή και επίκουρου καθηγητή Νικόλαου Λουγιάκη και η βιολογική αξιολόγηση των ενώσεων έγινε με φαρμακολογικές και βιοφυσικές μεθόδους από το εργαστήριο φαρμακολογίας του καθηγητή Graham Ladds στο Πανεπιστήμιο του Cambridge. Η εισαγωγή ομάδας 3-φαινυλίου, μαζί με μια ομάδα 7-βενζυλαμίνης και μια ομάδα 1-μεθυλίου στην πυραζολοπυριδαζίνη παρήγαγε την ένωση ανταγωνιστή 10b με 26 nM συγγένεια δέσμευσης (Ki) και χρόνος παραμονής στον υποδοχέα (RT) 60 λεπτά για τον A_1R, 7,4 nM Ki και RT = 73 λεπτά για τον A_3R και χαμηλό μM Ki για τον A_{2B}R. Η αντικατάσταση του N-μεθυλίου στον δακτύλιο της πυραζόλης είχε εντυπωσιακή επίδραση στη βιοδραστικότητα, καθώς το αντίστοιχο 2-μεθυλ-3-φαινυλικό παράγωγο 15b, δεν είχε σημαντική συγγένεια δέσμευσης, ενώ όταν η 3-φαινυλική ομάδα του 10b αντικαταστάθηκε από μια ομάδα ισοπροπυλίου, το αποτέλεσμα που προέκυψε, το αντίστοιχο παράγωγο 10a, είχε σημαντικά μειωμένη συγγένεια δέσμευσης. Συγκρίναμε τα προφίλ δέσμευσης των 10b και 15b με προσομοιώσεις μοριακής δυναμικής (MD) και τα αποτελέσματα υποδήλωσαν ότι η ομάδα 2-μεθυλίου στο 15b εμποδίζει την δημιουργία δεσμών υδρογόνου με το N6.55 που θεωρείται κρίσιμο αμινοξύ για τη σταθεροποίηση μέσα στην ορθοστερική κοιλότητα. Οι πειραματικές

μελέτες γενετικής μετάλλαξης για το 10b στον A_1R παρείχαν αποτελέσματα που συμπληρώνουν τις παρατηρήσεις από τις προσομοιώσεις MD. Δείξαμε ότι η μετάλλαξη $L250_{6.51}A$ οδήγησε μόνο σε μια ελαφρά μείωση της συγγένειας δέσμευσης όσον αφορά το 10b, ενώ η μετάλλαξη $Y271_{7.46}A$ προκάλεσε μια μείωση 10 φορές στην συγγένεια πρόσδεσης αυτού του παραγώγου. Η μετάλλαξη σε αλανίνη των αμινοξέων $T91_{3.36}$, $H251_{6.52}$ ή $S267_{7.42}$, που βρίσκονται βαθιά στην ορθοστερική θέση δέσμευσης, δεν επηρέασε την συγγένεια δέσμευσης.

Στο Κεφάλαιο 4, αναφέρεται ο εντοπισμός των 7-(φαινυλαμίνων)-πυραζολο[3,4-κ]πυριδίνων L2-L10, A15 και A17 ως νανομοριακοί ανταγωνιστές των A_1R/A_3R, με την ένωση 3-φαινυλ-5-κυανο-7-(τριμεθοξιφαινυλαμίνο)-πυραζολο[3,4-κ]πυριδίνης (A17) να εμφανίζει την υψηλότερη συγγένεια και για τους δύο υποδοχείς όπως καθορίστηκε φαρμακολογικά με τη δοκιμασία NanoBRET. Στις προσομοιώσεις MD, δύο πιθανοί προσανατολισμοί δεσμεύσεων του A17 παρήγαγαν σταθερά σύμπλοκα μέσα στην ορθοστερική περιοχή του A_1R. Επιλέξαμε τον πιο πιθανό προσανατολισμό βασιζόμενοι στις μελέτες μεταλλαξηγένεσις. Ενδιαφέρον έδειξε η μετάλλαξη του αμινοξέος $L250_{6.51}$ σε αλανίνη, η οποία αύξησε την συγγένεια δέσμευσης του A17 για τον A_1R. Εξετάσαμε τις σχέσεις δομής-δράσης κατά τον A_1R χρησιμοποιώντας υπολογισμούς θερμοδυναμικής ολοκλήρωσης (TI/MD), μέθοδος που απορρέει χωρίς προσεγγίσεις (ab initio) από θεωρήματα στατιστικής μηχανικής για θερμοδυναμικά συστήματα, που εφαρμόστηκε σε ολόκληρο το σύστημα GPCR-μεμβράνης, το οποίο έδειξε καλή συσχέτιση ($r = 0,73$) μεταξύ των υπολογισμένων και των πειραματικών αποτελεσμάτων.

Στο Κεφάλαιο 5, αναπτύξαμε ένα υπολογιστικό μοντέλο του ανενεργού A_3R, που δεν έχει ακόμα επιλυθεί πειραματικά, για σκοπούς σχεδιασμού φαρμάκων. Δοκιμάσαμε πέντε υπολογιστικά ομόλογο μοντέλα του ανενεργού A_3R που είναι είτε διαθέσιμα δημόσια είτε διαθέσιμα από ένα διαδικτυακό εργαλείο. Καταλήξαμε στα υπολογιστικά Μοντέλα 1 και 2 που παράχθηκαν από πειραματικές δομές του ανενεργού $A_{2A}R$ ή του A_1R και το βασισμένο στο AlphaFold2 Μοντέλο 3. Διαπιστώσαμε ότι τα μοντέλα έδειξαν σχετική συμφωνία στον προσανατολισμό των πλευρικών αλυσίδων στην ορθοστερική περιόχη πρόσδεσης, εκτός από την ανώτερη περιοχή όπου τα Μοντέλα 1, 2 διέφεραν από το Μοντέλο 3 στον προσανατολισμό των πλευρικών αλυσίδων των αμινοξέων $R173_{5.34}$, $M172_{5.33}$ και $M174_{5.35}$ που βρίσκονται στο εξωκυττάριο βρόγχο 2 (EL2) και θεωρητικά θα μπορούσαν να λειτουργούν ως εμπόδιο στην έξοδο των φαρμάκων. Συγκρίναμε τα Μοντέλα 1-3 ως προς τις προβλέψεις της πειραματικά καθορισμένης θερμοδυναμικής και κινητικής σταθερότητας για την σειρά των αντγωνιστών πυραζολο[3,4-κ]πυριδίνων. Τα μοντέλα πρωτεΐνης 1-3 στους υπολογισμούς TI/MD παρουσίασαν καλή συσχέτιση (συντελεστής συσχέτισης Pearson $r = 0,74$, 0,62 και 0,67, αντίστοιχα) μεταξύ των υπολογισμένων και των πειραματικών αποτελεσμάτων.

Οι υπολογισμοί πρόβλεψης της κινητικής πρόσδεσης των ανταγωνιστών στους υποδοχείς με την μέθοδο τRAMD, κατέταξαν αποτελεσματικά τις ενώσεις ανάλογα με τον χρόνο παραμονής τους μέσα στον υποδοχέα χρησιμοποιώντας τα Μοντέλα 1, 2, αντίθετα στο Μοντέλο 3 ο προσανατολισμός της $R173_{5.34}$ που βρίσκεται στην κορυφή της διαδρομής εξόδου των φαρμάκων επηρέασε τη έξοδο των ενώσεων. Με τη βελτιστοποίηση του προσανατολισμού των πλευρικών αλυσίδων των αμινοξέων $M172_{5.33}$, $R173_{5.34}$, $M174_{5.35}$ στο Μοντέλο 3 δημιουργήθηκε το βελτιστοποιημένο Μοντέλο 3. Οι προσομοιώσεις του τ-RAMD χρησιμοποιώντας το βελτιστοποιημένο μοντέλο 3 κατέταξαν σωστά τις ενώσεις ανάλογα με τον χρόνο παραμονής τους μέσα στον υποδοχέα δεσμεύσης. Επιπλέον, η απόδοση των υπολογισμών TI/MD με το βελτιστοποιημένο Μοντέλο 3 βελτιώθηκε, καθώς ο συντελεστής συσχέτισης Pearson αυξήθηκε από r = 0,67 σε r = 0,84, ενώ η μέση ανισορροπία μειώθηκε από 0,81 kcal mol^{-1} σε 0,56 kcal mol^{-1}.

Acknowledgments

I would like to express my deep gratitude for IKY Foundation, which was my sole source of funding of my PhD thesis work. Then I would like to acknowledge the following people whose contribution was crucial for the successful completion of my PhD thesis:

I extend my special thanks to Prof. Antonios Kolocouris for his trust, guidance, and our fruitful discussions over the years. His mentorship has been invaluable in helping me grasp the fundamentals of drug design and the theoretical underpinnings of various computational methods.

I would like to thank Prof. Graham Ladds, member of the counseling committee, who contributed actively to the completion of this doctoral thesis by conducting the pharmacological work that complement my research at the Dept of Pharmacology, Cambridge.

Furthermore, my gratitude goes to Prof. Marakos Panagiotis, Prof. Pouli Nicole, and Assistant Prof. Nikolaos Lougiakis, a member of the examination committee, for their synthesis of the chemical compounds studied in this thesis.

Special thanks to Dr. Georgios Lamprinidis for his invaluable assistance in setting up and maintaining the workstations used in this research, as well as for his support with the algorithms. I also appreciate the insightful comments provided by Dr. Daria Kokh on the algorithms.

I am immensely thankful to all the current and former members of Prof. Antonios Kolocouris' lab that were fellow travelers to this journey, particular to my dear friend, Dr Eva Tzortzini, that made this journey feasible and pleasant.

Lastly, my heartfelt thanks to my family for supporting me on this journey. Without them I would never have been possible to begin this journey.

List of Publications

The following publications and presentation are a result of work done during the thesis:

1. **Stampelou M**., Ladds G., Kolocouris A., Computational Model for the Unresolved, Inactive A3R for Drug Design Purposes. (Submitted)

2. **Stampelou M***, Suchankova A*, Tzortzini E, et al. Dual A1/A3 Adenosine Receptor Antagonists: Binding Kinetics and Structure-Activity Relationship Studies Using Mutagenesis and Alchemical Binding Free Energy Calculations, J. Med. Chem., 2022 (first co-authors) (doi: 10.1021/acs.jmedchem.2c01123)

3. Suchankova A.*, **Stampelou M.***, Koutsouki K.*, et al. Discovery of a High Affinity Adenosine A1/A3 Receptor Antagonist with a Novel 7-Amino-pyrazolo[3,4-d]pyridazine Scaffold, Med. Chem. Lett., 2022, 13 (6), 923–934 (*first co-authors)

Talk: Dual A1/A3 Adenosine Receptor Antagonists: Binding Kinetics and SAR Studies Using Mutagenesis and Alchemical Binding Free Energy Calculations, EFMC 2022, Nice, France, September 2022

Table of Contents

List of Figures

List of Tables

Abbreviations

GPCR	G-protein coupled receptors
GDP	Guanosine diphosphate
GTP	Guanosine triphosphate
AC	Adenylyl cyclase
cAMP	Cyclic adenosine monophosphate
PKA	Protein kinase A
PLC-β	Phospholipase C-beta
PIP2	Phosphatidylinositol 4,5-bisphosphate
IP3	Inositol trisphosphate
DAG	Diacylglycerol
PKC	Protein kinase C
PI3K	Phosphoinositide 3-Kinase
PIP3	Phosphatidylinositol (3,4,5)-trisphosphate
MAPK	Mitogen-Activated Protein Kinase
ERK	Extracellular signal-regulated kinase
JNK	c-Jun N-terminal kinase
FZD	Frizzled
SMO	Smoothened
ECD	Extracellular domain
mGlu	Metabotropic glutamate receptors
VFT	Venus flytrap
GEF	Guanine nucleotide exchange factors
NC-IUPHAR	International Union of Pharmacology, Committee on Receptor Nomenclature and Classification
PDB	Protein data bank
TM	Transmembrane
SBDD	Structure-Based Drug Design
cryo-EM	Cryo–electron microscopy
MECA	Melanocortin, Endothelial, Cannabinoid and Adenosine receptors
SOG	Somatostatin, Opioid and Galanin
EC	Extracellular
IC	Intracellular
EL	Extracellular loop
IL	Intracellular loop
GRK	GPCR kinases
AR	Adenosine receptor
Ado	Adenosine

CNS	Central nervous system
COPD	Chronic obstructive pulmonary disease
NECA	1-(6-amino-9H-purin-9-yl)-1-deoxy-N-ethyl-β-D-ribofuranuronamide or 5'-(N-ethylcarboxamido)adenosine
IB-MECA	1-deoxy-1-[6-[[(3iodophenyl)methyl]amino]-9H-purin-9-yl]-N-methyl-β-D-ribofuranuronamide
HEMADO	2-(1-hexynyl)N6-methyladenosine
ZM241385	4-[2-[7-amino-2-(2-furyl)-1,2,4-triazolo-[1,5-a][1,3,5]triazin-5-ylamino]ethyl]phenol
FDA	Food and Drug Administration
PAM	Positive allosteric modulator
NAM	Negative allosteric modulators
MRCs	Multiple receptor conformations
AF	AlphaFold
SP	standard precision
XP	extra precision
MD	Molecular dynamics
PBC	Periodic Boundary Condition
NVT	constant number of particles, volume, and temperature
NPT	constant number of particles, pressure, and temperature
FF	Force field
PME	Particle Mesh Ewald
MM/PBSA	Molecular Mechanics - Poisson Boltzmann
MM/GBSA	Molecular Mechanics - Generalized Born Surface Area
LIE	Linear Interaction Energy
TI	Thermodynamic Integration
FEP	Free-Energy Perturbation
SMD	Steered molecular dynamics
PMF	Potential of mean force
VS	virtual screening
GPU	Graphics processing unit
SASA	solvent-accessible surface area
MBAR	Multistate Bennett Acceptance Ratio
RT	Residence time
SPR	surface plasmon resonance
BRET	bioluminescence resonance energy transfer
NanoBRET	Nano bioluminescence resonance energy transfer
MSM	Markov State Modelling
GaMD	Gaussian accelerated Molecular Dynamics
SEEKR	Simulation Enabled Estimation of Kinetic Rates
InMetaD	Multiple Infrequent Metadynamics
CVs	collective variables

ML	Machine Learning
RAMD	random acceleration molecular dynamics
β_2AR	β_2-adrenergic receptor
M_3R	muscarinic receptor M_3
mAChR M_2	muscarinic acetylcholine receptor M_2
CRF_1R	corticotropin-releasing factor type 1 receptor
τRAMD	τ-Random Acceleration Molecular Dynamics
hA_3R	human A_3R
pLDDT	predicted local-distance difference test
OPLS	Optimized Potentials for Liquid Simulations
RMSD	Root mean square deviation
MMFF94	Molecular mechanics force field 94
POPE	1-palmitoyl-2-oleoyl-*sn*-glycero-3-phosphoethanolamine
OPM	Orientations of Proteins in Membranes
GAFF	Generalized Amber Force Field
RESP	Restrained Electrostatic Potential
RESPA	Reversible reference system propagator algorithms
GUI	Graphical user interface
SID	Simulation interaction diagram
COM	centre of atoms
SEM	standard error of the mean
HEK293	human embryonic kidney 293
DMSO	Dimethyl sulfoxide
SAR	structure-activity relationship
mue	mean unsigned error
PI	predictive index
MRM	$M172^{5.33}$, $R173^{5.34}$, $M174^{5.35}$

Chapter 1.

Introduction

1. Introduction

1.1 G-protein coupled receptors (GPCRs)

G protein-coupled receptors (GPCRs) are the largest family of cell membrane receptors and have the ability to recognize a wide range of ligands, including photons and large protein molecules. [1,2] These receptors play a crucial role in regulating numerous physiological processes in various body systems, such as the skeletal, muscular, nervous, endocrine, urinary, and digestive systems, among others. Given their significance in human physiology, dysfunctions in GPCRs can lead to severe diseases, making them highly desirable targets for pharmaceutical intervention. In fact, GPCRs represent the largest protein family that current approved drugs target, with approximately 700 drugs on the market (around 35% of all approved drugs) specifically designed to interact with GPCRs. These numbers are expected to continue increasing as extensive research is being conducted to explore the druggability of GPCRs.[3,4]

Despite the diversity of natural GPCRs ligands, there exist several receptor subfamilies in which all proteins respond to a single endogenous agonist: for example, all GPCRs in the adrenergic subfamily are activated by epinephrine while all muscarinic receptors naturally bind acetylcholine and its derivatives. GPCR subtypes within a subfamily usually have distinct amino acid sequences, tissue distributions and/or functional and pharmacological profiles; however, their ligand binding pockets are highly conserved within the subfamily. The similarity of the orthosteric binding pockets poses a challenge for design of subtype selective ligands which remains one of the main hurdles in development of safe and effective medications targeting GPCRs [5].

1.1.1 GPCR signaling

The signaling pathway initiated by GPCRs involves the activation of G-proteins, which are intracellular proteins that act as molecular switches. Upon ligand binding to the GPCR, conformational changes occur that facilitate the interaction of the receptor with specific G-proteins. This interaction leads to the exchange of GDP (guanosine diphosphate) for GTP (guanosine triphosphate) on the G-protein, causing its activation.

G proteins are composed of three distinct α, β, and γ subunits. There are five subtypes of Gβ subunits and 12 subtypes of Gγ subunits that form constitutive Gβγ heterodimers. The Gα subunits are categorized into four main subtypes: Gαs, Gαi/o, Gαq/11, and Gα12/13. [6]

Both subunits have been shown to modulate the activity of different downstream effector proteins (Figure 1-1).

Their signaling cascades in more detail:

Gαs: Activation of Gαs stimulates adenylyl cyclase (AC), leading to an increase in cyclic adenosine monophosphate (cAMP) levels. Elevated cAMP levels then activate protein kinase A (PKA), which phosphorylates target proteins, resulting in diverse cellular responses such as increased heart rate, smooth muscle relaxation, and hormone secretion.

Gαi/o: Activation of Gαi/o inhibits AC, reducing cAMP levels and PKA activity. This leads to decreased cellular responses, including reduced heart rate, smooth muscle contraction, and neurotransmitter release inhibition.

Gαq/11: Activation of Gαq/11 stimulates phospholipase C-beta (PLC-β), leading to the hydrolysis of phosphatidylinositol 4,5-bisphosphate (PIP2) into inositol trisphosphate (IP3) and diacylglycerol (DAG). IP3 triggers the release of calcium ions from intracellular stores, while DAG activates protein kinase C (PKC). These events result in diverse cellular responses, including smooth muscle contraction, secretion, and cell growth.

Gα12/13: Activation of Gα12/13 leads to the activation of Rho family small GTPases, such as RhoA. These GTPases regulate actin cytoskeleton dynamics and cell shape changes, influencing processes such as cell migration, adhesion, and cell growth. [6–11]

While Gα subunits often receive the most attention, Gβγ subunits are equally critical for transmitting signals and modulating cellular responses. Gβγ subunits can regulate AC activity, either by inhibiting or stimulating its function. They can activate Phosphoinositide 3-Kinase (PI3K), a lipid kinase involved in cell growth, survival, and migration. Activation of PI3K by Gβγ

subunits leads to the production of phosphatidylinositol (3,4,5)-trisphosphate (PIP3), which recruits and activates downstream effectors involved in cellular responses such as cell proliferation and cytoskeletal rearrangement. They can also activate Mitogen-Activated Protein Kinase (MAPK) signaling pathways, including the extracellular signal-regulated kinase (ERK), c-Jun N-terminal kinase (JNK), and p38 pathways. Activation of these pathways by Gβγ subunits contributes to cellular processes such as cell proliferation, differentiation, and gene expression. Gβγ subunits can modulate intracellular calcium levels by directly interacting with calcium channels or by regulating calcium release from intracellular stores. This calcium signaling events are crucial for diverse cellular processes, including neurotransmitter release, muscle contraction, and gene expression. [1213]

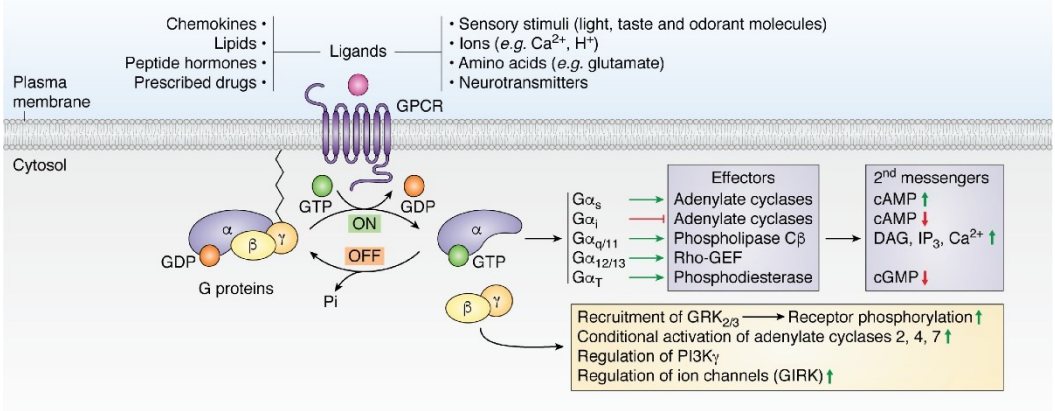

***Figure 1-1**: Diversity of G-protein-coupled receptor signaling. Upon ligand agonist binding, the receptor adopts an active-state conformation and interacts with one or multiple G proteins (Gαβγ), initiating a cascade of events. Specifically, the interaction facilitates the exchange of GDP for GTP on the Gα subunit and consequently, Gα and Gβγ subunits dissociate, enabling them to activate (→) or inhibit (—|) various effectors, which in turn regulate intracellular levels of second messengers. Adapted from Sutkeviciute and Vilardaga 2020* [11].

1.1.2 GPCR family

According to their sequence and function, GPCRs can be classified into six main sub-families, four of which contain mammalian GPCRs (Figure 1-2). Class A receptors, also known as rhodopsin-like receptors (80% of GPCRs, and most well studied); Class B secretin-like; Class C metabotropic glutamate receptors; and Class F frizzled (FZD) or smoothened (SMO) receptors. Class D and Class E families are composed of non-mammalian GPCRs. Class D family are fungal mating pheromone receptors while Class E family contains cAMP receptors from slime molds.

- **Class A**: The rhodopsin-like family (Class A) is the largest family of GPCRs found in most organisms. It includes > 700 members with 197 receptors with known ligands, > 400 olfactory receptors and 87 orphans. Within this family, members are recognized for their extensive range of ligands, encompassing hormones, peptides, odorants, and even photons of light. Given that the rhodopsin-like family constitutes over 80% of the GPCRs found in humans [14], it has garnered considerable attention in research efforts focusing on potential therapeutic advantages. The class A receptors according to Fredrikson et al. [15,16], it can be further divided into four main branches:

  - **α branch**: prostaglandin, amine, opsin, melatonin and MECA receptors (which include Melanocortin, Endothelial, Cannabinoid and Adenosine receptors),

  - **β branch**: most peptide receptors,

  - **γ branch**: SOG (for Somatostatin, Opioid and Galanin) receptors, melanin-concentrating hormone receptors and chemokine receptors, and

  - **δ branch**: Mas-related receptors, glycoprotein receptors, purine receptors and olfactory receptors.

- **Class B**: The secretin-like family (Class B) is another significant group of GPCRs. An important feature of this family is its large N-terminal extracellular domain (ECD), which plays a vital role in ligand recognition and binding, typically peptides or hormones. [17]

  - **Class B1** (secretin receptor family) includes 15 receptors with known ligands and 26 orphans. This class includes the calcitonin receptors, corticotropin-releasing factor receptors, glucagon receptor family, parathyroid hormone receptors and vasoactive intestinal peptide, pituitary adenylate cyclase-activating polypeptide and growth-hormone-releasing hormone receptors.

- **Class B2** (adhesion receptor family) includes 34 receptors, which possess a large extracellular N-termini.

- **Class C**: Metabotropic glutamate receptors (mGlu) (Class C) were discovered relatively late compared to the other GPCR families. The mGlu receptors bind a diverse set of ligands, such as amino acids, Ca2+ and pheromones. [18] These receptors possess a large ECD that forms a distinct structure known as the Venus flytrap (VFT) module. When a ligand binds to one lobe of the VFT, the other lobe closes, triggering a conformational change that is transmitted to the rest of the protein through a cysteine-rich region. They function as dimers, which are either covalently linked by disulfide bonds or through shared ion binding. [19]
- **Class F**: Frizzled or Smoothened receptors (Class F) contain a cysteine-rich domain in their N-terminus that binds lipoglycoproteins of the Wingless family. [20] More recently, both Frizzled and Smoothened receptors have been shown to also function as canonical GPCRs, Frizzled proteins, in particular, serve as guanine nucleotide exchange factors (GEFs) for Gαi/o proteins, while Smoothened acts as a GEF for Gαi. [21,22] Additionally, GPCRs belonging to the related adhesion group frequently possess cadherin or integrin domains, and many of these receptors exhibit auto-proteolytic activity. [23] The ligands for these receptors encompass various components of the extracellular matrix, including collagen. [24]

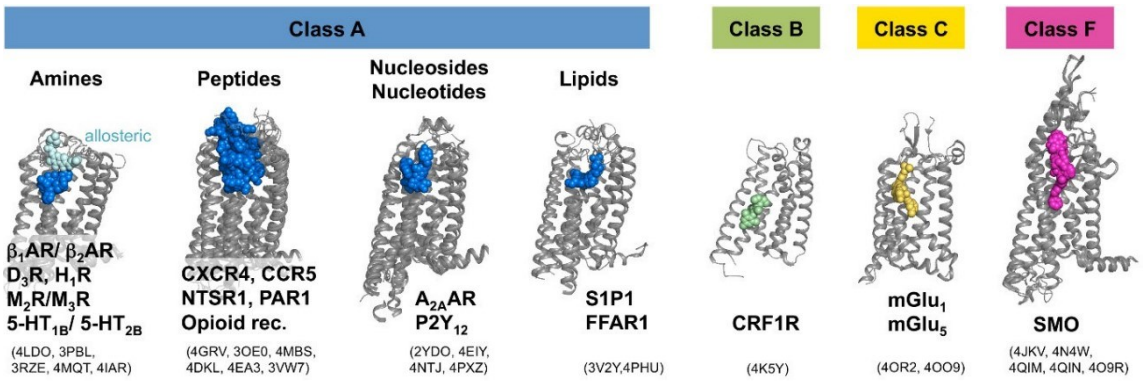

***Figure 1-2**:* Crystal structures of representative mammalian GPCR-ligand complexes from classes A, B, C, and F presenting diverse ligand-binding pockets*. Class A GPCRs are further subdivided into aminergic-like (β1AR/β2AR, D3R, H1R, M2R/M3R, 5-HT1B/5-HT2B)), peptide-like (CXCR4, CCR5, NTSR1, PAR1, Opioid receptor), nucleotide-like (A2AR, P2Y12), and lipid-like receptors (S1P1, FFAR1). Similarly, representative structures for class B (CRF1), class C (mGlu1, mGlu5 , and class F (SMO) are shown. Receptors are shown in cartoon representation and the ligands are shown as surface models. The PDB-IDs of the structures used for this graphic are indicated. Adapted from Shonberg et al. 2015.* [25]

Alternatively, GPCRs are classified into the GRAFS system, with each letter of the acronym standing for the most representative member of the family i.e., Glutamate, Rhodopsin, Adhesion, Frizzled/Taste2, Secretin. [15,26]

The International Union of Pharmacology, Committee on Receptor Nomenclature and Classification (NC-IUPHAR) [27](see http://www.guidetopharmacology.org/) recommends using the A-F system classification.

1.1.3 GPCR structures

All proteins in the GPCRs family share a common structure with seven-transmembrane (TM) α-helices, (TM1-TM7), which detect and transduce diverse external stimuli across the cell membrane, the diversity of which is particularly high for class A GPCRs, [4,28] and includes ions, small molecules, peptides, and globular proteins. [16]

In recent years, the field of GPCRs structural biology has experienced a significant resurgence, with numerous new experimentally resolved structures. [29] This progress is attributed to remarkable technological advancements in both membrane protein engineering and crystallography, which have facilitated an exponential growth in the determination of GPCR structures. These structures include receptors in both energetically stable inactive and active conformations, stabilized by either a heterotrimeric G protein or a G protein mimetic nanobody. Consequently, these solved structures not only offer molecular insights into ligand binding mechanisms, activation processes, allosteric modulation, and receptor dimerization but also open new avenues for Structure-Based Drug Design (SBDD).

For many years, the main choice in how to determine the structure of a GPCR coupled to a heterotrimeric G protein, was the X-ray crystallography. However, the disadvantage of the X-ray crystallography lies in the difficulty of producing good quality crystals of a GPCR coupled to a heterotrimeric G protein. New methods have been developed, such as lipidic cubic phase and cryo–electron microscopy (cryo-EM), in order to determine the structures of the GPCRs. In the cryo-EM method, it is noteworthy that even the low-resolution structures exhibit a high degree of flexibility, which stands in contrast to X-ray crystallography. [30].

The first protein found to be organized into seven transmembrane domains and finally became a model for structural studies of the GPCRs was bacteriorhodopsin [31], the major light-sensitive

protein of the purple membrane of Halobacterium halobium, and since bacteriorhodopsin's structure many GPCRs structures have been solved.

Common structural elements of the GPCR A family

Owing to the technological advances of X-ray crystallography and cryo-EM, during the last 2 decades, much has been learned about the structural characteristics of GPCRs.

All class A GPCRs exhibit common structural features consisting of seven transmembrane helices (TM1–TM7) linked by three extracellular loops (EL1–3 or ECLs) and three intracellular loops (IL1–3 or ICLs) (Figure 1-3) , the length of these loops varies between the members of the GPCR family. This 7TM bundle can be further divided into two modules: the extracellular (EC) and intracellular (IC) modules. The N-terminus, located on the extracellular side, and the ECLs play crucial roles in recognizing a wide array of ligands and modulating ligand entry. ECLs often contain disulfide bridges, vital for maintaining loop stability. [29]

The 7TM bundle constitutes the main structural core that undergoes conformational changes upon ligand binding, transmitting signals from the extracellular to the intracellular region. On the other hand, the C-terminus and the ICLs interact with G proteins, arrestins, GPCR kinases (GRKs), and other downstream signaling effectors, crucial for signal transduction and other receptor modulatory functions. The intracellular region is relatively conserved due to the limited types of downstream signaling effectors. The C-terminal region often contains a 3–4 turn α-helix, known as helix 8 that is characterized by a common [F(RK)xx(FL)xxx] amphiphilic motif and it carries a palmitoylation site that is responsible for anchoring helix 8 to the membrane.- [32]

The general numbering scheme for GPCRs is proposed by Ballesteros and Weinstein [33]. In essence, every residue is numbered as X.YY, where X corresponds to the transmembrane helix (X=[1,7]) and YY is a correlative number in the protein sequence, but taking as a reference position (YY=50) the most conserved residue in the given helix: Asn in TM1 (98%), Asp in TM2 (93%), Arg in TM3 (95%), Trp in TM4 (96%), Pro in TM5 (76%), Pro in TM6 (98%) and, Pro in TM7 (93%).

One of the most conserved motifs among Class A GPCRs, as proposed by the rhodopsin structure [31] is the amino acids glutamate acid/aspartic acid–arginine–tyrosine, i.e., the D[E]R$^{3.50}$Y motif in TM3 that has a significant role in regulating GPCR conformational states.

This motif forms a salt bridge with D/E$^{6.30}$ in TM6, the so called "Ionic lock" that may play a role in restraining the fully inactive conformation of the class A receptors. This ionic lock is considered a hallmark of the inactive conformation of GPCRs, obstructing G-protein binding at the cytoplasmic region. Furthermore, the W$^{6.48}$ xP motif in TM6 is regarded as one of the micro-switches that exhibit significantly different conformations in the active state compared to the inactive state of the receptor. Another conserved motif is the NP$^{7.50}$xxY motif in TM7, which also plays a vital role in GPCR activation. The extracellular loop regions in GPCR structures also show similarities. Particularly, a highly conserved disulfide bond between Cys$^{3.25}$ at the extracellular tip of TM3 and a cysteine residue in ECL2 is observed in most GPCR structures. This disulfide bond significantly contributes to stabilizing the extracellular region's conformation and helps the entrance to the ligand-binding pocket. [32]

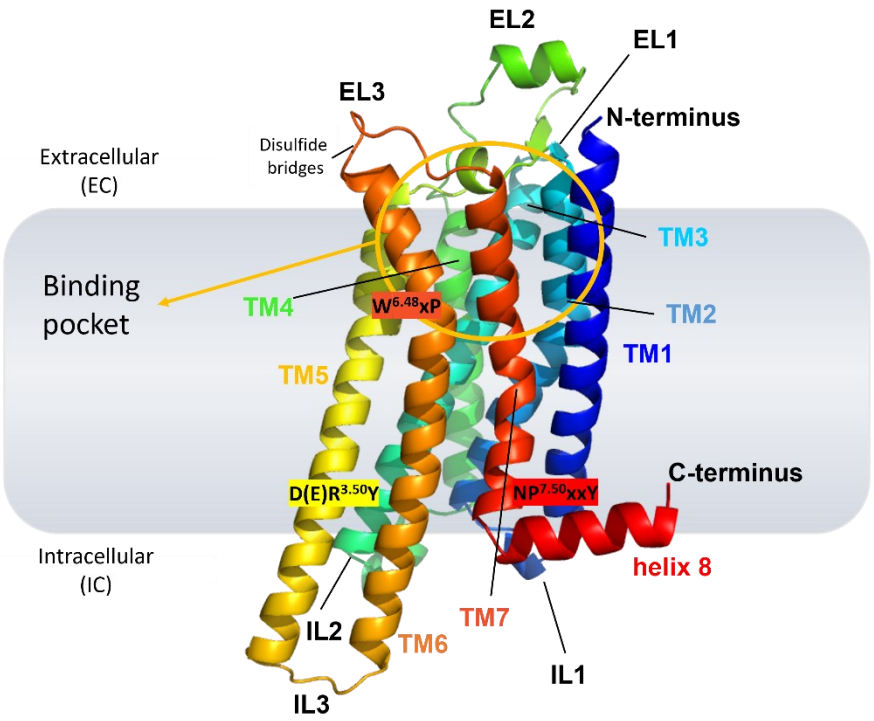

***Figure 1-3**: General architecture and structural features of GPCRs. The 7TM bundle (TM1–7) and key structural features are shown on an example of the Adenosine Receptor A_{2A}R crystal structure (PDB ID: 3eml)[34]. GPCRs are characterized by an extracellular N-terminus, followed by seven transmembrane α-helices (TM1-TM7) each shown in a different color. TM helices are connected by three intracellular (IL1-IL3) and three extracellular loops (EL1-EL3) and finally an intracellular C-terminus. The TM module (considered as the highly conserved component of GPCRs) shows characteristic hydrophobic patterns and several functionally potent signature sequence motifs, including the D(E)RY motif in TM3, the CWxP motif in TM6, and the NPxxY motif in TM7, which are also highlighted. The seven transmembrane helices form a cavity within the plasma membrane that serves as a ligand-binding domain (orange circle) that is often covered by EL2.*

GPCRs are activated by agonist ligand binding in the orthosteric binding pocket located within the upper half of the TM core. This binding event is relayed to the extracellular site of the receptor through allosteric interaction networks that are distinct for each GPCR class but converge in a common GPCR activation hallmark—the mobilization and outward movement of TM6. The outward movement of TM6 leads to the opening of the cytosolic cavity of the GPCRs, allowing the subsequent binding and activation of the heterotrimeric G proteins. (Figure 1-4)

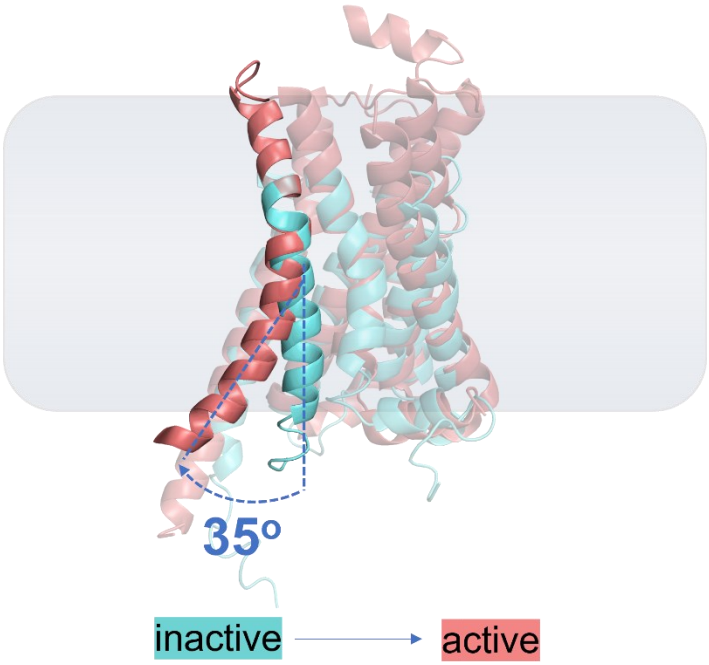

Figure 1-4*: Comparison of inactive → active state transition between representative class A β2 adrenergic receptor. The common activation hallmark is an outward movement of TM6. The inactive- and active-state structures are shown as semi-transparent cyan and pink cartoons, respectively, with TM6 helices highlighted as an opaque cartoon and dashed lines connected with an arrow depicting transition from the inactive to the active state. The superimposed structures are as follows: inactive-state (PDB entry 2R4R)* [35] *and active-state (PDB entry 3SN6)* [36] *β2AR. The G protein is not depicted in the active-state structure.*

Despite sharing a common 7TM architecture, GPCRs represent an intriguing model of finely tuned recognition modules. This is attributed to their ability to recognize a wide range of ligands with distinct physicochemical and structural properties, highlighting an extraordinary convergence in signaling and regulatory processes.

1.2 Adenosine Receptors (ARs)

Adenosine receptors (ARs) are class A GPCRs that are widely distributed throughout the human body. These receptors play crucial roles in various physiological and pathological processes, making them attractive targets for drug development. Understanding the tissue distribution, functions, and structures of adenosine receptors is essential for understanding their significance in both health and disease. There are four subtypes of adenosine receptors: A_1, A_{2A}, A_{2B}, and A_3. Each subtype has distinct functions and signal transduction mechanisms. Among the four subtypes the most similar are the A_1 and A_3 ARs (49% sequence similarity) and the A_{2A} and A_{2B} ARs (59% similarity).

1.2.1 Adenosine receptors as drug targets

ARs natural ligand is adenosine (Ado), an endogenous purine nucleoside which is released in response to cellular stress and inflammation. Each subtype has a different affinity for adenosine with the A_1R having the highest affinity at approximately 70 nM and the $A_{2A}R$ having a lower affinity at approximately 150 nM. The A_{2B} and A_3 receptors have a much lower affinity at 5100 nM and 6500 nM, respectively. [37]

Adenosine is involved in the regulation of various biological functions in different tissues and organ systems, including cardiovascular, liver, renal, respiratory and central nervous system (CNS) through its receptors. [38] When adenosine levels are low, it binds preferentially with A_1R or A_3R and activates Gi/o protein, thus reducing AC and PKA activity. Instead, when adenosine levels are higher, its binding is favored to $A_{2A}R$ or $A_{2B}R$, activates Gs protein, and stimulates the AC/cAMP/PKA cascade. [39]Therefore, adenosine depending on its concentration may affect several physiological or pathological processes.

The development of drugs targeting ARs is a topic of active research. Scientists and pharmaceutical companies are exploring various approaches, including the design of selective agonists, antagonists, and allosteric modulators for each receptor subtype (Figure 1-5). The aim is to develop drugs with improved efficacy, selectivity, and reduced side effects. ARs are present in virtually all tissues and organs. This widespread distribution reflects the diverse functions that these receptors serve in various physiological and pathological processes. The ARs are prominently expressed in specific locations and exert their effects through signaling pathways

involving the activation of G-proteins and the subsequent modulation of intracellular signaling cascades. However, the widespread presence of ARs increases the likelihood of side effects, making the promising potential of selective AR modulators quite a challenging task. [40]

The functions and tissue distribution of each AR subtype, as well as the diseases in which ARs are involved, are presented in summary below and in (Figure 1-5).

A_1R

The A_1R is the most conserved adenosine receptor subtype among species, and it is widely expressed throughout the body with the highest levels found in the brain. It is highly concentrated in regions involved in sleep regulation, such as the basal forebrain and the hypothalamus. Additionally, A_1 receptors are found in areas involved in pain perception, such as the spinal cord and the periaqueductal gray. Within the cardiovascular system, A_1Rs are expressed in cardiac muscle cells and blood vessels. Activation of A_1R in the heart leads to a decrease in heart rate, resulting in a cardioprotective effect. In blood vessels, A1 receptors are involved in regulating vascular tone and blood pressure. They are also present in smooth muscle cells of the lungs, where they modulate bronchoconstriction and airway diameter. In the gastrointestinal tract, they are found in the liver, where they are involved in the regulation of glucose and lipid metabolism. [38] A_1R is an attractive pharmacological target, since its antagonists have been explored as kidney-protective agents, cognitive enhancers, and antiasthmatic and CNS agents. [41] [40]

$A_{2A}R$

$A_{2A}R$ antagonists have emerged as an attractive approach to treat Parkinson, sickle cell and infectious diseases, cancer, ischemia reperfusion injury, diabetic nephropathy, cognition, and other CNS disorders. [42] Activation of $A_{2A}R$ in the brain influences the release of neurotransmitters like dopamine, which is essential for movement and pleasure. Additionally, A_{2A} receptors play a role in cognitive functions, including attention, learning, and memory. They have been also implicated in neurodegenerative disorders; $A_{2A}R$ antagonists have shown promise in alleviating motor symptoms associated with Parkinson's disease and they may have therapeutic implications in managing neuroinflammation in Alzheimer's disease.

In peripheral tissues, $A_{2A}Rs$ are involved in the modulation of inflammation, blood flow, angiogenesis and the control of cancer pathogenesis. [38] Within the cardiovascular system, $A_{2A}Rs$ are expressed in cardiac muscle cells and blood vessels. $A_{2A}R$ agonists promote vasodilation and improved blood flow, making them promising candidates for the management of hypertension

and ischemic heart disease. In the lungs, they are important targets for the treatment of respiratory conditions, such as asthma and chronic obstructive pulmonary disease (COPD). A_{2A}Rs are found in immune cells and their agonists have been investigated as potential treatments for inflammatory conditions such as rheumatoid arthritis and inflammatory bowel disease. [41] [40]

A_{2B}R

The A_{2B} receptor is prominently found in various tissues, including the lungs, immune cells, and blood vessels but mostly in low abundance. A_{2B}R antagonists may be useful for the treatment of asthma, COPD. They are also present in immune cells, including T cells and macrophages. Activation of A_{2B}R on immune cells can modulate immune responses and influence inflammation. [38] Furthermore, A_{2B}Rs are expressed in blood vessels, where they contribute to the regulation of vascular tone and blood flow.

A_3R

A_3R is a target for a number of inflammatory diseases, including asthma, glaucoma, COPD, rheumatoid arthritis and ischemic injury. [38] In addition, evidence is emerging to suggest that the A_3R is over-expressed in various tumor cells compared to normal cells, presenting the possibility that A_3R may be a viable drug target against cancer cell proliferation.[43] In the brain, they are expressed in regions involved in pain perception and inflammation regulation. They are also expressed in immune cells, including mast cells, neutrophils, and macrophages. A_3R activation has been implicated in the regulation of mast cell degranulation, which plays a role in allergic responses and asthma. Within the cardiovascular system, activation of A_3R can have cardioprotective effects, including reducing myocardial injury during ischemia and reperfusion. In blood vessels, A_3R activation can influence vascular tone and regulate blood flow. [41] [40]

Understanding the functions of ARs provides valuable insights into their potential as therapeutic targets and their implications in various physiological and pathological conditions. Targeting ARs with selective or non-selective drugs holds promise for the development of treatments for sleep disorders, neurological disorders, pain management, cardiovascular diseases, respiratory conditions, gastrointestinal disorders, metabolic disorders, immune disorders, inflammatory conditions and certain types of cancer.

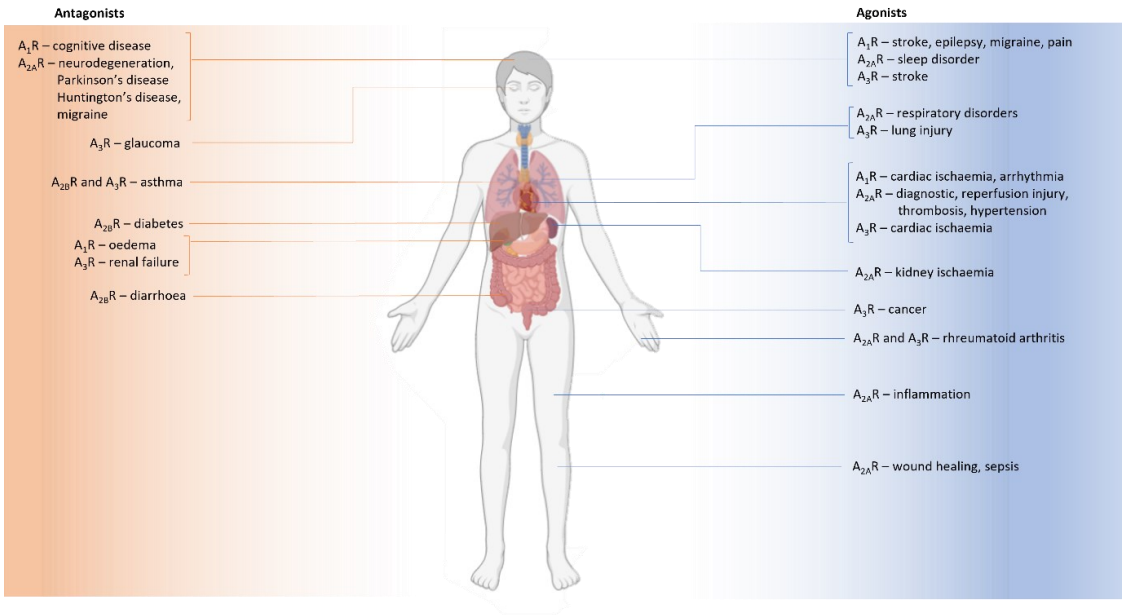

***Figure 1-5**: Disease targets for selective adenosine receptor agonists and antagonists. Most promising prospects exist for treatment of arrhythmias, ischemia of the heart, pain, neurodegenerative diseases, sleep disorders, inflammation, cancer and glaucoma.*

1.2.2 Structures

Understanding the structures of ARs is crucial for elucidating their mechanisms of action and designing selective or non-selective drugs targeting these receptors. The four subtypes share common GPCRs structural features. However, each subtype exhibits distinct structural features and differential affinities for adenosine and selective ligands.

The below Figures (Figure 1-6, Figure 1-7) show the structures of adenosine and other representative agonists, like the 1-(6-amino-9H-purin-9-yl)-1-deoxy-N-ethyl-β-D-ribofuranuronamide or 5'-(N-ethylcarboxamido)adenosine (**NECA**), the 1-deoxy-1-[6-[[(3-iodophenyl)methyl]amino]-9H-purin-9-yl]-N-methyl-β-D-ribofuranuronamide (**IB-MECA**), the 2-(1-hexynyl)-N6-methyladenosine (**HEMADO**) etc, and some common ARs antagonists like caffeine, theophylline and the A_{2A} and A_{2B} antagonist 4-[2-[7-amino-2-(2-furyl)-1,2,4-triazolo-[1,5-a][1,3,5]triazin-5-ylamino]ethyl]phenol (**ZM241385**) that will be discussed further below.

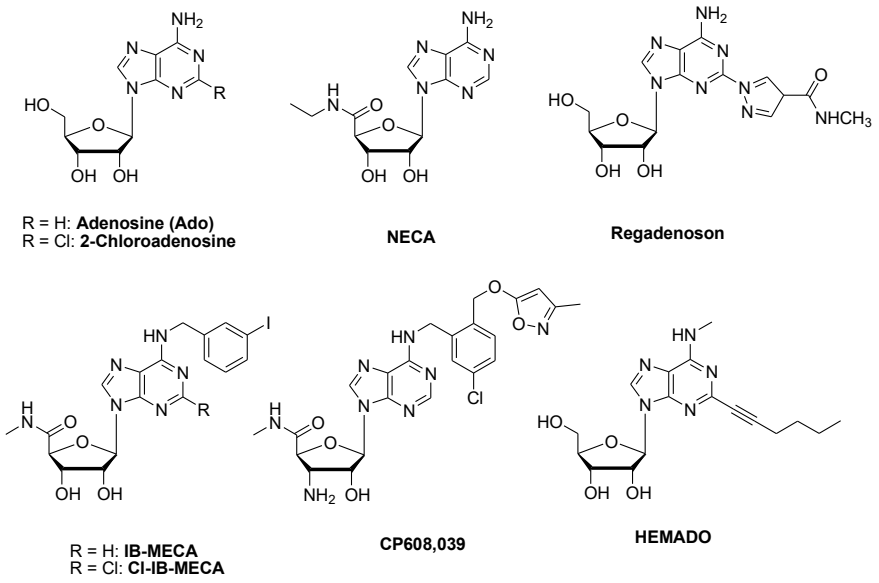

***Figure 1-6**: Chemical structures of representative ARs agonists.*

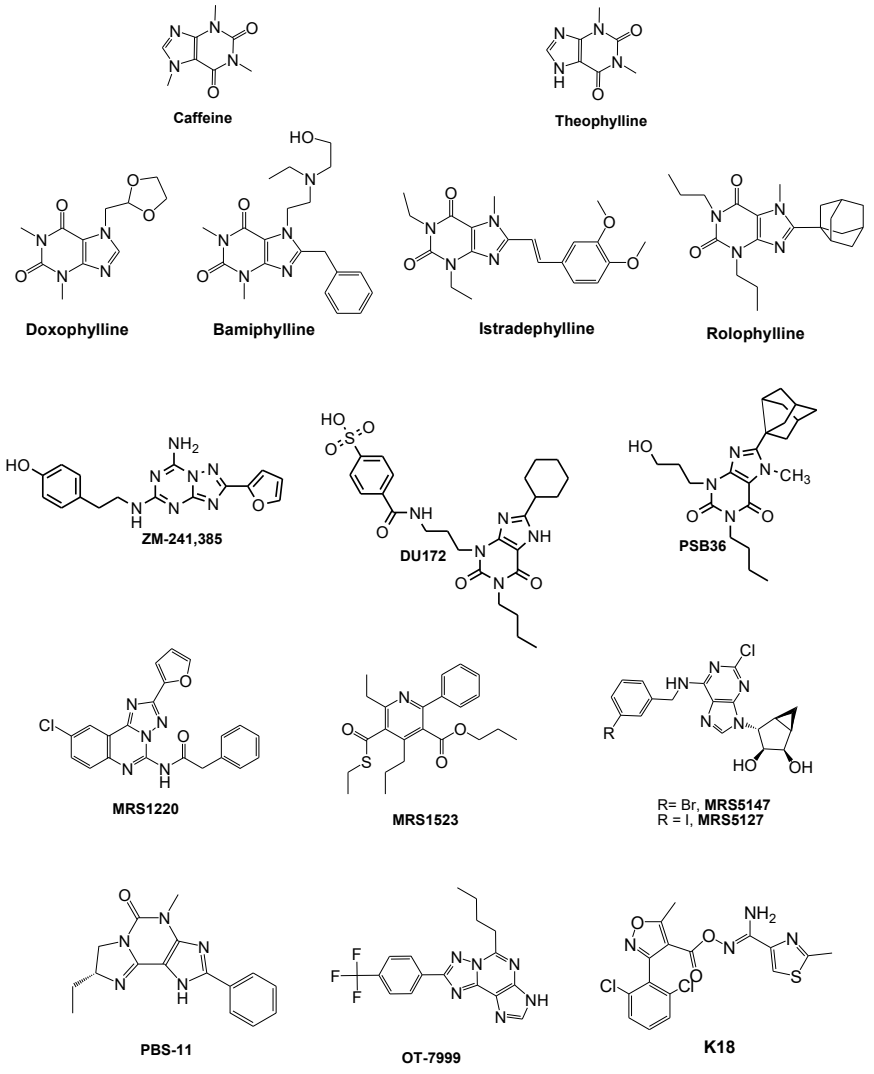

***Figure 1-7**: Chemical structures of representative ARs antagonists.*

The publication of the X-ray structure of $A_{2A}R$ bound to the antagonist **ZM241385** (Figure 1-7) in 2008 [34], revealed the binding mode of this antagonist (see Figure 1-8B). This significant advancement significantly improved the methodologies for membrane protein crystallization and structural biology techniques. Additionally, the $A_{2A}R$-**ZM241385** complex structure paved the way for highly successful structure-based approaches in ligand discovery, resulting in elevated hit rates and the identification of novel ligands. [44]

This milestone subsequently facilitated the experimental determination of three out of four AR subtypes. These structures have yielded valuable insights into the ligand binding pockets and the conformational changes that occur upon receptor activation. The structural similarities among adenosine receptor subtypes allow for the design of ligands with varying affinities and selectivity.

Since 2008, $A_{2A}R$ has received extensive attention and was considered a prototypical receptor within the GPCR superfamily. $A_{2A}R$ structures with different types of ligands were determined by crystallography or cryo-EM, revealing the inactive, intermediate, and fully active conformations. The binding mode of agonists like **Ado** and **NECA** (Figure 1-6) were resolved using X-ray crystallography [45 46 47 48 49] or cryo-EM.[30], respectively. Additionally, the binding mode of several antagonists (Figure 1-7) i.e. **ZM241385**, [34,50] **PSB36**, caffeine and theophylline[51 52 53 54] inside the $A_{2A}R$ and one bound to an engineered G protein [47] have been determined since 2008.

Similarly, structures of the A_1 subtype receptor (A_1R) have also been determined, providing insights into its structure-function relationship. These structures show the binding of A_1R with the antagonists **DU172** [55] (Figure 1-7, Figure 1-8B) and **PSB36** [56] and the adenosine-bound A_1R-G_i complex. [57]

More recently, the A_{2B} subtype receptor ($A_{2B}R$) has been investigated, and its structures have been reported [58,59]. The $A_{2B}R$ structure exhibits a larger extracellular region compared to other adenosine receptor subtypes. This region is involved in interactions with ligands and may contribute to the receptor's selectivity. The $A_{2B}R$ structure also provides insights into its binding pocket and conformational changes upon ligand binding, facilitating the design of specific drugs targeting this receptor.

However, the detailed structure of the A_3 subtype adenosine receptor (A_3R) is yet to be resolved, and further research is needed to obtain a comprehensive understanding of its molecular architecture. Therefore, homology modeling must be employed to study A_3R in complex with ligands.

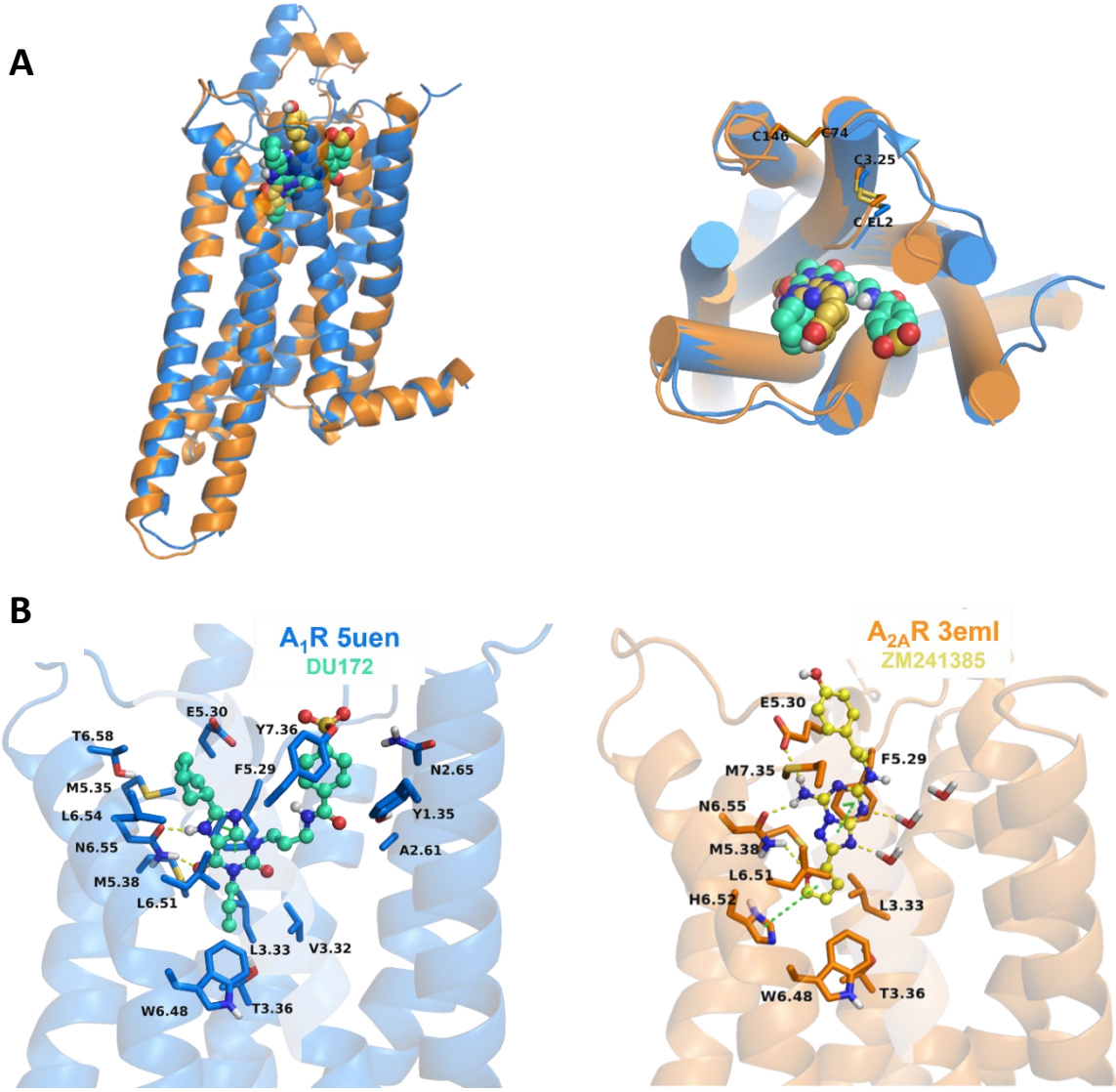

***Figure 1-8**: Comparison of the experimentally resolved structures of A1R (PDB ID 5UEN [55]) and A2AR (PDB ID 3EML [34]) (A) side and top view structural comparison. (B) Binding modes of DU172 (A1R) and ZM241385 (A2AR). The complex is viewed from the membrane side facing helices TM6 and TM7 with the view of TM7 partially omitted. The A1R is colored in blue and the A2AR in orange; Binding site residues are shown as sticks; DU172 (cyan) and ZM241385 (yellow) are shown as stick-ball models.* Yellow dashed lines represent H-bonds, green dashed lines represent π-stacking interactions.

ARs structures have revealed critical determinants in shaping the orthosteric binding sites, influencing ligand recognition, and defining the receptor's pharmacological profile. In more detail, it has been reported that the EL2 may orchestrate a network of interactions which may stabilize the inactive conformation of the receptor and/or kinetically control the receptor-ligand recognition [60,61]. A_{2B}Rs are characterized by the longest EL2 (≥38 amino acids) while in A_3 subtype, EL2 is the shortest (≥28 amino acids). [62] Despite the high degree of structural diversity

with respect to EL2 in family A GPCRs, there is one feature that is conserved in the vast majority of GPCRs i.e. a disulfide bond between EL2 and the top of TM3 (Cys3.25) (Figure 1-8A). This disulfide bond effectively tethers EL2 on the top of the TM helical bundle and provides a very important conformational constraint of the EL2. Some GPCRs have additional disulfide bonds between different ELs such as for example between EL2-EL1 in $A_{2A}R$. Additionally, the $A_{2A}R$ subtype also possesses an additional intra-loop disulfide bond within EL3, in common with melanocortin receptors and human histamine receptor 1. These "additional" disulfide bonds contribute to reduce the flexibility of ELs and, consequently, they peculiarly sculpt the topography of the extracellular portion of the receptor in proximity of the orthosteric binding cleft. Finally, only one cysteine-bridge, linking TM3 to EL2 in $A_{2B}R$ models, is detectable.

If the orthosteric binding area is compared for the ARs, the A_1 subtype has a much closer homology to $A_{2A}R$. Although A_1R differs from $A_{2A}R$ by only four residue changes in the periphery of the binding pocket, the shape of the binding area differs according to the recently published X-ray structure of A_1R in complex with the covalently bound antagonist **DU172** [55]**.** It was showed that due to movements of TM1, TM2, TM3 and TM7 and EL3 in A_1R., binding cavity is very wide and open compared to $A_{2A}R$ which is elongated and narrower. (Figure 1-8) The $A_{2A}R$ pocket is narrower with Met(7.35) acting as a gatekeeper (see Figure 1-8B) and preventing entry and binding of bulky substituents. The compact structure of the TM bundle of the $A_{2A}R$ is consistent with its unique disulphide bond, C74-C146, through which the beginning of TM3 is tightly connected with the end of EL2 allowing for shifts in 1, 2, and 3 TMs as suggested. Both A_1 and A_3Rs lack this disulphide bond. According to ref. [55], TM7 also tilts towards TM6, possibly as a result of a shorter EL3 in the A_1R due to the deletion of one amino acid; EL3 is also shorter by one amino acid in A_3R. These differences in ELs tethering result in the different shape of binding site and influence especially the approach of the ligand. A_1R binding area includes a common orthosteric binding region and a secondary one, i.e., there is a common region covered by **ZM241385** inside $A_{2A}R$ or **DU172** inside A_1R despite their different orientation and height into the cavity and the different shape and extension of the binding area (Figure 1-8). A_1, A_{2A}, $A_{2B}Rs$ contain the E(5.30) residue, except A_3R which have a valine in (5.30) position. This glutamate acid residue in (5.30) position may play a key role in high affinity ligand binding through the formation of a strong hydrogen bond, for example, with an unsubstituted exocyclic amine. Instead, the valine in (5.30) position of A_3R may allow bulky substituents fitting, for example, bulky substituents on amino group or other lipophilic moieties at this region.

The structural information of adenosine receptors has paved the way for the development of selective or non-selective drugs that target these receptors. Selective ligands that specifically

bind to a particular adenosine receptor subtype have been developed for therapeutic applications. These ligands can modulate the activity of the receptors, leading to various physiological effects. Furthermore, the structural insights into adenosine receptors have allowed the design of non-selective ligands that can target multiple receptor subtypes simultaneously. These ligands offer the advantage of broader efficacy in modulating adenosine receptor signaling.

1.2.3 Agonists and antagonists

The main approach for discovering AR agonists has been modification of adenosine itself. Optimization of **Ado** has been achieved after structural modifications of the ribose moiety and by substitutions on the adenine ring and few structures are shown in Figure 1-6**.** [63] However, **NECA** and analogues are non-selective AR agonists and their side effects include chest pain, flushing, dyspnoea and low blood pressure through the activation or inhibition of different AR subtypes.[64] Among the developed agonists [65–69] **IB-MECA** (CF101, Piclidenoson, and its 2-chloro analogue, **Cl-IB-MECA** (CF102, Namodenoson) are the most potent, subtype-selective and widely used A_3R agonists that have progressed to advanced clinical trials for the treatment of inflammation and cancer, respectively.[70,71] Both compounds [63] inhibit tumor cell growth according to *in vitro* and *in vivo* tumor models.[72–74]. Other potent and selective A_3R agonists, which have been synthesized as analogues of **NECA** and **IB-MECA** include **CP-608,039** [65], **HEMADO** [67], etc. Despite early setbacks, 2008 has been marked by successful FDA approval of the new generation $A_{2A}R$ selective agonist regadenoson as a coronary vasodilator for use in myocardial perfusion imaging. This breakthrough, along with other advances in preclinical and clinical studies [41] boosts interest to development of a new generation of bio-available and safe agonists and antagonists for adenosine receptors. [5]

Similarly, the main approach for the discovery of AR antagonists (Figure 1-7) has been modification of xanthines such as the non-selective antagonists caffeine and theophylline. Selective human A_1R or $hA_{2A}R$ antagonists have already reached market. The hA_1R antagonist **theophylline** is a natural product and **doxophylline**, **bamifylline** , have been approved in the market against paroxysmal supraventricular tachycardia and asthma, respectively [75,76] (Figure 1-7). A phase III clinical trial of the selective hA_1R antagonist **rolofylline** has been developed for the treatment of congestive heart failure but although has shown excellent tolerability of the

drug, but lack of efficacy. [77] The selective $hA_{2A}R$ antagonist **istradefylline** was studied in phase III clinical trials and is currently approved as Parkinson disease therapy in Japan. [78]

A_3R antagonists haven't entered clinical trials so far. One reason may be the large species differences between hA_3R and rodent A_3Rs that impair antagonists' development through mice models. [79–81] The affinity at the human subtype is usually considerably higher than in the rat A_3R (rA_3R). [79,80] Early efforts to discover selective antagonists primarily involved extensive pharmacological screening of various heterocyclic compounds with a non-purine structure. The first nonxanthine heterocyclic derivatives found to be selective for the hA_3R were **MRS1220** ((N-[9-chloro-2-(2-furanyl)[1,2,4]triazolo[1,5-c]quinazolin-5-yl]benzeneacetamide) and its derivative **MRS1523** (5-propyl-2-ethyl-4-propyl-3-(ethylsulfanylcarbonyl)-6-phenylpyridine-5-carboxylate) [82,83] **MRS5147** (1' R, 2' R, 3' S, 4' R, 5' S)-4'-[2-chloro-6- (3-bromobenzylamino)-purine]-2', 3'-O-dihydroxybicyclo- [3.1.0]hexane) and its 3-iodo analogue **MRS5127** are highly selective A_3R antagonists in human, based on a conformationally constrained ribose-like ring that is truncated at the 5' position [84]. Cyclized derivatives of xanthines, such as the **PSB-11** (R)-4-methyl-8-ethyl-2-phenyl-4,5,7,8-tetrahydro-1H-imidazo[2,1-i]purin-5-one), are also A_3R-selective [41]. Selective A_3R antagonists are used for studies of several diseases, such as the heterocyclic derivatives **OT-7999** (5-n-butyl-8-(4-trifluoromethylphenyl)-3H-[1,2,4]triazolo-[5,1-i]purine)which has been used for the treatment of glaucoma studies [85], and other such antagonists are under consideration for treatment of cancer, stroke, and inflammation [40,86]. No selective A_3R antagonists have yet reached human trials.

In a previous work of our lab, from *in silico* screening of Maybridge HitFinder Library [87] we identified new hits in collaboration with Prof. N. Klotz (Wurtzburg, Germany) using radiolabeled assays and Prof. G. Ladds (Dept of Pharmacology, Cambridge) using Nano bioluminescence resonance energy transfer (NanoBRET) assays and functional assays. These include antagonist **K18,** with low micromolar affinities against hA_3R. [87] We investigated the structural features of the orthosteric binding profile of the agonist **IB-MECA** and antagonist **K18** in complex with the experimentally unresolved hA_3R using MD simulations, site-directed mutagenesis experiments and functional assays. [88–90]

1.2.4 Allosteric modulators

Allosteric modulation, which involves ligands binding to sites other than the primary binding site of a receptor, has gained significant attention in recent years. [91–93] These ligands can modify the receptor's response to stimuli. Positive allosteric modulators (PAMs) enhance agonist-mediated responses, while negative allosteric modulators (NAMs) attenuate the response.

A recent review article [93] summarizes the recent findings of allosteric modulators for ARs. Several allosteric modulators targeting A_1 and various A_3 ARs have been identified, and their validation in diverse preclinical scenarios has shown promising outcomes. In contrast, the quest for allosteric modulators for A_{2A} and A_{2B} ARs has been less successful, but the findings obtained thus far are still encouraging.

Allosteric modulators of ARs hold great potential as valuable pharmacological tools, capable of potentially surpassing the limitations associated with orthosteric ligands. However, developing allosteric modulators for ARs and GPCRs in general remains challenging. Detection of allosteric behavior is also limited, and some modulators may not have been correctly identified initially. Additionally, the binding of NAMs may resemble that of competitors, further complicating the identification process. Structural determination through techniques like crystallography and cryo-EM has been instrumental in identifying allosteric binding sites. [94]

1.2.5 Dual Antagonists

Dual antagonists are a class of drugs that simultaneously block two or more subtypes of adenosine receptors. These compounds have the ability to bind to multiple adenosine receptor subtypes, thereby inhibiting their activity and modulating downstream signaling pathways. The development of adenosine receptor dual antagonists has gained attention as a potential therapeutic strategy for various conditions. The potential applications of adenosine receptor dual antagonists could include the development of treatments for various diseases with enhanced therapeutic effects and simplified drug regimens. It is also known that multi-target drugs for treatment of complex diseases are considered safer than drug combinations since they have lower toxicities and a lower risk of drug-drug interactions. [95]

Thus, the development of dual- or multi-target drugs can offer significant advantages. A dual $hA_{2B}R/hA_3R$ antagonist was designed as an anti-asthmatic agent. [96] Recent data suggested that

dual $hA_1R/hA_{2A}R$ antagonists may have therapeutic value against Parkinson's disease and epilepsy. [97] By blocking these receptors, these dual antagonists may help modulate neurotransmitter release and improve motor symptoms or reduce seizure activity. [98–100] Dual antagonism of $A_1R/A_{2A}R$ has also opened up new prospects for the treatment of diabetes. [100] Additionally, a recent study on the pyridone-substituted triazolopyrimidine scaffold showed great potential as a novel foundation for advancing the development of dual $A_1R/A_{2A}R$ antagonists as a potential treatment for the ischemic stroke. [100]

No pharmacological data on dual hA_1R/hA_3R ligands have been published. Antagonists of both hA_1R and hA_3R, targeting the same Gi-mediated pathway, may be useful and might even show synergistic effects for the treatment of important diseases including (i) acute kidney injury and kidney failure, [101] (ii) inflammatory pulmonary disease, asthma, allergy, [102] and (iii) Alzheimer's disease. [103–105]

Developing adenosine receptor dual antagonists poses certain challenges, including achieving sufficient selectivity for the desired receptor subtypes and managing potential side effects resulting from the simultaneous blockade of multiple receptors. However, advancements in medicinal chemistry and structure-based drug design could facilitate the discovery and optimization of dual antagonists with improved selectivity and pharmacokinetic properties. Further research and development efforts are needed to refine the selectivity, efficacy, and safety profiles of such dual antagonists. The exploration of adenosine receptor dual antagonists opens new possibilities for pharmacological interventions and may contribute to improved patient outcomes in various disease settings.

Chapter 2.

Methodology

2. Methodology

The aim of this chapter is to give a general overview of the computational chemistry techniques employed through the present thesis followed by a section of brief descriptions of the protocols of the computational methods used.

Computational chemistry, which belongs to a part of the *in-silico* realm, studies molecular systems through the application of computational models and simulations (numerical algorithms) with the aim of understanding their structure and/or properties.

Computational chemistry has revolutionized the drug discovery process by accelerating and optimizing the identification and design of potential drug candidates. Through the simulation of molecular interactions, binding affinities, and pharmacokinetic properties, enables the screening of vast chemical libraries, predict the activity of molecules, and prioritize the most promising candidates for experimental validation. Moreover, computational chemistry aids in the understanding of structure-activity relationships, guiding the modification of lead compounds to enhance their potency, and selectivity.

2.1 Theory

2.1.1 Homology Modelling

Homology modeling is a computational technique used for predicting the three-dimensional structure of a target protein by using the structure of a related protein with a known 3D structure as a template. The process involves aligning the amino acid sequence of the target protein with a template protein and then constructing a model based on the template's structural information. The underlying principle behind homology modeling is the observation that structural features are often more conserved throughout evolution than the exact amino

acid sequence. Therefore, if two proteins share significant sequence similarity, their structures are likely to be similar as well. [106,107]

The accuracy and reliability of a homology model depends on the degree of sequence identity and similarity between the target and template proteins. Higher sequence identity and similarity typically result in more accurate models. However, certain regions of the model, especially loop regions, can be challenging to predict accurately due to insertions or deletions in the sequence, making them less conserved. Consequently, loop regions are often the most error-prone parts of the homology model.

Unlike A_1R [55–57] and $A_{2A}R$ subtypes [30,34,45,47,49,51,54] and more recently the $A_{2B}R$ subtype [58,59], the detailed structure of the A_3R subtype has yet to be resolved. GPCRs structures' predictions based on homology templates have long provided reliable models when an experimentally determined structure of a closely related protein homolog is available.[108,109] Therefore, homology models have been used for drug design and interpretation of biological potencies for agonists [89,110] and antagonists [89,110] [111,112] at the A_3R and have been generated from both agonist- or antagonist-bound $A_{2A}R$ or A_1R X-ray structures.

The first essential step is to compare the sequence of unknown structure (ex. A_3R) with known structures stored in the PDB database [113], to align their sequences and choose the best candidate. The alignment allows the transfer of structural information from the template to the target, generating a reliable three-dimensional model of the adenosine receptor. The high-resolution crystal structure of $A_{2A}R$ in complex with an antagonist (PDB ID 3EML [34]) provides an excellent template as $A_{2A}R$ is closely related to A3 with a 55% sequence similarity. Homology modelling of A_3R based on A_1R crystal structure (PDB ID 5UEN [55]) has a sequence similarity of 54%.

Once the model is generated, it undergoes refinement through various computational techniques to improve its accuracy and reliability. Techniques such as molecular dynamics simulations and energy minimization are applied to optimize the model's structure and address any steric clashes or structural distortions. Additionally, the quality of the homology model is assessed through various validation metrics, such as Ramachandran plots [114] which assess the stereochemical quality of the model. Some computational tools available for model building are MODELLER software [115] and SWISS-MODEL server [116], a fully automated workflow that simplifies the homology modelling process.

Additionally, several intricate techniques have been developed for generating A_3R models, such as the creation of hybrid models by incorporating multiple template structures [117], ligand-guided

model optimization [111,112,118], and sampling of multiple receptor conformations (MRCs) followed by docking studies [110].

In recent years, significant advancements in homology modelling have been driven by breakthroughs in machine learning and deep learning algorithms such as AlphaFold2 (AF2) [119,120]and RoseTTAFold [121] that can generate accurate models for essentially any sequence. These methods utilize a deep neural network architecture that integrates multiple sequence alignment and co-evolutionary information to predict protein structures. They can predict not only the overall fold but also the spatial arrangements of side chains, which are critical for ligand binding and receptor activation.

In the case of GPCRs, AF2 has a bias towards either the active or inactive conformation of the receptor and can only predict one state. However, a more sophisticated method has been developed based on AF2, known as the Multi-state Alpha Fold method [122], which considers the conformational switch between the active and inactive states that occurs upon ligand binding. This method has been shown to accurately predict the structures of GPCRs in different states, making it a valuable tool for studying their function and developing new drugs.

By incorporating all the available homology modeling techniques, researchers can now generate highly accurate models of ARs with unprecedented precision. These models provide valuable insights into the receptor-ligand interactions and allosteric regulation, enabling the rational design of novel drugs targeting ARs. As computational methods continue to evolve, homology modeling will continue to be a vital tool in the field of structural biology, facilitating our understanding of ARs and guiding the development of therapeutic interventions for various diseases and conditions.

2.1.2 Molecular Docking

Docking in the field of molecular modeling is a method that makes predictions for the most preferable placement of a molecule within a receptor when they bound to each other to form a stable complex [123]. Molecular docking is one of the most widely applied techniques in the field of drug design, because of its ability to give predictions about the possible binding mode of a small molecule ligand within a protein target binding site. [124]

In the common rigid molecular docking method, only the ligand is flexible. However, both the ligand and protein are characterized by flexibility. More sophisticated and computationally demanding model correspond to the “induced fit” method, where both the ligand and the protein adjust their structures to achieve an overall "best-fit". [125]

Every docking program includes two steps components for its normal execution:

1. Explore the conformational landscape of the small molecule to find the best candidate binding modes (poses) within the receptor. This is done using sampling methods [126] that can be categorized based on the degree of flexibility of the molecules involved in the calculations, such as rigid (both molecules are kept rigid), semi-flexible (where the protein is kept rigid while the molecules are allowed to be flexible), and flexible docking (where both the protein and molecules are allowed to be flexible). Each of these methods provides valuable insights into the interactions between the small molecule ligands and the receptor, aiding in the identification of potential binding sites and the most favorable binding configurations.

2. Rank the generated poses of potential binding modes and evaluate their binding affinity using a scoring function [127]. There are three main types of scoring functions:
   - **Force-field based**: These functions take into account both intermolecular and intramolecular interactions. The scoring is based on the sum of energy contributions from various forces, such as van der Waals interactions, electrostatic interactions, and hydrogen bonding, among others. These interactions are calculated using force-field parameters and equations that describe the physical properties of the molecules.
   - **Empirical**: These functions use multiple linear regressions to combine various energy terms with coefficients that are adjusted to fit experimental data. The energy terms encompass contributions from different aspects of the molecular interactions, and the coefficients are optimized to produce scores that correlate well with experimental binding affinities.
   - **Knowledge based**: These scoring functions utilize statistical analysis of intermolecular contacts found in large 3D databases. By applying the principles of Boltzmann statistics, potentials are derived from the observed frequencies of different interactions. This approach leverages existing knowledge about molecular interactions to estimate binding affinities.

Docking softwares used in this study:

GOLD Software [128] is a widely used molecular docking program that efficiently explores the conformational space of ligands and protein receptors to predict binding modes and assess ligand-protein interactions. Gold software has available four scoring functions (GoldScore, ChemScore, ASP and ChemPLP). In this work, ChemScore [129] scoring function (empirical) was used for the Molecular Docking calculations. ChemScore scoring function incorporates the term, ΔG, that represents the total free energy change that occurs on ligand binding.

Glide (Induced Fit Docking) [130] is a molecular docking method that considers the flexibility of both the ligand and the receptor, allowing for structural adjustments to occur in the active site during the docking process. The available scoring functions are GlideScore SP (standard precision) and XP (extra precision). In this work, Glide SP scoring function [131] was used, an empirical scoring function that evaluates the interaction energy between ligands and protein binding sites.

2.1.3 Molecular Dynamics (MDs)

Molecular dynamics (MD) is a method that aims at understanding the time-evolution of a molecular system represented by a set of particles with defined positions, based on an initial structure like an X-ray crystallography, NMR or homology model. Starting from this initial structure and assigning initial velocities to each atom (from a statistical mechanics approach, the Boltzmann distribution at a given temperature). Sequential coordinates and velocities are then computed by integrating Newton's equation of motion. [132]

The outcome is a trajectory that shows the temporal evolution of atomic positions and velocities influenced by all system atoms. However, due to the large number of particles interacting with each other, analytically solving equation of motion is difficult, so it is necessary to perform numerical integration using methods, such as Leapfrog integrator. [133] This is an extension of the Verlet algorithm, [134] so named because the particle positions are updated at integer timesteps, whilst velocities are updated at half-integer timesteps, thus essentially 'leap-frogging' over one another. The relationships for updating positions, r, and velocities, v, within the leap-frog integrator are given by:

$$r(t+\delta t) = r(t) + v\left(t+\frac{\delta t}{2}\right)\delta t$$

$$v\left(t+\frac{\delta t}{2}\right) = v\left(t-\frac{\delta t}{2}\right) + a(t)\delta t$$

Where $a(t)$ is the acceleration of particle i at time t calculated from $\frac{F_i(t)}{m_i}$.

This process is contingent on knowing particle velocities from the prior step. Thus, the question arises as to the origin of initial velocities. In general, such initial random velocities at the start of a simulation are canonically taken from a Maxwell-Boltzmann distribution at a user-specified temperature.

The frequency with which the equations of motion are integrated is determined by the time step, δt, specified by the user. The careful choice of the time interval significantly impacts the stability of the simulation. A value too small is computationally inefficient and limits sampling of phase space, whilst too high a value may fail to adequately sample bond vibrations, and may lead to deviation from their equilibrium values, resulting in the accumulation of artefactually high forces and simulation errors. The choice of an appropriate time step is determined by force field, system composition, integrators, and bond constraints.

Covalent bonds with high vibrational frequency are typically constrained to their equilibrium value within MD simulations. Constraint algorithms are implemented after particle coordinates have been updated by the integrator; and act to correct deviations from equilibrium bond lengths. This is particularly useful for bonds undergoing high frequency vibrations, such as those between heavy atoms and hydrogens, and allows for a larger timestep to be applied. The LINCS algorithm [135] was applied to constrain covalent bonds within this thesis.

The standard approach for simulating the behavior of a transmembrane protein complex is typically to embed the structure in a box that contains a lipid bilayer and water solvent. To avoid problems with boundary effects caused by the finite size of the box (unit cell), periodic boundary conditions (PBCs) are used, where the unit cell is surrounded by infinite replicas of itself. [136] The geometry of the unit cell satisfies perfect two-dimensional tiling, and when an object passes through one side of the unit cell, it re-appears on the opposite side with the same velocity. The large systems approximated by PBCs consist of an infinite number of unit cells. In computer simulations, one of these is the original simulation box, and others are copies called images. During the simulation, only the properties of the original simulation box need to be recorded

and propagated. The minimum-image convention is a common form of PBC particle bookkeeping in which each individual particle in the simulation interacts with the closest image of the remaining particles in the system.

Prior to initiation of a MD simulation, systems are generally subjected to an energy minimization step. Such a procedure involves iteratively adjusting atomic coordinates to reach a local minimum in the potential energy landscape, described by a force field. This is key in alleviating incorrect geometries and steric clashes which may be present in the initial system configuration. Leaving such features uncorrected may result in the accumulation of unacceptably high forces and unstable simulations. Within this thesis the steepest descent algorithm [137] is used.

MD simulations are typically run in the NVT (constant number of particles, volume, and temperature also known as canonical ensemble) or the NPT (constant number of particles, pressure, and temperature or isothermal-isobaric ensemble) statistical mechanical ensembles. For simulations that contain a lipid bilayer the NPT ensemble is generally employed. To keep pressure and temperature constant, simulations are performed with a barostat (one for each system component: protein, lipids and solvent), and thermostats, respectively.

Force Fields

Τα μοριακά χαρακτηριστικά που χαρακτηρίζουν κάθε άτομο του συστήματος καθορίζουν τις αλληλεπιδράσεις και τη δυναμική τους κατά τη διάρκεια της προσομοίωσης. Η μαθηματική συνάρτηση και οι παράμετροι που επιτρέπουν τον υπολογισμό της δυναμικής ενέργειας (E) του συστήματος με βάση τη θέση των ατόμων ονομάζονται "force field" (FFs). Οι πιο χρησιμοποιούμενοι force fields στη μοριακή δυναμική των βιολογικών μακρομορίων είναι οι AMBER, CHARMM, GROMOS και OPLS, με κάθε έναν από αυτούς να έχει ελαφρώς διαφορετικά πρωτόκολλα παραμετροποίησης αλλά, τελικά, παρόμοιες βασικές μαθηματικές μορφές.

Μια τυπική συνάρτηση force field περιλαμβάνει δεσμευμένους όρους που ορίζουν τις ενδομοριακές αλληλεπιδράσεις στο σύστημα και μη-δεσμευμένους όρους που καταγράφουν κυρίως τις αλληλεπιδράσεις μεταξύ μορίων ανάμεσα στον εξωτερικό χώρο του συστήματος:

$$U(r^n) = \sum U_{bonded} + \sum U_{non-bonded}$$

Where U is the potential energy of n particles, with positions given by r^n.

These components may be further subdivided into the energy terms:

$$U = \sum \frac{1}{2} K_b (b - b_0)^2 \quad : \text{bonds}$$
$$+ \sum \frac{1}{2} K_\theta (\theta - \theta_0)^2 \quad : \text{angles}$$
$$+ \sum K_\varphi [1 - \cos(n\varphi + \delta)] \quad : \text{torsions}$$

bonded

$$+ \sum \varepsilon \left[\left(\frac{r_0}{r}\right)^{12} - 2\left(\frac{r_0}{r}\right)^{6} \right] \quad : \text{Lennard-Jones}$$
$$+ \sum \frac{q_i q_j}{4\pi\, \varepsilon_0\, r_{ij}} \quad : \text{Coulomb}$$

non – bonded

With each term of the equation above accounting for the energy of all bonds, all angles, all torsion angles, all non-bonded pairs (Lennard-Jones), and all partial charges (Coulomb) respectively.

Bonded interaction terms describe forces within between covalently bonded particles, which arise as a function of those covalent linkages. They include terms describing bond stretching, bending of angles, and rotations about bonds. Both bonds and angles terms are described by harmonic potentials (Hooke's law), where b and b_0 are the current bond length and its equilibrium value, θ and θ_0 are the current angle value and its equilibrium value and K_b, K_θ are the bond and angle force constants between atoms. The torsion term, also referred as dihedral is often represented as a sum of cosine function, where ϕ is the torsion angle, n is the multiplicity, δ is the phase angle and K_ϕ is the dihedral force constant between atoms.

Non-bonded interaction terms consist of two energy terms: van der Waals and electrostatic interactions, which are implemented through the Lennard-Jones 12-6 potential (van der Waals or Lennard-Jones) and the Coulombic potential, respectively. The Lennard-Jones potential is a mathematical model that approximates the interaction between a pair of atoms, accounting for two distinct forces, one attractive and another repulsive, where ε is a parameter defining the depth of the energy minimum, r is the distance between the 2 atoms and r_0 is the energy expressed as an inverse power function of the distance between the considered 2 atoms. Finally, the last term in the force field equation is the Coulombic potential, where q_i and q_j are the partial charges assigned to atoms i and j, ε_0 is the dielectric constant and r_{ij} is the relative distance between these atoms.

The computation of non-bonded interactions is the most time-consuming part of a MD simulation as the evaluation of the forces scales quadratically with the number of atoms in the system if no approximation is used. Therefore, a distance cut-off of about 1nm is typically used for non-bonded interactions. The same truncation strategy of Coulomb interactions causes problems in simulations. Therefore long-ranged electrostatic interactions beyond a certain cutoff (typically 1 nm) are not truncated but considered using Particle Mesh Ewald (PME) [142] methods.

2.1.4 Free Energy Calculations

Relative binding free energy calculations offer an attractive approach to predict protein–ligand binding affinities *in silico* using molecular simulations and statistical mechanics to compute free energy differences between congeneric molecules.

Free energy calculations play a pivotal role in computational chemistry and molecular modeling, offering valuable insights into the thermodynamic properties and energetics of molecular systems. These calculations provide a means to predict and quantify the stability, binding affinities, and reaction pathways of molecules in diverse chemical and biological contexts. By assessing the changes in free energy associated with molecular interactions or transformations, we can gain a deeper understanding of complex processes such as ligand binding. In this dynamic field, various approaches and algorithms have been developed to tackle the challenges of accurate and efficient free energy estimation, contributing to a more comprehensive comprehension of molecular behavior at the atomic level.

Free energy calculations methods can be divided into:

- **Endpoint Methods:**

MM/PBSA and MM/GBSA: Molecular Mechanics - Poisson Boltzmann (MM/PBSA) or Molecular Mechanics - Generalized Born Surface Area (MM/GBSA) methods combine molecular mechanics and continuum solvent models to estimate free energies of binding or solvation based on molecular structures. [143,144]

Linear Interaction Energy (LIE): LIE estimates free energy changes by considering non-bonded interactions between ligand and protein atoms. [145,146]

- **Pathway or Alchemical methods:**

Thermodynamic Integration (TI): TI computes free energy changes by gradually transforming one system into another while calculating the work done along the transformation path. [147]

Free Energy Perturbation (FEP): FEP involves changing a system by adding or mutating atoms and then calculating the free energy difference between the initial and modified systems.[148]

- **Pulling Methods or Nonequilibrium:**

Steered MD (SMD): In contrast with free-energy calculations carried out at thermodynamic equilibrium, SMD utilizes either a constant or a time-varying force, responsible for marked deviations from equilibrium conditions. [149]

Umbrella Sampling: This method involves running multiple simulations with a harmonic restraint that keeps the ligand at different positions along the unbinding pathway. The potential of mean force (PMF) is then computed from these simulations to determine the binding free energy. [150]

These methods offer various approaches to estimating free energy changes in molecular systems, each tailored to different types of simulations and research questions.

Virtual screening (VS) protocols including docking calculations and an additional end-point binding free energy calculation MM/PBSA or MM/GBSA method [143,144] have been applied and identified novel hits for GPCRs. [118,151–157] In our lab, we have also participated toward this effort using a combination of docking and MM/PBSA calculations. [87] However, the hit-to-lead discovery process warrants more accurate binding free energy calculations. [158] In this context, the accuracy of alchemical relative binding free energies calculations of antagonists with Free-Energy Perturbation coupled with MD simulations (FEP/MD) and a thermodynamic cycle method (TI/MD) using experimental structures of ligand-GPCR class A systems, e.g., antagonists in complex with $A_{2A}R$, [156,159–164] was previously established.

A significant challenge associated with alchemical methods is the slow convergence of the free energy differences and the high computational cost**.** [165,166] However, there has been a recent emergence of software designed to execute TI and FEP calculations utilizing graphics processing units (GPUs). [165,166]

Additionally, advanced force fields and sampling algorithms have been recently produced that are capable of predicting relative binding free energies at a high level of accuracy. [167,168] These advancements coupled with a workflow automation [169,170]have enabled free energy simulations to be performed in a rigorous, high-throughput mode.

Next, the methods employed for the purposes of this thesis will be further discussed.

MM/PBSA and MM/GBSA

Calculating binding energies in ligand-receptor complexes is of fundamental importance in finding a candidate drug molecule in this approach. [171] The huge number of interactions between the solvent molecules and the system consisting of a ligand L which binds to a receptor R to form a complex R – L, hampers the accuracy of the calculation of an accurate value for ΔG_{bind}. MM/PBSA or MM/GBSA methods use the thermodynamic cycle shown in **Scheme 2.1**

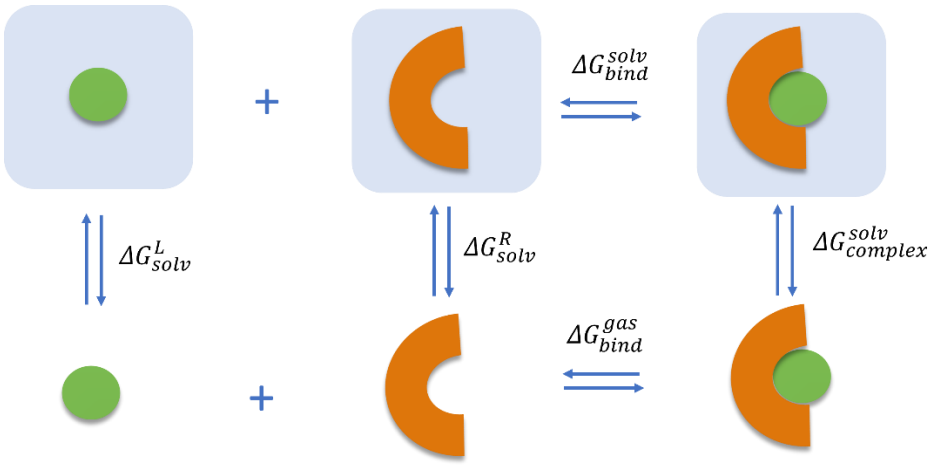

Scheme 2.1. The free energy for the formation of ligand L - receptor R complex can be calculated using the end-points of this thermodynamic cycle including the bound and unbound states of the ligand. According to thermodynamic cycle the ΔG_{bind} is calculated using **equation (2.1)**

$$\Delta G^{solv}_{bind} = \Delta G^{\text{gas}}_{\text{bind}} + \Delta G^{solv}_{complex} - \left(\Delta G^{R}_{\text{solv}} + \Delta G^{L}_{\text{solv}}\right) \quad (2.1)$$

This can be transformed to **equation 2.2** [172]

$$\Delta G_{bind} = \Delta H - T\Delta S$$

$$= \Delta E_{MM} + \left(\Delta G^{\text{solv}}_{complex} - \Delta G^{R}_{\text{solv}} - \Delta G^{L}_{\text{solv}}\right) - T\Delta S \quad (2.2)$$

If entropy change is taken to be approximately zero or if we compare complexes with similar entropy changes then **equation 2.2** can be transformed to **equation 2.3** for the calculation of effective binding free energies (ΔG_{eff}).

$$\Delta G_{eff} = \Delta E_{MM} + \Delta G_{solv} \quad (2.3)$$

$$\Delta E_{MM} = \Delta E_{int} + \Delta E_{elec} + \Delta E_{vdW} \quad (2.4)$$

$$\Delta G_{solv} = \Delta G_{PB/GB} + \Delta G_{SA} \quad (2.5)$$

The terms for each complex ΔE_{MM} and ΔG_{solv} are calculated using **equations (2.4)** and **(2.5)**.

ΔE_{MM} defines the interaction energy between the receptor and the ligand, as calculated by molecular mechanics in the gas phase and includes the changes in the internal energies ΔE_{int} (bond, angle, and dihedral energies), electrostatic energies ΔE_{ele}, and the van der Waals energies ΔE_{vdW}.

ΔG_{solv} is the desolvation free energy for transferring the ligand (L) or the receptor (R) or the complex from water to the binding area. ΔG_{solv} is the sum of the electrostatic solvation energy $\Delta G_{PB/GB}$ (polar contribution or ΔG_P) and the non-polar contribution ΔG_{SA} (or ΔG_{NP}) between the solute and the continuum solvent.

The **polar contribution** of the solvation binding free energy in medium is given by the **equation (2.6)**

$$G_P = -\frac{1}{2}\sum_i q(r_i)\,\varphi_i(r_i) \quad (2.6)$$

The difference in electrostatic energy between water (ε_{solute}=80) and protein (ε_{solute}=1) ΔG_P, for L, R and complex is given by the **equation (2.7)**

$$\Delta G_P = -\frac{1}{2}\sum_i q_i(\varphi_i^{80} - \varphi_i^{1}) \quad (2.7)$$

The calculation of electrostatic potential φ_i needed to compute ΔG_P can be calculated using the Poisson Boltzmann (PB) or Generalized Born (GB) equations. [173]

In MD applications, the associated computational costs are often very high, as the $\Delta G_{PB/GB}$ needs to be solved every time the conformation of a molecule changes. To reduce the computational cost, the GB model can be applied as an approximation of the PB equation [174].

Here, ΔG_P is the contribution of the Coulomb and Born energy in the two dielectric environments according to **equation (2.8)**

$$\Delta G_{\mathrm{P}} = \left(-(1\text{-}\frac{1}{\varepsilon})\right)\sum_{i=1}^{N}\sum_{j\neq i}^{N}\frac{q_i q_j}{r_{ij}} - \frac{1}{2}(\left(1\text{-}\frac{1}{\varepsilon}\right)\sum_{i=1}^{N}\frac{q_i^2}{R_i} \qquad (2.8)$$

where q_i and R_i are the charges and atomic radii for each atom *i* from the *N* atoms.

The choice of the solute dielectric constant (ε) is strictly system-dependent and requires precise study of the binding sites to obtain the most suitable ε. Although ε is dependent on the characteristics of the binding site (a higher ε for a highly charged binding site and a lower ε for a hydrophobic site), frequently the calculations are best with ε = 2−4, especially in larger data sets of diverse proteins. [175] Since the atomic charges used to calculate polar solvation energy have fixed values, they cannot be adapted to respond to the dielectric changes when a solute is solvated in the solvent. Therefore, a charge model that takes the solvent effect into account is critical for the accurate calculation of solvation free energies. Applying a single dielectric constant ε to describe the heterogeneous dielectric environment of a solute can cause errors.

For membrane proteins, like GPCRs, to account for the lipophilic environment of the membrane, a heterogeneous dielectric implicit membrane model can be used along the bilayer z-axis. [176–178]

The **non-polar contribution** of solvation free energy is calculated according to **equation (2.9)**

$$\Delta G_{NP} = \gamma SASA + \beta \quad (2.9)$$

where SASA (solvent accessible surface area) is the total area that the solvent can access around solute, γ is surface tension and β is an added as a correction factor. Typical values for γ and β are 0.005420 kcal mol^{-1}Å^{-2} and -1.008000 kcal mol^{-1}, respectively.

Since the continuum models ignore all information about water molecules in water-exposed binding sites (including the number and entropy changes) before and after ligand binding

sometimes the treatment of the water molecules as a part of the receptor, provides improved results in some cases [179–182]. Another way is to replace the desolvation in MM/GBSA by the free energy combined with displacement of binding-site water molecules upon ligand binding estimated by the WaterMap approach, which yields varying results**.** [183]

Usually, the binding free energy methods like MM/PBSA or MM/GBSA are applied in a set of congeneric series of compounds and can provide good accuracy regarding the correlation between calculated ΔG_{bind} and experimental pK_i values for K_i's covering a range of 10^3 corresponding to a $\Delta\Delta G_{bind}$ scale equal to 4-5 kcal mol^{-1}. [184,185]

The computational duration is 50 times longer with the PB model. [186]. The accuracy of the calculated energy using the GB approach is compromised at the expense of computational speed. The correlation and the computational demands make the GB approach attractive, especially for qualitative analysis, though the GB method in principle is not as accurate as PB. [144] However, some studies have shown that optimal prediction of MM/GBSA with a solute dielectric constant of 2.0 is better than using MM/PBSA for 98 ligand complexes. [143]

TI/MD

The TI/MD method has been described in ref [147]. To compare two ligands 0 and 1 binding to a receptor, the calculation of $\Delta A_1(\mathrm{b})$ and $\Delta A_0(\mathrm{b})$, respectively, is needed and then the difference $\Delta\Delta A_{0\rightarrow 1}$, i.e., $\Delta\Delta A_{0,1}$ (b). The calculation of $\Delta A_1(\mathrm{b})$ and $\Delta A_0(\mathrm{b})$ is computationally demanded because it includes large changes between the two states and doing free energy calculations for the two states alone often have very large errors. Free energy is a state function, thus the free energy difference between states is independent of the path that connects them. Thus, we can construct a thermodynamic path that takes us through a set of states that improve phase space overlap between states that can be unphysical, meaning that the intermediate states do not have to be observable experimentally. The calculation of the relative binding free energies for two ligands bound to a receptor can be performed instead using the MBAR method [187] and applying a thermodynamic cycle (**Scheme 2.2**), [188–190] i.e., using the ΔG values obtained for the transformations of the ligands in the bound (b) and the solvent (s; water) state $\Delta G_{0,1}$(b) and $\Delta G_{0,1}$(s), respectively, according to **equation (2.10)**

$$\Delta\Delta A_{\mathrm{b},0\to1} \text{ or } \Delta\Delta A_{\mathrm{b},0,1} = \Delta A_{\mathrm{b},1} - \Delta A_{\mathrm{b},0} = \Delta A_{0,1}(b) - \Delta A_{0,1}(s) \qquad (2.10)$$

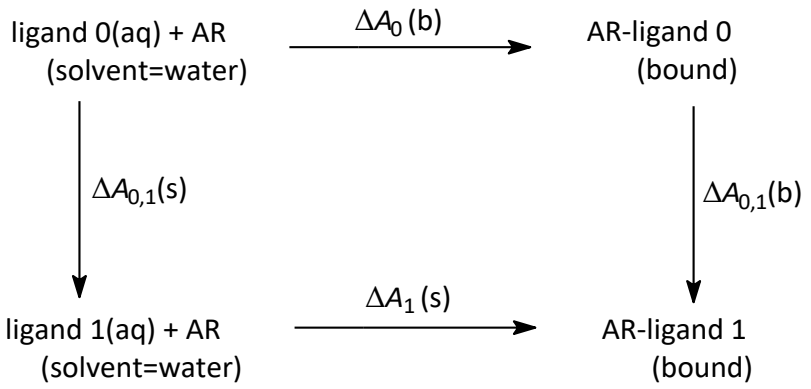

Scheme 2.2. Thermodynamic cycle used for the calculation of relative binding free energies.

Using this method, we can calculate the difference between $\Delta A_{0,1}(b)$ and $\Delta A_{0,1}(s)$ which corresponds to the unphysical alchemical transformation 0 → 1 in the bound and in the water state, known as alchemical transformation which may be chosen to include small change or perturbation of ligand structure to lower the error for the free energy perturbation calculation.

To put this mathematically, we can improve our results by constructing high phase space overlap intermediates and calculating the free energy difference $\Delta\Delta A_{0\to1}$ by the sum of the binding free energy differences between the intermediate states. Briefly, a thermodynamic parameter λ that smoothly connects states 0 and 1 through a λ-dependent potential $U(r^N; \lambda)$, such that $U(r^N; 0) = U_0(r^N)$ and $U(r^N; 1) = U_1(r^N)$. The transformation is broken down into a series of M steps corresponding to a set of λ values $\lambda_1, \lambda_2, ..., \lambda_M$ ranging from 0 to 1, such that there is sufficient phase space overlap between neighboring intermediate λ states. The TI method computes the free energy change of transformation 0 → 1 by integrating the Boltzmann averaged $dU(\lambda)/d\lambda$ as is described **in equation (2.11).**

$$\Delta A_{0\to1} = \int_0^1 d\lambda \langle \frac{dU(r^N;\lambda)}{d\lambda} \rangle_\lambda$$

$$= \Delta A_{0\to1} \approx \sum_{k=1}^{M} w_k \langle \frac{dU(r^N;\lambda)}{d\lambda} \rangle_{\lambda_k} \qquad (2.11)$$

where the second sum indicates numerical integration over M quadrature points (λ_k, for k = 1, ..., M) with associated weights w_k. A linear extrapolation between states can be applied for the construction of $U_1(r^N; \lambda)$ while with Amber18 softcore potentials [190–192] the LJ and Coulomb term potentials are described according to **equation (2.12).**

$$U(r^N;\lambda) = U_0^{SC}(r^N;\lambda) + \lambda \Delta U^{SC}(r^N;\lambda)$$
$$= U_0^{SC}(r^N;\lambda) + \lambda\left(U_1^{SC}(r^N;1-\lambda) - U_0^{SC}(r^N;\lambda)\right) \quad (2.12)$$

Multistate Bennett Acceptance Ratio (MBAR) method [187] calculates the free energy difference between neighboring intermediate states using **equation (2.13)**

$$\Delta A_{\lambda\to\lambda+1} = -ln\ ln\ \frac{\langle wexp(-\beta U_{\lambda+1})\rangle_\lambda}{\langle wexp(-\beta U_{\lambda+1})\rangle_{\lambda+1}} \quad (2.13)$$

where w is a function of $A(\lambda)$ and $A(\lambda + 1)$. The equation is solved iteratively to give the free energy change of neighboring states $\Delta A(\lambda \rightarrow \lambda + 1)$, which via combination yield the overall free energy change. MBAR method has been shown to minimize the variance in the calculated free energies, by making more efficient use of the simulation data. [187,193–195]

2.1.5 Binding Kinetics

The binding equilibrium dissociation constant (K_d) has been traditionally considered fundamental for understanding structure-activity relationships and for efficient drug design. However, over the past few years, the significance of calculating binding kinetic rates and understanding the binding mechanisms of drugs with their target proteins has emerged in the drug design process. [196–198 199–201]

The rate in which the drug tackles the binding process is called the on-rate or the association rate constant (k_{on}). An efficacious drug usually has high k_{on} values. The k_{on} constant is usually expressed in $M^{-1}\ s^{-1}$, since it depends on the concentration of the drug. The k_{on} value can be an indicator of the selectivity of the drug and how fast the drug can sample the surface of the target molecule and find the binding site. Protein or drug dynamics or thermal fluctuations may cause

the unbinding of the drug. The rate at which the drug leaves the binding site is called the off-rate or the dissociation rate constant (k_{off}) and is usually expressed in s^{-1}. Another important parameter for binding kinetics is the residence time (RT or τ). The RT is the time a drug stays in the binding pocket [202] and can be calculated by the following equation:

$$\tau = 1/k_{off}$$

Experimental methods such as surface plasmon resonance (SPR) and bioluminescence resonance energy transfer (BRET) can be used for measuring k_{off} and RT values.

Residence time can be directly linked to the drug activity, efficacious drugs usually have long residence times. The more a drug stays in the binding site, the more it can interfere with the function of the target protein. [203] A ligand can have a high binding affinity value against the target protein *in vitro* in early stages of development, but a sufficiently long RT value is usually required to proceed in the clinical phases. [196] Moreover, in *in vivo* systems, such as the human body, the pharmacokinetics and pharmacodynamics play an important role while the drug is constantly involved in off-target interactions, metabolism, and excretion. Longer residence times mean more time in the bound state, away from these off-target events.

Indeed, many studies, including studies on GPCRs, have shown that the RT can exhibit a better correlation with *in vivo* drug efficacy. [204,205] An in-depth knowledge and the understanding of the molecular determinants [206] of drug–receptor binding kinetics at GPCRs is required to successfully target this class of proteins. [207–210] Experimental data and evidence for the binding kinetics of orthosteric AR ligands have been reviewed [211] including antagonists [199–201] and agonists [212,213] that bind the orthosteric binding area of ARs.

New approaches for computing ligand–receptor binding kinetics

The growing evidence that the efficacy of a drug can be correlated to protein binding kinetics has emerged the development of novel methods aimed at computing rate constants for ligand-receptor binding events. Computing accurately the residence times or the dissociation rates, poses challenges with conventional MDs alone due to the extensive sampling required. In this regards, enhanced sampling methods have been developed to simulate biomolecular binding and dissociation processes and predict the associated binding kinetic rates.

The methods are mainly divided into two types, absolute methods for computing absolute association (k_{on}) and/or dissociation (k_{off}) rate constants and relative methods to describe how residence times of several compounds compare and rank them according to their binding kinetics and whether ligands are considered fast (residence time t < 20 min) or slow (t > 40 min). Obtaining the absolute kinetic constant is difficult and often time-consuming. Ranking and finding correlations is usually faster and more likely to be used by industry to prioritize drugs.

Absolute kinetic rates could be estimated with <1 μs of total simulation time using enhanced sampling methods such as the Markov State Modelling (MSM)[214–216], Weighted Ensemble[217–219], Gaussian accelerated Molecular Dynamics (GaMD) [220,221], and Simulation Enabled Estimation of Kinetic Rates (SEEKR)[222–225].

Metadynamics [226,227]or Multiple Infrequent Metadynamics (InMetaD) simulations [228–232] have been widely applied to investigate the ligand binding kinetics. However, Metadynamics simulations challenge is to accurately define collective variables (CVs), which requires expert knowledge of the studied systems. To overcome this challenge, Machine Learning (ML) has been incorporated into Metadynamics simulations. Filizola et al [233] developed a novel approach, which combined InMetaD and ML methods to predict the dissociation kinetic rates of two drugs (morphine and bruprenorphine) in the μ-opioid receptor.

Relative kinetic rates prediction methods, that allow high-throughput simulations of large datasets and rank compounds according to their unbinding rates are Random Acceleration Molecular Dynamics (RAMD), [234,235] scaled MD [236,237] and steered MD. [238]

Scaled MD [236,237] has been mainly used for the prediction of k_{off} values. Mollica et al. used scaled MD to correctly rank a congeneric series of four $A_{2A}R$ antagonists based on their residence times. [239] RAMD, a similar method to Scaled MD, is mainly used to qualitatively predict dissociation rates. Nunes-Alves et al [234] performed RAMD simulations to predict ligand dissociation rates of T4 lysozyme.

Coarse-grained Molecular dynamics [240,241] have also been used to capture protein - ligand kinetic pathways. [242]

The on-line toolbox, KBbox [243] (kbbox.h-its.org) contains descriptions of the different methods, along with some tutorials and guidance on usage.

The trypsin-benzamidine system is the most widely used system for benchmarking different methods. This is mainly because of the system's relatively small size, as well as the relatively fast association rate. Other systems that had been studied are Hsp90 [236,237,244] and kinases[245–248] .

Studies have been also performed to GPCRs, e.g., in β_2-adrenergic receptor (β_2AR), [249,250] muscarinic receptor M_3 (M_3R), [251] muscarinic acetylcholine receptor M_2 (mAChR M_2), [250] corticotropin-releasing factor type 1 receptor (CRF_1R). [252]

τRAMD method

In the present work, a recently developed method τ-Random Acceleration Molecular Dynamics (τRAMD)[235], is applied for the studied ARs systems. τRAMD is an efficient computational workflow that enables the prediction of drug-protein relative RTs. The method is based on the random acceleration molecular dynamics (RAMD) [253] method, an enhanced sampling procedure that was originally developed for exploring ligand egress pathways from buried binding sites in proteins.

The probability of a ligand leaving the binding site through a given exit path, p_{tot}, can be considered as an equal of the probability of the ligand finding the entrance to the exit path, p_I, and the probability of the ligand passing through it p_{II}. i.e.:

$$p_{tot} = p_{\mathrm{I}} \cdot p_{\mathrm{II}}$$

The RAMD method enables computation of an estimation of the p_{tot}, as the method permits a ligand to find an exit path without *a priori* directional bias. Assuming that ligand exit occurs over one single energy barrier, ΔG_{II}, one can apply the theory of activated complexes. p_{II} is thus associated with ΔG_{II} and p_I is a pre-exponential factor. k_{off}, which is proportional to p_{tot}, can therefore be written as:

$$k_{off} \propto p_{tot} = p_{\mathrm{I}}\, e^{-\frac{\Delta G_{\mathrm{II}}}{RT}}$$

This model is a simplification of the complex free energy profile that is expected along a ligand exit pathway in a protein.

The τRAMD workflow is summarized in Figure 2-1. In the RAMD method, during a standard MD simulation of the protein-ligand complex, a small additional force ($\vec{F}$) with a random orientation is applied to the ligand to facilitate its unbinding. The force's direction is randomly reassigned when the ligand's movement within a defined time frame drops below a predetermined

threshold distance. The application of the random force allows the acceleration of the egress event to be observed in a short simulation of several nanoseconds. Unlike other enhanced sampling methods, τRAMD does not require any advance knowledge of the dissociation pathway or extensive parameter fitting. The only user-set parameter is the magnitude of the random force, which mainly affects the simulation time required.

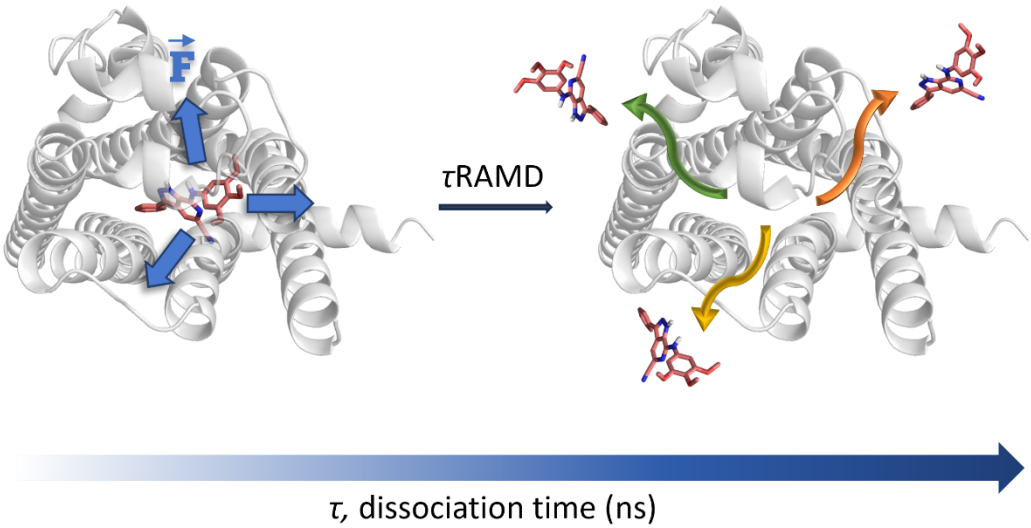

***Figure 2-1**: Illustration of the application of the τRAMD workflow to simulate the dissociation of a drug-like compound from a target protein.*

τRAMD is a very flexible and computationally inexpensive that can be used to rank a set of small molecules that bind to given protein target by their dissociation rates or residence times and to build this information into the rational drug design workflows for the design of new molecules or ligand optimization. In addition to implementations in the NAMD and AMBER software packages, RAMD has recently been implemented in GROMACS molecular simulation engine for simulations on CPU or GPU nodes. In this thesis the calculations are run on Gromacs-RAMD version 2.0.

2.2 Methods

2.2.1 Protein Models

Residues will be described by their amino acid identity (single letter code) and position (amino acid number) within the specific GPCR with the Ballesteros and Weinstein numbering. [254]. All His were protonated on the Nε. [112] [255]

Model of WT A_1R-antagonist complex

The X-ray WT A_1R – **DU172** structure with PDB ID 5UEN [55] was used for the purpose of this study.

Model of WT A_{2B}R-antagonist complex

We superimposed the experimental crystal structure **ZM241385** - A_{2A}R complex (PDB ID 3EML[34]) to the WT A_{2B}R model from Adenosiland web-service. [256] Then, the A_{2A}R protein was removed resulting in the WT A_{2B}R - **ZM241385** model used in the study described on Chapter 3.

Three Models of WT A_3R-antagonist complex

Model 1: As it has been previously described in ref. [257], we used the template-based homology model for inactive A_3R WT derived from Adenosiland web-service [256] or from ref. [258] that was built using the crystal structure of the complex hA_{2A}R - **ZM241385** (PDB ID 3EML [34]) as a template which has a 56% sequence similarity (32.38% sequence identity) to hA_3R (Figure S1). A model from ref. [259] generated from A_1R (PDB ID 5UEN [55]), which has a 54% sequence similarity (40% sequence identity) to hA_3R (Figure S1), was also compared; the A_3R complexes after 100ns-MD simulations converged to the same protein structure observed with homology models derived from A_{2A}R as described. Their sequence alignment was carried out using Jalview 2.11.2.6. [116] The side chain of V169$^{5.30}$ was rotated to increase the free space for ligands binding. [5]

A_3R Model 1 was used for the study described in Chapters 3 and 4.

Model 2: An inactive A_3R homology model was used as described in ref. [110] Their homology models were initially generated from a convenient modelling program and then were further refined by sampling MRCs. The resulted MRCs were examined by docking calculations of representative nucleoside ligands, and the model with the most reasonable binding mode was selected for further optimisation using MD simulations. Using their homology models, along with MD simulation and structural network analysis, they observed the boundary between agonist and antagonist activity.

Model 3: We used the ML-based homology model derived from GPCRdb [260] that contains predictions for GPCRs in active and inactive forms via the advanced multi-state AF method. [122] For the study described in Chapter 5, we used the inactive state of A_3R. The predicted local-distance difference test (pLDDT) for modelled transmembrane residues was > 70, the disordered intracellular C-terminus was discarded. Residues $R173^{5.34}$, $M172^{5.33}$ and $M174^{5.35}$ (MRM motif) that have a different orientation compared to the other two models, demonstrate a very low confidence level (pLDDT < 50). The optimized Model 3 was derived with modification of MRM motif orientation.

A_3R Models 1, 2, 3 and optimized model 3 were used for the study described in Chapter 5.

All protein models were optimized using the Protein Preparation Wizard in Schrödinger suite 2021 (Protein Preparation Wizard; Epik, Schrödinger, LLC, New York, NY, 2021). [261] In this process, the bond orders and disulfide bonds were assigned and N- and C-termini of the protein models were capped by acetyl and N-methyl-amino groups, respectively. All hydrogens of each protein complex were minimized with the OPLS2005 force field [262,263] for by means of Maestro/Macromodel 9.6 [264] using a distance-dependent dielectric constant of 4.0. The molecular mechanics minimizations were performed with the conjugate gradient method and a threshold value of 2.4 10^{-5} kcal mol^{-1} $Å^{-1}$ as the convergence criterion. Each protein model was subjected in an all-atom minimization using the OPLS2005 force field [262,263] with heavy atom root mean square deviation (RMSD) value constrained to 0.30 Å until the root mean square of conjugate-gradient value reached < 0.05 kcal·mol^{-1}·$Å^{-1}$. Models were then utilized for molecular docking calculations.

2.2.2 Molecular Docking Calculations

Ligand preparation

The 2D structures of the studied compounds were sketched with Marvin Program (Marvin version 21.17.0, ChemAxon (https://www.chemaxon.com)) and model-built with Schrödinger 2021-1 platform (Schrödinger Release 2021-1: Protein Preparation Wizard; Epik, Schrödinger, LLC, New York, NY, 2021; Impact, Schrödinger, LLC, New York, NY; Prime, Schrödinger, LLC, New York, NY, 2021) and minimized using the conjugate gradient method, the MMFF94 force field [265] and a distance-dependent dielectric constant of 4.0 until a convergence threshold of 2.4 10^{-5} kcal mol^{-1} $Å^{-1}$ was reached. Ionization states of the compounds at pH 7.5 were tested using Epik program [266] implemented in Schrödinger suite (Prime, Schrödinger, LLC, New York, NY, 2021). Energy minimization of the compounds' 3D structures was performed using the OPLS2005 [262,263] force field force field.

Gold software Docking Calculations

The molecular docking calculations of the studied compounds of Chapters 3 and 4 with A_1R, $A_{2B}R$ or A_3R were performed using GOLD software [267] [128] and ChemScore [129] as the scoring function. The models of WT A_1R - **DU172**, WT A_3R - **ZM241385**, WT $A_{2B}R$ - **ZM241385** were used as templates for the molecular docking calculations of the antagonists to the binding area of each of the receptors. Each compound was docked in the binding site of **ZM241385** in the A_3R-**ZM241385** model or **DU172** in A_1R - **DU172**, model or **ZM241385** in the $A_{2B}R$-**ZM241385** model in an area of 15 Å̊ around the ligand using the experimental coordinates of **ZM241385** or **DU172** and 20 genetic algorithm runs were applied for each docking calculation. The top-scoring docking poses were used for MD simulations to investigate the binding profile of the tested compounds inside the receptors.

Induced Fit Docking Calculations

Molecular docking simulations for Chapter 5 were performed using the induced-fit docking protocol of Schrödinger suite 2021 (Induced-fit Docking, Schrödinger, LLC, New York, NY, 2021) in standard protocol (standard precision) which allows flexibility of both the ligand and the

entire binding site. Ligand **ZM241385** (from $A_{2A}R$ - **ZM241385** (PDB ID 3EML [34] was used as template for the molecular docking calculations of the antagonists to the binding area of each of the A_3R models. Thus, the grid boxes for the binding site were built considering the coordinates of **ZM241385**. Docking was performed using a softened potential, i.e. the van der Waals scaling factor was set at 0.5 for both receptor and ligand. The Prime refinement step was set on side chains prediction of amino acid residues within 5 Å of the ligand. Subsequently, a minimization of the same set of residues and the ligand for each protein/ligand complex pose was performed. After this stage, any receptor structure in each pose reflects an induced fit to the ligand structure and conformation. For each ligand docked, a maximum of 20 poses was retained. The binding was analyzed and the top-scoring docking poses were used for MD simulations to investigate the binding profile of the tested compounds at inactive A_3R.

2.2.3 MD simulations

System preparation

Each protein-ligand complex was inserted in a pre-equilibrated hydrated 1-palmitoyl-2-oleoyl-*sn*-glycero-3-phosphoethanolamine (POPE) membrane bilayer according to OPM (Orientations of Proteins in Membranes) database. [268] The orthorhombic periodic box boundaries were set 12 Å away from the protein using the System Builder utility of Desmond v4.9 (Schrödinger Release 2021-1**:** Desmond Molecular Dynamics System, D. E. Shaw Research, New York, NY, 2021. Maestro-Desmond Interoperability Tools, Schrödinger, New York, NY, 2021). The membrane bilayer consisted by ca. 170 lipids and 16,000 TIP3P [269] water molecules. Sodium and chloride ions were added randomly in the water phase to neutralize the system and reach the experimental salt concentration of 0.150 M NaCl. The total number of atoms of the complex was approximately 75,000 and the simulation box dimensions was ca. 88 x 76 x 113$Å^3$. We used the Desmond Viparr tool to assign the amber99sb [270,271] force field parameters for the calculation of the protein, lipids and intermolecular interactions, and the Generalized Amber Force Field (GAFF) [167] parameters for the ligands. Ligand atomic charges were computed using the Restrained Electrostatic Potential (RESP) [272] fitting for the electrostatic potentials calculated with Gaussian03 [273] at the HF/6-31G* [274] level of theory and the antechamber of AmberTools18. [275]

MD simulation protocol

100 ns-MD simulations at constant pressure (NPT) were performed for the tested compounds in complex with AR receptors embedded in POPE bilayers using Desmond v4.9 software, the Desmond MD algorithm [276] with amber99sb [270,271] force field to investigate their binding interactions.

The MD simulation protocol consists of a series of MD simulations designed to relax the system, while not deviating substantially from the initial coordinates. During the first stage, a simulation was run for 200 ps at 10 K in the NVT ensemble (constant volume, temperature and number of atoms), with solute-heavy atoms restrained by a force constant of 50 kcal mol $Å^{-2}$. The temperature was raised to 310 K during a 200 ps MD simulation in the NPT ensemble (constant pressure, temperature and number of atoms), with the same force constant applied to the solute atoms. The temperature of 310 K was used in MD simulations in order to ensure that the membrane state is above the main phase transition temperature of 298 K for POPE bilayers. [277] The heating was then followed by equilibration simulations. First, two 1 ns stages of NPT equilibration were performed. In the first 1 ns stage, the heavy atoms of the system were restrained by applying a force constant of 10 kcal mol^{-1} $Å^{-2}$, and in the second 1 ns stage, the heavy atoms of the protein-ligand complex were restrained by applying a force constant of 2 kcal mol^{-1} $Å^{-2}$ to equilibrate water and lipid molecules. In the production phase, the relaxed systems were simulated without restraints in the NPT ensemble for 100 ns. Replicas of the system were saved every 50 ps.

In the MD simulations the PME method was employed to calculate long-range electrostatic interactions with a grid spacing of 0.8 Å. The SHAKE method was used to constrain heavy atom-hydrogen bonds at ideal lengths and angles.[278] Van der Waals and short-range electrostatic interactions were smoothly truncated at 12 Å. [279] The Nosé-Hoover thermostat [280] was utilized to maintain a constant temperature in all MD simulations, and the Martyna-Tobias-Klein method [281] was used to control the pressure. The equations of motion were integrated using the multistep reversible reference system propagator algorithms (RESPA) [282] integrator with an inner time step of 2 fs for bonded interactions and non-bonded interactions within the cutoff of 12 Å. An outer time step of 6.0 fs was used for non-bonded interactions beyond the cutoff.

Two MD simulation repeats were performed for each complex using the same starting structure and applying randomized velocities. All the MD simulations with Desmond software were run on GTX 1060 GPUs in lab workstations or the ARIS Supercomputer.

Trajectories visualization

The visualization of the desmond MD simulation trajectories was performed using the graphical user interface (GUI) of Maestro and the protein− ligand interaction analysis was carried out with a simulation interaction diagram (SID) tool, available with a Desmond v4.9 program. For the calculation of hydrogen bond interactions, a distance of 2.5 Å between donor and acceptor heavy atoms, and angle ≥120° between donor-hydrogen-acceptor atoms and ≥90° between hydrogen-acceptor-bonded atom. Non-specific hydrophobic contacts were identified when the side chain of a hydrophobic residue fell within 3.6 Å from a ligand's aromatic or aliphatic carbon, while π–π interactions were characterized by stacking of two aromatic groups face-to-face or face-to-edge. Water-mediated interactions were characterized when the distance between donor and acceptor atoms was 2.7 Å, as well as an angle ≥110° between donor-hydrogen acceptor atoms and ≥80° between hydrogen-acceptor-bonded atoms.

The generation of Figures for the representative frames were carried out using Pymol Molecular Graphics System, Version 2.3.5 Schrödinger, LLC. [283]

2.2.4 Binding Free Energy Calculations

MM/GBSA calculation

For the MM/GBSA calculations, structural ensembles were extracted in intervals of 40 ps from the last 20 ns MD simulation for each complex. Prior to the calculations all water molecules, ions, and lipids were removed, except 20 waters in the vicinity of the ligand, [284] and the structures were positioned such that the geometric centre of each complex was located at the coordinate origin. The MD trajectories were processed with the Python library MDAnalysis [285] in order to extract the 20 water molecules closest to any atom in the ligand for each of the 501 frames. During the MM/GBSA calculations, the explicit water molecules were considered as being part of the protein. Binding free energies of compounds in complex with A_1R or A_3R were estimated using the 1-trajectory MM/GBSA approach. [144]

A dielectric constant ε_{solute} = 1 was applied to the binding area and to account for the lipophilic environment of the protein a heterogeneous dielectric implicit membrane model was used along the bilayer z-axis. [176–178] The post-processing thermal_mmgbsa.py script of the Schrodinger Suite was used which takes snapshots from the MD simulations trajectory and calculates ΔG_{eff}.

Alchemical TI/MD calculation

For the TI/MD calculations, the relaxed complexes of the tested compounds at A_1R or A_3R from the 100ns-MD simulations in a POPE lipid bilayer with the amber99sb [270,271] force field were used as starting structures for the calculations of the alchemical transformations. TI/MD calculations were also performed for the ligands in solution.

Setups were performed using structures of the complexes that were already equilibrated from the 100ns-MD simulations. The relaxed complexes were embedded in a POPE lipid bilayer extending 12 Å beyond the solutes using the CHARM-GUI web-based graphical user tool. [286]Sodium and chloride ions were randomly added in the aqueous phase to neutralize the system based on a Monte-Carlo approach. Each ligand-AR complex in the bilayer was processed by the LEaP module in AmberTools18 under the Amber18 software package.[275] Proteins, ligands, and water were described with ff14sb [287], GAFF1.8 [167], and TIP3P force fields [269], respectively, and intermolecular interactions with ff14sb force field. Atom types, bonded and van der Waals parameters for ligands were added using Antechamber and Parmchk2 in the Amber18 tool set. [275]Partial charges for ligands were obtained using RESP fitting [272] for the electrostatic potentials calculated with Gaussian03 [288] at the Hartree-Fock (HF)/6-31G* [274] level of theory and the antechamber of AmberTools18.

Thus, initial geometries were minimized using 20,000 steps of steepest descent minimization at λ=0.5. These minimized geometries were then used for simulations at all λ values. Eleven λ values were applied, equally spaced between 0.0 to 1.0. Each MD simulation was heated to 310 K for 500 ps using the Langevin thermostat (dynamics) [289]for temperature control, as implemented in Amber18, [275,290] employing a Langevin collision frequency of 2.0 ps^{-1} in the presence of harmonic restraint with force constant 10 kcal mol^{-1} $Å^{-2}$ on all membrane, protein, and ligand atoms. The temperature of 310 K was used in MD simulations to ensure that the membrane state is above the main phase transition temperature of 298 K for POPE bilayers. [277] The Berendsen barostat [291] was used to adjust the density over 500 ps at constant pressure

(NPTγ) (with γ = 10 dyn cm^{-1}), with a target pressure of 1 bar and a 2 ps coupling time. Then, the 500 ps of constant volume equilibration (NVT) was followed by 2 ns NVT production simulation without restraints. Energies were recorded every 1 ps, and coordinates were saved every 10 ps. Production simulations recalculated the potential energy at each λ value every 1 ps for later analysis with MBAR. [187,195]

The bond constraint SHAKE [278] algorithm was disabled for TI mutations in AMBER GPU-TI module pmemdGTI, [166] and therefore a time step of 1 fs was used for all MD simulations. Long range electrostatics were calculated using PME, with a 1 Å grid, and short-range non-bonding interactions were truncated at 12 Å with a continuum model long range correction applied for energy and pressure.

For each alchemical calculation, the 1-step protocol was performed, ie. disappearing one ligand and appearing the other ligand simultaneously, and the electrostatic and van der Waals interactions are scaled simultaneously using softcore potentials from real atoms that are transformed into dummy atoms. [190] Alternatively, in the 3-step "decharge-vdW-recharge" protocol, the atoms of the first ligand are first decharged, then undergo a van der Waals interactions transformation using softcore potentials, and then recharged to the final state (second ligand). [190] The 1-step protocol is a less computational expensive and more accurate approach to free energy estimates according to recent studies. [192] However, for the **L9** → **L8** transformation (see Chapter 4) the 3-step protocol was applied because it has been observed that TI calculation converges poorly with 1-step protocol if the substituent that is involved in the transformation include a large numbers of atoms. [292]

The final states 0 and 1 of the alchemical calculations 0 → 1 or 1 → 0, ie. the structures of ligand 0-AR and 1-AR complexes as resulted from the alchemical transformations were compared with these complexes structure resulted from converged 100ns-MD simulations. This was performed to certify that the 2 ns MD simulation for each λ-state during the alchemical calculations was enough for the complexes 0-AR and 1-AR to converge to same structure with 100ns-MD simulations. Two repeats were performed for each alchemical transformation. Experimental relative binding free energies were estimated using the experimental binding affinities according to equation 2.14.

$$\Delta\Delta G_{0\to1}(\mathrm{b})\exp = -1.9872\,T\,(\mathrm{p}K\mathrm{d},1-\mathrm{p}K\mathrm{d},2) \qquad (2.14)$$

2.2.5 Binding Kinetics Calculations

For the binding kinetics calculations, the τRAMD algorithm was used. The complete workflow for the τRAMD method includes a preparation step for the system setup, several sets of conventional MD simulations and RAMD simulations as well as the trajectory analysis to compute relative residence times, as described below.

System preparation

Four representative ligands (**A17**, **L4**-**6**) that have a wide range of RT values (see Chapter 5, Table 5-2) were selected to test the reliability of the τRAMD method using the three different models of A_3R. The relaxed complexes of the four representative ligands from the 100ns-MD simulations were used as starting structures for the τRAMD protocol [234,235,293,250] which (for which a tutorial can be found at https://kbbox.h-its.org/). For the first step of preparation, we employed the Amber20 software [294] as described in the τRAMD protocol [234,235,293,250] which generate topology and coordinate files for simulations with Amber software, each complex in the POPE bilayer was processed by the LEaP module in AmberTools20 under the Amber20 software package to assign the ff19sb [295] and GAFF [167] force fields as described above in the TI/MD section.

Equilibration MD Simulation Protocol

First, the system was minimized (with restraints on all heavy atoms except water and ions of 500, 50, 5 and 0.5 kcal mol^{-1} $Å^{-2}$ each for 500 steps of steepest descent minimization followed by 1000 steps of conjugate gradient and then 1500 steps without restraints). It was then heated up to 310K for 100 ps (NVT- Langevin) with restraints of 50 mol^{-1} $Å^{-2}$. Then the system was further equilibrated by applying gradually decreasing restraints on the heavy atoms of the protein and ligand for 100ps (50, 25, 10 and 5 kcal mol^{-1} $Å^{-2}$) followed by a small equilibration step without restrains (5ns) and by applying random velocities, as the membrane systems used where already relaxed from the previous 100ns-MD simulation. In all simulations, non-bonded Coulombic and Lennard-Jones interactions were truncated at a cut-off of 12 Å. Periodic boundary conditions were applied, and long-range Coulombic interactions were treated using the PME method. A time step of 2 fs was used, and the SHAKE algorithm was employed to constrain bonds involving hydrogen atoms.

For the Gromacs simulations, we transformed the final output of the equilibrated systems from Amber to Gromacs using ParmEd. [296] We then conducted short NVT simulations with v-rescale temperature coupling for a duration of 5 ns. Subsequently, we generated four independent trajectories (4 replicas) of conventional MD simulations under NPT conditions using the Nosé−Hoover thermostat and Parrinello−Rahman barostat, with each trajectory spanning 20 ns. To ensure trajectory diversity, velocities were initialized from the Maxwell distribution. The resulting final coordinates and velocities were utilized for the simulation of dissociation trajectories using RAMD, which was carried out under the same NPT conditions.

τRAMD simulations protocol - Calculation of residence times

A series of 15 RAMD dissociation trajectories were generated using the starting snapshots obtained from the four replicas mentioned earlier. The default parameters of the RAMD protocol, as described in detail in the τRAMD protocol [293] were retained. The external force was applied to the centre of atoms (COM) of the ligand and the ligand displacement was assessed every 100 fs. If the ligand displacement was less than 0.025 Å, a new random force orientation was selected. Once the ligand's COM reached a predefined distance of 50 Å from the binding site, it was considered dissociated, and the dissociation time was recorded. The length of the RAMD trajectory was limited to 24 h wall-clock time due to the configuration of the utilized computer cluster (ARIS Supercomputer). Within this time, ∼ 40 ns of simulation time could be achieved. The external force magnitude was defined as 8 kcal/mol Å based on the dissociation time of the slowest dissociating compound (**L6**).

To obtain the residence time for each replica, a bootstrapping procedure consisting of 5000 rounds with 80% randomly selected samples was performed. This procedure aims to converge to a Gaussian-like distribution if the sampling is sufficient. The final relative residence time (τRAMD) was determined as the mean value across all replicas. Computed relative residence times were plotted against the corresponding experimental RT values (τ exp). The mean standard deviations of the computed residence times were computed as defined in the previously reported τRAMD protocol of ref [235].

The visualization of the RAMD trajectories was performed using VMD 1.9.4 [297] and the protein−ligand interaction analysis was carried out with the MDanalysis toolkit[285].

Chapter 3.

Identification of high affinity dual A_1/A_3 antagonist with novel 7-Amino pyrazolo[3,4-d]pyridazine Scaffold

Investigation of the binding profiles to ARs using MD simulations and mutagenesis experiments.

3. Identification of high affinity dual A_1/A_3 antagonist with novel 7-Amino-pyrazolo[3,4-d]pyridazine Scaffold

Investigation of the binding profiles to ARs using MD simulations and mutagenesis experiments.

3.1 Purpose of the study

It has been reported that non-xanthine pyrazole bicyclic derivatives that bind to ARs are pyrazolo[4,3-*d*]pyrimidines, pyrazolo[1,5-*c*]quinazolines, pyrazolo[3,4-*b*]pyridines, pyrazolo[3,4-*b*]pyridines, pyrazolo-[4,3-*e*]-1,2,4-triazolo-[1,5-*c*]pyrimidines, pyrazolo-[3,4-*c*] or -[4,3-*c*]quinolines, pyrazolo-[4,3-*d*]pyrimidinones, pyrazolo-[3,4-*d*]pyrimidines, and pyrazolo-[1,5-*a*]pyridines [298–300].

In the work described in this Chapter, in collaboration with Prof Marakos, Prof Pouli and Assist. Prof Lougiakis, we initially designed a novel pyrazolo[3,4-*d*]pyridazine scaffold for activity at the ARs. The objective was to design compounds having an alkyl or aryl group, such as a phenyl moiety, directed towards the lower region of the receptor for anchoring purposes. Simultaneously, a larger, more flexible aryl-containing group, such as anilino or aminobenzyl, was designed to orient towards the upper portion of the binding site, thereby enhancing interactions with residues located within EL2.

A new series of 7-amino-pyrazolo[3,4-*d*]pyridazine derivatives were synthesised as reported in ref [301] . The new derivatives' binding affinities against the different ARs were determined using functional cAMP accumulation assays and fluorescent ligand displacement binding studies. After the pharmacological characterization by Prof Graham Ladds, we identified the 26nM A_1R / 7 nM A_3R / <1μM A_{2B}R antagonist 1-methyl-3-phenyl-7-benzylaminopyrazolo[3,4-*d*]pyridazine (**10b**)

as a lead compound. Strikingly, compound **15b**, the 2-methyl congener of **10b**, had lower affinity by > 100-fold against A_1R or A_3R or $A_{2B}R$.

The computational studies involved the comparison of the binding interactions of the regio-isomers **10b** and **15b** with MD simulations in order to suggest the critical mechanisms for the stabilization inside the orthosteric binding cavity. The results suggested that the 2-methyl group in **15b** hinders the formation of hydrogen bonding interactions with $N^{6.55}$ which is a key residue for ligand stabilization. Mutagenesis experiments for **10b** against A_1R provided results that complement the observations from MD simulations. We showed that $L250^{6.51}A$ mutation resulted in only a slight reduction of binding affinity concerning **10b** while the $Y271^{7.36}A$ mutation caused a 10-fold reduction in binding affinity of this compound. Mutation to alanine of residues $T91^{3.36}$, $H251^{6.52}$ or $S267^{7.32}$, which are deep in the orthosteric binding affinity, did not affect binding affinity.

3.2 Results & Discussion

3.2.1 Similarity calculations

Upon searching CHEMBL [302,303] database for similar compounds as antagonists to ARs using a TanimotoCombo [304] coefficient > 0.85, we did not find the pyrazolo[3,4-*d*]pyridazine scaffold suggesting that it is novel ring system for the development of ARs ligands. Representative nonxanthine pyrazolo derivatives include pyrazolo-[4,3-*e*]-1,2,4-triazolo-[1,5-*c*]pyrimidines, pyrazolo-[3,4-*c*] or -[4,3-*c*]quinolines, pyrazolo-[4,3-*d*]pyrimidinones, pyrazolo-[3,4-*d*]pyrimidines, and pyrazolo-[1,5-*a*]pyridines. [305]

All the 3D similarity calculations were performed with Canvas program (Schrödinger Release 2021-1: Canvas, Schrödinger, LLC, New York, NY, 2021). [306]

3.2.2 Biological Results

Compounds were pharmacological characterized to validate the *in-silico* predictions for the purpose of this study by the laboratory of Dr Graham Ladds, Dept. of Pharmacology, University of Cambridge as described in references [90,301,307] and as reported in Chapter 6 of the Doctoral thesis of Dr Anna Hilser (University of Cambridge). [308] The pharmacological evaluation included cAMP assays assessing the activity of compounds at ARs, quantifying binding parameters using a NanoBRET-based saturation binding assay and determination of kinetic parameters of **10b** binding at A_3R, A_1R using the NanoBRET method.

Compounds **10a-c** and **15a-c** were pharmacologically evaluated to assess their activity, as antagonists, against the different human AR subtypes as described previously [90] using functional cAMP assay and the equilibrium dissociation constant (pK_d) was calculated for each compound (Table 3-1). Of the compounds tested, **10b** displayed the highest affinity at the different AR subtypes with greater selectivity towards the A_1R and A_3R than the $A_{2B}R$ (Table S1). Using the Schild plot analysis, **10b**'s affinity (pA_2/pK_b) was calculated at 21 nM at the A_1R and 55 nM at the A_3R while only 1.7 µM at the $A_{2B}R$ (Table S1).

To independently verify the affinities determined using the functional cAMP assay, a previously described NanoBRET binding assay (see ref [90]) was performed to directly quantify the potential antagonists binding to the A_1R and A_3R (Table 3-1). The $A_{2B}R$ was not included in this analysis since the pK_d of **10a** and **10b** at the $A_{2B}R$ were estimated to be below 1 µM (Table 3-1). Consistent with the Schild analysis compound **10b** displayed the highest affinity at the A_1R and A_3R (A_1R: pK_i = 7.95 ± 0.09; A_3R: pK_i = 7.89 ± 0.11). Of the remaining compounds, **10a** displayed weak affinity at the A_3R (pK_i: 6.42 ± 0.28), which was in agreement with the Schild regression estimate, but failed to bind A_1R making an estimate for its affinity unreliable. All the other compounds failed to bind A_1R or A_3R except for **15a** and **15c** which did display some binding at the A_3R but. Significantly, **15b** a regio-isomeric derivative of **10b** that contains a *N*-methyl substitution to 1-NH, failed to bind either AR subtype.

We next investigated the real-time binding kinetics [90,309,310,211] of **10b** at the A_3R, A_1R using NanoBRET binding method as described in [90].The kinetics of binding were determined for **10b** against A_1R (K_{on} = 51.4 ± 0.26 x 10^5 M^{-1} min^{-1}, K_{off} = 0.019 ±0.003 min^{-1} with a pK_D = 7.46 ± 0.1 and RT = 59.8 ± 12.7 min) and against A_3R (K_{on} = 25.6 ± 0.1 x 10^5 M^{-1} min^{-1}, K_{off} = 0.014 ±0.002 min^{-1} with a pK_D = 7.26 ± 0.05 and RT = 72.58 ± 8.8 min). None of the other compounds were able to be analyzed using this method due to their extremely fast K_{off} rate (> 2 min^{-1}). For compound

10b there was excellent agreement between pK_D (K_{on}/K_{off}) of the compounds from the kinetics assays and the Schild analysis (pA_2/pK_b) and fair agreement (~ 3.16-fold) with the saturation binding assays (pK_i).

Table 3-1: Chemical structures, antagonistic potencies (pEC_{50} in presence of NECA [a]) and affinities (pK_i [b]) of 7-amino-pyrazolo[3,4-*d*]pyridazines **10a-c**, **15a-c** against A_1R and A_3R. Data

	A_1R		**A_3R**	
Compound	pEC_{50} of NECA in presence of compound[a]	pK_i [b]	pEC_{50} of NECA in presence of compound[a]	pK_i [b]
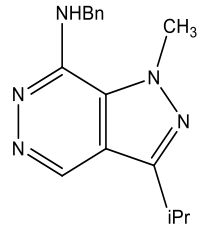 **10a**	8.15 ± 0.12**	5.17 ± 1.13#	9.04 ± 0.11	6.42 ± 0.28
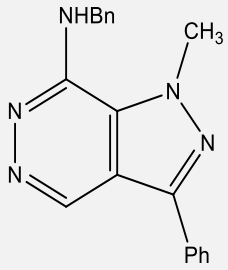 **10b**	7.15 ± 0.07***	7.95 ± 0.09 ***	7.80 ± 0.10***	7.89 ± 0.11*
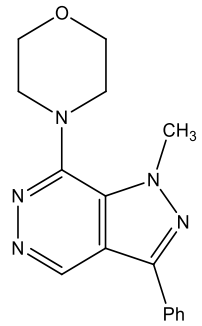 **10c**	9.01 ± 0.16	< 5.0	9.50 ± 0.12	< 5.0

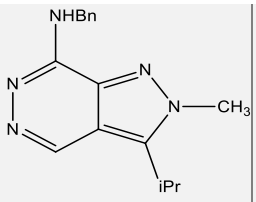 **15a**	8.62 ± 0.15	<5.0	8.94 ± 0.11*	5.77 ± 0.27[#]
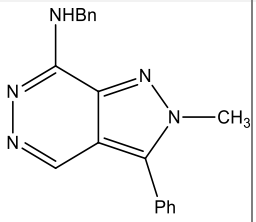 **15b**	8.82 ± 0.15	< 5.0	9.33 ± 0.13	< 5.0
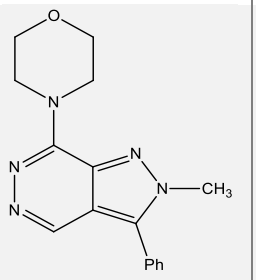 **15C**	8.96 ± 0.18	< 5.0	9.27 ± 0.16	6.44 ± 0.23[#]
DPCPX	6.03 ± 0.16	9.23 ± 0.08	-	-
MRS1220	7.32 ± 0.09	7.29 ± 0.27	7.44 ± 0.02[#]	9.94 ±0.11
NECA	8.74 ± 0.15	6.69 ± 0.10	9.39 ± 0.11	7.05 ± 0.07

[a] Mean ± SEM; Functional activities of at least 3 independent repeats

[b] Mean ± SEM; Equilibrium binding affinities of the ligands measured with NanoBRET against WT A_3R or A_1R; NECA was used as positive control as described in ref [90].

[#] Due to high affinity of MRS1220, 10 nM was used to enable measurement of full dose-response curve of NECA in order to determine pEC_{50}.

Statistical significance compared to NECA was determined, at $p < 0.05$, through One-Way ANOVA with Dunnett's post-test (*, $p < 0.05$; **, $p < 0.01$; ***, $p < 0.001$; ****, $p < 0.0001$).

Adapted from the Doctoral Thesis of Dr Anna Hilser [308] and ref [301].

3.2.3 Binding Profile of the 7-Aminopyrazolo[3,4-d]pyridazines to A_1R and A_3R using MD simulations and Mutagenesis experiments.

MD simulations

Having pharmacologically evaluated the different compounds, molecular docking calculations followed to provide insights into how they bind to the ARs. **10a-10c** were docked into the orthosteric binding site of the A_1R and **10b**, **15b** into $A_{2B}R$ and A_3R (the amino acid sequences of A_1R, A_3R, $A_{2B}R$ in the orthosteric binding area are shown in Scheme 3.1) using the ChemScore as the scoring function [270,271] with the highest score docking pose being inserted into a hydrated POPE bilayer. The complexes were subjected to 100ns-MD simulations with amber99sb [270,271] and then the MD simulations trajectory was analyzed (Table 3-2). The MD simulations showed that the 7-benzylamino-pyrazolo[3,4-*d*]pyridazine **10b** substituted with N^1Me and a 3-phenyl group, formed a stable complex with all three ARs with $RMSD_{protein}$ value < 2.1 Å. Starting from the same docking pose of **10b** in A_1R (Figure 3-1B), or A_3R (Figure 3-2B), the mean frame from MD simulations was close to the starting docking pose in A_1R ($RMSD_{lig}$ = 1.21 Å) while in A_3R the ligand moved considerably into the cleft between TM3, TM5 and TM6 helices ($RMSD_{lig}$ = 4.88 Å). Thus, starting from the same binding pose for **10b**, the MD simulations produced two different binding orientations at A_1R and A_3R. This is due also to the fact that A_1R has a broader binding area, expanded towards TM1, TM2, compared to the other ARs, according to the X-ray structures of A_1R in complex with antagonists. [55,56] A similar AR ligand reported in the literature is the 4-(2-phenethyl)amino 1-phenylethyl pyrazolo[3,4-*b*]pyridine (Tc = 0.15), which binds with a similar docking pose to **10b** to A_1R. [311]We also docked a representative adenine derivative that binds A_1R, e.g. *N*9-methyl,*N*6-benzyl adenine, and found a similar docking pose (Figure 3-3).

Inside the A_1R orthosteric site, compound **10b** formed hydrogen bonds through its pyrazole or pyridazine nitrogen donor groups to the amide side chain of $N254^{6.55}$ or imidazole side chain of $H278^{7.43}$. Furthermore, **10b**, was stabilized in the orthosteric binding site through π-π interactions between its pyrazolo[3,4-*d*]pyridazine or phenyl rings with $F171^{5.29}$, $H251^{6.52}$ and $W247^{6.48}$, respectively. The benzylamino group of the **10b** oriented towards the widened TM2 area in A_1R forming hydrophobic interactions with $A66^{2.61}$ and $I69^{2.64}$. Furthermore, **10b** was found to positioned deep in the binding pocket interacting with $V87^{3.32}$ or $W247^{6.48}$ while the 3-phenyl-pyrazole aligned close to the side chains of $M180^{5.38}$ and $L250^{6.51}$ (Figure 3-1). In the A_3R compound **10b** was stabilized through formation of hydrogen bonding interactions with $N254^{6.55}$ and $H278^{7.43}$ and hydrophobic interactions with $L90^{3.32}$, $L91^{3.33}$, $F168^{5.29}$, $M177^{5.38}$, $L246^{6.51}$ and

I268$^{7.39}$ (Figure 3-2B). Finally, the interaction profile for **10b** was very similar inside $A_{2B}R$ to that observed for the A_1R (Figure 3-2A), though **10b** showed weak hydrogen bonding interactions with N254$^{6.55}$.

Pharmacologically, compounds **10b** and **15b**, differed considerably in their affinity to the ARs (Table 3-1). Comparing MD simulations for **15b** with **10b** in the orthosteric binding area of the A_1R, the A_3R (or also $A_{2B}R$) show that starting from a similar docking pose the substitution from N^1Me, 2-*N*H (found in **10b)** to N^1H, N^2Me (in **15b**) results in **15b** failing to generate hydrogen bonds with N$^{6.55}$ because of the steric repulsion between 2-methyl and the amide side chain of N$^{6.55}$; (see Figure 3-1D, 3-2C,D) for this reason also **15a**, **15c** were inactive. Although many ligands can have similar docking poses, subtle changes in the ligand substitution pattern can result in significant changes in binding and this can be followed only with MD simulations. Considering the two active compounds, **10a** and **10b**, replacement of the 3-phenyl group (found in **10b**) with a 3-isopropyl group (generating **10a**) results in a remarkable reduction of affinity. This is due to **10a** losing significant π-π interactions with H251$^{6.52}$ and hydrophobic interactions with residues deeper in the binding site such as W247$^{6.48}$, L250$^{6.51}$ and V87$^{3.32}$ (Figure 3-1). Finally, the substitution of **10b**'s 7-benzylamino by the more rigid morpholinyl group (found in **10c**) resulted in reduced affinity to the ARs. The more rigid morpholino group in **10c** repels F171$^{5.29}$, so the ligand rotates and moves at the bottom of the binding area, losing hydrogen bonding interactions with N254$^{6.55}$ and weaking its hydrophobic interaction with critical residues, e.g. F171$^{5.29}$ and L250$^{6.51}$ (Figure 3-1). With an accuracy ± 4 kcal mol^{-1}, the MM/GBSA method[144,312] only provides an approximation when applied to structure-activity relationships for analogs in the same series. Nevertheless, the MM/GBSA binding free energy calculations for ligands **10a-c** against A_1R (Table 3-2), using the OPLS2005 force field [262,263] and a hydrophobic slab as implicit membrane model and including the waters in the orthosteric binding area [176–178], predicted fairly the stability of **10a-c** in complex with A_1R with binding free energy values (after neglecting entropy) ΔG_{eff} = -94.50 kcal mol^{-1}, -96.42 kcal mol^{-1}, -85.35 kcal mol^{-1}.

Residues	3.33	5.29	5.30	5.38	5.42	6.48	6.51	6.52	6.55	6.66	6.67	7.32	7.35	7.36	7.39
A_1R	L	F	E	M	N	W	L	H	N	K	K	S	T	Y	I
A_3R	L	F	V	M	S	W	L	S	N	V	V	Q	L	Y	I
$A_{2B}R$	L	F	E	M	N	W	V	H	N	K	N	K	M	N	I

Scheme 3.1. *Sequence alignment of the residues surrounding the binding site of A_1R, A_3R and $A_{2B}R$ (Ballesteros-Weinstein numbering is applied). Colored in yellow columns show residues that differ in side chain polarity, volume, rigidity.*

Table 3-2: MD simulations results of 7-amino-pyrazolo[3,4-d]pyridazines 10a-c, 15b in complex with A1R, A3R or A2BR and MM/GBSA calculations results for 10a-c in complex with A1R.

compound	A_1R			A_3R			$A_{2B}R$		
	$RMSD_{ligand}$ [a]	$RMSD_{protein}$ [b]	ΔG_{eff} [c]	$RMSD_{ligand}$ [a]	$RMSD_{protein}$ [b]	ΔG_{eff} [c]	$RMSD_{ligand}$ [a]	$RMSD_{protein}$ [b]	ΔG_{eff} [c]
10a	2.21 ± 0.42	2.14 ± 0.14	-94.50 ± 5.93	-	-	-	-	-	-
10b	1.29 ± 0.31	1.21 ± 0.17	-96.4 ± 5.93	4.88 ±0.66	2.01 ± 0.21	-101.9 ± 5.02	1.53 ± 0.41	2.08 ± 0.56	-94.19 ± 6.06
10c	1.53 ± 0.37	1.66 ± 0.24	-85.35 ± 5.97	-	-	-	-	-	-
15b	2.38 ± 0.45	2.03 0.19	-	3.19 ± 0.45	2.86 ± 0.15	-	6.77 ± 0.38	2.50 ± 0.14	-

[a] Mean±SD (Å); Ligand RMSD is calculated after superposition of each protein-ligand complex to that of the starting structure (snapshot

[b] Mean±SD (Å); Protein RMSD is calculated for the Cα atoms of the α-helices, for the last 50 ns of the trajectories, using as starting structure snapshot 0 of the production MD simulation.

[c] Mean±SEM; Calculated effective binding free energy (kcal mol^{-1}) between ligand and receptor. ΔG_{eff} is calculated from the last 20 ns of the trajectories using 40 ps intervals (ie. 500 frames per trajectory) using a MM/GBSA model that is taking into account the membrane as hydrophobic slab. Mean from three 20ns-MD simulations.

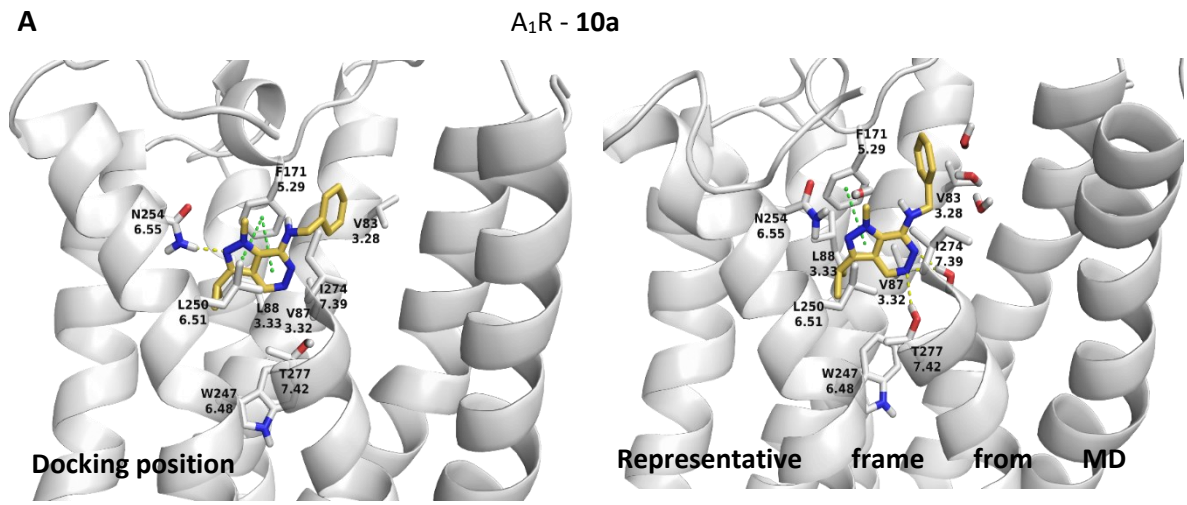

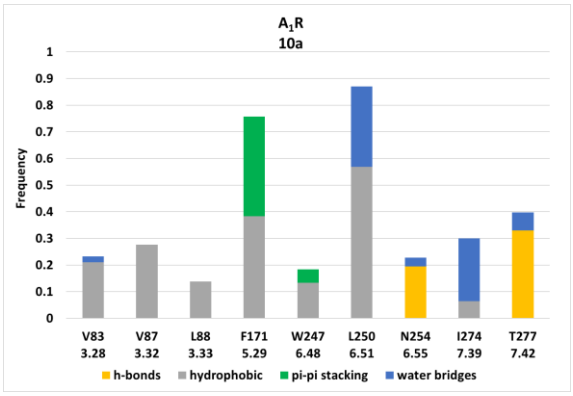
A1R
10a
Frequency
V83 3.28
V87 3.32
L88 3.33
F171 5.29
W247 6.48
L250 6.51
N254 6.55
I274 7.39
T277 7.42
h-bonds
hydrophobic
pi-pi stacking
water bridges

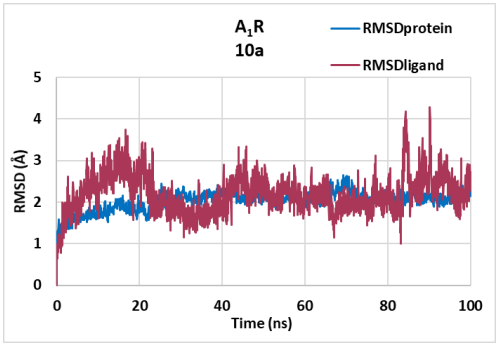
A1R
10a
RMSDprotein
RMSDligand
RMSD (Å)
Time (ns)

B A_1R – **10b**

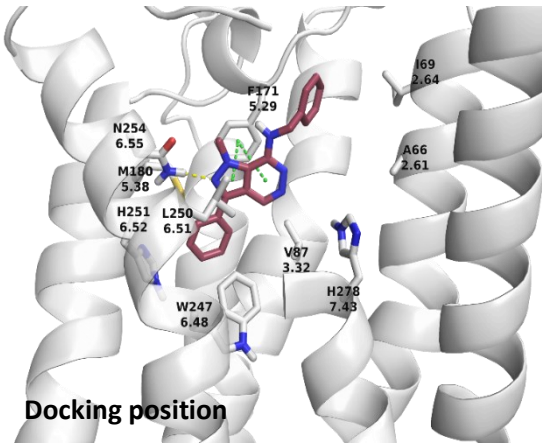
I69 2.64
F171 5.29
N254 6.55
A66 2.61
M180 5.38
H251 6.52
L250 6.51
V87 3.32
H278 7.43
W247 6.48
Docking position

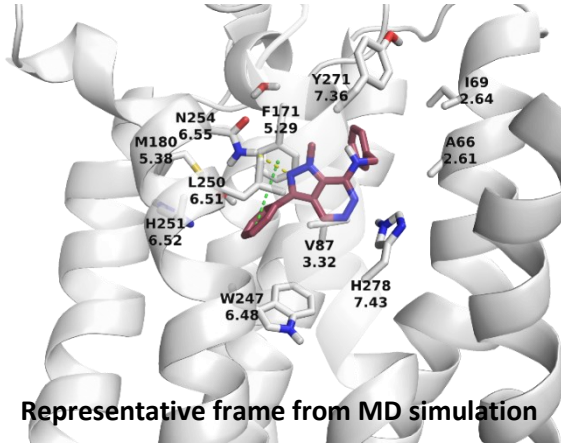
Y271 7.36
I69 2.64
N254 6.55
F171 5.29
M180 5.38
A66 2.61
L250 6.51
H251 6.52
V87 3.32
H278 7.43
W247 6.48
Representative frame from MD simulation

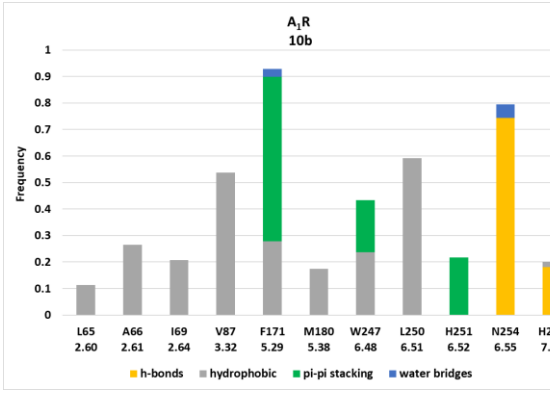
A1R
10b
Frequency
L65 2.60
A66 2.61
I69 2.64
V87 3.32
F171 5.29
M180 5.38
W247 6.48
L250 6.51
H251 6.52
N254 6.55
h-bonds
hydrophobic
pi-pi stacking
water bridges

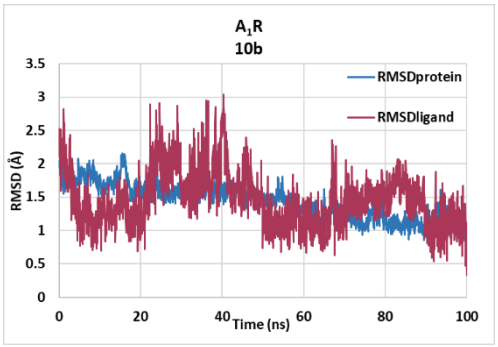
A1R
10b
RMSDprotein
RMSDligand
RMSD (Å)
Time (ns)

C A_1R – **10c**

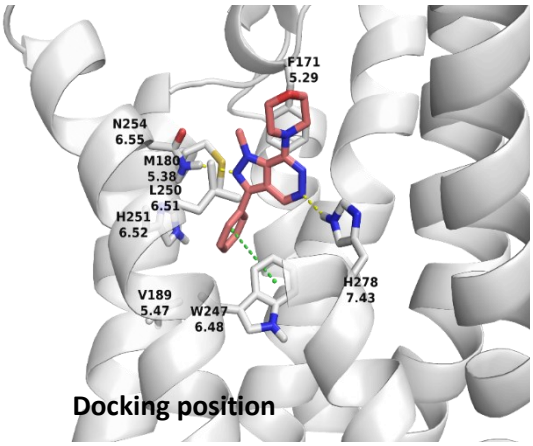

Docking position

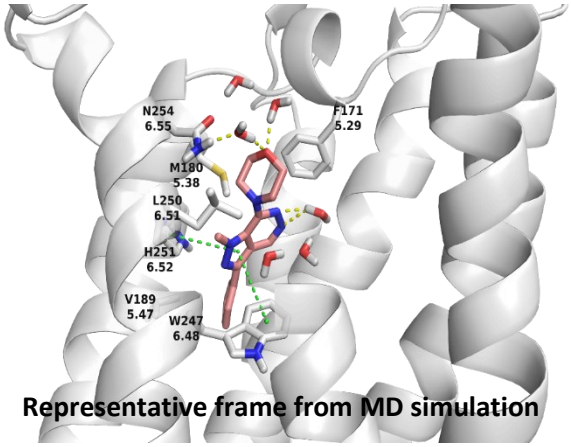

Representative frame from MD simulation

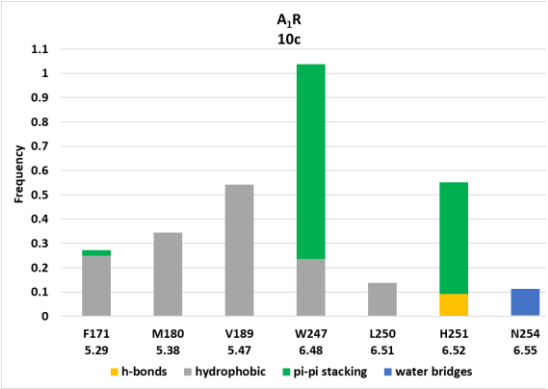

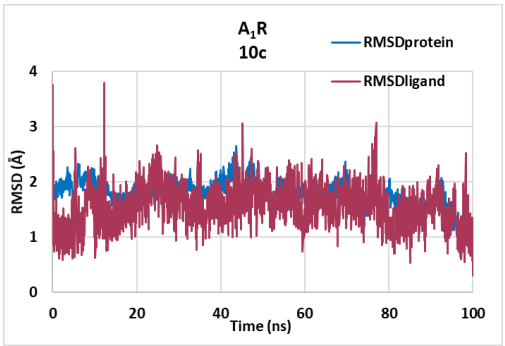

D A_1R – **15b**

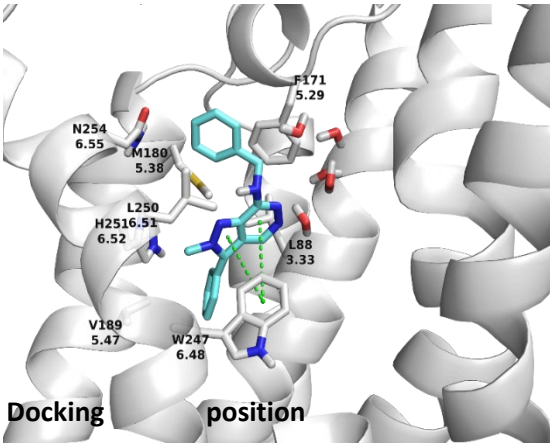

Docking position

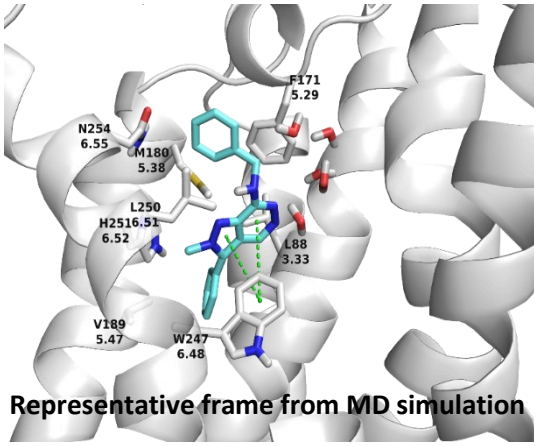

Representative frame from MD simulation

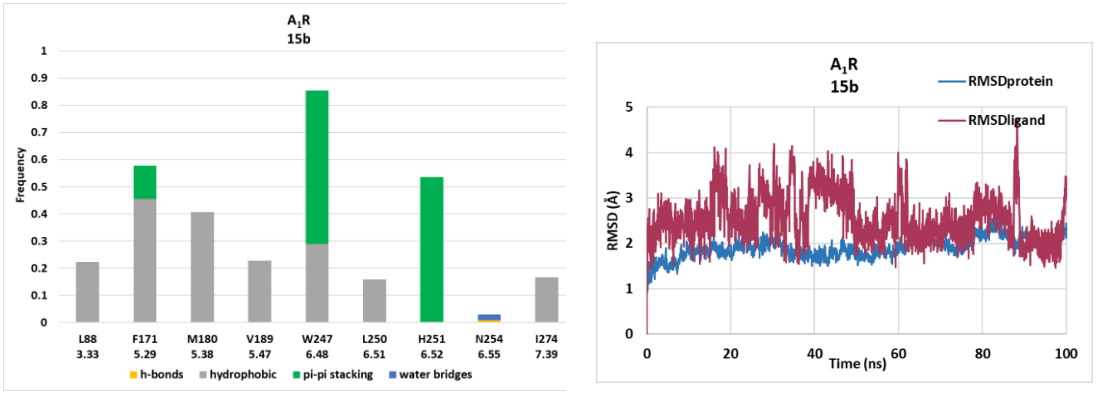

Figure 3-1: *(A)-(C) 100ns-MD simulations of* ***10a-c*** *inside the orthosteric binding area of A_1R. (D) 100ns-MD simulations of* ***15b*** *inside the orthosteric binding area A_1R.Are shown starting structure (docking pose) and representative frames from MD simulations, receptor-ligand interaction frequency histograms and RMSD plots of protein Ca (RMSDprotein; blue plots) and ligand heavy atoms (RMSDligand; red plots) inside the orthosteric binding area of WT A1R or A3R. Bars are plotted only for residues with interaction frequencies ≥ 0.2. Colour scheme: Ligand=brown sticks, receptor=white cartoon and sticks, hydrogen bonding interactions=yellow (dashes or bars), π-π interactions=green (dashes or bars); hydrophobic interactions=grey; water bridges-blue. For the protein models of A1R in complex with 10a-c or 15b in complex with A1R was used the experimental structure of the inactive form for A1R in complex with an antagonist (PDB ID 5UEN [55]).*

A A_{2B}R - **10b**

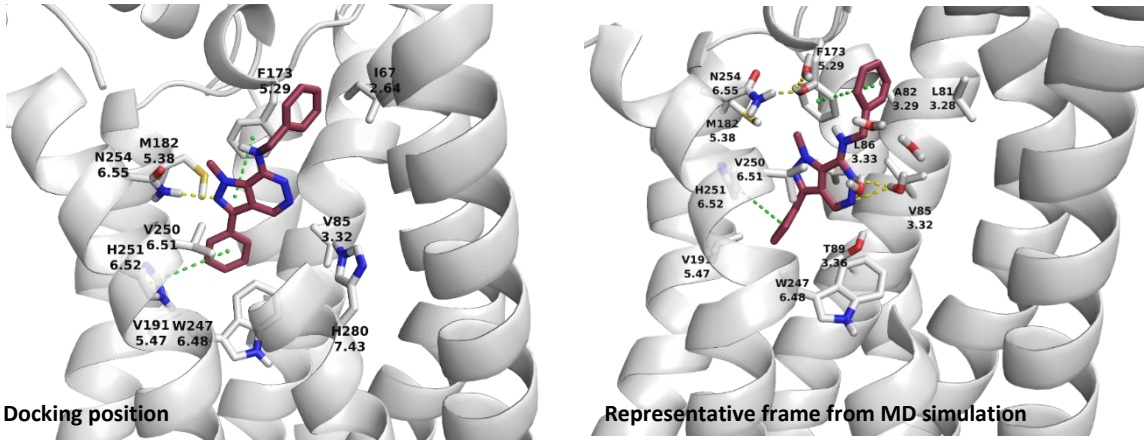

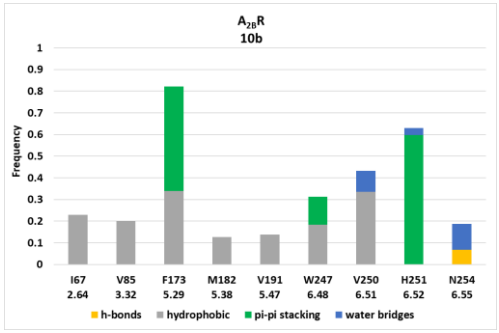

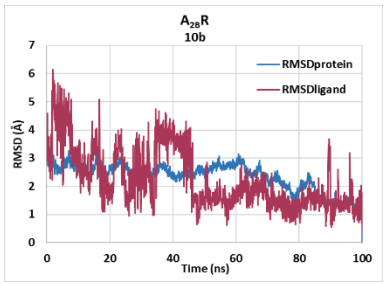

B A_3R-**10b**

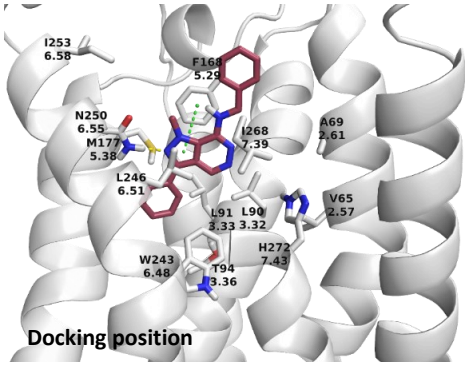

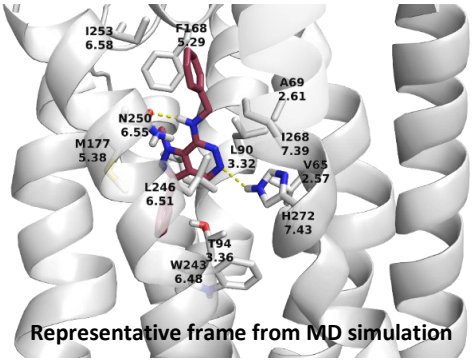

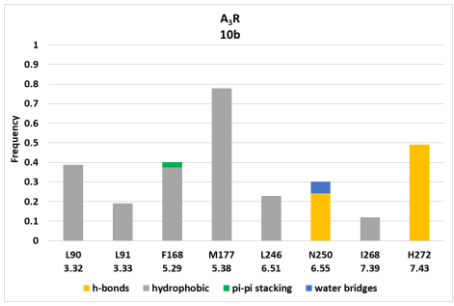

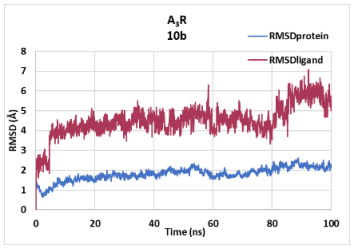

C $A_{2B}R$ - **15b**

For **15b** – $A_{2B}R$ complex a similar binding pose as **10b** – $A_{2B}R$ was used. After 100ns molecular dynamic simulation, **15b** leaves the binding pocket and enters the membrane area through an opening between TM6 and TM7. The RMSD of this ligand (6.77 ± 0.38 Å) is also indicative of a ligand translation from the starting position.

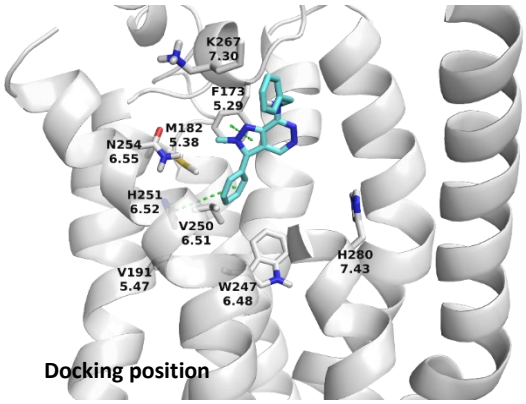

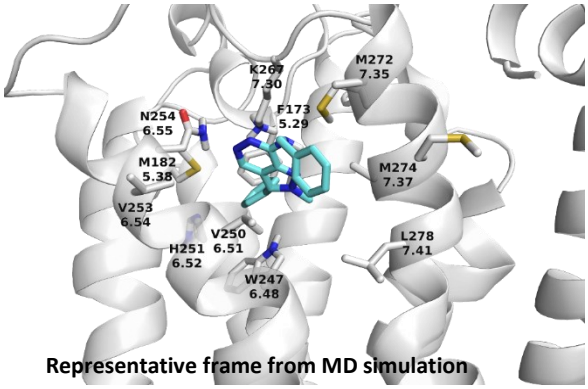

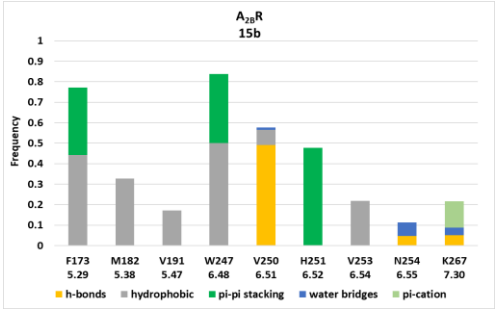

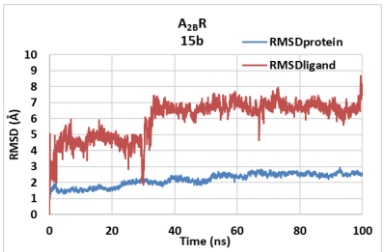

D A_3R - **15b**

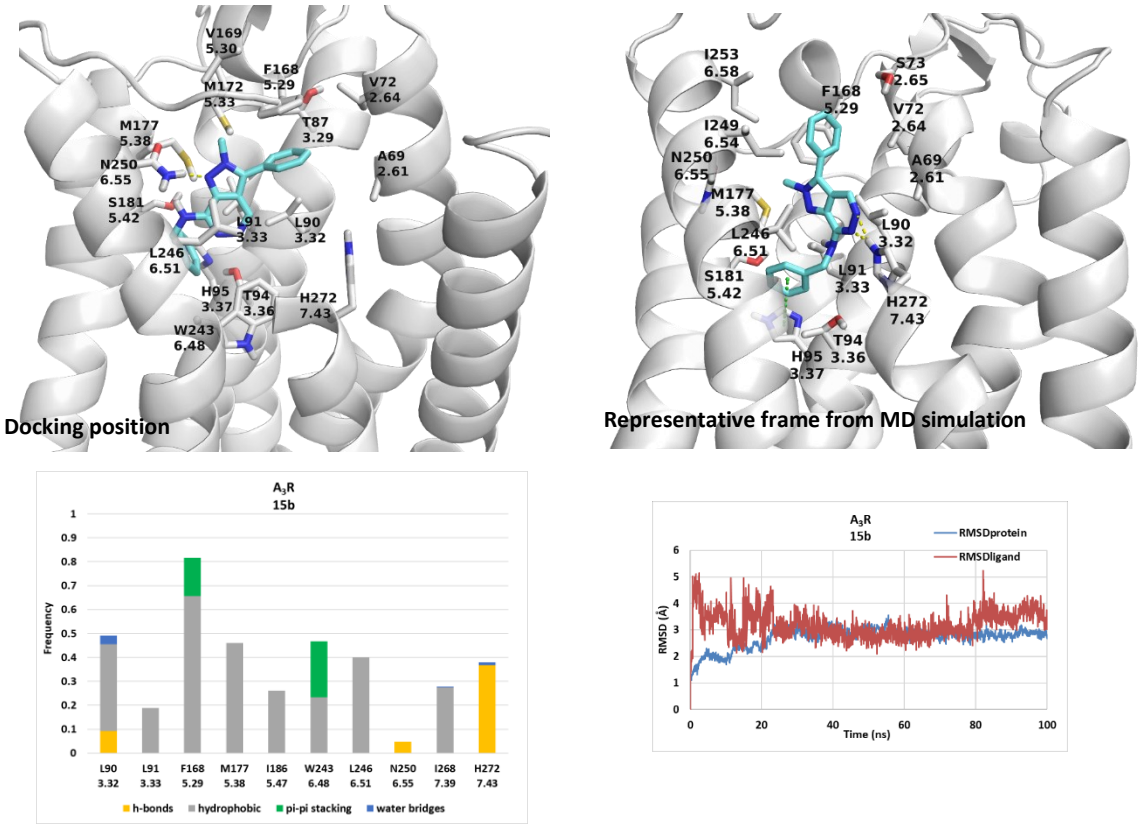

Figure 3-1: Docking poses and representative frames, receptor-ligand interaction frequency histograms and RMSD graphs from 100ns-MD simulations of **10b** (A)-(B) inside the orthosteric binding area of WT A2BR or A3R and (C),(D) **15b** inside the orthosteric binding area of WT A2BR ,A3R, respectively. Bars are plotted only for residues with interaction frequencies ≥ 0.2. Color scheme: Ligand=**10b** dark red, **15b** cyan sticks, receptor=white cartoon and sticks, hydrogen bonding interactions=yellow (dashes or bars), π-π interactions=green (dashes or bars); hydrophobic interactions=grey; water bridges=blue. RMSD graphs of protein Ca (RMSDprotein; blue plots) and ligand heavy atoms (RMSDligand; red plots).

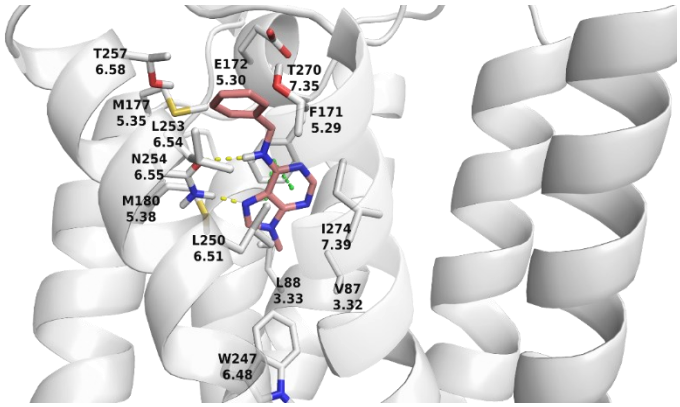

***Figure 2-3**: N9-methyl,N6-benzyl adenine inside the orthosteric binding area of WT A_1R; from docking calculations. .Color scheme: Ligand=light pink sticks, receptor=white cartoon and sticks, hydrogen bonding interactions=yellow (dashes), π-π interactions=green (dashes).*

Mutagenesis experiments to study 10b binding to A_1R.

We have previously observed that mutation of residues that do not directly interact with the ligands, (e.g. $V^{5.30}$ for A_3R, which is more than 4 Å apart from the ligand inside the orthosteric binding area) can, through allosteric interactions due to the plasticity of the binding area, significantly affect ligand affinity. [89,257,313]As such it is not always straight forward to determine the effects of a mutation on affinity properties. Despite this caveat, we next used mutational analysis combined with NanoBRET to determine the important residues required for **10b** binding to A_1R. The mutation of $L250^{6.51}A$ resulted in only a slight reduction of binding affinity for **10b** (Table 3-2) despite the MD simulations suggesting that the ligand should be close enough to $L250^{6.51}$ to enable hydrophobic interactions. It is possible that residues $H251^{6.52}$ and $W247^{6.48}$ could contribute to the stabilization of **10b** with hydrophobic interactions even if $L250^{6.51}$ is mutated to alanine. It is noteworthy that mutation of $E172^{5.30}$ (which is also more than 4 Å apart from the ligand inside the orthosteric binding area) to alanine also did not significantly change the binding affinity (Table 3-2).

In addition, mutation of $H251^{6.52}A$ has been reported to reduced antagonist affinity against and A_3R [257,313]although here it did not have any effect on **10b** affinity at the A_1R. Other residues of interest to mutate were $T91^{3.36}A$ and $S267^{7.32}A$, which are deep in the orthosteric pocket. Interestingly, we found that mutation to alanine of these residues, also did not have a significant effect on the binding affinity of **10b** (Table 3-3**Table** 3-1).

The biggest effect in this study was observed for the $Y271^{7.36}A$ mutation which caused a ~10-fold reduction in binding affinity of **10b** (Table 3-3). Since the MD simulations showed contacts with $H278^{7.43}$ and not $Y271^{7.36}$, the mutation $Y271^{7.36}A$ in the A_1R might affect binding of **10b** through contact with $H278^{7.43}$. We performed the MD simulation of **10b** in complex with $Y271^{7.36}A$ A_1R and observed that the ligand loses its hydrogen bonding interactions with the orthosteric binding area (Figure 3-4).

Table 3-3: Binding affinities (pK_i) for **10b** measured using saturation NanoBRET binding against WT A_1R and mutant A_1Rs. Data retrieved from

A_1R	pK_i	Effect on affinity
WT	7.68 ± 0.11	baseline
T91$^{3.36}$A	7.68 ± 0.07	no change
E172$^{5.30}$ A	7.34 ± 0.06	no significant change
L250$^{6.51}$ A	7.57 ± 0.04	no significant change
H251$^{6.52}$A	7.62 ± 0.06	no significant change
S267$^{7.32}$A	7.86 ± 0.03	no significant change
Y271$^{7.36}$A	6.99 ± 0.05	~10-fold reduction

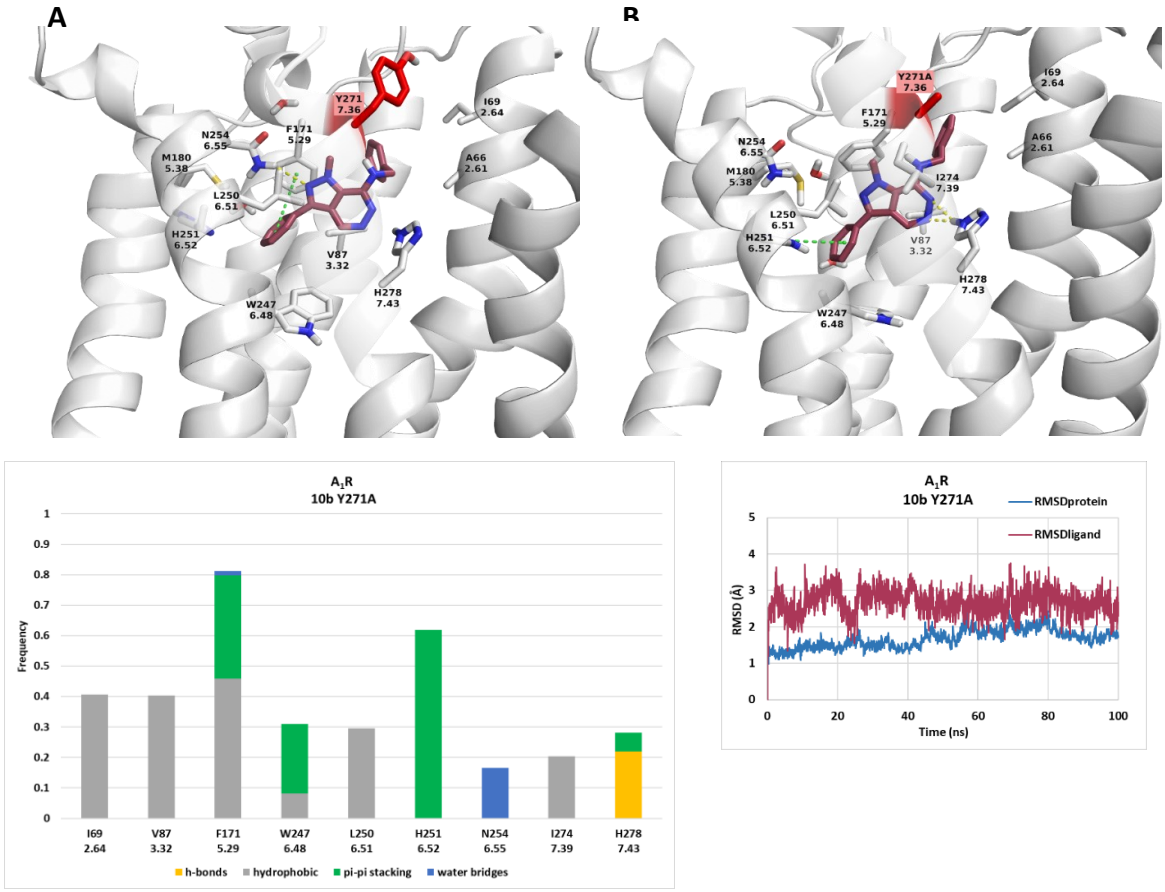

***Figure 3-3**: Representative frames from 100ns-MD simulations of (A) **10b** inside the orthosteric binding area of WT A_1R; (B) **10b** inside mutant Y271A A_1R. Receptor-ligand interaction frequency histogram and RMSD graphs of protein Ca (RMSDprotein; blue plot) and ligand heavy atoms (RMSDligand; red plot). Bars are plotted only for residues with interaction frequencies ≥ 0.2. Color scheme: Ligand=brown sticks, receptor=white cartoon and sticks, hydrogen bonding interactions=yellow (dashes or bars), π-π interactions=green (dashes or bars); hydrophobic interactions=grey; water bridges=blue.*

Chapter 4.

Identification of high affinity dual A_1/A_3 AR antagonists with a novel pyrazolo[3,4-c]pyridine Scaffold

Binding Kinetics and SAR Studies Using Mutagenesis and Alchemical Binding Free Energy Calculations

4. Identification of high affinity Dual A_1/A_3 AR antagonists with a novel pyrazolo[3,4-c]pyridine Scaffold

Binding Kinetics and Structure–Activity Relationship Studies Using Mutagenesis and Alchemical Binding Free Energy Calculations

4.1 Purpose of the study

In this study, two rounds of screening for compounds that acted as antagonists against ARs were performed [in total, 52 molecules tested with chemical structures defining 7 classes of compounds (Table 4-1). The tested compounds belonged to National and Kapodistrian University of Athens *in-house* compounds library. The pyrazolo[3,4-c]pyridine (shown with blue color in Scheme 4.1) was found as a novel pharmacophore which, upon introduction of different substituents, led to high-affinity antagonist activity against both the A_1R and A_3R. Potent antagonists were also identified in two classes of pyrazolo[3,4-c]pyridines, the 7-aminoaryl-3-aryl-5-substituted-pyrazolo[3,4-*c*]pyridines and 3- of 3-(N-acyl)amino-5-aminoaryl-pyrazolo[3,4-*c*]pyridines as shown in Scheme 4.1. These compounds were characterized for their pharmacological activity using both functional inhibition of cAMP accumulation assays and competition for binding of a fluorescent tracer. These studies revealed that compound **A17** displayed a high K_{on} and a low K_{off} for both the A_1R and A_3R, which resulted in a low nanomolar affinity; **A17** (Scheme 4.1), at the A_1R, had a K_d of 5.62 nM and a residence time (RT of 41.33 min) and at the A_3R, the K_d was 13.5 nM with a RT of 47.23 min.

To interpret the interactions of these ligands within the orthosteric binding area of A_1R, for which experimental structures with bound antagonists have been resolved, [55,56] we performed MD simulations, mutagenesis experiments, binding free energy calculations using the approximate MM/GBSA method [144] with an implicit membrane and by taking into account the waters inside the binding area. [177] [314] For the accurate description of the structure-activity

relationships (SARs), the TI/MD method and a thermodynamic cycle were applied while including the whole ligands-GPCR membrane system in the calculations. The aim was to explore how the experimentally measured relative binding free energies correlated with the calculated values. The accuracy of relative binding free energies calculation for ligands-GPCR systems have been studied previously using FEP/MD method and a thermodynamic cycle. [156]

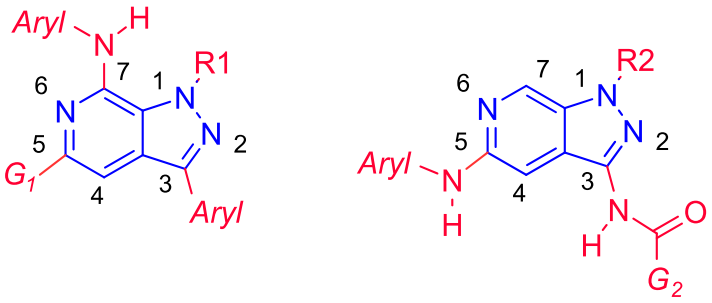

Scheme 4.1 : Chemical structures of 7-aminoaryl-3-phenyl-5-substituted-pyrazolo[3,4-c]pyridines and 3-(N-acyl)amino-5-anilino-pyrazolo[3,4-c]pyridines. The pyrazolo[3,4-c]pyridine pharmacophore is shown in blue color and the attached substituents in red color.

4.2 Results

4.2.1 Compound selection

A functional screen was performed initially of 30 compounds (**A9–18**, **A20**, **A25–29**, and **A32–A45**) from our *in-house* library for the identification of A_3R ligands (Table S2) which were selected after computation of their TanimotoCombo coefficient (Tc) [304] and subsequent comparison of the Tc values with compounds in CHEMBL database [303]. The 7-anilino-3-phenyl pyrazolo-[3,4-*c*]pyridines had a Tc = 0.4 compared to 9-anilino imidazo[4,5-*c*]quinoline A_3R antagonists, [315] the 3-(N-acyl)amino 5-anilino pyrazolo-[3,4-*c*]pyridines had a Tc = 0.2-0.3 compared to 2,4-diaminoquinazoline A_3R antagonists, [316] the N-piperazinyl acetamides of aminopyridino quinazolines had a Tc = 0.22-0.35 compared to N-piperazinyloacetamido aminopyrimidines with antagonistic activity against all ARs, [317] nucleoside derivatives had a Tc = 0.3-0.6 when compared to known agonists or antagonists against all ARs. [69,318–320]

4.2.2 Biological results

Compounds were pharmacological characterized to validate the *in-silico* predictions for the purpose of this study by the laboratory of Dr Graham Ladds, Dept. of Pharmacology, University of Cambridge as described in references [90,301,307] . The pharmacological evaluation included cAMP assays assessing the activity of compounds at ARs, quantifying binding parameters using a NanoBRET-based saturation binding assay and determination of kinetic parameters of compounds binding at A_3R, A_1R using the NanoBRET method. Relevant figures and data can be found in the references [90,301,307] and in Chapter 6 of the Doctoral thesis of Dr Anna Hilser (University of Cambridge, 2022). [308]

Three New Lead Compounds Have A_1R and A_3R Subtype Selectivity.

The *in-house* library of 30 antiproliferative compounds (Table S2) was initially screened using cAMP accumulation assays [321,322] at A_3R. From this functional screen we identified five compounds, **A10**, **A15**, **A17**, **A26** and **A45** as potential A_3R antagonists (Table 4-1). The nucleosides **A10** and **A45** were discontinued in the study since they showed the weakest activity. The three remaining compounds were all pyrazolo[3,4-c]pyridines. Compounds **A15** and **A17** have the same substituents at 5- and 7-positions but have isopropyl and phenyl group at 3-position, respectively. Compound **A26** has different substitution pattern with an acetamido and anilino groups at 3- and 5-position, respectively.

The similarities between the four AR subtypes often result in reduced selectivity of potential antagonists. The subtype selectivity of **A15**/**A17** and **A26** was explored at the different ARs in a functional cAMP assay as described previously [90]. Both **A15** and **A26** showed a lack of efficacy at the **NECA**-stimulated $A_{2A}R$ and $A_{2B}R$ but were able to antagonise the A_1R, although **A15** showed weaker efficacy than **A26**. **A17** also was able to antagonise the A_1R alongside the A_3R with high efficacy (Table 4-1) but did also display, very weak efficacy at the $A_{2B}R$ (pK_d = 5.50 ±0.12)(Table S3). These data indicate that all three compounds showed high subtype selectivity for both the A_1R and A_3R.

Table 4-1: Binding affinities measured using Schild curves (K_d) or BRET method (K_i) and functional activities for **A15**, **A17**, **L2**-**L10**, and **A26**, **L12**, **L15**, **L21** against A_3R or A_1R.

COMPOUND		A_3R			A_1R		
		pIC_{50} in presence of **NECA** [a]	pK_d [b]	pK_i [c]	pIC_{50} in presence of **NECA** [a]	pK_d [b]	pK_i [c]
A15	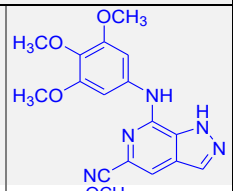	8.71 ± 0.14	5.91 ± 0.19	5.49 ± 0.10	7.99 ± 0.14	6.91 ± 0.18	6.64 ± 0.1
A17	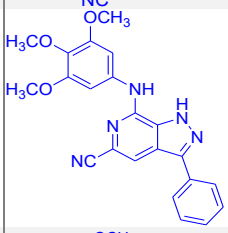	**7.12 ± 0.13**	**7.87 ± 0.18**	**8.01 ± 0.06**	**6.70 ± 0.10**	**8.25 ± 0.15**	**8.36 ± 0.10**
L2	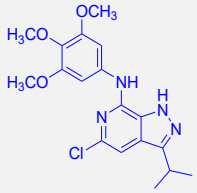	8.55 ± 0.13	6.26 ± 0.18	6.20 ± 0.06	8.30 ± 0.15	6.54 ± 0.19	6.54 ± 0.07
L3	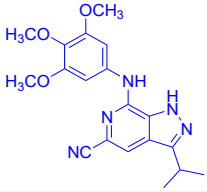	8.42 ± 0.19	6.45 ± 0.23	6.22 ± 0.10	**8.49 ± 0.17**	**6.28 ± 0.20**	**7.91 ± 0.09**
L4	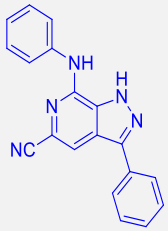	**7.22 ± 0.09**	**7.77 ± 0.16**	**7.36 ± 0.05**	**7.87 ± 0.10**	**7.04 ± 0.14**	**6.67 ± 0.18**
L5	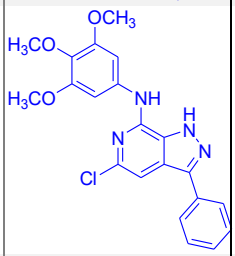	**7.91 ± 0.10**	**7.05 ± 0.2**	**7.26 ± 0.03**	8.54 ± 0.14	6.20 ± 0.18	6.66 ± 0.14
L6	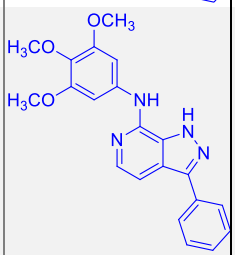	8.29 ± 0.10	6.60 ± 0.24	7.00 ± 0.10	8.72 ± 0.23	6.84 ± 0.23	6.78 ± 0.30

L7	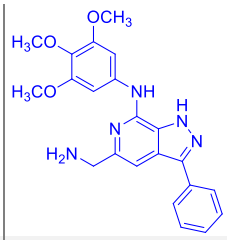	8.31 ± 0.21	6.59 ± 0.25	6.88 ± 0.08	**7.64 ± 0.14**	**7.29 ± 0.18**	**7.64 ± 0.57**
L8	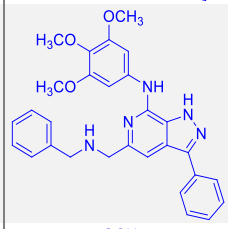	8.14 ± 0.20	6.80 ± 0.24	7.19 ± 0.10	**8.41 ± 0.22**	**7.18 ± 0.25**	**6.69 ± 0.30**
L9	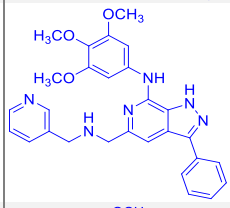	**8.05 ± 0.10**	**6.89 ± 0.20**	**7.19 ± 0.07**	**7.92 ± 0.11**	**6.99 ± 0.16**	**7.20 ± 0.04**
L10	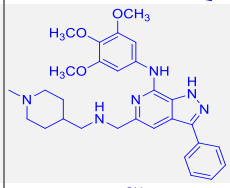	8.56 ± 0.20	6.24 ± 0.24	6.72 ± 0.09	8.33 ± 0.15	6.50 ± 0.19	6.13 ± 0.08
A26	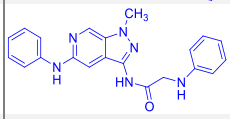	**7.91 ± 0.19**	**7.05 ±0.22**	**7.07 ± 0.08**	8.58 ± 0.10	6.13 ± 0.17	6.53 ± 0.27
L12	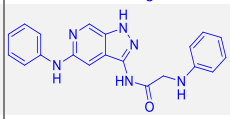	8.52 ± 0.21	6.31± 0.24	6.33 ± 0.09	8.16 ± 0.09	6.71 ± 0.14	6.44 ± 0.11
L15	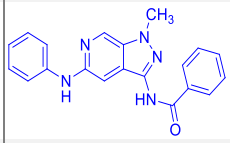	8.17 ± 0.20	6.77 ± 0.24	6.95 ± 0.08	8.30 ± 0.14	6.54 ± 0.17	6.02 ± 0.14
L21	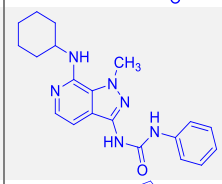	8.37 ± 0.19	6.52 ± 0.2	6.60 ± 0.13	8.85 ± 0.12	<6.0	<6.0
MRS 1220	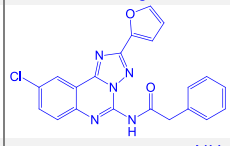	-	10.01 ±[#]	9.94 ±0.11	7.32 ± 0.09	7.62 ± 0.14	7.29 ± 0.27
NECA	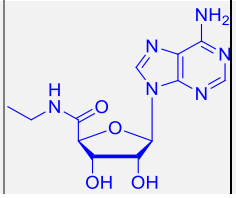	9.03 ± 0.13	-	6.63 ± 0.15	8.95 ± 0.10	-	7.08 ± 0.05

[a] Functional activities (pIC_{50} values in presence of NECA) for the ligands as mean ± standard error of the mean (SEM) of at least 3 independent repeats, conducted in duplicate – values.

[b] Dissociation constant (pK_d) of the ligands as mean ± SEM of at least 3 independent repeats, conducted in duplicate as determined using the Schild analysis.

[c] Equilibrium binding affinities of the ligands measured with NanoBRET against WT A_3R or A_1R; NECA was used as positive control as described in ref [90].

[#] Value obtained from ref [90] using IB-MECA as an agonist.

Adapted from the Doctoral Thesis of Dr Anna Hilser [308] and ref [307] .

Pyrazolo[3,4-c]pyridine, a Novel Scaffold for the Development of AR Antagonists.

Having identified that **A15**/**A17** and **A26** have a potential scaffold with which to design A_1R/A_3R antagonists, a second screening round of 22 compounds was performed using only **A15**/**A17** and **A26** analogues (**L1-L22**). Thus, compounds **L1-11** were derivatives of **A15**/**A17** and **L12-L22** derivatives of **A26** (Table S2). From this screen the 12 additional compounds **L2-L10, L12, L15, L21** (Tables 4-1, S4) were identified as statistically significant potential antagonists at the A_1R/A_3R, through their ability to elevate cAMP accumulation when compared to forskolin and **NECA** co-stimulation. [307] Between these 12 compounds, 11 compounds showed a lack of efficacy at the **NECA**-stimulated $A_{2A}R$ and $A_{2B}R$ except for **L4** which, analogous to **A17**, showed very weak efficacy at the $A_{2B}R$ (pK_d = 5.77 ± 0.12; Tables S4) but were able to antagonise the A_1R or A_3R.

The compounds **A15**/**A17** and their analogues **L2-L10** are all pyrazolo[3,4-c]pyridines and contain an alkyl or phenyl group at 3-position, an anilino group at 7-position and a cyano-, or a chloro- or an aminomethyl or N-(arylmethyl)-2-aminomethyl group at 5-position (Table 4-1). Compounds **A26** and its analogues **L12, L15, L21** are pyrazolo[3,4-c]pyridines substituted with a 3-(N-anilinoacetyl)amino and 3-(N-benzoyl)amino or 3-(N-phenylureido) groups, respectively. Compounds **A26**, **L12**, **L15** are also substituted with a 5-anilino group and compound **L21** with the 7-(N-cyclohexanylamino) group.

The identified pyrazolo[3,4-c]pyridine derivatives provide a novel scaffold for the development of ARs antagonists. Representative nonxanthine pyrazolo derivatives that have been reported as ARs ligands include pyrazolo-[4,3-*e*]-1,2,4-triazolo-[1,5-*c*]pyrimidines, pyrazolo-[3,4-*c*] or -[4,3-*c*]quinolines, pyrazolo-[4,3-*d*]pyrimdinones, pyrazolo-[3,4-*d*]pyrimidines, and pyrazolo-[1,5-*a*]pyridines. [305] Searching in ChEMBL using similarity-based parameters for **A15**/**A17** or **A26**, that is, a Tc value > 0.85, non similar compounds or any other pyrazolo[3,4-c]pyridines as ARs antagonists were found.

Functional activities measurements of the 15 pyrazolo[3,4-c]pyridines showed that all compounds caused a reduction in **NECA** potency at the A_3R, characteristic of competitive antagonism all-be-it with varying extents (Table 4-1). Moreover, some of the compounds also showed antagonism at the A_1R although compounds **L5**, **A26** displayed only weak effects on **NECA** potency while **L21** was inactive (Table 4-1, Table S5). When analyzed using Schild analysis [323] ,the data enabled a crude estimation of the dissociation constant (pK_d) of each antagonist at the two AR subtypes. **L21** did not display any activity at the A_1R.

Competition binding assays and determination of kinetic parameters using NanoBRET

To provide a more quantitatively accurate estimate of the pK_D for all 15 pyrazolo[3,4-c]pyridines at the A_3R and A_1R, a BRET-based competition binding assay was performed as described previously [90] (Table 4-2). The NanoBRET binding assay also enables the determination of the kinetics of the compounds binding, which Schild regression does not, as have been reported in previous studies [90 309 324,210,211]. The reciprocal of the K_{off} enables a determination of the RT of the compound. [90] Beyond this, the pK_D of the compounds (k_4/k_3) was also determined from the kinetics assays and was compared to those determined from the saturation binding assays and the Schild analysis. Estimates of the kinetics of binding were determined for most of the **A17** and **A26**-based derivatives except for **A15**, **L2**, and **L3** at the A_3R and **L21** at the A_1R which failed to provide a reliable fit to the data, likely due to their high K_d values (Table 4-2).

Many of the compounds showed a good agreement between the different methods used to determine their affinities as compared in Table 4-1 and Table 4-2. Thus, consistent with the Schild analysis, compound **A17** displayed the highest affinity at the A_3R followed by **L4 > L6 = L5 = A26 = L9**. At A_1R **A17** also had the highest affinity with the rank order of affinities being **A17 > L3 > L9 > L7 > L4**. All the other compounds displayed weaker affinities. The comparison of the affinity constants calculated by the NanoBRET binding assays and the Schild analysis once again showed close agreement except for compound **L3** at the A_1R where the affinities determined in the BRET binding assays were 50-fold higher than in the Schild analysis. This may indicate that **L3** has unusual properties compared to the other compounds tested here.

Table 4-2: Kinetics of binding for the **A17**- and **A26**-panels of compounds to the orthosteric binding area at the A_3R and A_1R.

	A_3R				**A_1R**			
COMPOUND	Kon (k_3) x10^5 M^{-1} [a]	Koff (k_4) min^{-1} [b]	pK_D Kinetics [c]	RT (mins) [d]	Kon (k_3) x10^5 M^{-1} [a]	Koff (k_4) min^{-1} [b]	pK_D Kinetics [c]	RT (mins) [d]
A15	**<50**	**<0.4**	**N.D.**	**>2**	3.18 ±1.0	0.03 ±0.006	6.99 ±0.21	38.7 ±8.8
A17	21.3 ±1.2	0.021 ±0.003	8.00 ±0.32	47.23± 8.2	139.7 ±1.5	0.024 ±0.009	8.76 ±0.07	41.31 ±4.56
L2	**<50**	**<0.4**	**N.D.**	**>2**	1.72 ±0.3	0.048 ±0.01	6.55 ±0.03	22.9 ±4.3
L3	**<50**	**<0.4**	**N.D.**	**>2**	45.07 ±3.4	0.061 ±0.002	7.86 ±0.45	16.3 ±0.3
L4	8.2 ±0.5	0.026 ±0.006	7.58 ±0.32	46.72 ±4.5	11.5 ±4.0	0.051 ±0.004	7.21 ±0.51	20.61 ±3.4
L5	3.65 ±0.6	0.031 ±0.01	7.07 ±0.22	32.05 ±6.3	2.79 ±0.29	0.055 ±0.001	6.70 ±0.54	18.2 ±4.37
L6	24.7 ±3.8	0.18 ±0.02	7.13 ±0.55	5.55 ±2.6	5.23 ±0.45	0.036 ±0.005	6.88 ±0.23	27.72 ±3.7
L7	4.8 ±2.4	0.105 ±0.04	6.59 ±0.73	9.55 ±3.5	9.63 ±2.5	0.039 ±0.004	7.39 ±0.40	25.34 ±4.9
L8	9.33 ±1.4	0.173 ±0.067	**6.73 ±0.45**	**5.78**	2.34 ±0.6	0.054 ±0.005	6.37 ±0.11	18.50 ±2.6
L9	5.62 ±1.0	0.054 ±0.02	7.0 ±0.33	17.85 ±4.3	8.17 ±1.4	0.02 ±0.015	7.54 ±0.10	43.96 ±2.1
L10	3.38 ±1.1	0.01 ±0.001	6.56 ±0.43	10.85 ±3.4	1.65 ±0.4	0.04 ±0.007	6.64 ±0.03	31.43 ±7.1
A26	12.45 ±1.8	0.096 ±0.03	7.11 ±0.45	10.4±3.4	3.36 ±1.6	0.134 ±0.003	6.40 ±0.18	7.47 ±2.2
L12	1.45 ±0.3	0.051 ±0.03	6.45 ±0.22	19.04 ±5.6	1.84 ±0.4	0.052 ±0.003	6.55 ±0.40	19.23 ±4.5
L15	**<50**	**<0.4**	**N.D.**	**>2**	0.834 ±0.3	0.071 ±0.004	6.07 ±0.22	14.06 ±2.4
L21	**<50**	**<0.4**	**N.D**	**>2**	**<50**	**<0.4**	**ND**	**>2**
MRS1220	3250 ±2.8[#]	0.025 0.005[#]	10.11[#]	40.32[#]	14.54 ±0.4	0.023 ±0.0008	7.80 ±0.2	43.67 ±5.6

[a] K_{on} (k_3) for ligands as determined using NanoBRET binding assays and determined through fitting with the 'Kinetics of competitive binding' model.
[b] K_{off} (k_4) for ligands determined as in a.
[c] Kinetic dissociation constant (pK_d) for each ligand as determined from K_{on}/K_{off}.
[d] Residence time of each ligand as determined by the reciprocal of the K_{off}.
[#] Value obtained from ref [90].
Note – values in bold could not be fitted using the 'kinetics of competitive binding' model.
Adapted from the Doctoral Thesis of Dr Anna Hilser [308] and ref [307] .

From this data we observed that the most interesting potencies at 1 μM concentration (indicated in bold in Table 4-1) include: (a) **L3** or **L4**, **L5**, **L7**,**L8**, **L9**, **A17**, which are pyrazolo-[3,4-*c*]pyridines with isopropyl or phenyl group at 3-position, respectively, a cyano or chloro or aminomethyl or N-(arylmethyl)aminomethyl group at 5-position and an anilino group at 7-position, (b) **A26**, which is 3-(N-acyl)amino-5-anilino pyrazolo-[3,4-*c*]pyridine. The affinity range for the **A17** series, including compounds **L2**-**L10**, **A15** was between low micromolar to low nanomolar. The affinity range for **A26** series, including compounds **L12**, **L15**, **L21,** was between low micromolar to 100 nM. Using these different methods revealed that, at the A_3R, both **A17** and **L4** displayed a low nanomolar affinity, while **A26**, **L5**, **L8** and **L9** had mid-nanomolar affinities with the remaining compounds showing low affinities. At the A_1R, only **A17** displayed a low nanomolar affinity while the five compounds **L4** and **L6**-**L9** displayed mid-nanomolar to low nanomolar affinities. We can observe that **A26** displayed a 5-fold selectivity for A_3R while **L7** is 6-fold selective for A_1R.

Compared to **A15**, the phenyl group in **A17** increased the binding affinity by ~17-fold at A_1R and considerably increased it at A_3R (Tables 4-1, 4-2). The affinity was increased with the size of the 3-substituent according to the p$K_{\underline{d}}$ values for **L3** and **A17**, showing that the phenyl group was favored over the isopropyl group. Removal of the 5-cyano group in compound **L6** resulted in a reduction of affinity of ~100-fold at the A_1R and ~7-fold at the A_3R. Similarly, when the cyano in **A17** was changed to chlorine group in **L5** the affinity was reduced ~100-fold for A_1R and ~5-fold for A_3R. Changing the cyano group in **A17** to an aminomethyl group in **L7** reduced its affinity at both receptors by ~25-fold. Affinity was increased by ~3-fold at both receptors, when three methoxy groups (**A17**) were added to the phenyl group of **L4**. No change was observed in the affinity against A_3R between **L8** and **L9**. However, the presence of a pyridinyl group in **L9** (compared to phenyl group in **L8**) led to a 15-fold increased affinity of **L9** against A_1R compared to **L8**. The molecular basis of these changes for A_1R-ligand complexes, i.e. the SARs, will be discussed in the TI/MD calculations section.

The highest affinity compounds at the A_3R, ie. **A17**, **L4**, **L5**, displayed the longest RT = 35-50 min. Some of the compounds, which displayed the highest affinity (**A17** and **L9**) at the A_1R, also displayed the longest RTs (40 – 50 min).

4.2.3 Binding Profile of the novel pyrazolo[3,4-c]pyridines using MD Simulations and Mutagenesis Experiments

To investigate the binding profile of the antagonists shown in Table 4-1 at the A_1R [for which an X-ray structure in complex with an antagonist have been resolved (PDB ID 5UEN [55])], MD simulations were performed. Using GOLD software [267] and the ChemScore as scoring function,[129], molecular docking calculations of these compounds into the orthosteric binding site of the A_1R were carried out. All docking poses showed that the anilino group oriented towards the extracellular side of the membrane. The anilino group was oriented towards EL2 (as in docking pose 1 shown in Figure 4-1A) or toward the water environment (docking pose 2 shown in Figure 4-1B). Similar binding poses for the antagonist **ZM241385** in complex with $A_{2A}R$ have been observed in the X-ray structures PDB ID 4EIY[53] or 3EML[34] respectively. However, only docking pose 1 agreed with our mutagenesis data described below. Within the 100ns-MD simulation time, the total energy and RMSD of the protein backbone C_α atoms reached a plateau, and the systems were considered equilibrated and suitable for statistical analysis (Table 4-3). The $RMSD_{prot}$ values were between 2-3 Å except in cases of the ligands **L8, L9** which having an increased girth produced $RMSD_{prot}$ values 3-3.5 Å.

Table 4-3: $RMSD_{lig}$, $RMSD_{prot}$ for A15, L2-L10, A17, and A26, L12, L15, L21 against A_1R and OPLS2005-calculated MM/GBSA binding free energies (ΔG_{eff}) from the amber99sb 100ns-MD simulations using an implicit membrane model, for A15, L2-L10, A17, against A_1R.

Compound	$RMSD_{lig}$ [a]	$RMSD_{prot}$ [b]	ΔG_{eff} [c]
A15	5.77 ± 0.42	2.07 ± 0.15	-99.37 ± 6.88
A17	2.81 ± 0.19	1.90 ± 0.20	-120.21 ± 7.25
L2	3.22 ± 0.36	1.78 ± 0.13	n.d.
L3	3.50 ± 0.40	2.42 ± 0.47	-118.06 ±7.18
L4	2.10 ± 0.20	1.71 ± 0.32	-91.10 ± 6.62
L5	2.90 ± 0.84	1.80 ± 0.14	-125.22 ± 7.60
L6	4.39 ± 0.39	1.96 ± 0.13	-105.14 ± 6.99
L7	1.36 ± 0.15	2.12 ± 0.16	-135.53 ± 5.95
L8	3.8 ± 0.29	2.0 ± 0.2	-141.21 ± 9.17
L9	3.54 ± 0.08	1.86 ± 0.13	-140.51 ± 9.36
L10	3.07 ± 0.28	2.18 ± 0.28	-162.58 ± 9.79

A26	2.30 ± 0.3	2.51 ± 0.08	n.d.
L12	2.13 ± 0.20	1.66 ± 0.34	n.d.
L15	n.d.	n.d.	n.d.
L21	4.79 ± 0.38	3.78 ± 0.18	n.d.
MRS1220	n.d.	n.d.	n.d.

[a] Mean±SD (Å); Ligand RMSD is calculated after superposition of each protein-ligand complex to that of the starting structure

[b] Mean±SD (Å); Protein RMSD is calculated for the Cα atoms of the α-helices, for the last 50 ns of the trajectories, using as starting structure snapshot 0 of the production MD simulation.

[c] Mean±SEM; Calculated effective binding free energy (kcal mol^{-1}) between ligand and receptor. ΔG_{eff} is calculated from the last 20 ns of the trajectories using 40 ps intervals (ie. 500 frames per trajectory) using a MM/GBSA model that is taking into account the membrane as hydrophobic slab. Mean from three 20ns-MD simulations. **,** n.d., not determined.

MD simulations of A1R- A17 complex

The selected docking pose was embedded in 12 Å hydrated POPE lipid buffer and the system was subjected to 100ns-MD simulations with the amber99sb [270,271] force field. Using docking pose 1, the MD simulations of the A_1R-**A17** complex showed that **A17** made interactions (> 20% frequency) with F171$^{5.29}$, E172$^{5.30}$, M180$^{5.38}$, W247$^{6.48}$, L250$^{6.51}$, H251$^{6.52}$, N254$^{6.55}$, I274$^{7.39}$ (Figure 4-1A). In addition, the A_1R-**A17** complex was stabilized by:

(a) Direct hydrogen bonding interactions between both the pyrazole 1-NH and anilino NH groups of the ligand and the amide side chain carbonyl of N254$^{6.55}$ and between anilino NH group and carboxylate side chain of E172$^{5.30}$.

(b) Hydrogen bonds between the cyano group of the ligand with waters that are inserted in the region between the ligand and TM1-TM2.

(c) π-π stacking interactions between the core pyrazolo-[3,4-*c*]pyridine scaffold and the F171$^{5.29}$ side chain phenyl and between the ligand phenyl substituent and the imidazole of H251$^{6.52}$ or indole of W247$^{6.48}$.

(d) Hydrophobic interactions between:

(i)the trimethoxy-phenyl group of the ligand, which is directed either towards the water exposed area of the receptor or to EL2, and I274$^{7.39}$.

(ii) the pyrazole ring of the ligand and M180$^{5.38}$, L246$^{6.51}$.

(iii) the phenyl ring of the ligand, which was oriented deeper into the receptor from the pyrazole scaffold, and W247$^{6.48}$.

In comparison, starting from docking pose 2 (Figure 4-1B), in which the anilino group was oriented toward the water environment, the MD simulations showed that **A17** did not form hydrogen bonding interactions with E172$^{5.30}$ but did form hydrogen bonds with L250$^{6.51}$, H251$^{6.55}$, and T270$^{7.35}$. We next considered the hydrophobic interactions; **A17** had diminished interactions with M180$^{5.38}$, W247$^{6.48}$, and L250$^{6.51}$ but formed contacts with Y271$^{7.36}$ and π–π interactions with H251$^{6.52}$. Where the 3-phenyl group was oriented extracellularly and the flexible 7-anilino group was oriented toward the bottom of the receptor, no docking pose was obtained. To achieve such a pose, manual docking is needed; however, the MD simulations showed that the complex with A_1R was unstable due to the Pauli repulsion of the 7-anilino group with the bottom part of the receptor.

A

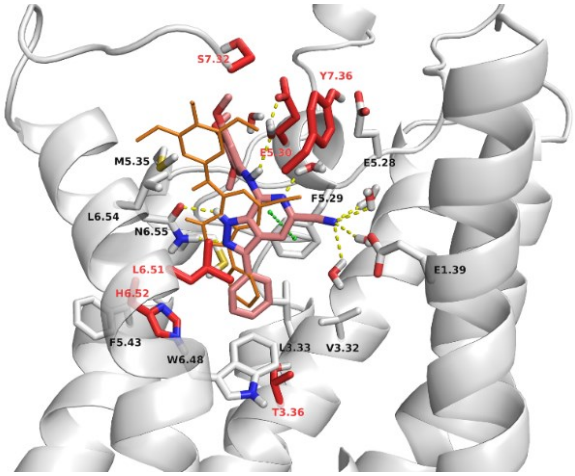
S7.32
Y7.36
E5.30
E5.28
M5.35
F5.29
L6.54
N6.55
L6.51
E1.39
H6.52
F5.43
W6.48
L3.33
V3.32
T3.36

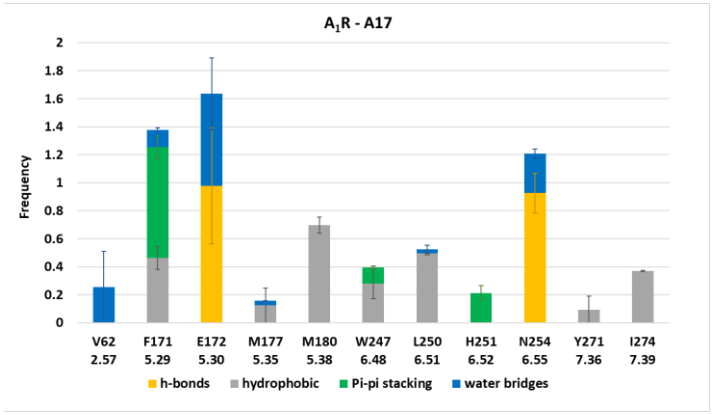
A1R - A17
Frequency
2
1.8
1.6
1.4
1.2
1
0.8
0.6
0.4
0.2
0
V62 2.57
F171 5.29
E172 5.30
M177 5.35
M180 5.38
W247 6.48
L250 6.51
H251 6.52
N254 6.55
Y271 7.36
I274 7.39
h-bonds
hydrophobic
Pi-pi stacking
water bridges

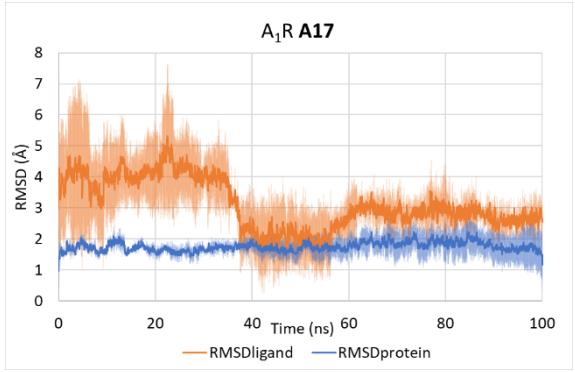
A1R A17
RMSD (Å)
8
7
6
5
4
3
2
1
0
0
20
40
60
80
100
Time (ns)
RMSDligand
RMSDprotein

B

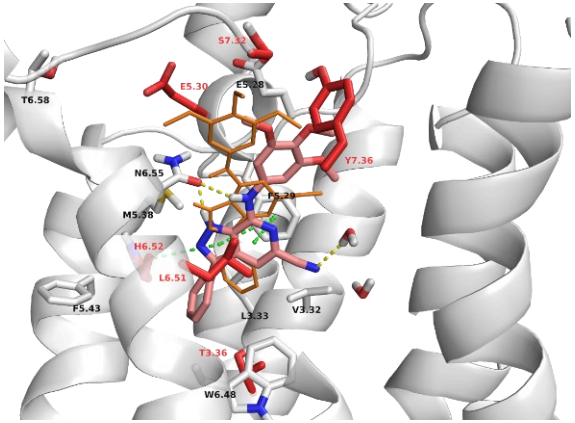
S7.32
E5.30
E5.28
T6.58
Y7.36
N6.55
F5.29
M5.38
H6.52
L6.51
F5.43
L3.33
V3.32
T3.36
W6.48

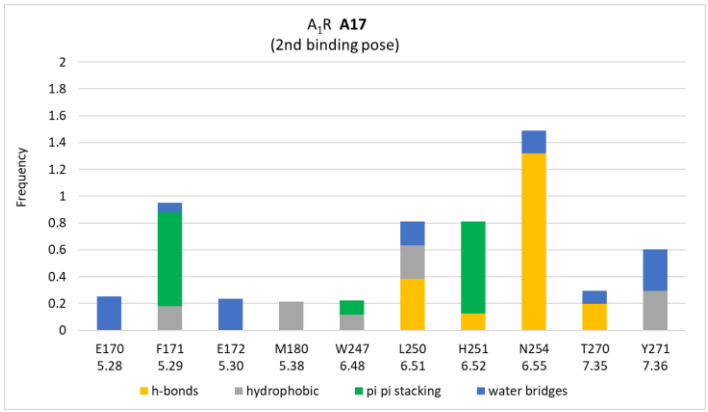
A1R A17
(2nd binding pose)
Frequency
2
1.8
1.6
1.4
1.2
1
0.8
0.6
0.4
0.2
0
E170 5.28
F171 5.29
E172 5.30
M180 5.38
W247 6.48
L250 6.51
H251 6.52
N254 6.55
T270 7.35
Y271 7.36
h-bonds
hydrophobic
pi pi stacking
water bridges

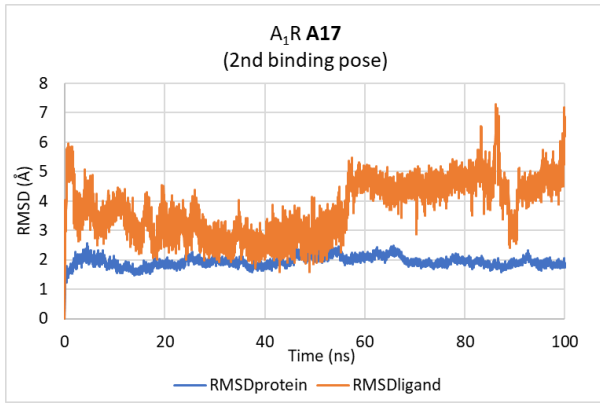
A1R A17
(2nd binding pose)
RMSD (Å)
8
7
6
5
4
3
2
1
0
0
20
40
60
80
100
Time (ns)
RMSDprotein
RMSDligand

***Figure 4-1**: Representative frames, receptor-ligand interaction frequency histograms and RMSD plots of **A17** inside the orthosteric binding area of WT A_1R from 100ns-MD simulations using the amber99sb force field. with (A) binding pose 1 or (B) binding pose 2. Bars are plotted only for residues with interaction frequencies ≥ 0.2. Color scheme in frames or bar plots: ligand is shown with pink sticks and ligand's starting position with an orange wire, receptor is shown with a white cartoon and sticks, hydrogen bonding interactions are shown with yellow dashes or bars, π-π interactions are shown with green dashes or bars; hydrophobic interactions are shown with grey bars; water bridges are shown with blue bars. Mutagenesis experiments were performed for A1R with point mutations to alanine of residues shown in red sticks and/or noted in red color in the frame. For MD simulations we used the experimental structure of the inactive form of A1R (PDB ID 5UEN) in complex with an antagonist.*

MD simulations for the A17 and A26 series A_1R complexes

L4-L7. **L4-L7** contain the main 3-phenyl-5-substituted-7-anilino pyrazolo[3,4-c]pyridine scaffold and compared to **A17** the substituent changes at 7- or/and 5-position. Thus, **L6** or **L5** or **L7** has no substituent or a chlorine or an aminomethyl group at 5-position, respectively, while in **L4** the phenyl group of 7-anilino substituent is unsubstituted (no trimethoxy groups attached). These substituent changes had significant changes in binding affinity as previously discussed and further SARs are discussed in the TI/MD sections. The MD simulations showed that **L4-L7** remained stable inside the orthosteric binding area of A_1R during the MD simulation (Figures 4-2) but in compounds **L6, L5** the interactions between the ligand and residues $N254^{6.55}$, $E172^{5.30}$, $M180^{5.38}$, $W247^{6.48}$ are weakened (Figures 4-2). The effect of the 5-aminomethyl group in the binding mode of **L7** is remarkable. The MD simulations showed that **L7**, compared to **A17**, can interact inside the orthosteric binding area of A_1R with $F171^{5.29}$, $W247^{6.48}$. However, **L7** is inclined towards TM3, TM7 and moves deeper in the binding area due to protonated 5-aminomethyl group which is attracted strongly by $H278^{7.43}$, losing direct hydrogen bonding interactions with $N254^{6.55}$/$E172^{5.30}$ and hydrophobic contacts with $M180^{5.38}$, $L250^{6.51}$. As is shown in Figure 4-2 the ligand forms direct hydrogen bonds mainly with $H278^{7.43}$, water-mediated hydrogen bonds with $T277^{7.42}$, $E172^{5.30}$, $N184^{5.42}$ and van der Waals contacts with TM3 residues $V87^{3.32}$, $T91^{3.36}$ and with TM7 residue $I274^{7.39}$.

L8, L9. Compounds **L8** or **L9** have a phenylmethyl or 3-(pyridinyl)methyl group connected with the 5-aminomethyl group of compound **L7**. The MD simulations showed that compounds **L8, L9** are stabilized inside the binding area. Compounds **L8** and **L9** form contacts through all their groups with A_1R and are extended inside the binding area from TM6 to TM2 because of the long chain substituent at 5-position (Figure 4-2). Compared to **A17, L8** adopts the same position and

binding interactions, ie. with residues F171$^{5.29}$, E172$^{5.30}$, M180$^{5.38}$, W247$^{6.48}$, L250$^{6.51}$, N254$^{6.55}$ inside the orthosteric binding area of A_1R. **L9** ligand in A_1R forms additionally hydrogen bonding interactions through the ammonium group in 5-aminomethyl moiety with H278$^{7.43}$ and hydrophobic contacts through its pyridinylmethyl group with V62$^{2.57}$, A66$^{2.61}$, V87$^{3.32}$ and I274$^{7.39}$. Similarly, **L8** showed contacts with A66$^{2.61}$ (Figure 4-2). These contacts are favoured due to the stabilization of the pyridinylmethyl or benzyl group close to TM2, TM3.

A26, L12 . After several MD simulation repeats we observed that 3-(N-anilinoacetyl)amino-5-anilino-pyrazolo[3,4-c]pyridine **L12** and its 1-methyl analog **A26** have the 3-(N-anilinoacetyl)amino oriented deep in the binding pocket and the 5-anilino group oriented towards TM2 (Figure 4-2).

A15-A_1R

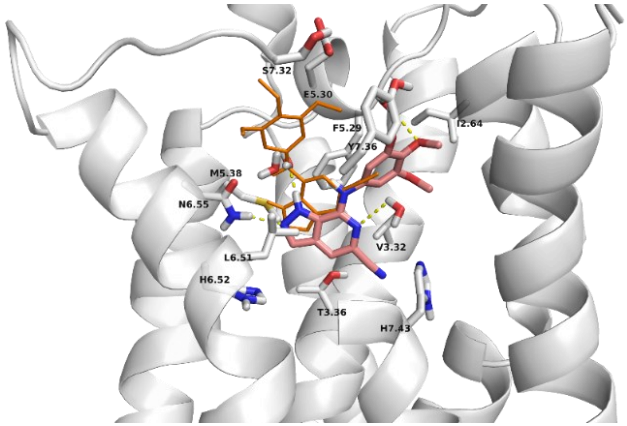

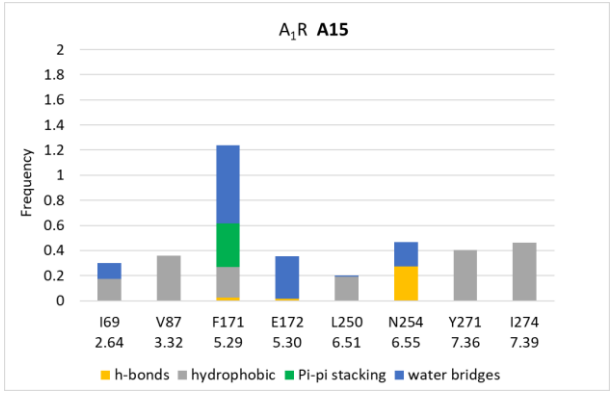

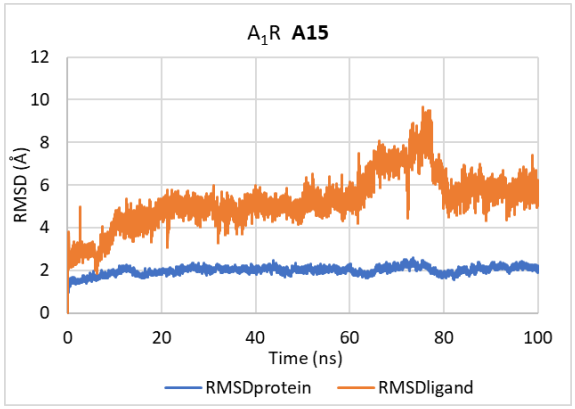

L2-A_1R

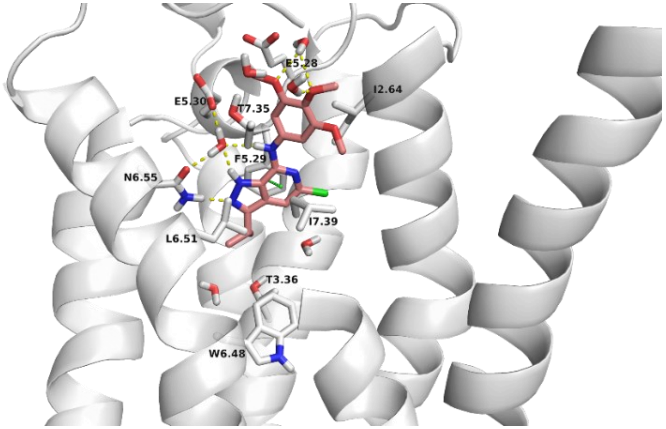

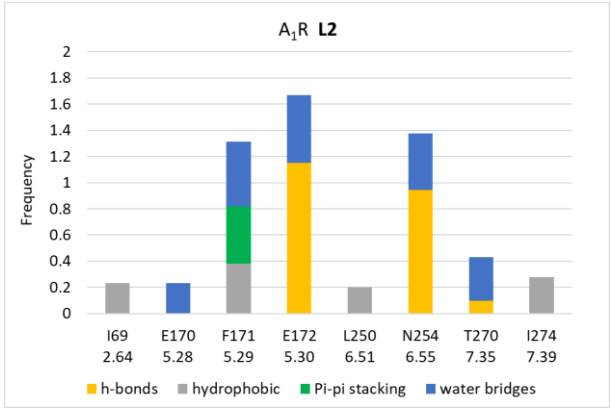

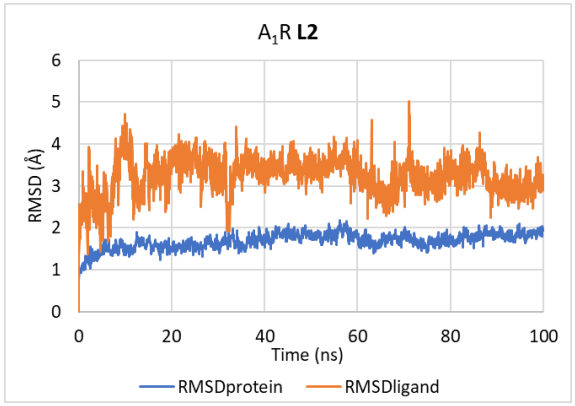

L3-A_1R

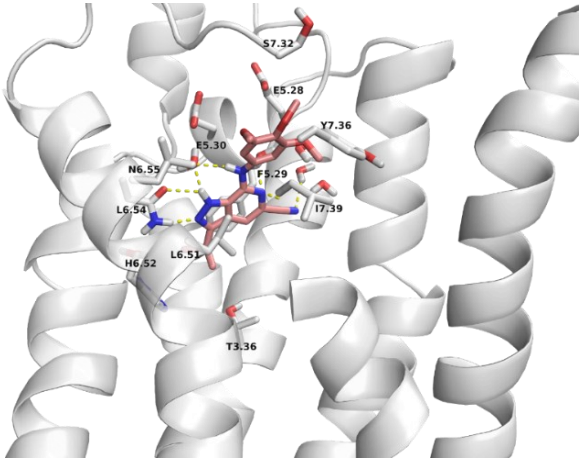
S7.32
E5.28
Y7.36
E5.30
N6.55
F5.29
L6.54
I7.39
L6.51
H6.52
T3.36

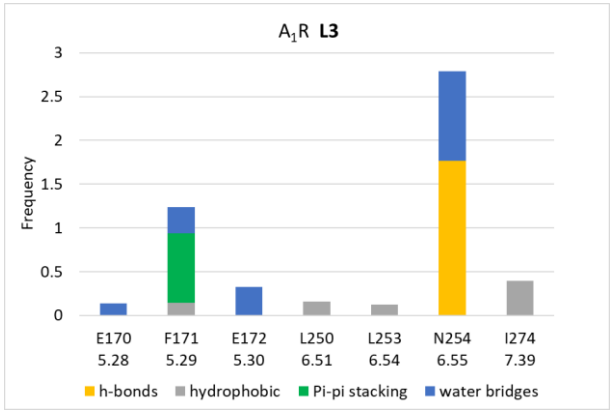
A1R L3
Frequency
3
2.5
2
1.5
1
0.5
0
E170 5.28
F171 5.29
E172 5.30
L250 6.51
L253 6.54
N254 6.55
I274 7.39
h-bonds
hydrophobic
Pi-pi stacking
water bridges

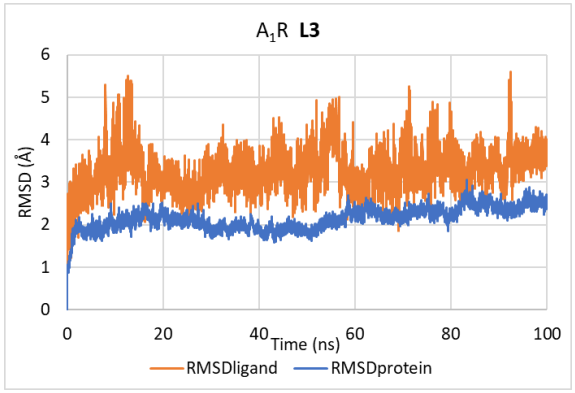
A1R L3
RMSD (Å)
Time (ns)
RMSDligand
RMSDprotein

L4-A_1R

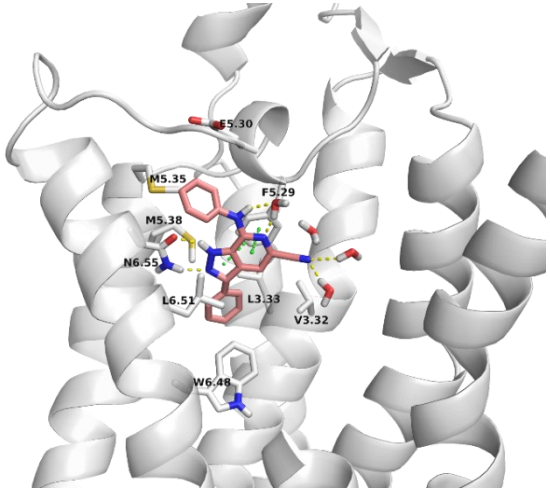
E5.30
M5.35
F5.29
M5.38
N6.55
L6.51
L3.33
V3.32
W6.48

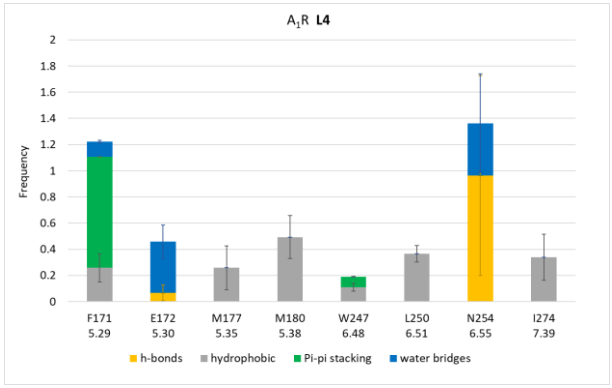
A1R L4
Frequency
F171 5.29
E172 5.30
M177 5.35
M180 5.38
W247 6.48
L250 6.51
N254 6.55
I274 7.39
h-bonds
hydrophobic
Pi-pi stacking
water bridges

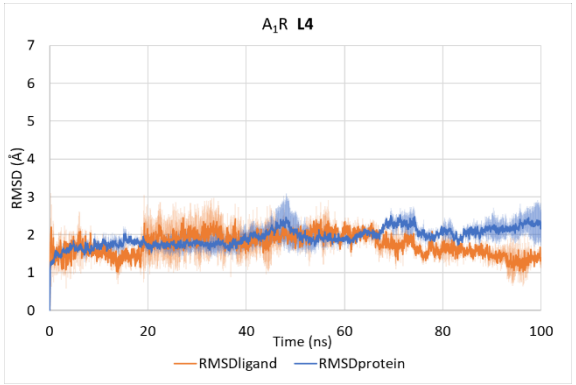
A1R L4
RMSD (Å)
Time (ns)
RMSDligand
RMSDprotein

L5-A_1R

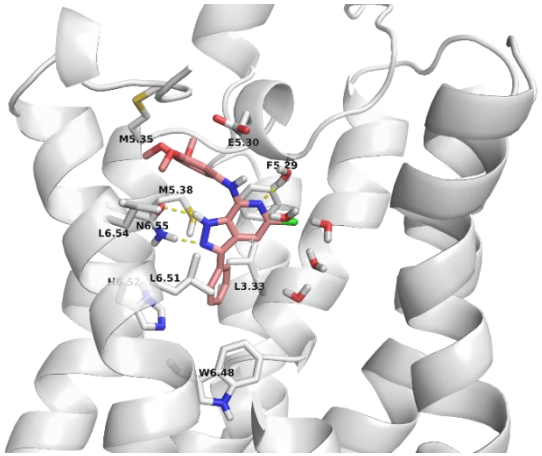
M5.35
E5.30
F5.29
M5.38
N6.55
L6.54
L6.51
L3.33
W6.48

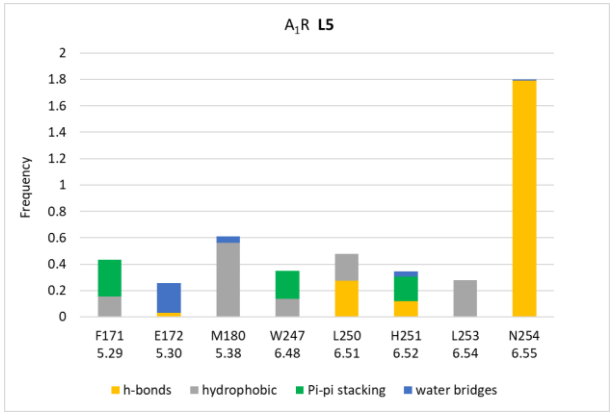
A1R L5
Frequency
2
1.8
1.6
1.4
1.2
1
0.8
0.6
0.4
0.2
0
F171 5.29
E172 5.30
M180 5.38
W247 6.48
L250 6.51
H251 6.52
L253 6.54
N254 6.55
h-bonds
hydrophobic
Pi-pi stacking
water bridges

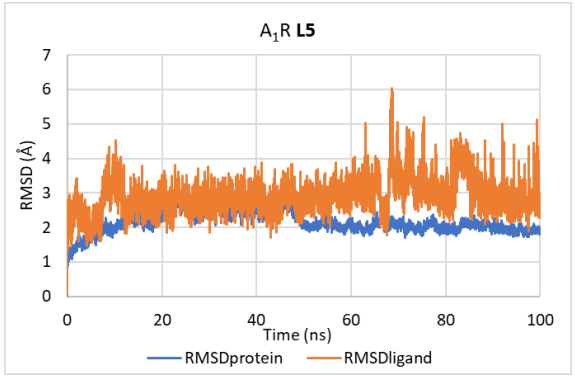
A1R L5
RMSD (Å)
7
6
5
4
3
2
1
0
0
20
40
60
80
100
Time (ns)
RMSDprotein
RMSDligand

L6-A_1R

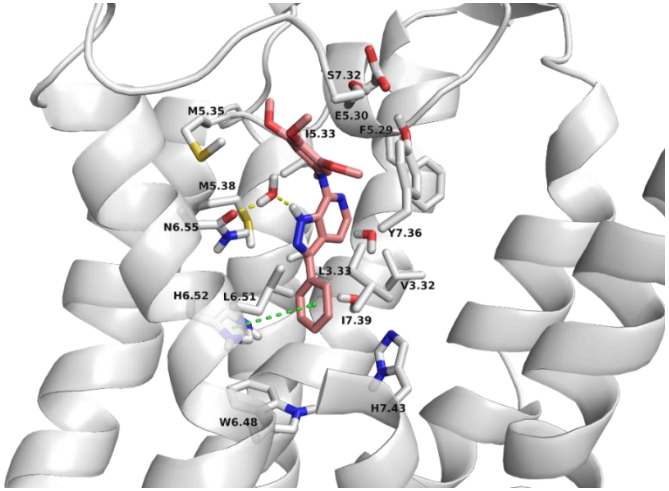
S7.32
M5.35
E5.30
I5.33
F5.29
M5.38
N6.55
Y7.36
L3.33
V3.32
H6.52
L6.51
I7.39
H7.43
W6.48

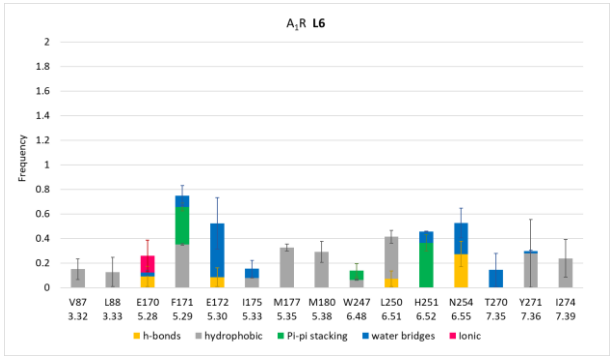
A1R L6
Frequency
2
1.8
1.6
1.4
1.2
1
0.8
0.6
0.4
0.2
0
V87 3.32
L88 3.33
E170 5.28
F171 5.29
E172 5.30
I175 5.33
M177 5.35
M180 5.38
W247 6.48
L250 6.51
H251 6.52
N254 6.55
T270 7.35
Y271 7.36
I274 7.39
h-bonds
hydrophobic
Pi-pi stacking
water bridges
Ionic

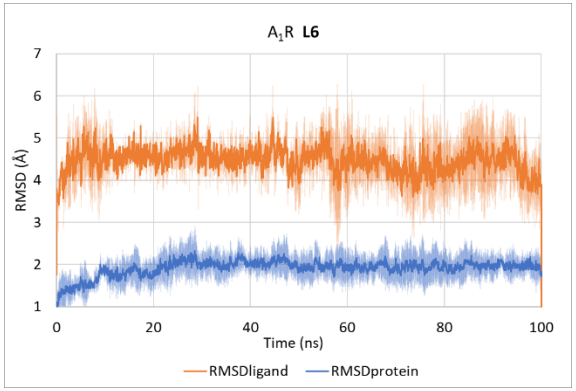
A1R L6
RMSD (Å)
7
6
5
4
3
2
1
0
20
40
60
80
100
Time (ns)
RMSDligand
RMSDprotein

L7-A_1R

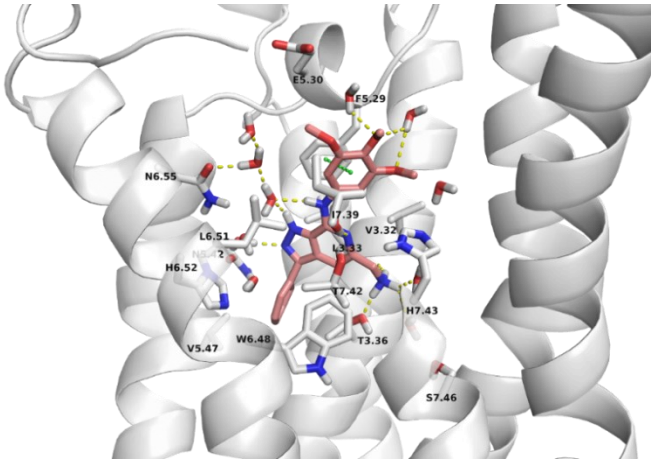
E5.30
F5.29
N6.55
I7.39
V3.32
L6.51
L3.33
H6.52
T7.42
H7.43
W6.48
T3.36
V5.47
S7.46

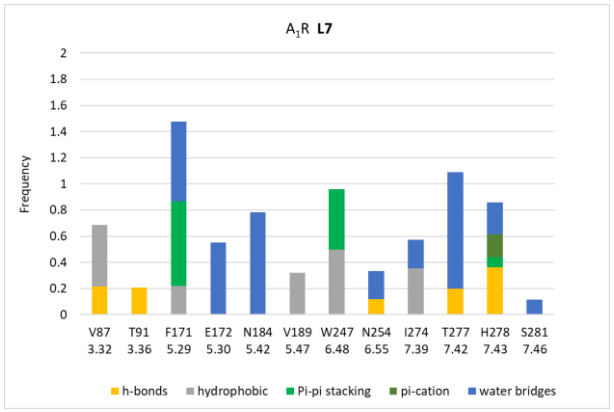
A1R L7
Frequency
V87 3.32
T91 3.36
F171 5.29
E172 5.30
N184 5.42
V189 5.47
W247 6.48
N254 6.55
I274 7.39
T277 7.42
H278 7.43
S281 7.46
h-bonds
hydrophobic
Pi-pi stacking
pi-cation
water bridges

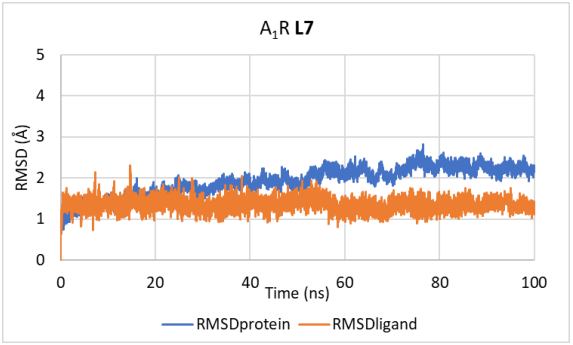
A1R L7
RMSD (Å)
Time (ns)
RMSDprotein
RMSDligand

L8-A_1R

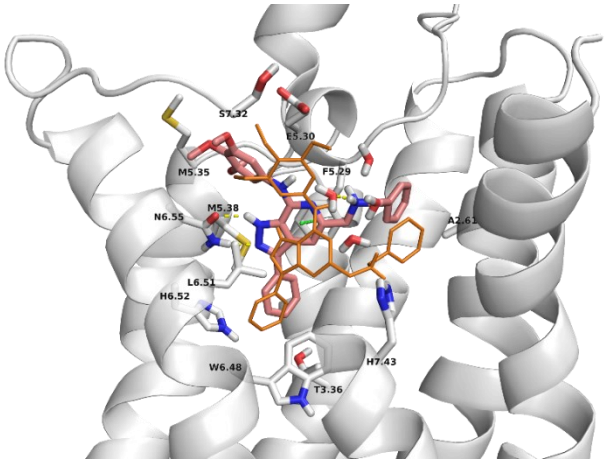
S7.32
E5.30
M5.35
F5.29
M5.38
N6.55
A2.61
L6.51
H6.52
W6.48
H7.43
T3.36

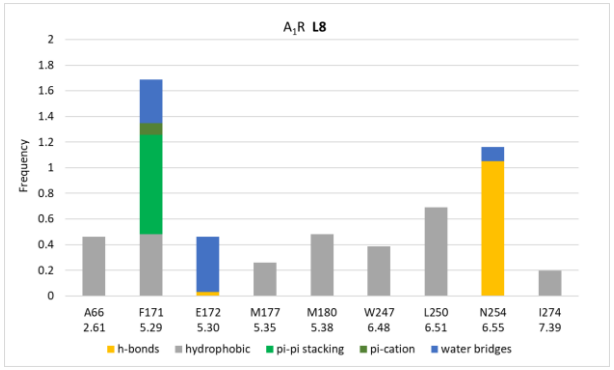
A1R L8
Frequency
A66 2.61
F171 5.29
E172 5.30
M177 5.35
M180 5.38
W247 6.48
L250 6.51
N254 6.55
I274 7.39
h-bonds
hydrophobic
pi-pi stacking
pi-cation
water bridges

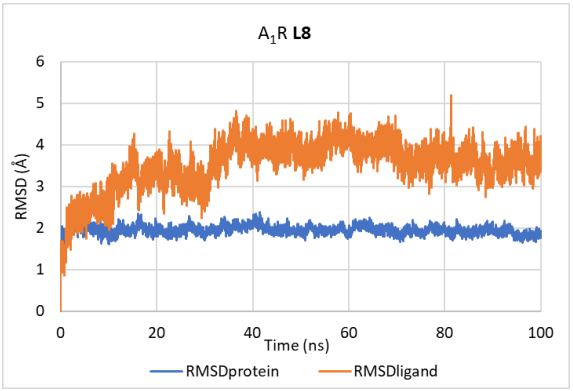
A1R L8
RMSD (Å)
Time (ns)
RMSDprotein
RMSDligand

L9-A_1R

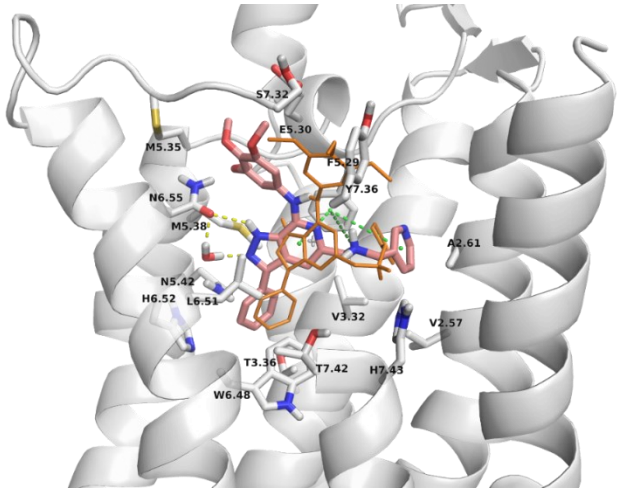

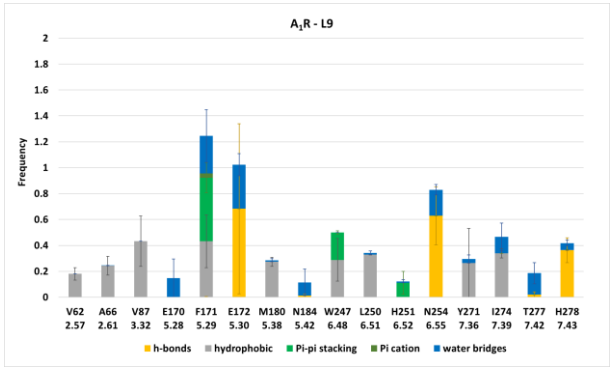

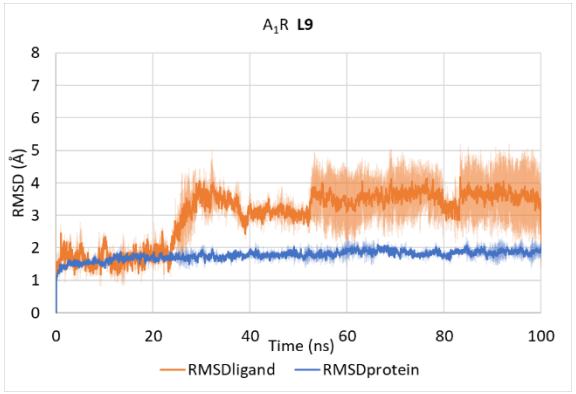

L10-A_1R

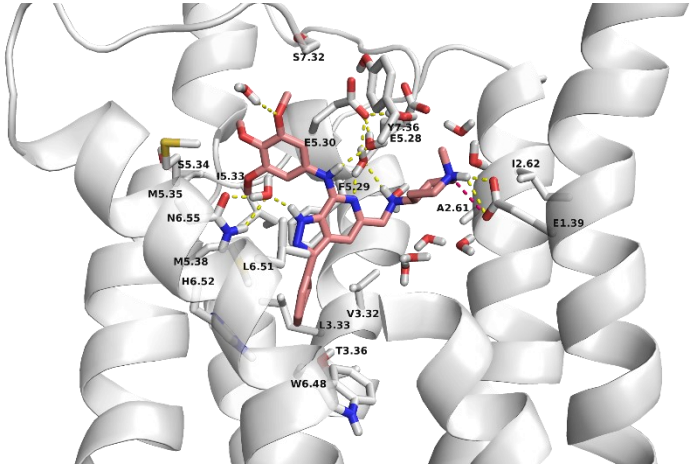

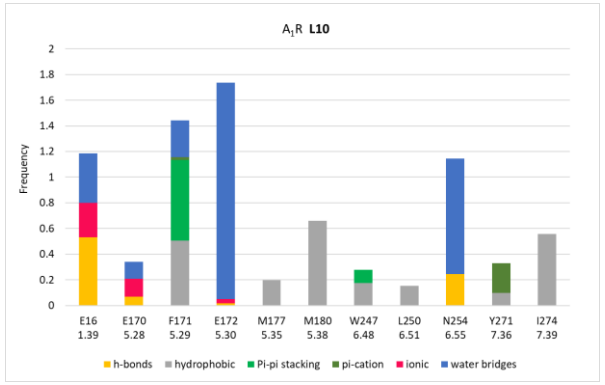

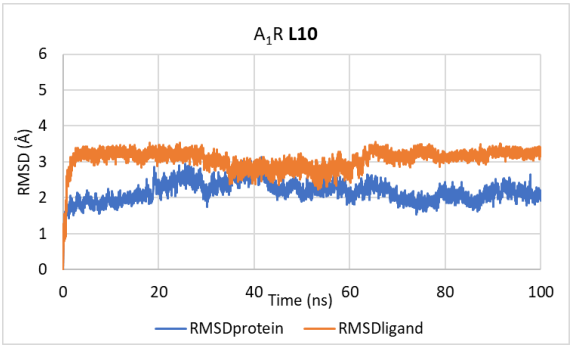

A26-A_1R

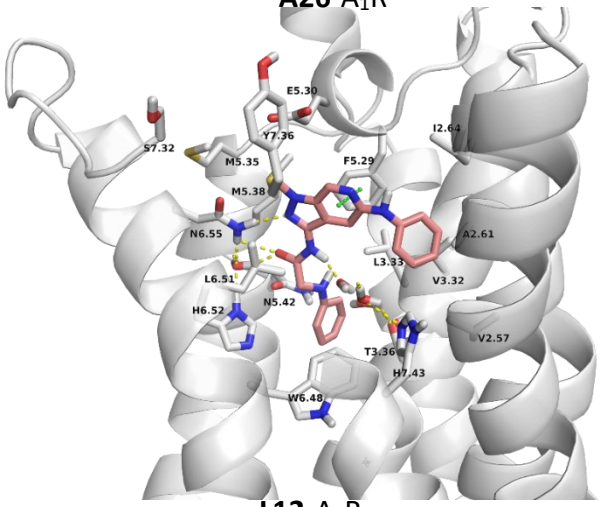

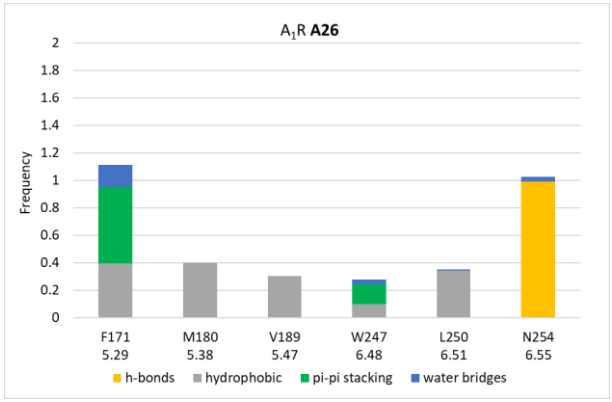

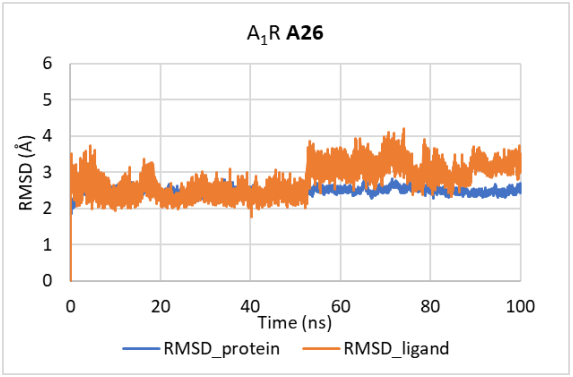

L12-A_1R

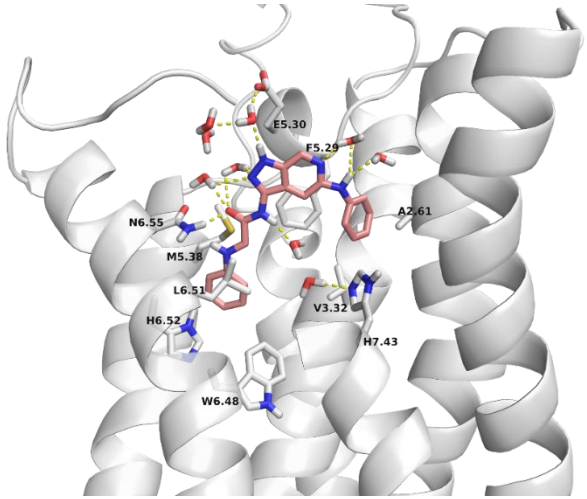

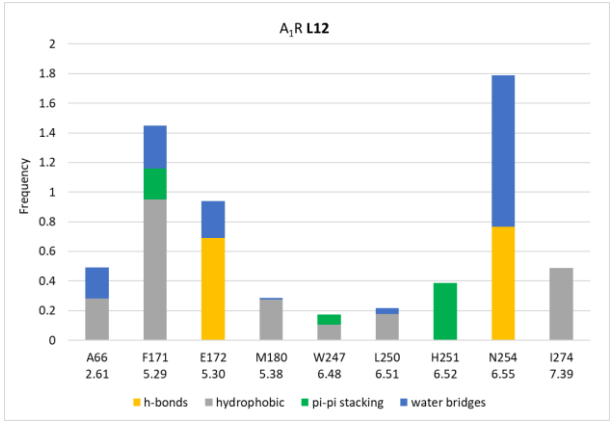

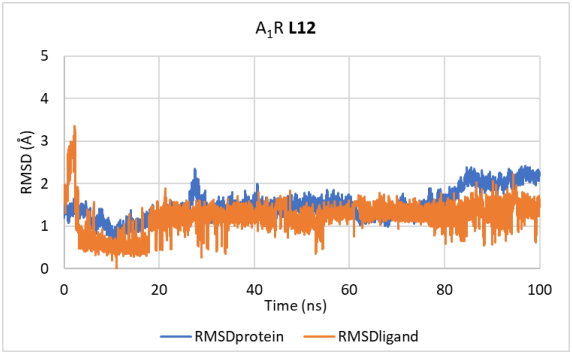

Figure 4-2: *Representative frames of ligands **A15**, **L2**- **L10**, **A26**, **L12** inside the orthosteric binding area of A1R from 100ns-MD simulations. (left hand part). In each panel are shown the receptor-ligand interaction frequency histogram and the RMSD plots for the Ca atoms (blue) and the ligand heavy atoms (orange). Bars are plotted only for residues with interaction frequencies ≥ 0.2. If RMSDlig ≥ 4.5, starting position of the ligand inside binding area is shown in orange lines. Color scheme: Ligang=pink sticks, receptor=white cartoon and sticks, hydrogen bonding interactions=yellow (dashes or bars), π-π interactions=green (dashes or bars); hydrophobic interactions=grey; water bridges-blue. For the protein models of A1R was used the experimental structure of the inactive form for A1R (PDB ID 5UEN) in complex with an antagonist.*

Mutational Analysis of A17

To experimentally investigate residues that were suggested to be important for the binding of **A17** and **A26**, mutagenesis combined with NanoBRET-based competition binding [90] were conducted (Table 4-4). For completeness, the affinity of A_1R for the agonist **NECA** at each mutant was determined. The amino acid residues tested are shown in Figures 4-1 for docking pose 1 and docking pose 2. The A_1R mutants T91$^{3.36}$A, E172$^{5.30}$A, L250$^{6.54}$A and H251$^{6.52}$A all displayed reduced affinity for the fluorescent tracer CA200645 compared to WT A_1R, while mutants S267$^{7.32}$A and Y271$^{7.36}$A showed little difference in effect. As regards **NECA**, A_1R mutants E172$^{5.30}$A, Y271$^{7.36}$A reduce affinity, S267$^{7.32}$A maintain affinity and H251$^{6.52}$A increase affinity. Previous findings have also shown that mutation of S267$^{7.32}$A significantly reduced **NECA's** affinity to the $A_{2A}R$. [325] No binding for **NECA** at T91$^{3.36}$A or L250$^{6.51}$A mutants could be determined, since in agreement to similar observations for $A_{2A}R$ [326] and our findings [89] for A_3R, **NECA** binds to the orthosteric binding area through hydrogen bonding to T91$^{3.36}$ at the bottom of the binding area.

Table 4-4: Binding affinities for CA200645, NECA and **A17**, measured using NanoBRET against WT and mutant A_1Rs.

	Mutation	K_d (nM) [a]	pK_d		Effect on affinity
Residue's location in the binding area		**CA200645**	**A17**	**NECA**	
	WT	76.37 ± 9.37	7.87 ± 0.06	6.67 ± 0.05	baseline

Bottom	T91$^{3.36}$A	166.35 ± 17.36	8.37 ± 0.07 **	n.b. [b]	~3.2-fold increase
Upper	E172$^{5.30}$A	116.04 ± 12.22	7.63 ± 0.08	5.38 ± 0.06 **	~0.5-fold reduction
Middle	L250$^{6.51}$A	158.28 ± 17.37	8.44 ± 0.05 **	n.b. [a]	~3.8-fold increase
Middle	H251$^{6.52}$A	145.19 ± 19.13	8.03 ± 0.10*	8.04 ± 0.10 **	~1.5-fold increase
Upper	S267$^{7.32}$A	70.99 ± 7.03	8.10 ± 0.16 **	6.31 ± 0.10	~1.5-fold increase
Upper	Y271$^{7.36}$A	71.10 ± 7.68	7.82 ± 0.04	5.45 ± 0.06 **	no significant change

[a] Affinity constant for CA200645 binding to mutant A_1R receptors.

[b] n.b. **NECA** was unable to displace **CA200645** at the mutant receptor

Statistical significance (* $p < 0.05$, ** $p < 0.01$,) determined using ANOVA and Dunnett' s post-test.

Adapted from the Doctoral Thesis of Dr Anna Hilser [308] and ref [307] .

The mutations H251$^{6.52}$A or S267$^{7.32}$A in the middle or upper regions of the binding site increased the affinity of **A17** by ~ 1.5-fold (Table 4-4). The effect of H251$^{6.52}$A mutation is usually the same observed for antagonists against A_3R [89,90,257,327] or against A_{2A}R. [325] Alanine mutation of T91$^{3.36}$A or L250$^{6.51}$A in the bottom or middle region caused a 3.2- and 3.8-fold increase in the affinity of A17, respectively (Table 4-4), while displaying no significant effect for **A26** (see Table S6). This agreed with other reports describing how mutating T91$^{3.36}$ to Ala increased the affinity of antagonist **LUF5834**, [328] to A_{2A}R and of other non-nucleoside antagonists for A_1R. [325,329] Previously, we and other groups showed that mutation of residue T91$^{3.36}$ to alanine had a negligible effect on the affinity of antagonists to A_3R [89,90,257,327] or for A_{2A}R, [325,329] respectively. The result for L250$^{6.51}$A was a bit unexpected, since L250$^{6.51}$ is key-to-recognition, highly conserved residue in all four AR subtypes and its mutation to Ala often causes a reduction or blockage of binding (see for examples our results for A_3R in refs [87,90]). The mutant E172$^{5.30}$A in the upper region of the receptor displayed reduced affinity by 10% while mutation Y271$^{7.36}$A did not change the affinity of **A17**.

From the MD simulations of WT A_1R-**A17** complex starting from docking pose 1 (see Figure 4-1A), **A17** forms π-π interactions with H251$^{6.52}$ and strong hydrophobic interactions with L250$^{6.51}$, strong hydrogen bonding interaction with E172$^{5.30}$, and almost no interaction with Y271$^{7.36}$, while T91$^{3.36}$ and S267$^{7.32}$ were at a distance > 4 Å from the ligand and their effect was allosteric.

From the MD simulations of WT A_1R-**A17** complex starting from docking pose 2 (see Figure 4-1B), **A17** forms strong π-π interactions with H251$^{6.52}$ and strong hydrogen bonding interactions with L250$^{6.51}$. Hydrogen bonding interactions with E172$^{5.30}$ were not observed nor were interactions with Y271$^{7.36}$, while both T91$^{3.36}$ and S267$^{7.32}$ were again distant from **A17**.

To further explore which of the two docking poses agreed with the mutagenesis data, MD simulations of Y271$^{7.36}$A A_1R were performed in complex with **A17** in each competing pose. The simulations (Figure 4-3) showed that Y271$^{7.36}$A A_1R reduced the binding interactions of **A17** in docking pose 2 but maintained the interactions in docking pose 1, which agreed with our mutagenesis data. Docking pose 1 was further evaluated by exploring the effects of mutating S267$^{7.32}$A, of T91$^{3.36}$A or L250$^{6.51}$A and H251$^{6.52}$A, on the stability of the complex A_1R-**A17** by performing MD simulations. In all cases, although ligand lost hydrogen bonding with E172$^{5.30}$, the orthosteric binding area displayed plasticity with flexible residues recruited to the binding region to aid binding to **A17** (Figure 4-4). These findings agreed with the observations from the mutagenesis experiments that E172$^{5.30}$ was not very important for binding of **A17** to A_1R and that its mutation to Ala caused only a small reduction in affinity (Table 4-4). Based on these findings, the docking pose 1 was selected to carry out the simulations of **A17** analogues.

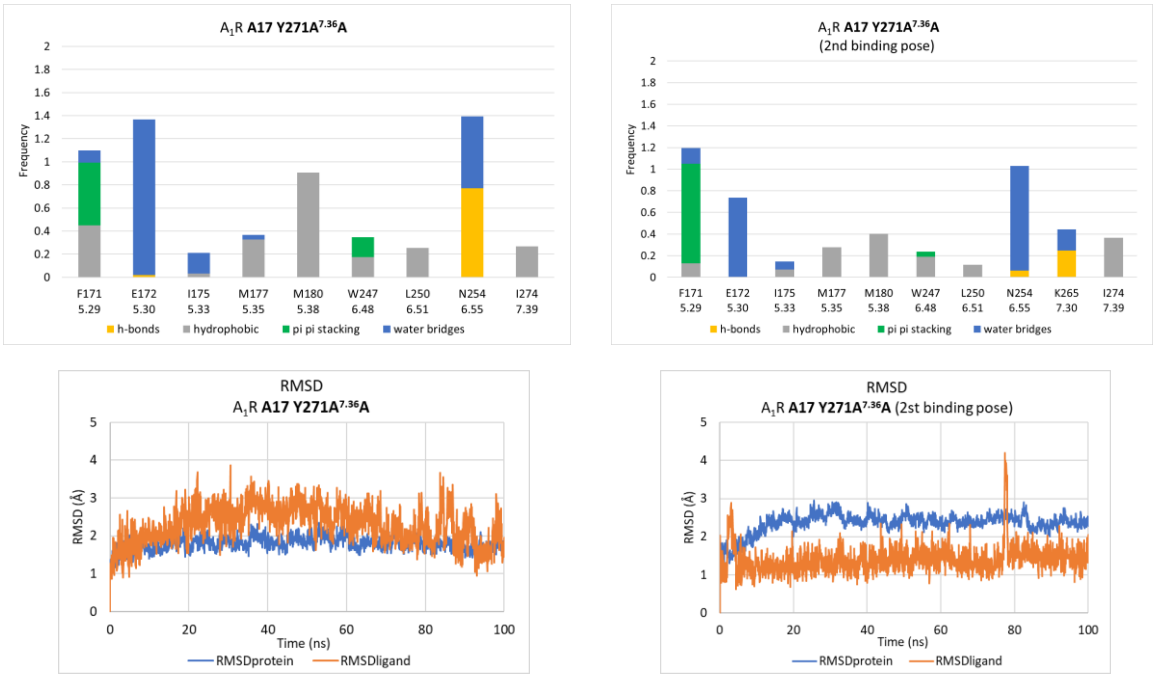

***Figure 4-3**: Receptor-ligand interaction frequency histogram and the RMSD plots of 100ns-MD simulations of Y271$^{7.36}$A A_1R in complex with A17 using docking pose 1 (left hand part) or docking pose 2 (right hand part). RMSD plots for the Cα atoms (blue) and the ligand heavy atoms (orange). Bars are plotted only for residues with interaction frequencies ≥ 0.2.*

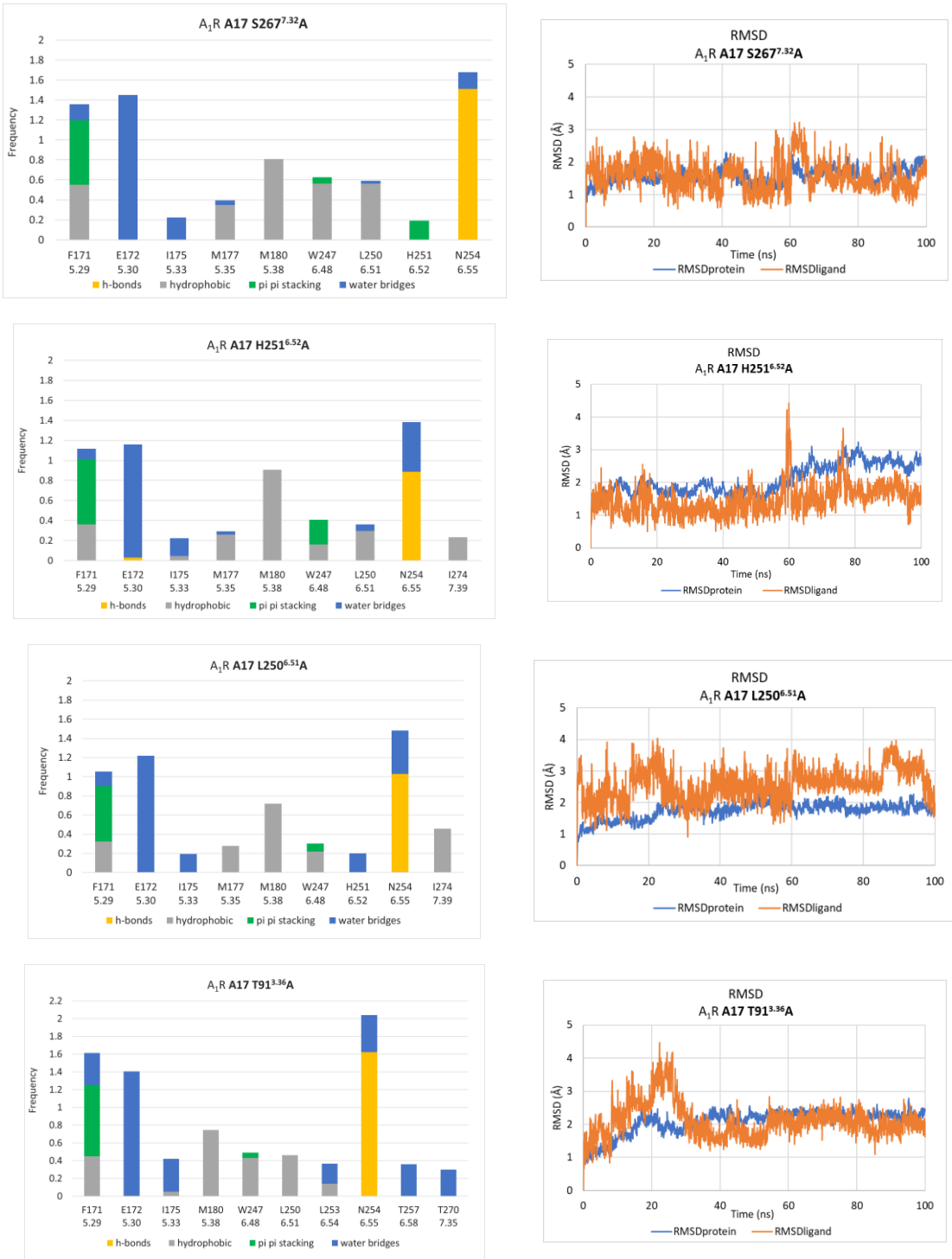

***Figure 4-4**: Receptor-ligand interaction frequency histogram and the RMSD plots of 100ns-MD simulations of S267$^{7.32}$A, H251$^{6.52}$A, L250$^{6.51}$A and T91$^{3.36}$A A_1Rs in complex with A17 from 100ns-MD.. In each panel are shown the receptor-ligand interaction frequency histogram and the RMSD plots for the Ca atoms (blue) and the ligand heavy atoms (orange). Bars are plotted only for residues with interaction frequencies ≥ 0.2.*

4.2.4 SAR Analysis of Ligand Binding Using Free Energy Calculations.

Alchemical Free Energy Calculations with TI/MD

The FEP/MD [330] and TI/MD [189,190] methods can provide accurate results for relative binding free energies with a method error 1 kcal mol^{-1}. We performed TI/MD calculations for the 9 alchemical transformations in the A_1R as listed in Table 4-5. The set of the studied compounds **A15**, **L2**–**L6**, **L8**, and **L9** cover ~100 units of Kd's range. The MD simulations of these compounds in complex with A_1R converged during 100-ns of production (Figure 4-1, 4-2) with an $RMSD_{protein}$ no higher than ~ 2 Å (Table 4-3). These refinements produced suitable structures of the complexes between A_1R and **A15, L2-L6, L8, L9** for using them with rigorous alchemical perturbation calculations. In the TI/MD simulations the last frames of the complexes from the alchemical perturbation calculations match the frames of the complexes from the 100ns-MD simulations.

Table 4-5: Relative binding free energies computed by TI/MD calculations ($\Delta\Delta G_{b,TI/MD}$ in kcal mol^{-1}) using alchemical transformations and a thermodynamic cycle, experimental values ($\Delta\Delta G_{b,exp}$ in kcal mol^{-1}) and deviation of calculated from experimental values ($|\Delta\Delta G_{b,TI/MD} - \Delta\Delta G_{b,exp}|$ in kcal mol^{-1}) for pairs of compounds complexed to A_1R.

alchemical perturbation	$\Delta\Delta G_{b,TI/MD}$	$\Delta\Delta G_{b,exp}$ [a]	$\lvert\Delta\Delta G_{b,TI/MD} - \Delta\Delta G_{b,exp}\rvert$
A15 → L3; 3H → 3iPr	-0.66 ± 0.07	-1.80 ± 0.09	1.14
A15 → A17; 3H → 3Ph	-1.06 ± 0.09	-2.44 ± 0.09	1.38
L3 → A17; 3iPr → 3Ph	-0.87 ± 0.09	-0.63 ± 0.09	0.24
L4 → A17; 7Ph → 7Ph(OMe)$_3$	-3.34 ± 0.10	-2.39 ± 0.15	0.95
L6 → A17; 5H → 5CN	-3.05 ± 0.05	-2.24 ± 0.20	0.81
L6 → L5; 5H → 5Cl	-0.67 ± 0.04	0.16 ± 0.22	0.83
L5 → A17; 5Cl → 5CN	-1.09 ± 0.07	-2.40 ± 0.12	1.31
L2 → L5; 5Cl → 5CN	-0.37 ± 0.07	-0.18 ± 0.11	0.19
L9 → L8; py → Ph [b]	0.71 ± 0.08	0.72 ± 0.17	0.01
			mue = 0.87 kcal mol^{-1}

[a] Experimental relative binding free energies ($\Delta\Delta G_{b,exp}$) were estimated using the experimental binding affinities pK_d (Table 4-2); [b] in the substituent at 5-position of the pyrazole ring.

Compared to **A15**, the presence of an alkyl substituent at 3-position anchors the ligand deeper into the receptor and forms hydrophobic interactions mostly with F182$^{5.43}$, W243$^{6.48}$ but also with L91$^{3.32}$. Thus, the presence of the isopropyl group in **L3** or phenyl group in **A17** at 3-position led to stronger binding as shown in the relative binding free energy values which are for **A15** → **L3** $\Delta\Delta G_{b,exp}$ = -1.80 ± 0.09 kcal mol^{-1} , $\Delta\Delta G_{b,TI/MD}$ = -0.66 kcal mol^{-1} and for **A15** → **A17** $\Delta\Delta G_{b,exp}$ = -2.44 ± 0.09 kcal mol^{-1}, $\Delta\Delta G_{b,TI/MD}$ = -1.06 kcal mol^{-1}. The binding affinity was increased with the size of this substituent as measured in the alchemical perturbation **L3** → **A17** with $\Delta\Delta G_{b,exp}$ = -0.63 kcal mol^{-1}, $\Delta\Delta G_{b,TI/MD}$ = -2.54 kcal mol^{-1} (Table 4-5) and in **L2** → **L5** with $\Delta\Delta G_{b,exp}$ = -0.18 ± 0.11kcal mol^{-1}, $\Delta\Delta G_{b,TI/MD}$ = -0.37 ± 0.07mol^{-1} conforming that phenyl group is favored over the isopropyl group.

The critical effect in binding free energy from replacing the hydrogen at 5-position with a chlorine or with a cyano group was examined with the alchemical perturbations **L6** → **L5** or **L6** → **A17** or **L5** → **A17** with $\Delta\Delta G_{b,exp}$ = 0.16 ± 0.22 kcal mol^{-1}, $\Delta\Delta G_{b,TI/MD}$ = -0.67 ± 0.04 kcal mol^{-1} or $\Delta\Delta G_{b,exp}$ = -2.24 ± 0.20 kcal mol^{-1}, $\Delta\Delta G_{b,TI/MD}$ = -3.05 ± 0.05 kcal mol^{-1} or $\Delta\Delta G_{b,exp}$ = -2.40 ± 0.12 kcal mol^{-1}, $\Delta\Delta G_{b,TI/MD}$ = -1.09 ± 0.09 kcal mol^{-1} which suggest that the change of hydrogen at 5-position with chlorine or cyano group increases binding free energy. Further changing chlorine at 5-position with a cyano group favors stronger binding. Compared to **L5, L6** in **A17** the combination of the cyano group and nitrogen at 7-position increased polarity of this ligand's part which can attract waters that enter the binding area between ligand and TM2, TM3. Thus, compared to **L5, L6**, in **A17** and **L4**, the 5-cyano group can form hydrogen bonding interactions with waters positioned between the ligand and TM2, TM3 (Figure 4-1). In **L6**, which lacked the 5-cyano group, the hydrogen bonding interactions with N254$^{6.55}$ and E172$^{5.30}$ as well as the hydrogen bonding interactions with waters that enter the area between the ligand and TM2, TM3, and the hydrophobic interactions with M180$^{5.38}$ and W247$^{6.48}$ were all reduced (Figure 4-2). By adding three methoxy groups in the phenyl group of the 7-anilino substituent, ligand's lipophilicity was enhanced and the desolvation penalty of **A17** compared to **L4** to reach the orthosteric binding area was reduced thus increasing the binding affinity. Due to the deletion of the methoxy group, the hydrophobic interaction with M180$^{5.38}$ was also diminished. This effect in binding free energy was predicted by the TI/MD calculations in alchemical transformation **L4** → **A17** with $\Delta\Delta G_{b,exp}$ = -3.34 ± 0.10 kcal mol^{-1}, $\Delta\Delta G_{b,TI/MD}$ = -2.39 ± 0.15 kcal mol^{-1}.

The orthosteric binding pocket could accommodate sizeable substituents at 5-position, e.g. the phenylmethyl group in **L8** or the 3-(pyridinyl)methyl group in **L9** connected with the 5-aminomethyl group of compound **L7** leading to K_d = 427 nM for **L8** or K_d = 29 nM for **L9** against A_1R (Table 4-2). The TI/MD predictions suggested that pyridinyl instead of phenyl as described

by the alchemical transformation **L8** → **L9** was favoured with $\Delta\Delta G_{b,exp}$ ($\Delta\Delta G_{b,TI/MD}$) binding free energy values -0.72 (-0.71) kcal mol^{-1} for A_1R. In **L9**, the increased length of the 5-substituent resulted in contacts with residues A66$^{2.61}$ and V62$^{2.57}$ of TM2, while the pyrazole ring was positioned close to TM5−TM7, thus increasing the π−π interactions with F171$^{5.29}$ and L250$^{6.51}$ and forming new interactions H278$^{7.43}$ (Figure 4-2). The increased hydrophobic interactions between the pyridinylmethyl group and V62$^{2.57}$, A66$^{2.61}$, V87$^{3.32}$ and I274$^{7.39}$ but particularly the hydrogen bonding interaction of pyridinyl nitrogen with H278$^{7.43}$ led to the ~ 15-fold increased affinity of **L9** compared to **L8**.We obtained (a) calculated relative binding free energy values that were quite close to the experimental values with mean unsigned error (mue) = 0.87 kcal mol^{-1} (Table 4-4); (b) a very good correlation coefficient r = 0.73 (*p* = 0.026) (Figure 4-5) between the calculated and the experimental relative binding free energies suggesting that the binding model used is reliable and the TI/MD calculations describe accurately the binding interactions against A_1R and can be used for structure-based drug design; [156,163,331,332] (c) the predictive index (PI) of Pearlman, [333] a measure for the correctness of the relative ranking of ligands according to binding free energy, was also high, (PI = 0.73). Overall, the TI/MD simulations can accurately calculate the changes in binding affinity between different substituents that we described only qualitatively in MD simulations section using the height of protein-ligand interactions frequency bars.

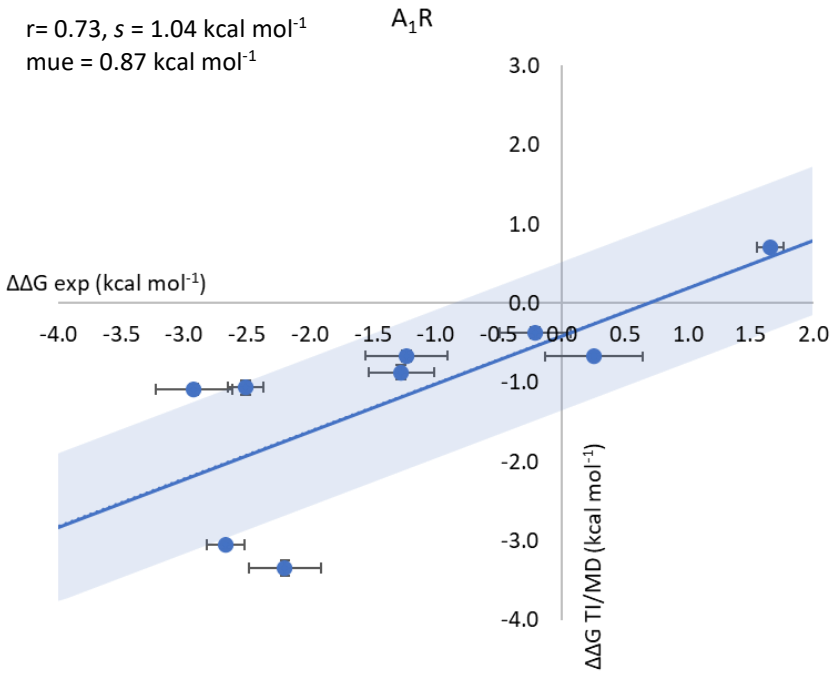

***Figure 4-5**: Computed ΔΔGb,TI/MD values plotted against ΔΔGb,exp values estimated by the experimental binding affinities pKd (Table 4-2) for A_1R. r: correlation coefficient, s: slope, mue: mean unsigned error.*

MM/GBSA calculations with an Implicit Membrane Model.

A post processing analysis of the MD simulations of the tested compounds **A15, L2-L10, A17** in complex with A_1R was applied with the MM/GBSA method variant using a hydrophobic slab as implicit membrane model and including waters in the orthosteric binding area, in a radius of 4 Å from the center of mass of the ligand [176–178] and the OPLS2005 [262,263] force field for the calculation of ligand-protein interactions.

Applying this approach showed that, compared to the highest affinity compound **A17** (ΔG_{eff} = -120.32 ± 7.25 kcal mol^{-1}), **L6** lacked the 5-electronegative substituent that had more positive binding free energy values (ΔG_{eff} = -105.14 ± 6.99 kcal mol^{-1}) (Table 4-3). Moreover, **L4** which lacked the trimethoxy substitution from the 7-anilino substituent also had a more positive binding free energy value, ΔG_{eff} = -91.10 ± 6.62 kcal mol^{-1}. Further, **L3** which contained a 3-isopropyl instead of 3-phenyl group had a ΔG_{eff} = -118.06 ± 7.18 kcal mol^{-1}, and **A15** (devoid of any substitution at 3-position) had a ΔG_{eff} = -99.37 ± 6.88 kcal mol^{-1}. However, the MM/GBSA method performed poorly at predicting other changes, for example in **L7** the presence of the 3-aminomethyl group or the 3-chloro group in **L5** led to ΔG_{eff} = -126.67 kcal mol^{-1} or ΔG_{eff} = -125.22 ± 7.60 kcal mol^{-1}, respectively, suggesting stronger binding affinity compared to **A17**. In **L8** and **L9**, the benzyl and N-(3-pyridinylmethyl)aminomethyl at 3-position led to ΔG_{eff} = -143.08 ± 7.68 kcal mol^{-1} and ΔG_{eff} = -140.46 ± 7.41 kcal mol^{-1}, respectively, showing erroneously stronger binding affinity compared to **L7** but also compare to **A17**. Similarly, **L10** had a ΔG_{eff} = -162.67 ± 8.79 kcal mol^{-1}, which suggested that **L10** was a stronger binder compared to **A17**.

Overall, compared to the most potent compound **A17** the MM/GBSA calculations showed correctly that the deletion of a group or substituent in **A17** results in much more positive ΔG_{eff} values, i.e. weaker binding without providing accurate relative free energy values (Figure 4-6). The accuracy in calculation of relative binding free energies for alchemical transformations is possible using perturbation methods based on statistical mechanics as we showed with TI/MD method and suggested by studies related to comparative performance of FEP/MD and the MM/PBSA method for water soluble proteins,[314,334] and membrane proteins including A_1R and $A_{2A}R$. [335]

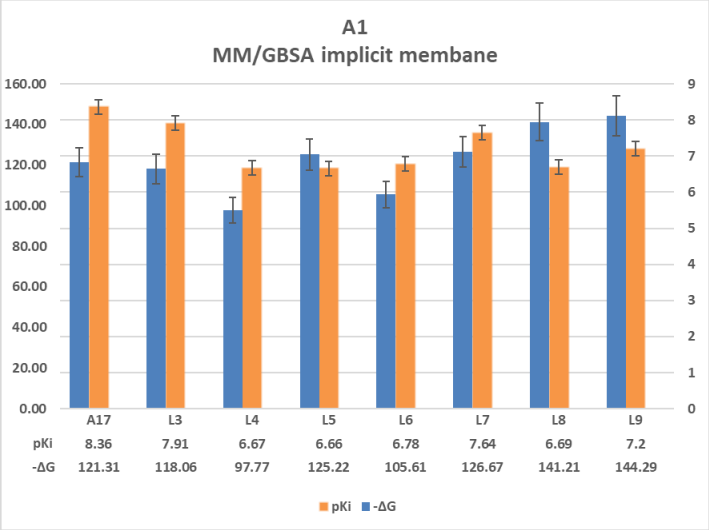

***Figure 4-6**: ΔGeff values from MM/GBSA calculations and experimental binding affinities pKi for A_1R. MM/GBSA calculations using a model that is taking into account the membrane as hydrophobic slab (blue bars) and pKi values measured using BRET (brown bars).*

4.3 Discussion

We, [87] [257] and other groups, [118,152–156] are motivated to identify new hits from virtual screening of ARs and modify them to lead compounds. However, the possibility of re-purposing compounds from *in-house* libraries [153] is an exciting opportunity and cost-effective process. We identified here the pyrazolo[3,4-c]pyridines **L2-L10, A15, A17** with a phenyl or isopropyl group at 3-position, an anilino group at 7-position and a cyano-, or chloro- or aminomethyl group or N-(arylmethyl)-2-aminomethyl group at 5-position with nanomolar to mid-nanomolar binding affinities at A_1R and A_3R. . Another second series, including 3-(N-acyl)amino 5-anilino pyrazolo-[3,4-*c*]pyridine **A26** and its analogues **L12, L15, L21** displayed low micromolar to 100 nM binding affinity against A_1R and A_3R.

The orthosteric binding areas of ARs are broad so, it is very interesting to observe that small changes in ligand's structure resulted in significant changes in affinity/activity and receptor selectivity. For example, the replacement in **A17** of the 5-cyano by the chloro group in **L5** reduced the affinity by ca. 30-fold and the deletion of the cyano group reduced the affinity by ca. 100-fold against A_1R. These changes reduced the affinity at to A_3R by 7-fold and by 20-fold respectively.

Some compounds showed high affinities and a diverse range of kinetic profiles. We found A_3R and A_1R antagonists with medium RT and much longer RTs. For compounds acting at the A_3R **A17, L4, L5** had the longer residence time with RT values between ca. 32-50 mins and **L6, L7, L10, A26** the shortest residence with RT values between ca. 5.6-11 mins. For compounds acting at the A_1R **A15, A17, L9, L10** had the longer residence time with RT values between ca. 30-44 mins and **L3, L5, L8, A26, L15** the shortest residence with RT values between ca. 7.5-19 mins. Compounds, which displayed high affinity at the A_3R, had RT between ca. 5-50 mins, and at A_1R between ca. 18-40 min (**L4, L6-L8**). The kinetic data showed that compared to not potent congeners the active compounds which displayed high affinity have similar association rate, for example at A_3R K_{on} = 21.3 x10^5 M^{-1} (**A17**) vs K_{on} = 4.8 x10^5 M^{-1} (**L7**) but much lower dissociation rate K_{off} = 0.021 min^{-1} (**A17**) vs 0.105 min^{-1} (**L7**) resulting in lower K_d's. Knowledge of target binding kinetics has been discussed to be very important for developing and selecting new AR antagonists in the early phase of drug discovery. [336,337]

The binding orientation of **A17** inside A_1R was selected between docking pose 1 and docking pose 2 that both produced stable **A17**$-A_1R$ complexes in MD simulations, based on the agreement with alanine scanning mutagenesis experiments and affinities measured with the NanoBRET method. We observed that mutations H251$^{6.52}$A, S267$^{7.32}$A increased the affinity of **A17** by ~ 1.5-, 1.7-fold, respectively while T91$^{3.36}$A and L250$^{6.51}$A increased the affinity of **A17** by 3.2- and 3.8-fold. Residues Y271$^{7.36}$ or E172$^{5.30}$ were not important for binding of **A17** to A_1R since their mutation to alanine had little effect upon **A17** affinity. The result for L250$^{6.51}$A was a bit unexpected because L250$^{6.51}$A is a highly conserved residue in all four AR subtypes where it is key to ligand recognition. Indeed, mutation of L250$^{6.51}$ to Ala had been reported to reduce or block affinity as our lab also showed previously. [87,90]

This contrasts with our studies on 7-Amino-pyrazolo[3,4-d]pyridazine, for which we showed that T91$^{3.36}$A and S271$^{7.42}$A did not significantly change the binding affinity (Chapter 3), suggesting that pyrazolo[3,4-*c*]pyridines are positioned below compound **10b** closer to the bottom part of the binding site. Y271$^{7.46}$A mutation did not affect binding affinity. This effect is in contrast to that observed previously for 7-Amino-pyrazolo[3,4-d]pyridazine **10b** for which we showed that Y271$^{7.46}$A mutation caused a ~10-fold reduction in binding affinity (See Chapter 3).

We selected docking pose 1 with the anilino group oriented toward EL2 because the MD simulations of **A17** with the mutant A_1R-Y271$^{7.36}$A maintained binding interactions with **A17**, which agreed with our mutagenesis experiments. The MD simulations of **A17** in complex with the A_1R mutants S267$^{7.32}$A or T91$^{3.36}$A or H251$^{6.52}$A or L250$^{6.51}$A starting from docking pose 1

produced complex with binding interactions that also agreed with our mutagenesis data. A novel observation from mutagenesis data for drug design purposes that when the L250$^{6.51}$ was changed to Ala the binding affinity of **A17** was significantly increased at A_1R.

Our MD simulations starting from docking pose 1 for the complexes with A_1R showed that **A17**, the most potent antagonist against A_1R, was stabilized inside the binding area by an array of co-operative interactions. Compound **A17** binds to A_1R and interacts with TM5 E170$^{5.28}$, F171$^{5.29}$, E172$^{5.30}$, M180$^{5.38}$, N184$^{5.42}$, TM6 W247$^{6.48}$, L250$^{6.51}$, H251$^{6.52}$, N254$^{6.55}$, TM7 T270$^{7.35}$, Y271$^{7.36}$ in A_1R. [338] ; its 5-cyano group in **A17** seems to be stabilized through hydrogen bonding interactions with waters that enter the binding area between the ligand and TM2 and TM3. In the case of **L9**, having an increased girth compared to **A17** due to the replacement of the cyano with N-(3-pyridinylmethyl)aminomethyl group the interactions with A_1R also include TM2, TM3 residues, eg. V62$^{2.57}$, A66$^{2.61}$, V87$^{3.32}$ but also additional residues at TM7, eg. I274$^{7.39}$, H278$^{7.43}$.

To explore a method that enabled the quantitative description of the SARs, we performed MM/GBSA calculations, using an implicit membrane model and taking into account the waters inside the binding area, and TI/MD simulations using the alchemical perturbations of these ligands. The TI/MD method produced a very good correlation coefficient (r = 0.73) between the calculated and experimental relative binding free energies for A_1R showing that the method can be used for heat-to-lead optimization of **A17**.

Chapter 5.

Computational Model for the Unresolved, Inactive Adenosine A_3 Receptor for Drug Design Purposes

5. Computational Model for the Unresolved, Inactive A_3R for Drug Design Purposes

5.1 Purpose of the study

In Chapter 4, we discovered the 3,5-disubstituted-7-(phenylamino)-pyrazolo[3,4-*c*]pyridines as dual A_1R/A_3R antagonists. We characterized them with kinetic binding measurements of rate and binding constants ($K_d=k_{off}/k_{on}$) at A_1R and A_3R and identified nanomolar (nM) 3-phenyl-7-(phenylamino)-pyrazolo[3,4-*c*]pyridines with high RT.

MD simulations of the resolved structures of several purinergic receptors [339,340] have enabled characterization of biomolecular binding pathways and kinetics which attract increasing attention in recent years. Computing accurately the residence time ($\tau = 1/K_{off}$) poses challenges with conventional MDs alone due to the extensive sampling required. Thus, several promising methods for computing ligand–receptor binding kinetics have been developed and enhanced sampling methods have greatly reduced the computational cost. [158,164,225,235,247,251,341–345] Studies have been performed to various GPCRs as described in Section 2.1.5.

For unresolved protein structures, homology models are developed based on available experimental structures of closely related protein homologs. [108,109] These homology models have been used to explore binding of both agonists and antagonists and for structure-based drug design purposes against hA_1R, [111,346] $hA_{2A}R$, [347] $hA_{2B}R$ [161,348] and hA_3R. [112,300,87,89,111,201,255,349–351] FEP/MD calculations of relative binding free energies have been successfully applied with homology models of GPCRs class A. [352]

It is important all developed homology models to be available from the published work in a suitable three-dimensional structural format than can be used for model evaluation. Overall, from the reported homology models of inactive hA_3R the publicly available models are based: (a) on experimental structure of inactive $hA_{2A}R$ with an antagonist provided in refs. [256,258,110]; (b) on experimental structure of hA_1R with an antagonist provided in ref. [259]; (c) on multi-state AF2 method. [122]

Here we used different homology models of inactive hA_3R in complex with our previously identified 3,5-disubstituted-7-(phenylamino)-pyrazolo[3,4-*c*]pyridine antagonists (Chapter 4) to explore the binding profile of these ligands and investigate the ability of these homology models to predict the experimental relative binding free energies and relative residence times of the antagonists against inactive A_3R. After filtering degenerate models, we came up with **Models 1-3**.

The TI/MD calculations were applied on the whole GPCR—membrane system with **Models 1-3** and resulted in a good to very good agreement between the calculated and experimental binding free energies (r = 0.74, 0.62 and 0.67, respectively). In contrast, the binding free energy calculations using the approximate MM/GBSA method [144] with an implicit membrane and considering the waters inside the binding area [177,314] failed to rank the ligands according to their experimental binding affinities.

For the kinetic binding calculations, the τRAMD method [234,235,293] was used, which was previously applied successfully for the accurate calculation of relative RT of ligands bound to the orthosteric binding site of GPCRs.

Compared to **Models 1, 2** we observed that in the multi-state AF2-based **Model 3** residues $M172^{5.33}$, $R173^{5.34}$, $M174^{5.35}$ (MRM motif) that lie on EL2 in the upper region of TM5 have significantly different side chain orientation and $R173^{5.34}$ cap the exit route of ligands. When the conformation of MRM motif was adjusted in **Model 3** the performance of the kinetic binding calculations with the **optimized Model 3** was considerably improved. The **optimized Model 3** was able: (a) to rank the ligands according to their experimental RT values with τRAMD calculations and (b) improved ligands' ranking according to their experimental relative binding free using TI/MD calculations, with a Pearson correlation coefficient and mean assigned error that was improved from r = 0.67 and 0.81 kcal mol^{-1} in **Model 3** to 0.84 and 0.56 kcal mol^{-1} in **optimized Model 3**.

5.2 Results

5.2.1 MD simulations of pyrazolo[3,4-c]pyridines in complex with inactive A_3R

In Table 5-1 are shown compounds **L3-L6, L9, A17** that bind to A_3R with dissociation constants (K_d's) that differ by ~ 100-fold, i.e., between K_d ~ 1000 nM in **A15** to K_d ~ 13.5 nM in **A17**, reported in Chapter 4 (Table 4-2).

We performed induced-fit docking calculations [130] to generate binding poses of the most potent 3-phenyl-5-cyano-7-(trimethoxyphenylamino)-pyrazolo[3,4-*c*]pyridine (**A17**) inside the orthosteric binding site of inactive hA_3R using five publicly available homology models. In the docking poses the phenylamino group was oriented towards the upper side of the binding site as calculated also inside hA_1R (Chapter 4). We embedded each of the five generated complexes from docking calculations in POPE bilayers and performed 100 ns-MD simulations with the amber99sb. [270,271] We showed previously that amber99sb performed accurately in describing the interactions of **NECA** inside the orthosteric binding site of $hA_{2A}R$ [89]compared with the X-ray structure of **NECA** - $hA_{2A}R$ complex (PDB ID 2YDV[45]) while the α-helix conformation of TM domains 1-7 remains stable.

Table 5-1: Chemical structure of 3,5-disubstituted-7-(phenylamino)-pyrazolo[3,4-*c*]pyridine antagonists against A_3R, experimental RT (RT_{exp}) and K_d values as reported in Chapter 4 (Table 4-2) .

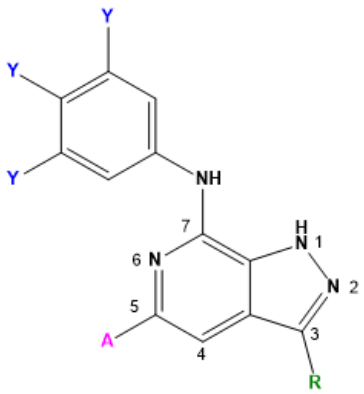

A15: Y=H, A=CN, R=H
A17: Y=OMe, A=CN, R=Ph
L2: Y=OMe, A=Cl, R=iPr
L3: Y=OMe, A=CN, R=iPr
L4: Y=H, A=CN, R=Ph
L5: Y=OMe, A=Cl, R=Ph
L6: Y=OMe, A=H, R=Ph
L8: Y=OMe, A=CH_2NHCH_2Ph, R=Ph
L9: Y=OMe, A=CH_2NHCH_2(3-py), R=Ph

LIGAND	p$K_{d,exp}$	RT_{exp} (min) [a]	LIGAND	p$K_{d,exp}$	RT_{exp} (min) [a]
A15	5.91 ± 0.19 [b,d]	>2 [d]	L5	7.07 ± 0.22 [c]	32.05 ± 6.30
A17	8.00 ± 0.32 [c]	47.23 ± 8.20	L6	7.13 ± 0.55 [c]	5.55 ± 2.60
L2	6.26 ± 0.18 [b,d]	>2 [d]	L8	6.73 ± 0.45 [c]	5.78
L3	6.45 ± 0.23 [b,d]	>2 [d]	L9	7.0 ± 0.33 [c]	17.85 ± 4.30
L4	7.58 ± 0.33 [c]	46.72 ± 4.50			

[a] RT_{exp} of each ligand as determined by the reciprocal of the $k_{off,exp}$.

[b] Equilibrium binding affinity constant (p$K_{i,exp}$) of a ligand against A_3R (Chapter 4).

[c] Kinetic dissociation constant (p$K_{d,exp}$) for each ligand as determined from $k_{on,exo}/k_{off,exp}$ with kinetic constants (Chapter 4).

[d] Values that could not be fitted using the 'kinetics of competitive binding' model.

We tested homology models of inactive hA_3R that were generated based on the crystal structure of an antagonist bound to $hA_{2A}R$ (PDB ID 3EML[34]) provided by Adenosiland web-service [256] and from ref. [258] or based on the crystal structure of an antagonist bound to A_1R (PDB ID 5UEN [55]) provided in ref. [259] (see Figure S1 and Methods Section 2.2.1). The MD simulations of the complexes between **A17** and hA_3R converged for all these homology models during the 100 ns-MD simulations with RMSD including protein (p) Cα carbons of all TM ($RMSD_{p,}(Cα)$) < ~ 2.1 Å.

These three homology models converged to a similar inactive hA_3R structure (Figure 5-1A) in complex with **A17** after the 100ns-MD simulations. Thus, we observed that the MD simulations of the **A17**-hA_3R complexes converged to ensembles that differ by $RMSD_p(Cα)$ 2.1 – 2.4 Å when all TMs were estimated and between 0.8-2 Å for same TMs between the homology models (Figure 5-1B).

A

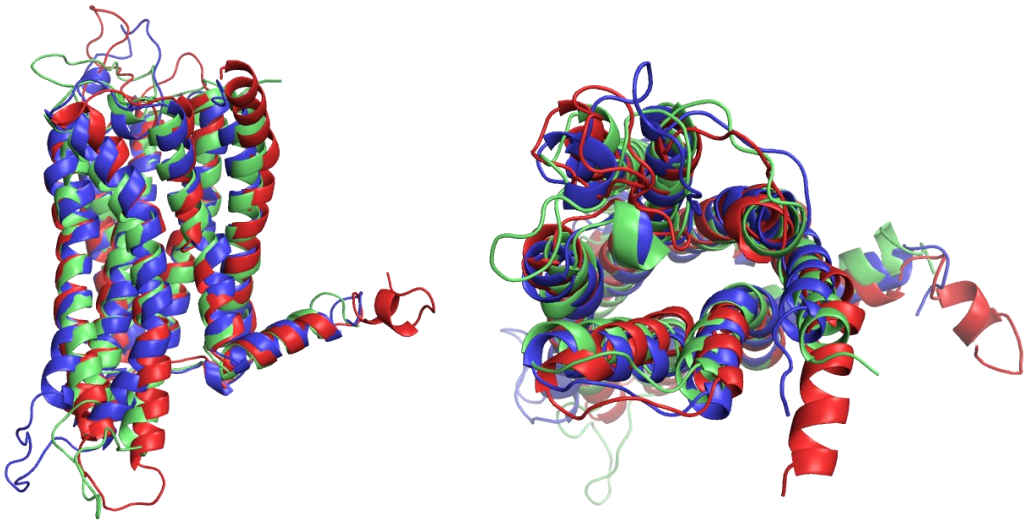

B

RMSD CA (Å)	helices	all	TM1	TM2	TM3	TM4	TM5	TM6	TM7
5uen - 3eml	**2.39**	**3.90**	1.63	1.57	1.17	1.13	1.99	1.64	1.46
5uen - ref 75,76	**2.33**	**3.96**	**2.15**	0.78	1.76	1.32	1.90	1.37	1.55
3eml - ref 75,76	**2.11**	**4.37**	**2.14**	1.74	1.58	1.74	1.92	1.35	1.07

***Figure 5-1**: Structure comparison of three homology protein models of inactive in its complex with antagonist **A17** embedded in phospholipid bilayers derived from 100ns-MD simulations with amber99sb. The homology models used for inactive A_3R were based on the crystal structure of an antagonist bound to $hA_{2A}R$ (PDB ID 3EML [34]) provided by Adenosiland web-service[256] and from ref. [258] or based on the crystal structure of an antagonist bound to A_1R (PDB ID 5UEN [55]) provided in ref. [259]. (A) Structure alignment; side view (left) and top view (right). (B) $RMSD_p(C\alpha)$ measures between pairs of these protein models; when $RMSD_p(C\alpha) > 2$ Å the values are highlighted in bold. Protein homology models are shown as cartoon and coloured dark red, dark blue, and light green, respectively.*

We merged these three homology models of inactive hA_3R structure to **Model 1**. Additionally, we tested the homology model provided in ref. [110] defined as **Model 2** and homology model which became available from GPCRdb [260] web-resource define as **Model 3**.

We observed that the MD simulations of the **A17**-hA_3R complexes converged to ensembles that differ by $RMSD_p(C\alpha)$ = 2.97 Å between **Model 1** and **Model 2**, $RMSD_p(C\alpha)$ = 2.92 Å between **Model 2** and **Model 3**, $RMSD_p(C\alpha)$ = 2.34 Å between **Model 1** and **Model 3** (Figure 5-2A,B). The most noticeable difference was observed in the conformation of TM2 and TM5 Cα carbons (Figure 5-2C). In **Model 3**, TM2 leaned towards the inside of the TM bundle compared to Model 1, with an Ala69 CA distance between the two models of 6.7 Å and an angle of 39 degrees between the upper sides of the TM2. This resulted in a narrower configuration in **Model 3**, whereas in **Model 1**, this region was the widest.

We measured also the $RMSD_p$(Cα) values for the orthosteric binding site (BS) ($RMSD_{p,BS}$ (Cα)) shown in Figure 5-3, and observed between **Model 1** and **Model 2** slight differences, more important in side-chains of residues Q167$^{5.28}$ and F168$^{5.29}$ the last being crucial for antagonist binding. However, in **Model 3**, there is a significant difference with **Models 1** and **2** in the upper region of TM5, where residue R173$^{5.34}$ in the EL2 faces the upper side of the binding site whereas in the other two models faces the outward region of the TMs bundle (Figure 5-3). The same observation applied to residues M172$^{5.33}$ and M174$^{5.35}$, being adjacent to R173$^{5.34}$ (MRM motif), which are facing the opposite direction in **Model 3** compared to the other two models. Figure 5-3 (right) shows the comparison of MRM motif for the three **Models 1-3**. Additionally, compared to **Models 1**, **2** residues Q167$^{5.28}$ and F168$^{5.29}$ in **Model 3** showed more important differences in their conformation.

A

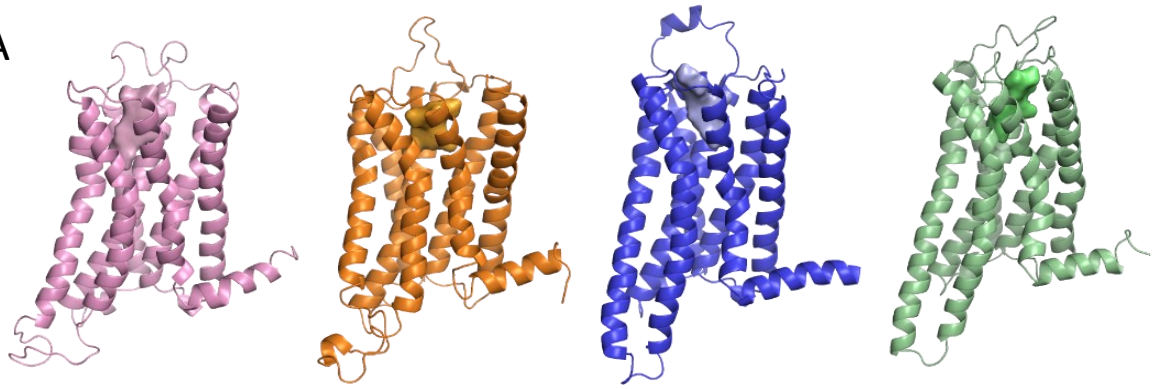

B

$RMSD_p$(Cα) (Å)	TM helices	all	TM1	TM2	TM3	TM4	TM5	TM6	TM7
Model 1 - Model 2	**2.97**	**4.87**	1.49	**2.35**	1.74	1.15	**2.21**	1.33	**2.12**
Model 2 - Model 3	**2.92**	**3.85**	1.86	1.36	1.84	1.28	**2.10**	1.19	1.69
Model 1 - Model 3	**2.34**	**4.43**	1.69	**2.75**	1.80	1.44	**2.42**	0.90	1.89
Model 1 - opt Model 3	**2.55**	**4.25**	1.17	**3.31**	1.65	1.46	**2.69**	1.30	**2.51**
Model 2 - opt Model 3	**3.10**	**3.89**	1.30	1.52	0.86	0.94	**2.68**	1.57	**2.34**
Model 3 - opt Model 3	**2.51**	**4.43**	1.64	1.18	0.78	1.13	**2.09**	1.27	1.64

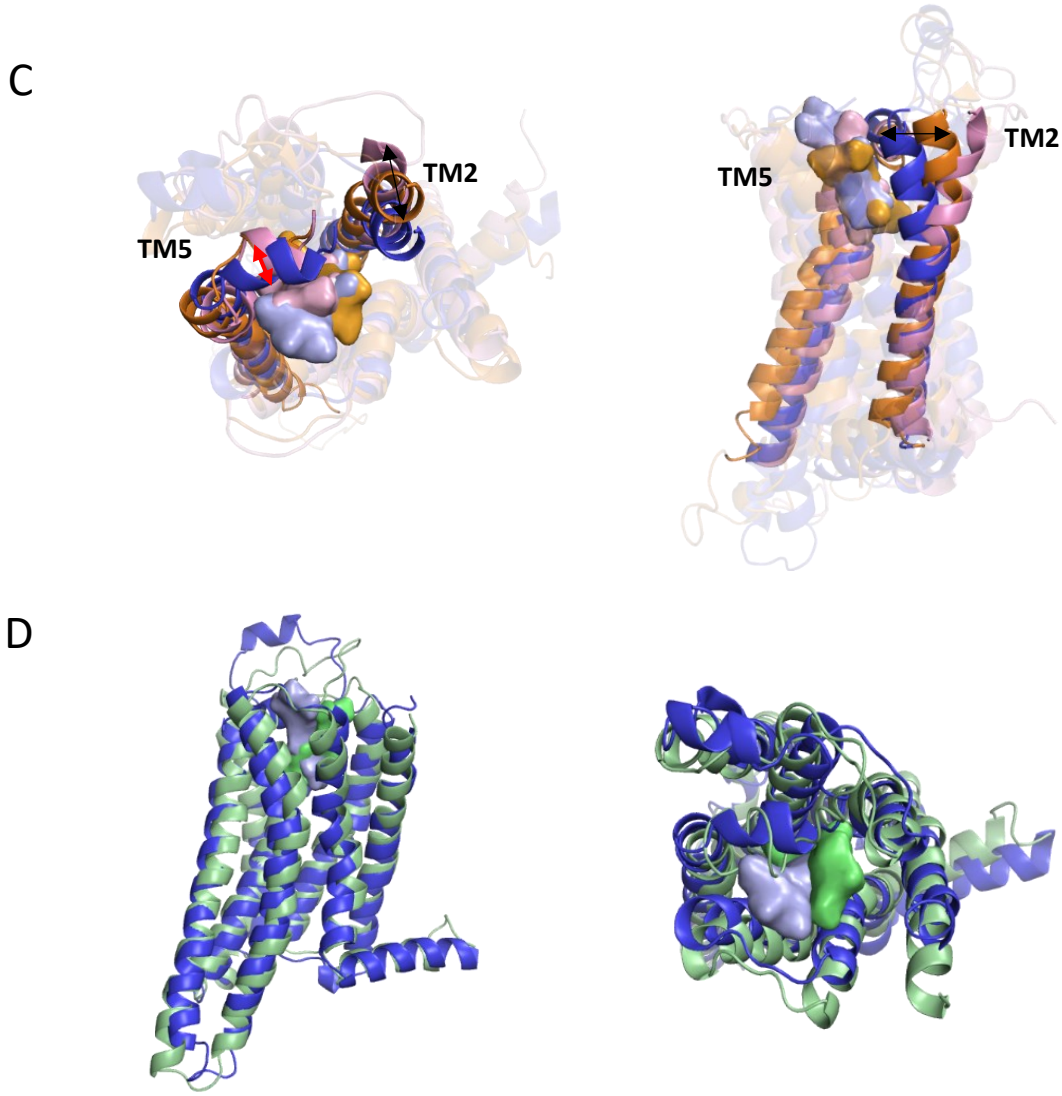

***Figure 5-2**: Measures and ligand positions from 100ns-MD simulations with amber99sb [270,271] of antagonist A17 - inactive hA3R complex embedded in phospholipid bilayers using inactive hA3R described with protein Models 1-3 or optimized Model 3. (A) Cartoon representation of protein models in complex with A17 shown in surface representation. Protein Models 1-3 and optimized Model 3 are coloured pink, orange, blue, and green, respectively. (B) RMSDp(Cα) measures between pairs of protein Models 1-3 and optimized Model 3; when RMSDp(Cα) > 2 Å the values are highlighted in bold. (C) Structure alignment (top view; left, side view; right) that indicated differences in TM2 and TM5. Black and red arrows show differences in TM2 and TM5 conformation, respectively, between protein Models 1-3 (up) and between Model 3 and optimized Model 3 (bottom).*

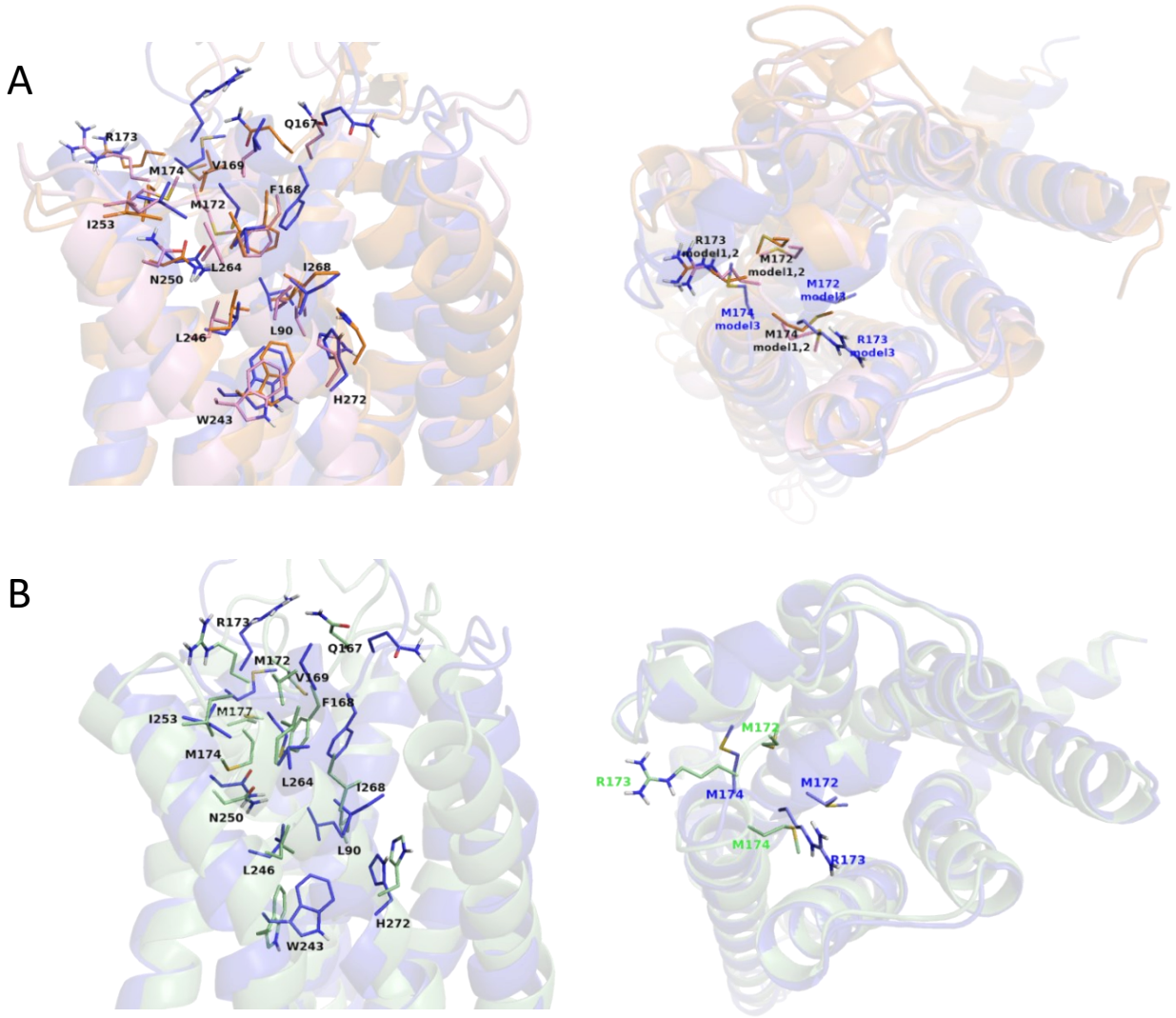

C

RMSD$_{p,BS}$ (Å)	with MRM	w/o MRM
Model 1 - Model 2	1.84	1.90
Model 2 - Model 3	**3.74**	**2.27**
Model 1 - Model 3	**3.37**	1.79
Model 1 - opt Model 3	**2.05**	1.91
Model 2 - opt Model 3	**2.47**	**2.39**
Model 3 - opt Model 3	**3.36**	0.71

Model 1
Model 2
Model 3
opt Model 3

***Figure 5-3**: Measures from 100ns-MD simulations with amber99sb [270,271] of antagonist A17 - inactive hA3R complex embedded in phospholipid bilayers using inactive hA3R described with Models 1-3 or optimized Model 3. Comparison of the orthosteric binding site (BS) area residues shown in sticks and labelled. Left: side view of the aligned BSs between (A) protein Models 1-3 and (B) between Model 3 and optimized Model 3. Right: top view of the aligned BSs focusing on the conformation differences in residues M1725.33, M1745.35, R1735.34 (MRM motif) between (A) Models 1-3 and (B) between Model 3 and optimized Model 3. (C) RMSD of the BS heavy atoms between pair of protein models; when RMSDp,BS (Cα) > 2 Å the values are shown in bold. Protein Models 1-3 and optimized Model 3 are coloured pink, orange, blue, and green, respectively.*

The induced-fit docking calculations [130] of the selected 3,5-disubstituted-7-(phenylamino)-pyrazolo[3,4-*c*]pyridines (**L3-L6, L9, A17**) inside the orthosteric binding site of inactive hA_3R in **Models 1-3** generate 27 complexes that were embedded in POPE bilayers and subjected to 100 ns MD simulations with the amber99sb [270,271]. The MD simulations of the complexes between the ligands and hA_3R converged during the 100 ns-MD simulations (Figure 5-4, 5-5), with RMSD value of the protein Cα carbons ($RMSD_{p,1}$ (Cα)) < ~ 2.6 Å for **Model 1**, $RMSD_{p,2}$(Ca) < ~ 2.5 Å for **Model 2** and $RMSD_{p,3}$(Ca) < ~ 2.8 Å for **Model** 3 (Table 5-2).

With all three **Models 1-3** the MD simulations of the hA_3R-**A17** complex showed that **A17** formed interactions (> 20% frequency) with $F168^{5.29}$, $V169^{5.30}$, $M177^{5.38}$, $W243^{6.48}$, $L246^{6.51}$, $N250^{6.55}$, $L264^{7.35}$, $I268^{7.39}$ (Figure 5-4). In more detail, we observed that the **A17**-hA_3R complex was stabilized by:

(a) Hydrogen bonding interactions between both the pyrazolo 1-NH and anilino NH groups of the ligand and the amide side chain carbonyl of $N250^{6.55}$ which are direct or water-mediated.
(b) Hydrogen bonds between the cyano group of the ligand with waters that are inserted in the region between the ligand and TM1-TM2.
(c) π-π stacking of aromatic rings between the core pyrazolo-[3,4-*c*]pyridine and the side chain phenyl of $F168^{5.29}$.
(d) Hydrophobic interactions between the pyrazole ring of the ligand and $L246^{6.51}$ possibly with $M177^{5.38}$.
(e) Hydrophobic interactions between the phenyl ring of the ligand, which is oriented deeper into the receptor from the pyrazole scaffold, and $L90^{3.32}$ and $W243^{6.48}$.
(f) The trimethoxyphenyl group has hydrophobic contacts with $V169^{5.30}$, $L264^{7.35}$, $I268^{7.39}$.
(g) A difference between Models **Models 1-3** is the orientation of the trimethoxyphenyl group of the ligand, which is directed towards the extracellular part (**Models 1, 2**) or ECL2 (**Model 3**).
(h) A second noticeable difference between the Models is observed in the interactions of **A17** observed with **Model 3**. In **Model 3 A17** forms hydrogen bonds with $R173^{5.34}$ through its methoxy group oxygens and hydrophobic interactions with $M172^{5.33}$, with these two residues oriented towards the binding site in this model, as described above (Figure 5-3, 5-4).

Selected results from MD simulations were plotted also for **L3-L6, L9** (Figure 5-5, RMSD plots are provided in the Appendix Figure S2). In case of **L9** the girth of the ligand is increased due to the 5-CH_2NHCH_2py substitution allowing interaction with TM2 ($L65^{2.57}$, $L68^{2.60}$ and $V72^{2.64}$).

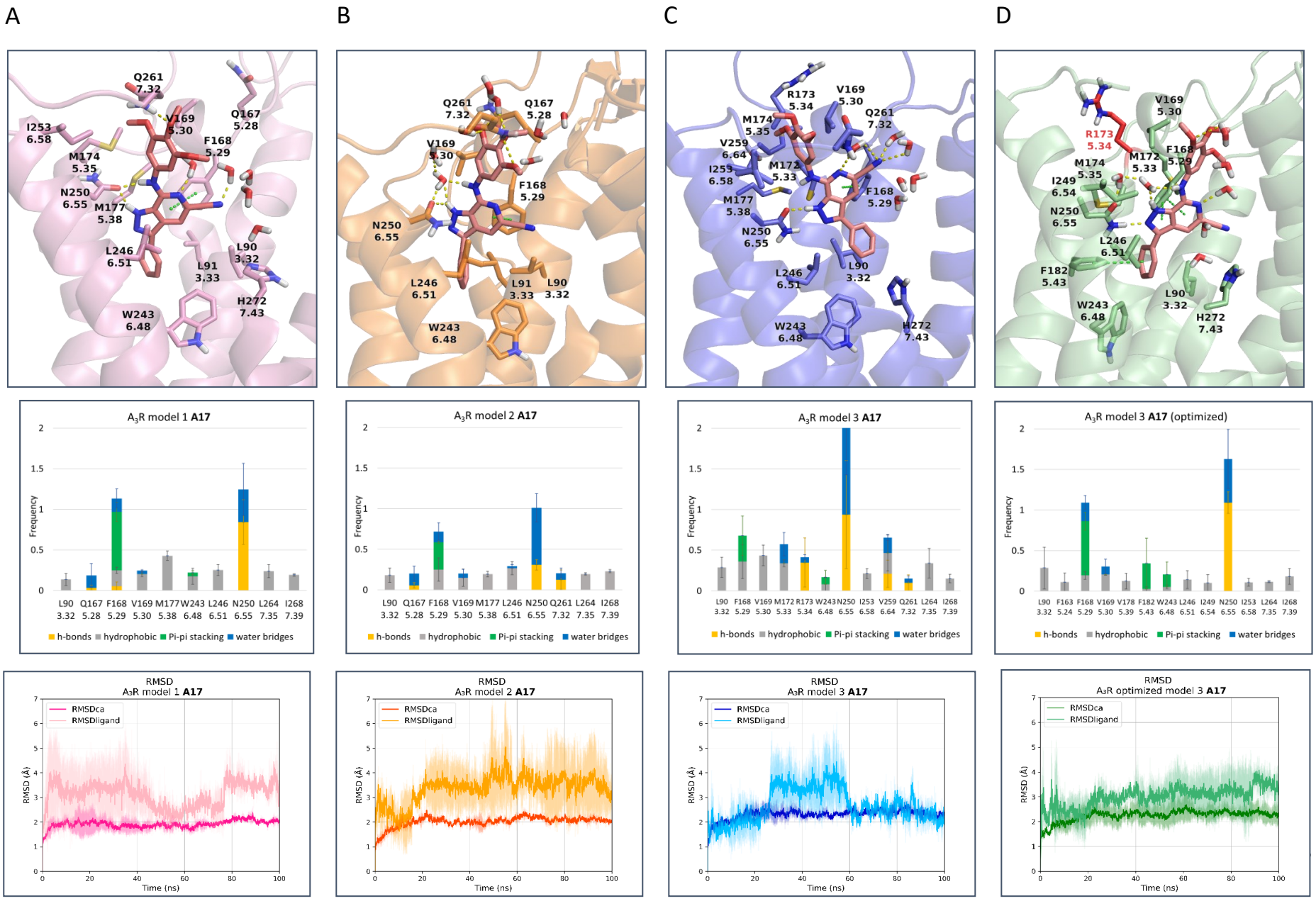
A
B
C
D
Q261 7.32
Q167 5.28
I253 6.58
V169 5.30
F168 5.29
M174 5.35
N250 6.55
M177 5.38
L246 6.51
L91 3.33
L90 3.32
H272 7.43
W243 6.48
R173 5.34
V259 6.64
I255 6.58
M172 5.33
I249 6.54
F182 5.43
A3R model 1 A17
A3R model 2 A17
A3R model 3 A17
A3R model 3 A17 (optimized)
Frequency
h-bonds
hydrophobic
Pi-pi stacking
water bridges
RMSD
A3R model 1 A17
A3R model 2 A17
A3R model 3 A17
A3R optimized model 3 A17
RMSDca
RMSDligand
RMSD (Å)
Time (ns)

***Figure 5-4**: Last frames, ligand interaction frequency histograms and RMSD plots from 100ns-MD simulations with amber99sb [270,271] of **A17**–hA3R complexes embedded in phospholipid bilayers using a homology model. (A) **Model 1**; (B) **Model 2**; (C) **Model 3**; (D) **Optimized Model 3**. Receptor models are shown as cartoon; ligand, and key interacting residues or waters at a distance < 4 Å from the ligand are shown as sticks while hydrogen bonding interactions between **A17** and A3R are shown with yellow dashes or green dashes respectively. Color scheme used in frames and RMSD plots: protein Model 1 is shown in pink, protein Model 2 in orange, protein Model 3 in blue, optimized Model 3 in green, ligand sticks in salmon. Color scheme used in protein-ligand frequency interaction bars: hydrogen bonds are shown in yellow, π-π interactions in green; hydrophobic interactions in grey; water bridges in blue. TM7 residues are hidden for clarity and only Q2617.32 and H2727.43 are shown.*

Table 5-2: Experimental dissociation constants, $RMSD_p$ and $RMSD_l$ for the 100ns-MD simulations with amber99sb for the complexes of inactive A_3R with antagonists **A17**, **L3**, **L4**, **L5**, **L6**, **L9** embedded in phospholipid bilayers using homology **Models 1-3** and **optimized Model 3**.

		MODEL 1		MODEL 2		MODEL 3		Optimized MODEL 3	
Compound	pK_D [a]	$RMSD_p$ [b]	$RMSD_l$ [c]	$RMSD_p$	$RMSD_l$	$RMSD_p$	$RMSD_l$	$RMSD_p$	$RMSD_l$
A17	8.00 ± 0.32	1.97 ± 0.13	3.03 ± 0.57	2.12 ± 0.09	3.64 ± 0.34	2.39 ± 0.11	2.66 ± 0.55	2.35 ± 0.1	3.25 ± 0.25
L3	6.22 ± 0.10	2.04 ± 0.06	3.54 ± 0.38	2.44 ± 0.11	4.38 ± 0.32	2.49 ± 0.10	5.36 ± 0.61	-	-
L4	7.58 ± 0.32	2.58 ± 0.08	2.99 ± 0.28	2.28 ± 0.1	3.42 ± 0.23	2.55 ± 0.12	3.58 ± 0.22	2.58 ± 0.15	3.48 ± 0.26
L5	7.07 ± 0.22	2.32 ± 0.08	2.19 ± 0.24	2.54 ± 0.17	3.26 ± 0.26	2.79 ± 0.16	3.58 ± 0.26	2.46 ± 0.13	3.38 ± 0.34
L6	7.13 ± 0.55	1.87 ± 0.12	3.88 ± 0.31	2.26 ± 0.11	3.25 ± 0.25	2.8 ± 0.19	5.63 ± 0.35	2.37 ± 0.15	3.77 ± 0.19
L9	7.00 ± 0.33	2.14 ± 0.06	3.36 ± 0.3	2.3 ± 0.16	2.83 ± 0.24	1.85 ± 0.11	3.03 ± 0.23	-	-

[a] See Table 5-1.

[b] Mean ± SD (Å); $RMSD_p$(Cα) was calculated from Ca atoms of only TM α-helices, from the last 50 ns of the MD simulations trajectories, using as starting structure snapshot 0 of the production MD simulation.

[c] Mean ± SD (Å); $RMSD_l$ was calculated after superposition of each protein-ligand complex to that of the starting structure (snapshot 0) based on the Cα atoms of the protein, for the last 50ns of the MD simulations trajectories.

A (L3)

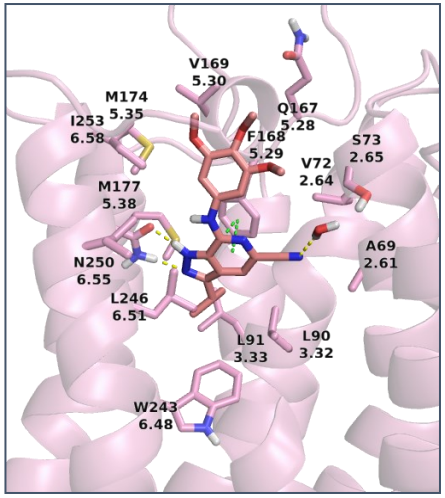
V169 5.30
M174 5.35
I253 6.58
Q167 5.28
F168 5.29
S73 2.65
V72 2.64
M177 5.38
A69 2.61
N250 6.55
L246 6.51
L91 3.33
L90 3.32
W243 6.48

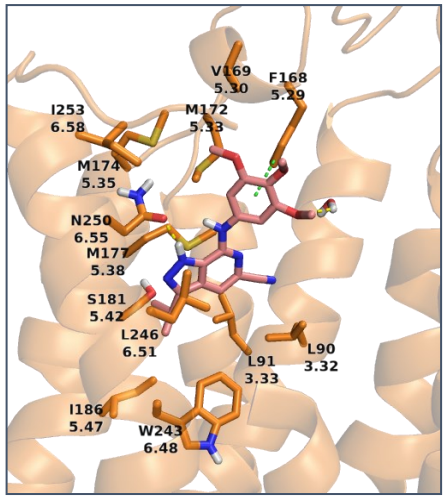
V169 5.30
F168 5.29
I253 6.58
M172 5.33
M174 5.35
N250 6.55
M177 5.38
S181 5.42
L246 6.51
L91 3.33
L90 3.32
I186 5.47
W243 6.48

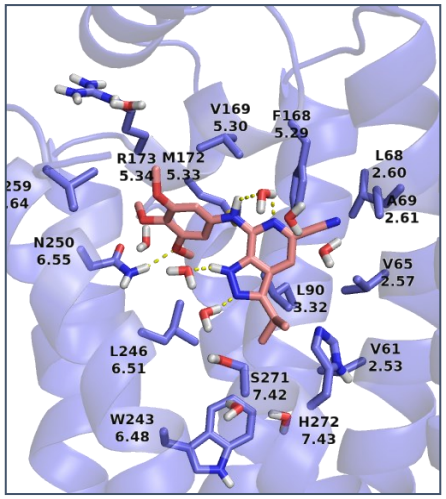
V169 5.30
F168 5.29
R173 5.34
M172 5.33
L68 2.60
A69 2.61
N250 6.55
V65 2.57
L90 3.32
L246 6.51
V61 2.53
S271 7.42
W243 6.48
H272 7.43

B (L4)

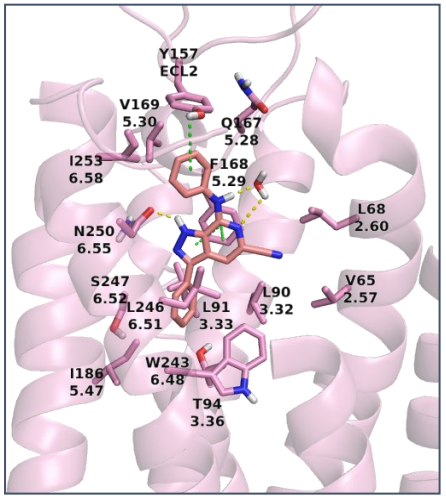
Y157 ECL2
V169 5.30
Q167 5.28
I253 6.58
F168 5.29
L68 2.60
N250 6.55
S247 6.52
L246 6.51
L91 3.33
L90 3.32
V65 2.57
I186 5.47
W243 6.48
T94 3.36

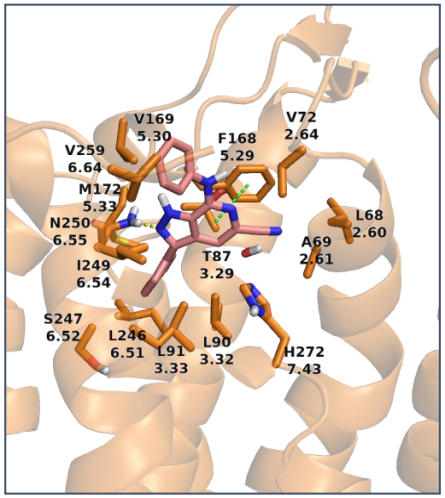
V169 5.30
V72 2.64
V259 6.64
F168 5.29
M172 5.33
N250 6.55
L68 2.60
A69 2.61
T87 3.29
I249 6.54
S247 6.52
L246 6.51
L91 3.33
L90 3.32
H272 7.43

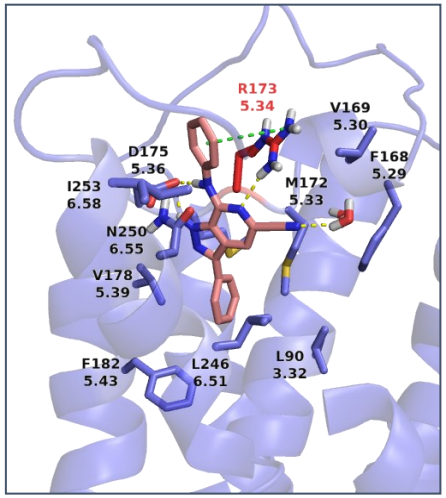
R173 5.34
V169 5.30
D175 5.36
F168 5.29
I253 6.58
M172 5.33
N250 6.55
V178 5.39
F182 5.43
L246 6.51
L90 3.32

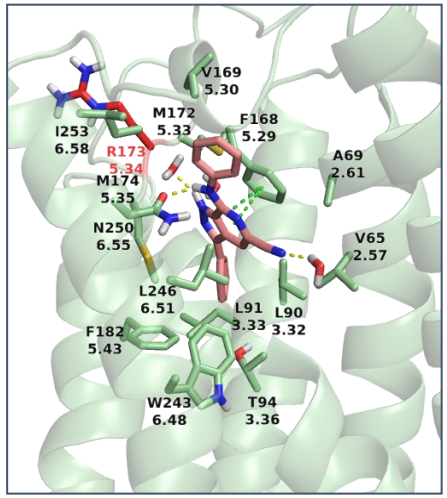
V169 5.30
M172 5.33
F168 5.29
I253 6.58
R173 5.34
A69 2.61
M174 5.35
N250 6.55
V65 2.57
L246 6.51
L91 3.33
L90 3.32
F182 5.43
W243 6.48
T94 3.36

C (L5)

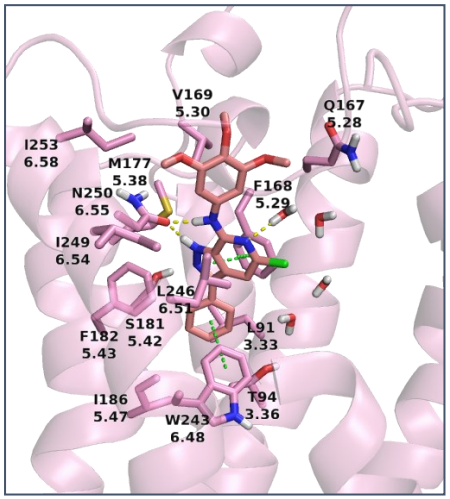
V169 5.30
Q167 5.28
I253 6.58
M177 5.38
N250 6.55
F168 5.29
I249 6.54
L246 6.51
S181 5.42
F182 5.43
L91 3.33
I186 5.47
T94 3.36
W243 6.48

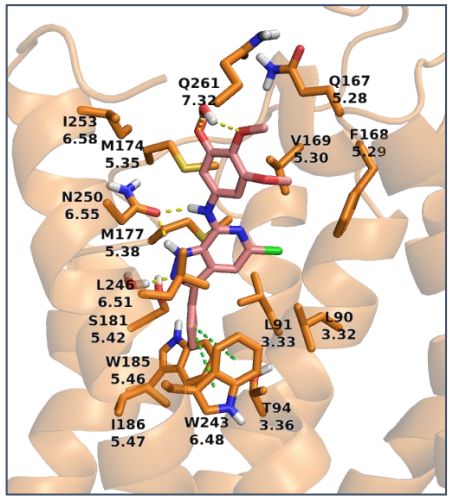
Q261 7.32
Q167 5.28
I253 6.58
M174 5.35
V169 5.30
F168 5.29
N250 6.55
M177 5.38
L246 6.51
S181 5.42
L91 3.33
L90 3.32
W185 5.46
T94 3.36
I186 5.47
W243 6.48

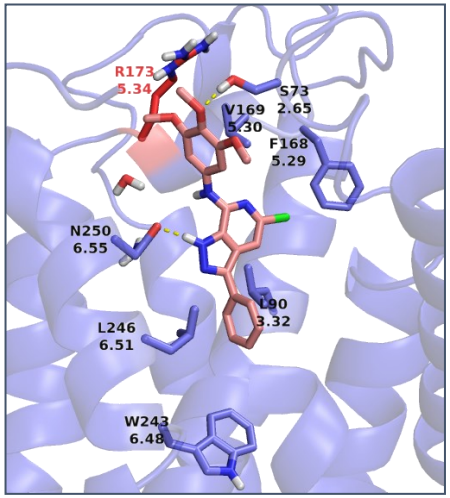
R173 5.34
S73 2.65
V169 5.30
F168 5.29
N250 6.55
L90 3.32
L246 6.51
W243 6.48

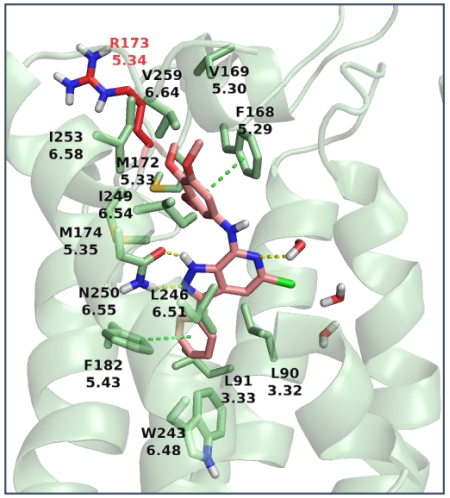
R173 5.34
V259 6.64
V169 5.30
F168 5.29
I253 6.58
M172 5.33
I249 6.54
M174 5.35
N250 6.55
L246 6.51
F182 5.43
L91 3.33
L90 3.32
W243 6.48

D (L6)

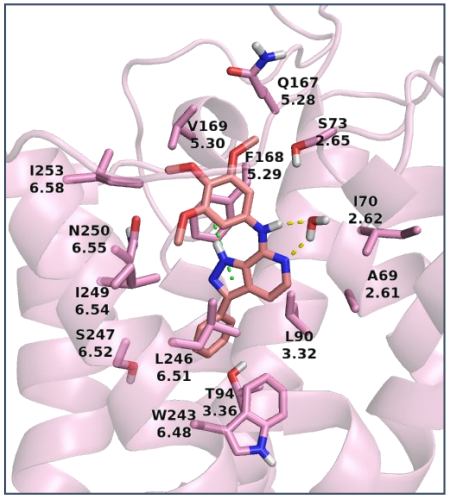
Q167 5.28
V169 5.30
S73 2.65
F168 5.29
I253 6.58
I70 2.62
N250 6.55
A69 2.61
I249 6.54
S247 6.52
L90 3.32
L246 6.51
T94 3.36
W243 6.48

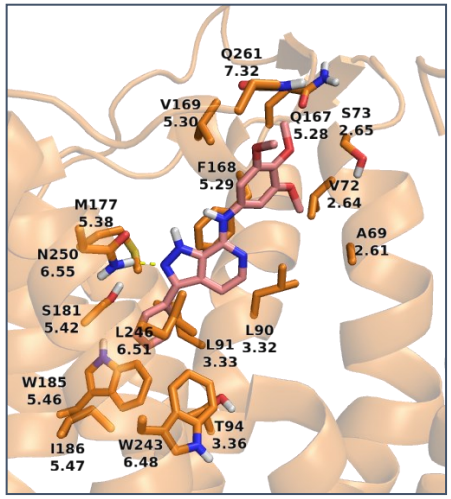
Q261 7.32
V169 5.30
Q167 5.28
S73 2.65
F168 5.29
V72 2.64
M177 5.38
A69 2.61
N250 6.55
S181 5.42
L246 6.51
L91 3.33
L90 3.32
W185 5.46
T94 3.36
I186 5.47
W243 6.48

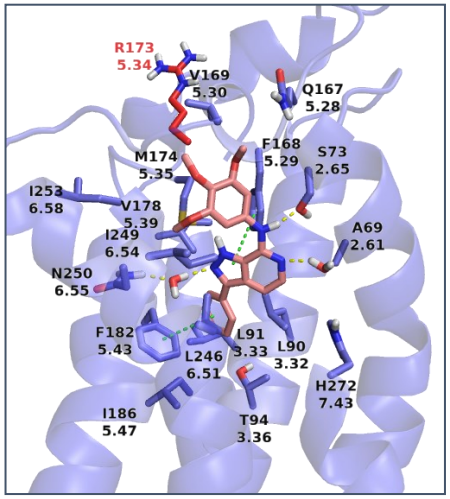
R173 5.34
V169 5.30
Q167 5.28
F168 5.29
S73 2.65
M174 5.35
I253 6.58
V178 5.39
I249 6.54
A69 2.61
N250 6.55
F182 5.43
L91 3.33
L90 3.32
L246 6.51
H272 7.43
I186 5.47
T94 3.36

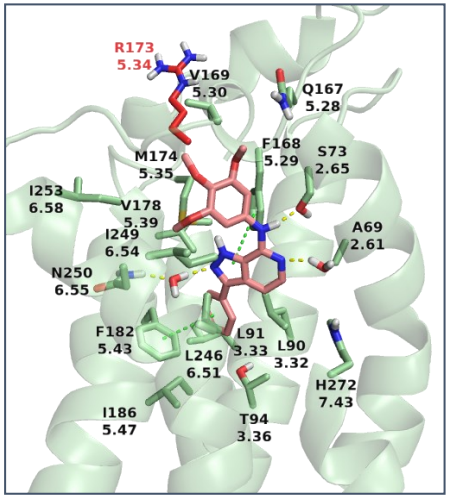
R173 5.34
V169 5.30
Q167 5.28
F168 5.29
S73 2.65
M174 5.35
I253 6.58
V178 5.39
I249 6.54
A69 2.61
N250 6.55
F182 5.43
L91 3.33
L90 3.32
L246 6.51
H272 7.43
I186 5.47
T94 3.36

E (L9)

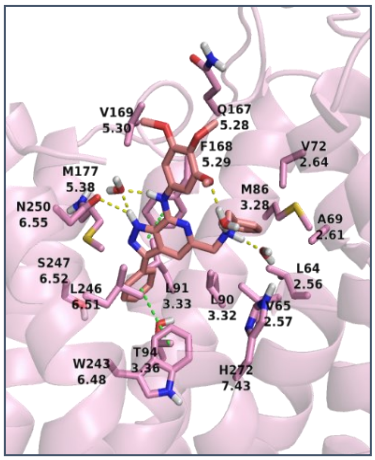
V169 5.30
Q167 5.28
F168 5.29
V72 2.64
M177 5.38
M86 3.28
N250 6.55
A69 2.61
S247 6.52
L64 2.56
L246 6.51
L91 3.33
L90 3.32
V65 2.57
T94 3.36
W243 6.48
H272 7.43

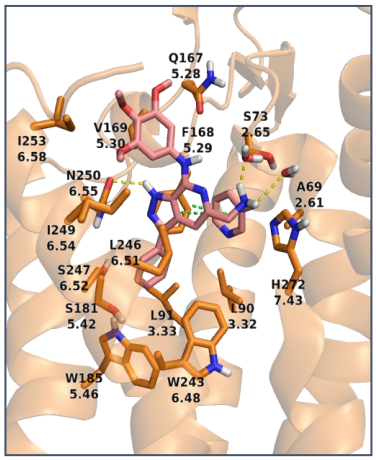
Q167 5.28
I253 6.58
V169 5.30
F168 5.29
S73 2.65
N250 6.55
A69 2.61
I249 6.54
L246 6.51
S247 6.52
H272 7.43
S181 5.42
L91 3.33
L90 3.32
W185 5.46
W243 6.48

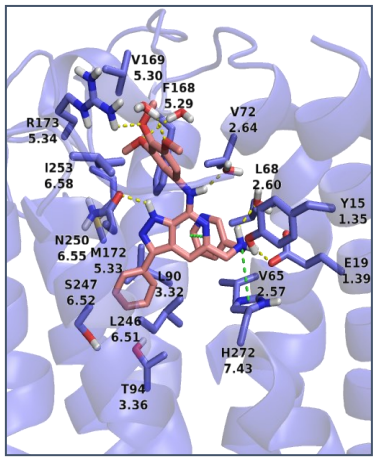
V169 5.30
F168 5.29
R173 5.34
V72 2.64
I253 6.58
L68 2.60
Y15 1.35
N250 6.55
M172 5.33
E19 1.39
S247 6.52
L90 3.32
V65 2.57
L246 6.51
H272 7.43
T94 3.36

F

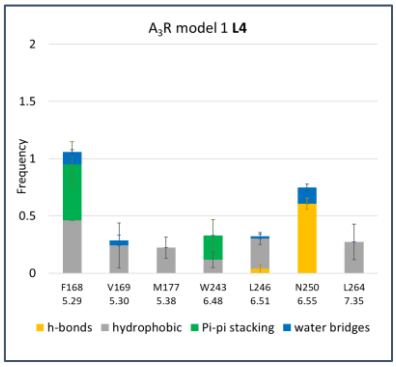
A3R model 1 L4
Frequency
F168 5.29
V169 5.30
M177 5.38
W243 6.48
L246 6.51
N250 6.55
L264 7.35
h-bonds
hydrophobic
Pi-pi stacking
water bridges

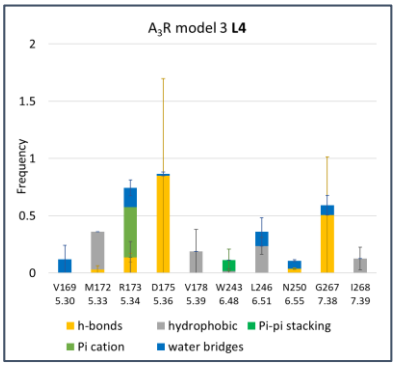
A3R model 3 L4
Frequency
V169 5.30
M172 5.33
R173 5.34
D175 5.36
V178 5.39
W243 6.48
L246 6.51
N250 6.55
G267 7.38
I268 7.39
h-bonds
hydrophobic
Pi-pi stacking
Pi cation
water bridges

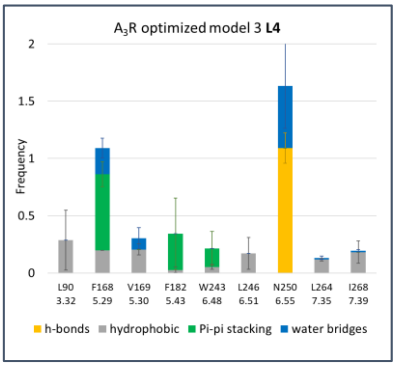
A3R optimized model 3 L4
Frequency
L90 3.32
F168 5.29
V169 5.30
F182 5.43
W243 6.48
L246 6.51
N250 6.55
L264 7.35
I268 7.39
h-bonds
hydrophobic
Pi-pi stacking
water bridges

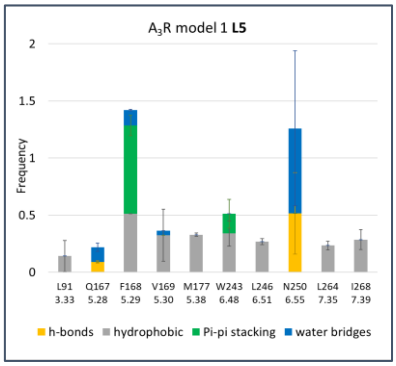
A3R model 1 L5
Frequency
L91 3.33
Q167 5.28
F168 5.29
V169 5.30
M177 5.38
W243 6.48
L246 6.51
N250 6.55
L264 7.35
I268 7.39
h-bonds
hydrophobic
Pi-pi stacking
water bridges

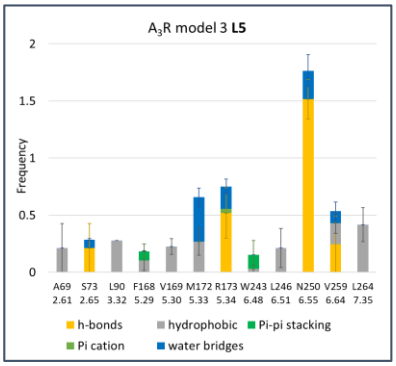
A3R model 3 L5
Frequency
A69 2.61
S73 2.65
L90 3.32
F168 5.29
V169 5.30
M172 5.33
R173 5.34
W243 6.48
L246 6.51
N250 6.55
V259 6.64
L264 7.35
h-bonds
hydrophobic
Pi-pi stacking
Pi cation
water bridges

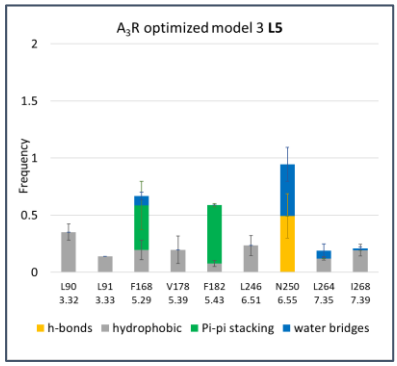
A3R optimized model 3 L5
Frequency
L90 3.32
L91 3.33
F168 5.29
V178 5.39
F182 5.43
L246 6.51
N250 6.55
L264 7.35
I268 7.39
h-bonds
hydrophobic
Pi-pi stacking
water bridges

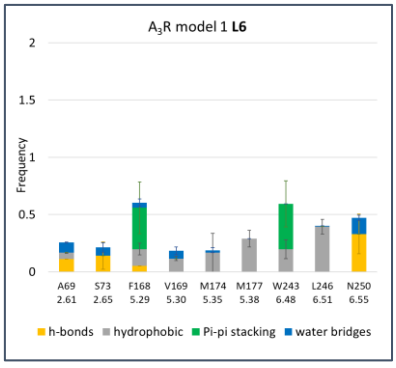
A3R model 1 L6
Frequency
A69 2.61
S73 2.65
F168 5.29
V169 5.30
M174 5.35
M177 5.38
W243 6.48
L246 6.51
N250 6.55
h-bonds
hydrophobic
Pi-pi stacking
water bridges

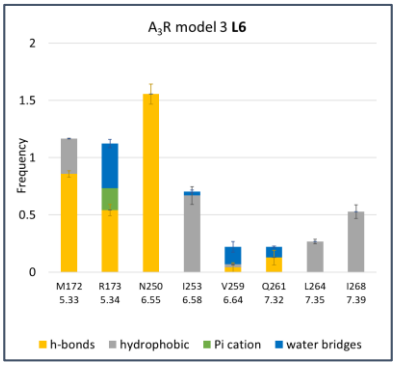
A3R model 3 L6
Frequency
M172 5.33
R173 5.34
N250 6.55
I253 6.58
V259 6.64
Q261 7.32
L264 7.35
I268 7.39
h-bonds
hydrophobic
Pi cation
water bridges

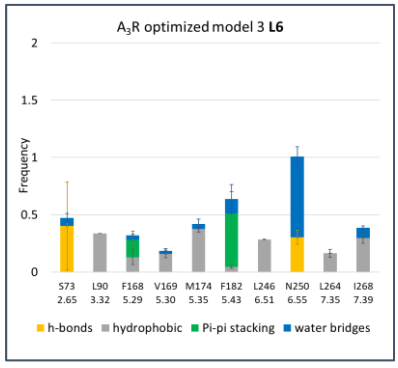
A3R optimized model 3 L6
Frequency
S73 2.65
L90 3.32
F168 5.29
V169 5.30
M174 5.35
F182 5.43
L246 6.51
N250 6.55
L264 7.35
I268 7.39
h-bonds
hydrophobic
Pi-pi stacking
water bridges

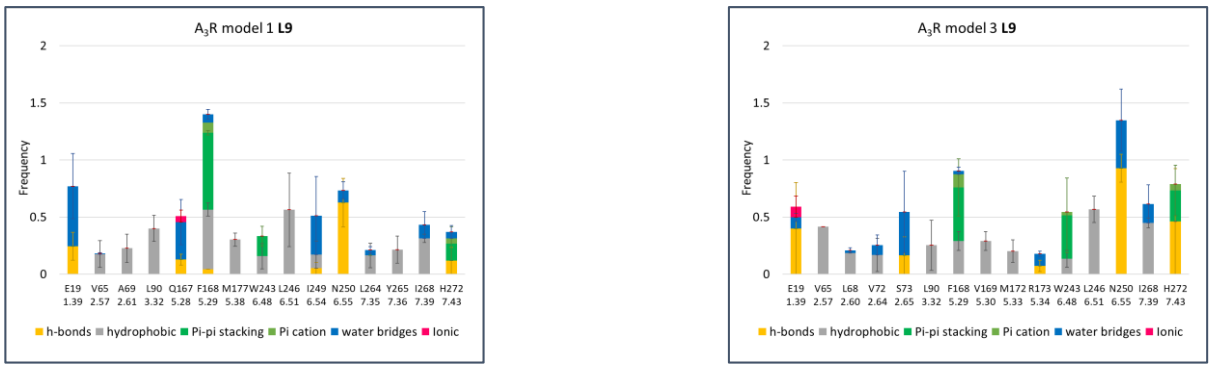

***Figure 5-5**: Last frames and ligand interaction frequency histograms of ligand – inactive A_3R complexes embedded in phospholipid bilayers from 100ns-MD simulations with amber99sb for the three homology models tested **Models 1-3** and **optimized Model 3**. (A) **L3** (B) **L4** (C) **L5** (D) **L6** (E) **L9** (F) interactions for **Model 1** (left), **Model 3** (center) and **optimized Model 3** (right).Receptor models are shown as cartoon; ligand or key interacting residues or waters are shown as sticks at a distance < 4 Å from the ligand, hydrogen bonding interactions and π-π interactions are shown with yellow dashes or green dashes respectively. Color scheme used in frames: protein Model 1 is shown in magenta, protein Model 2 in orange, protein Model 3 in blue, optimized Model 3 in green and ligand sticks in salmon. TM7 residues are hidden for clarity, only $Q261^{7.32}$ and $H272^{7.43}$ are shown.*

5.2.2 Comparison of the homology models of inactive A_3R based on experimental data from thermodynamics of binding and dissociation kinetics

Structure – dissociation rate relationships

Models 1-3 of inactive hA_3R were also evaluated for their predictive capability of the relative RT of ligands inside the receptor using the τRAMD method. The τRAMD method [234,235,293,250] performs a series of accelerated MD simulations with an additional randomly oriented force on the ligand. The experimental RT values of the ligands in Table 5-1 differ by ~ 10-fold with RT ~ 5.5 min in **L6** to RT ~ 47 min in **A17**.

As is shown in Table 5-3, we selected four ligands for the τRAMD simulations, ligand **L6** having a short experimental RT (RT= 5.55 ± 2.6 min), ligands **A17** and **L4** with long experimental RTs (RT = 47.23 ± 8.4 min and RT = 46.72 ± 4.5 min, respectively) and ligand **L5** (RT= 32.05 ± 6.3 min). We used the relaxed complexes from the 100ns-MD simulations of the four selected ligands with **Models 1-3** of inactive A_3R and further run four 5ns-MD simulation replicas with ff19sb [295] with each MD simulation trajectory being initialized with random velocities. Then, a series of 15

RAMD dissociation trajectories were generated using the starting snapshots obtained from these four replicas spanning 20 ns. The external force magnitude was chosen 8 kcal/mol Å based on the dissociation time of the quickest dissociating compound (**L6**) and the rest parameters were retained as described in the τRAMD protocol. [234,235,293,250]

Table 5-3: RT_{exp} values and calculated RT (RT_{calc}) values for ligands **A17**, **L4**, **L5**, **L6**; the latter were calculated with τRAMD method for the ligand - inactive hA_3R complexes embedded in phospholipid bilayers using ff19sb [295] with the protein **Models 1-3** or optimized **Model 3**.

		Model 1	Model 2	Model 3	Optimized Model 3
Ligand	**RT_{exp}** (min) [a]	**RT_{calc}** (ns)	**RT_{calc}** (ns)	**RT_{calc}** (ns)	**RT_{calc}** (ns)
A17	47.23 ± 8.4	3.08 ± 1.78	3.17 ± 2.88	4.79 ± 3.29	2.63 ± 0.89
L4	46.72 ± 4.5	2.72 ± 1.29	1.16 ± 0.82	1.31 ± 0.37	4.95 ± 1.64
L5	32.05 ± 6.3	1.17 ± 0.39	3.72 ± 1.35	13.69 ± 3.95	1.66 ± 0.19
L6	5.55 ± 2.6	0.49 ± 0.1	0.36 ± 0.07	4.96 ± 3.60	0.66 ± 0.18

[a] See **Table 5-1**.

Using **Model 1** and **Model 2**, the τRAMD method was able to separate the 'slow' from the 'fast' ligands successfully (see Table 5-3) with correlation coefficient between calculated and experimental RT values, r = 0.93, r = 0.53, respectively (see Figure 5-6). However, using AF2-derived **Model 3** the results were initially unsatisfactory (see Table 5-3, Figure 5-6), e.g., with **L5** being the slowest ligand and **L4** the faster that exit binding site (see Figure S3A).

As previously shown in experimental kinetic binding studies with hA_3R antagonists [199–201] and in the application of τRAMD with GPCRs [250] the residues structure and length of EL2 affects the dissociation of compounds because it can hinder the exit route. Residue $R173^{5.34}$ as well as the two adjacent residues $M172^{5.33}$ and $M174^{5.35}$ (MRM motif) that lie on EL2 seem to play a key role in the ligands' egress route. As it is shown in Figure 5-3, 5-4 these residues have different conformation in protein **Model 3** compared to **Models 1, 2**. In contrast to **Models 1, 2** in **Model 3** residue $R173^{5.34}$ is oriented towards the upper side of the binding site. The τRAMD calculations with **Model 3** showed that ligand **A17** during its exit from the binding site passed from residues

Q167$^{5.28}$, F168$^{5.29}$, V169$^{5.30}$, L246$^{6.51}$, I253$^{6.58}$, V259$^{6.64}$, L264$^{6.69}$, I268$^{6.73}$ as is shown in Figure S3B and in agreement with Figure 5-4C. Being in the upper side of the binding site of the receptor R173$^{5.34}$ can act as a closing lid that hinders the egress of ligands **L5, L6**. However, in the case of ligands **L4** and **A17** their 5-cyano group can form hydrogen bonding interactions with R173$^{5.34}$ and waters (in the upper area of the binding area between TM2, TM3 and the ligand) favoring ligands' exit from the binding site, as is shown in Figure S3B in agreement with Figure 5-4C. The τRAMD-based calculations revealed that **L5, L6** stayed longer inside binding area compared to **A17**, **L4**. In contrast, the experimental data showed that **A17** has the longest RT.

Thus, we rotated the side chains of MRM residues in **Model 3** to match the conformation they adopt in protein **Models 1,2** and ran the 100ns-MD simulations for the tested compounds **L4-L6**, **A17** in complex with inactive A_3R. The MD simulations of the complexes between the ligands and inactive hA_3R converged during the 100ns-MD simulations with $RMSD_{p,opt3}(C\alpha)$ < ~ 2.6 Å (Table 5-2, Figure 5-4, S2). In Figure 5-4D and Figure 5-5 snapshots for **A17** and **L4-L6** are shown respectively, inside the orthosteric binding site of inactive hA_3R with **optimized Model 3** are shown. While in **Model 3** R173$^{5.34}$ of EL2 that capped the binding area, in the **optimized Model** R173$^{5.34}$ was turned to face the outward region of the TMs bundle. In the **optimized Model 3**, the trimethoxy anilino group of **A17** was oriented towards the extracellular water face of the binding site instead forming hydrogen bonds with R173$^{5.34}$ in EL2 as is shown in Figure 5-4D.

In Figure 5-2, 5-3 were also included measures for comparison of the **optimized Model 3** with **Models 1-3**. As expected the most noticeable difference between **Model 3** and **optimized Model 3** was measured as $RMSD_p(Ca)$ ~ 2.1 Å in the conformation of TM5 (Figure 5-2B). In Figure 5-3 is shown that without considering the MRM motif modified orientation the binding site conformation between **Model 3** and **optimized Model 3** in their complexes with **A17** have after the MD simulations relaxation small difference with an $RMSD_{p,BS}$ (Cα) ~ 0.7 Å. However, when we modified the MRM motif orientation the $RMSD_{p,BS}$ (Cα) was ~ 3.4 Å.

The τRAMD calculations with **optimized Model 3** showed that compound **A17** during its exit from the binding site passed from residues Q167$^{5.28}$, F168$^{5.29}$, V169$^{5.30}$, L246$^{6.51}$, I253$^{6.58}$, V259$^{6.64}$, L264$^{6.69}$, I268$^{6.73}$ as is shown in Figure S3B and in agreement with Figure 5-4D. Using the **optimized Model 3**, the τRAMD calculations provide a satisfactory ranking of ligands **L4-L6, A17** according to their experimental RT values (Table 5-3, Figure 5-6).

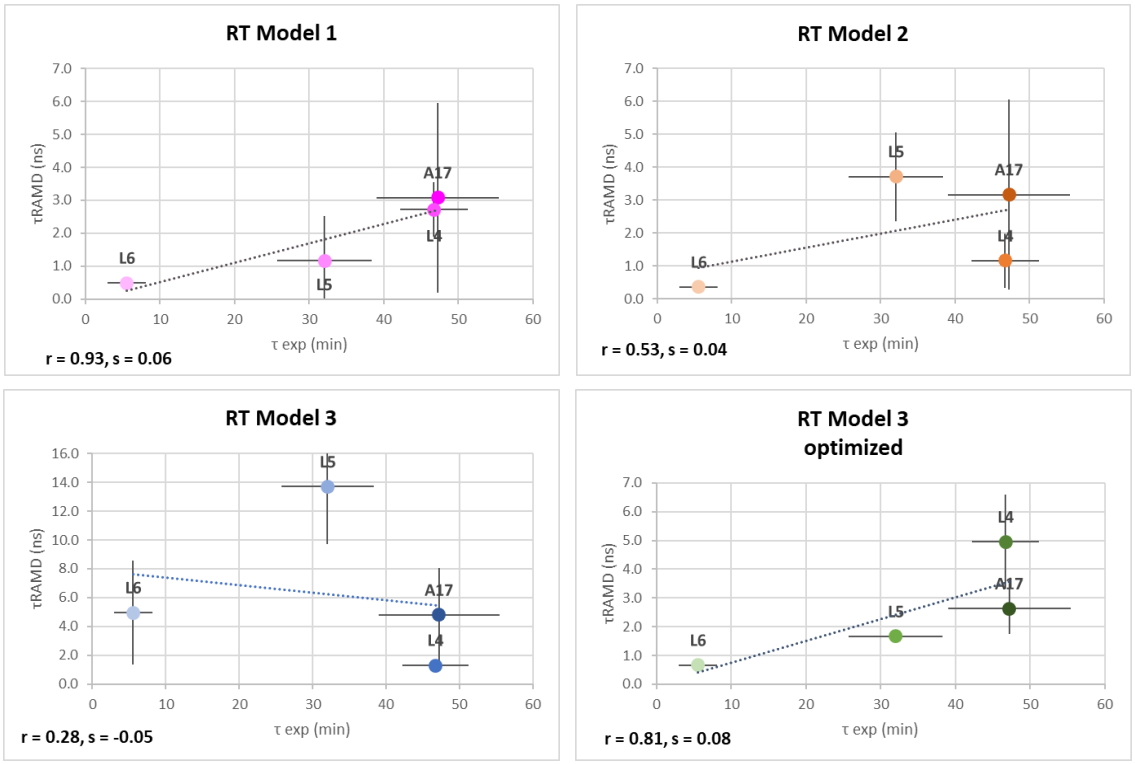

Figure 5-6: *Calculated RT values (ns) with τRAMD method for the ligand - inactive A_3R complexes embedded in phospholipid bilayers against experimental RT values (min) for ligands binding to inactive A_3R. Plots are coloured pink for* ***Model 1****, orange for* ***Model 2****, blue for* ***Model 3*** *and green for* ***optimized Model 3****; r: correlation coefficient, s: slope; long RT values are shown with dark color compared to short RT values; experimental errors are shown with horizontal line segments and computational method errors are shown with vertical line segments in the plotting points.*

Structure-binding affinity relationships from binding free energy calculations

In Table 5-4 we show the experimentally or the TI/MD-calculated relative binding free energies, $\Delta\Delta G_{b,exp}$ or $\Delta\Delta G_{b,TI/MD}$, respectively, that described the structure-activity relationships for these ligands against the inactive A_3R using **Models 1-3** and **optimized Model 3.** The experimental binding free energies were computed from the experimental dissociation constants determined in ref. [307] (Chapter 4) (see notes in Table 5-4). In our TI/MD simulations the last frames of the complexes from the alchemical perturbation calculations matched the last frames of the corresponding complexes from the 100ns-MD simulations (Figure 5-4, 5-5).

We observed that the binding affinity of the ligand is increased with the size of the substituent at the 3-position which can be anchored deeper into the receptor where it forms hydrophobic interactions mostly with $W243^{6.48}$ and $L90^{3.32}$. This is shown from the K_d's of the 3,5-disubstituted-7-(phenylamino)-pyrazolo[3,4-*c*]pyridines in Table 5-4 by changing the 3-

hydrogen in **A15** (pK_D = 5.49 ± 0.10) to 3-isopropyl group in **L3** (pK_D = 6.22 ± 0.10) or 3-phenyl group in **A17** (pK_D = 8.00 ± 0.32) showing a ~ 5-fold or ~ 324-fold increase in affinity. Similarly changing isopropyl group in **L2** (pK_D = 6.20 ± 0.06) to phenyl group in **L5** (pK_D = 7.07 ± 0.22) a 13-fold increase in affinity was observed. These results showed that 3-phenyl group is favored, as regards binding affinity, over the 3-isopropyl group or 3-hydrogen (see also Figure 5-5A). We observed this same effect also previously for hA_1R (Chapter 4). This effect of the 3-substitution can be quantitated by considering the alchemical perturbations **A15** → **L3** (3H → 3iPr), **A15** → **A17** (3H → 3Ph), **L3** → **A17** (3iPr → 3Ph), **L2** → **L5** (3iPr → 3Ph) and the corresponding $\Delta\Delta G_{b,exp}$ values and the TI/MD calculated values.

Thus, for **A15** → **L3** (3H → 3iPr), $\Delta\Delta G_{b,exp}$ = -1.04 ± 0.09 kcal mol^{-1} and the calculated values with **Models 1-3** and the **optimized Model 3** are $\Delta\Delta G_{b,TI/MD,1}$ = -1.04 ± 0.07 kcal mol^{-1}, $\Delta\Delta G_{b,TI/MD,2}$ = -1.30 ± 0.06 kcal mol^{-1}, $\Delta\Delta G_{b,TI/MD,3}$ = -1.31 ± 0.08 kcal mol^{-1} and $\Delta G_{b,TI/MD,opt3}$ = -2.47 ± 0.07 kcal mol^{-1} with deviation ($|\Delta\Delta G_{b,TI/MD} - \Delta\Delta G_{b,exp}|$, see Table 5-4) 0, 0.26, 0.27 and 1.43 kcal mol^{-1}, respectively. For **A15** → **A17** (3H → 3Ph), $\Delta\Delta G_{b,exp}$ = -3.56 ± 0.21 kcal mol^{-1} and the calculated values are $\Delta\Delta G_{b,TI/MD}$ = -4.05 ± 0.09, -6.24 ± 0.08, -3.93 ± 0.09 and -4.86 ± 0.09 kcal mol^{-1} with deviation 0.49, 2.68, 0.37 and 1.30 kcal mol^{-1}, respectively. For **L3** → **A17** (3iPr → 3Ph), $\Delta\Delta G_{b,exp}$ = -2.52 ± 0.21 kcal mol^{-1} and the calculated values are $\Delta\Delta G_{b,TI/MD}$ = -1.68 ± 0.09, -1.13 ± 0.08, -1.81 ± 0.09 and -2.45 ± 0.09 kcal mol^{-1} with deviation 0.84, 1.39, 0.71 and 0.07 kcal mol^{-1}, respectively. For **L2** → **L5** (3iPr → 3Ph), $\Delta\Delta G_{b,exp}$ = -1.23 ± 0.44 kcal mol^{-1} and the calculated values are $\Delta\Delta G_{b,TI/MD}$ = -2.24 ± 0.05, -1.20 ± 0.08, -0.68 ± 0.08 and -0.97 ± 0.05 kcal mol^{-1} with deviation 1.01, 0.03, 0.55 and 0.26 kcal mol^{-1}, respectively.

In comparison to **L4** (pK_D = 7.58 ± 0.32), three methoxy groups in the phenyl group of the 7-anilino substituent have been added in **A17** (pK_D = 8.00 ± 0.32). This substitution pattern boosts lipophilicity and enhances hydrophobic interactions with residues V169$^{5.30}$, L264$^{7.35}$, I268$^{7.39}$ located in the upper area of the binding site (Figure 5-4D, Figure 5-5B), increasing binding affinity according to $\Delta\Delta G_{b,exp}$ = -0.60 ± 0.32 kcal mol^{-1} for **L4** → **A17** (7Ph → 7Ph(OMe)$_3$. The TI/MD calculations showed a deviation 0.48 – 1.79 kcal mol^{-1} with **optimized Model 3** showing the lowest deviation.

The important effect in binding free energy from replacing the hydrogen at 5-position in **L6** (pK_D = 7.13 ± 0.55) with chlorine group in **L5** (pK_D = 7.07 ± 0.22) or with cyano group in **A17** (pK_D = 8.00 ± 0.32) is described by the alchemical perturbations **L6** → **L5** (5H → 5Cl) or **L6** → **A17** (5H → 5CN) or **L5** → **A17** (5Cl → 5CN) with $\Delta\Delta G_{b,exp}$ = 0.09 ± 0.39 or -1.23 ± 0.44 or -1.32 ± 0.27 kcal mol^{-1}, respectively (Table 5-4). By changing the hydrogen at the 5-position with a chlorine maintained

binding affinity but the replacement with cyano group increased affinity by ~ 10-fold. The TI/MD calculated values with the tested models for **L6** → **L5** (5H → 5Cl) are $\Delta\Delta G_{b,TI/MD}$ = -1.29 ± 0.05, -2.89 ± 0.03, -0.79 ± 0.04 and -0.39 ± 0.04 kcal mol^{-1} with deviation 1.38, 2.98, 0.88 and 0.48 kcal mol^{-1}, respectively. For **L6** → **A17** (5H → 5CN), $\Delta\Delta G_{b,TI/MD}$ = -0.61 ± 0.05, -3.68 ± 0.04, -1.48 ± 0.06 and -1.15 ± 0.05 kcal mol^{-1} with deviation 0.62, 2.45, 0.25 and 0.08 kcal mol^{-1}, respectively. For **L5 → A17** (5Cl → 5CN), $\Delta\Delta G_{b,TI/MD}$ = 0.40 ± 0.04, -0.91 ± 0.03, -0.10 ± 0.04 and -0.39 -1.48 ± 0.04 kcal mol^{-1} with deviation 1.72, 0.41, 1.22 and 0.93 kcal mol^{-1}, respectively.

Compared to **L6** (or also **L5**), the combination of the 5-cyano group and nitrogen at 6-position in **A17** increased polarity. Thus, in **L6**, which lacked the 5-cyano group, the hydrogen bonding interactions with N250$^{6.55}$ are reduced (Figure 5-4D, 5-5C,D) and the hydrogen bonding interactions with waters that enter area between the ligand and TM2, TM3 can't be formed.

The orthosteric binding pocket can also accommodate sizeable substituents at 5-position, e.g., the phenylmethyl group in **L8** or the 3-(pyridinyl)methyl group in **L9** that are linked to a 5-aminomethyl group. Ligands **L8** (pK_d = 6.73 ± 0.45) and **L9** (pK_d = 7.0 ± 0.33) have similar affinities at hA_3R (Table 5-3) differing by only ~ 1.8-fold, with pyridinyl group being slightly disfavored compared to the phenyl group according to the $\Delta G_{b,exp}$ = 0.38 ± 0.39 kcal mol^{-1} for the alchemical transformation **L9** → **L8**. The TI/MD predictions showed that $\Delta\Delta G_{b,TI/MD,1}$ = 0.99 kcal mol^{-1}, $\Delta\Delta G_{b,TI/MD,2}$ = 0.43 ± 0.09 kcal mol^{-1}, $\Delta\Delta G_{b,TI/MD,3}$ = -0.92 ± 0.09 kcal mol^{-1}, $\Delta\Delta G_{b,TI/MD,opt3}$ = 0.38 ± 0.09 kcal mol^{-1} with deviation 0.61, 0.05, 1.30, 0 kcal mol^{-1}, respectively (Table 5-3).

Table 5-4: Calculated relative binding free energies by the TI/MD method [189,190] with ff19sb [295] and a thermodynamic cycle for alchemical transformations of 3,5-disubstituted 7-(phenylamino)-pyrazolo[3,4-*c*]pyridines complexed to inactive A_3R and embedded in phospholipid bilayers, using protein **Models 1-3** and **optimized Model 3** ($\Delta\Delta G_{b,TI/MD,1}$, $\Delta\Delta G_{b,TI/MD,2}$ and $\Delta\Delta G_{b,TI/MD,3}$, $\Delta\Delta G_{b,TI/MD,opt3}$, respectively), experimental relative binding free energies ($\Delta\Delta G_{b,exp}$) and deviation of calculated from experimental values ($|\Delta\Delta G_{b,TI/MD} - \Delta\Delta G_{b,exp}|$) (free energies in kcal mol^{-1}).

			Model 1		Model 2		Model 3		Optimized Model 3	
No	**alchemical perturbation**	**$\Delta\Delta G_{b,exp}$** [a]	**$\Delta\Delta G_{b,TI/MD,1}$**	**$\lvert\Delta\Delta G_{b,TI/MD,1} - \Delta\Delta G_{b,exp}\rvert$**	**$\Delta\Delta G_{b,TI/MD,2}$**	**$\lvert\Delta\Delta G_{b,TI/MD,2} - \Delta\Delta G_{b,exp}\rvert$**	**$\Delta\Delta G_{b,TI/MD,3}$**	**$\lvert\Delta\Delta G_{b,TI/MD,3} - \Delta\Delta G_{b,exp}\rvert$**	**$\Delta\Delta G_{b,TI/MD,3}$**	**$\lvert\Delta\Delta G_{b,TI/MD,opt3} - \Delta\Delta G_{b,exp}\rvert$**
1	**A15 → L3**; R: 3-H→3-iPr	-1.04 ± 0.1	-1.04 ± 0.07	0.00	-1.30 ± 0.06	0.26	-1.31 ± 0.08	0.27	-2.47 ± 0.07	**1.43**
2	**A15 → A17**; R: 3-H→3-Ph	-3.56 ± 0.21	-4.05 ± 0.09	0.49	-6.24 ± 0.08	**2.68**	-3.93 ± 0.09	0.37	-4.86 ± 0.09	**1.30**
3	**L3 → A17**; R: 3-iPr→3-Ph	-2.52 ± 0.21	-1.68 ± 0.09	0.84	-1.13 ±0. 08	**1.39**	-1.81 ± 0.09	0.71	-2.45 ± 0.09	0.07
4	**L4 → A17**; Y: 7-Ph→7-Ph$(OMe)_3$	-0.60 ± 0.32	1.19 ± 0.09	**1.79** [b]	0.98 ± 0.10	**1.58**	-2.33 ± 0.12	**1.73**	-1.08 ± 0.11	0.48
5	**L6 → A17**; A: 5-H→5-CN	-1.23 ± 0.44	-0.61 ± 0.05	0.62	-3.68 ± 0.04	**2.45**	-1.48 ± 0.06	0.25	-1.15 ± 0.05	0.08
6	**L6 → L5**; A: 5-H→5-Cl	0.09 ± 0. 39	-1.29 ± 0.05	**1.38**	-2.89 ± 0.03	**2.98**	-0.79 ± 0.04	0.88	-0.39 ± 0.04	0.48
7	**L5 → A17**;	-1.32 ± 0.27	0.40 ± 0.04	**1.72**	-0.91 ± 0.03	0.41	-0.10 ± 0.04	**1.22**	-0.39 ± 0.04	0.93

	A: 5-Cl→5-CN								
8	**L2 → L5**; R: 3-iPr→3-Ph	-1.23 ± 0.14	-2.20 ± 0.05	0.97	-1.20 ± 0.08	0.03	-0.68 ± 0.08	0.55	-0.97 ± 0.10	0.26
9	**L9 → L8**; A: $5CH_2NHCH_2Ph$→ $5CH_2NHCH_2py$ [b]	0.38 ± 0.39	0.99 ± 0.08	0.61	0.43 ± 0.09	0.05	-0.92 ± 0.09	**1.30**	0.38 ± 0.09	0
			mue [c] = 0.94 kcal mol^{-1}		mue = **1.31** kcal mol^{-1}		mue = 0.81 kcal mol^{-1}		mue = 0.56 kcal mol^{-1}	

[a] Experimental relative binding free energies ($\Delta\Delta G_{b,exp}$) were computed using the experimental binding affinities (pK_d) determined in Chapter 4 and as described in ref. [307]; [b] values in bold and underlined showed a deviation > 1 kcal mol^{-1}; [c] mue = mean unsigned error or the mean of |ΔΔGb,TI/MD - ΔΔGb,exp| values.

Using homology **Model 1** we obtained calculated relative binding free energy values that have a mean unsigned error (mue) = 0.96 kcal mol^{-1} (see Table 5-4). We observed in 3 out of 9 cases a deviation of the calculated relative binding free energies from experimental values between 1.38-1.79 kcal mol^{-1}. In Figure 5-7 it is shown the very good correlation coefficient r = 0.74 (p = 0.0216) between the TI/MD calculated and the experimental relative binding free energies.

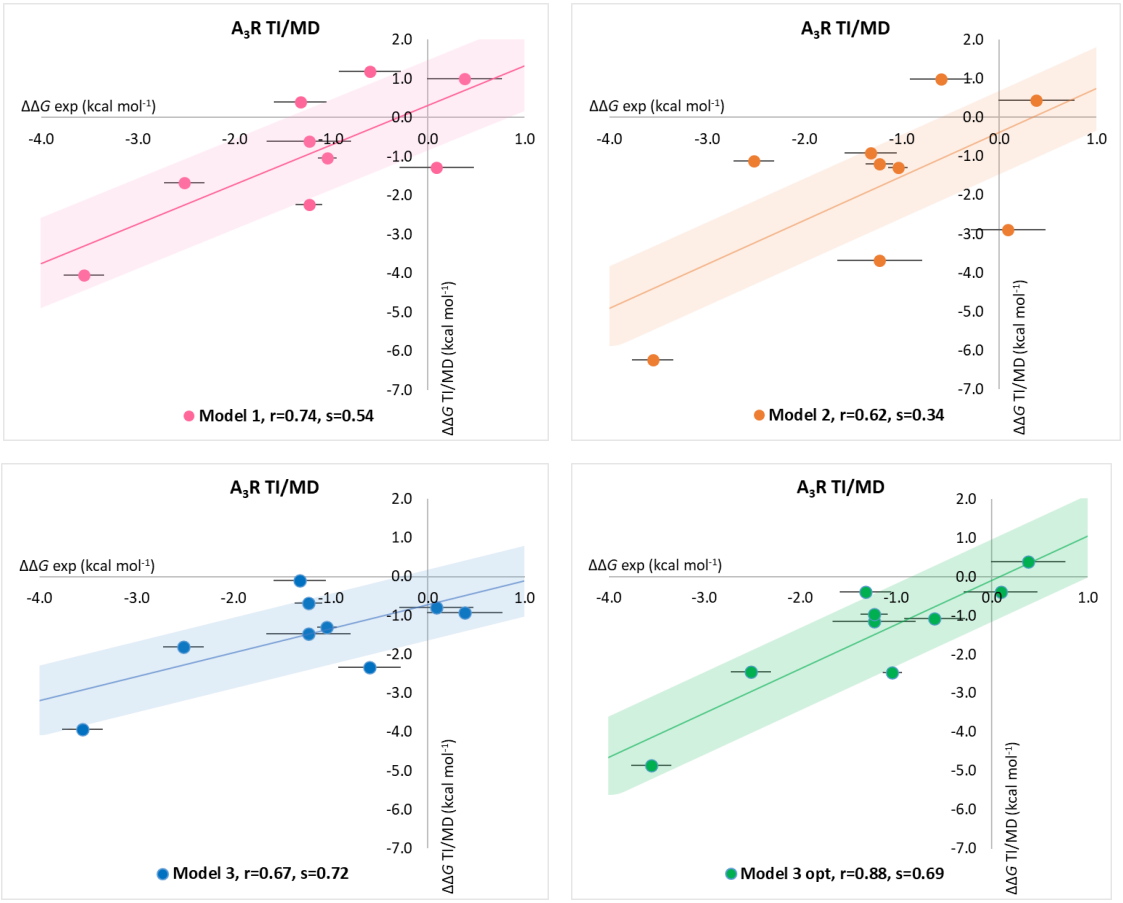

Figure 5-7: *Calculated $\Delta\Delta G_{b,TI/MD}$ values plotted against $\Delta\Delta G_{b,exp}$ values which were determined using the experimental binding affinities pK_d for ligands binding to inactive A_3R (Table 5-4); plots are coloured pink for* ***Model 1****, orange for* ***Model 2****, blue for* ***Model 3****, green for* ***optimized Model 3****; r: correlation coefficient, s: slope.*

Using homology **Model 2** the results showed mue = 1.31 kcal mol^{-1} with 5 out of 9 perturbations having a deviation between 1.39 - 2.98 kcal mol^{-1} (Table 5-4). In Figure 5-7 is shown that the correlation coefficient between the calculated and the experimental relative binding free energies is r = 0.62 (p = 0.0732).

With homology **Model 3**, the results showed mue = 0.81 kcal mol^{-1} and with 3 out of 9 perturbations having a deviation between 1.33 - 1.73 kcal mol^{-1} (Table 5-4) and a correlation coefficient r = 0.67 (p = 0.0505) between the calculated and the experimental relative binding free energies (Figure 5-7). When the **optimized Model 3** was used we obtained a correlation coefficient r = 0.88 (p = 0.0015), mue = 0.56 kcal mol^{-1} with only 2 alchemical perturbations having deviation between 1.30 - 1.43 kcal mol^{-1}. This suggested a computational model reliable to describe binding interactions of ligands against inactive A_3R.

A post processing analysis of the MD simulations of ligands **A15, L2-9, A17** in complex with inactive hA_3R was also tested using the MM/GBSA method. The MM/GBSA protocol was elaborated to include a hydrophobic slab as an implicit membrane model while including water molecules in the orthosteric binding area, to a radius of 4 Å from the center of mass of the ligand, [176–178] and the OPLS2005 [262,263] for the calculation of ligand-protein interactions. In Figure S4 and Table S7 are shown representatively results using **Model 1**. Compared to the most potent compound **A17**, the MM/GBSA method calculated the correct sign of binding free energy change when a group of atoms was deleted from **A17** (i.e., the cyano or the methoxy groups) without providing accurate relative binding free energy values. However, it failed to predict the sign of the binding free energy changes when a group at 3- or 5-position of in the phenylamino substituent was changed to another group.

5.3 Discussion

To explore the orthosteric binding area and design new antagonists against the unresolved hA_3R, accurate computational models are needed as regards calculation methods and protein model used. To achieve this aim, we explored the thermodynamic and kinetic binding SARs antagonists for a set of our previously identified antagonists against inactive hA_3R using TI/MD calculations of relative binding free energies and τRAMD calculations of relative RTs and comparing homology models of inactive hA_3R. We used five publicly available models which after filtering degenerate ones we came up with **Models 1-3** for inactive A_3R.

We used **Model 1** available from refs [256] [258] [259] and **Model 2** available from ref. [110] generated based on the crystal structures of inactive $A_{2A}R$ [34] or A_1R [55], respectively, and bioinformatics/chemoinformatics tools. We also used **Model 3** from GPCRdb [260] which has been generated based on a multi-state AF2 method. [122] AF2 has a bias towards either the active or

inactive conformation of the receptor and can only predict one state. Multi-state AF2 method is a more sophisticated method that has been developed based on AF2 which considers the conformational switch between the active and inactive states that occurs upon ligand binding. This method has been shown to accurately predict the structures of GPCRs in different states, making it a valuable tool for studying their function and developing new drugs.

We observed small differences between **Models 1-3** in the orientation of side chains of Q167$^{5.28}$, F168$^{5.29}$, V169$^{5.30}$, W243$^{6.48}$ that play important role in antagonistic binding. However, it was striking that in **Model 3** residues M172$^{5.33}$, R173$^{5.34}$, M174$^{5.35}$ (MRM motif) that lie in the upper region of TM5 on EL2 have significantly different side chain orientation compared to **Models 1,2**. EL2 residues affect the dissociation kinetics of the ligands and their RT inside the receptor. The EL2 is a challenging GPCR domain to be modelled because it is the longest and the most diverse loop of the three Els, [353,354] and in AF2-models EL2 is indicated as a low confidence region. [120]

We used the 3,5-disubstituted-7-(phenylamino)-pyrazolo[3,4-*c*]pyridine antagonists of hA_3R, **L3-L6, L9, A17,** for description of their binding profile and for some evaluation of the available homology models that will allow further development of the low nM leads as hA_3R antagonists, including compound **A17** and our other developed compounds. These antagonists (**L3-L6, L9, A17**) were previously identified and characterized with kinetic and equilibrium binding experiments (Chapter 4).

We applied induce-fit docking calculations and MD simulations in the complex of the 3,5-disubstituted-7-(phenylamino)-pyrazolo[3,4-*c*]pyridine antagonists with inactive A_3R. We observed that **A17** is stabilized inside the orthosteric binding area of inactive A_3R and binds between TM3 and TM5-TM7. Ligand **A17** forms attractive hydrophobic interactions with L90$^{3.32}$, W243$^{6.48}$, L246$^{6.51}$, L264$^{7.35}$, I268$^{7.39}$ at the bottom of the binding site, attractive hydrophobic interactions with V169$^{5.30}$ and possibly Q167$^{5.28}$, R173$^{5.34}$ at the top of the binding area, and in the middle area hydrogen bonding interactions with N250$^{6.55}$ and hydrophobic interactions with F168$^{5.29}$, M172$^{5.33}$, M177$^{5.38}$. Compared to **L4** (**Y=H**, A=CN, R=H; pK_D = 7.58 ± 0.33) these additional three methoxy groups in the phenyl group of the 7-anilino substituent in **A17** (**Y=OMe**, A=CN, R=H; pK_D = 8.00 ± 0.32) add affinity against inactive hA_3R, likely because they can lower the desolvation penalty of the ligand for entering binding site from bulk water phase and increase hydrophobic interactions with residues V169$^{5.30}$, L264$^{7.35}$, I268$^{7.39}$ (located in the upper area of the binding site). However, **A17** (RT = 47.23 ± 8.20 min) and **L4** (RT = 46.72 ± 4.50 min) have similar residence time values.

Mutagenic studies with other antagonists showed that residues Q92$^{3.34}$, H95$^{3.37}$, W243$^{6.48}$ at the bottom of the binding site and K152$^{5.13}$ in EL2, and H251$^{6.56}$ at the upper part are important for ligand recognition but not residue L244$^{6.49}$. [338] These residues are the same or lie close to the residues observed for **A17**. Additionally, in **Model 3** residues R173$^{5.34}$ in EL2 and Q167$^{5.28}$ on the top of the binding area can form hydrogen bonds with the methoxy group of the ligand. The 5-cyano group of **A17** is hydrogen bonded with waters that enter the binding area between ligand and TM2, TM3 and residues L90$^{3.32}$ and Q167$^{5.28}$. Compared to **L6** (Y=OMe, **A=H**, R=Ph; pK_D = 7.13 ± 0.55) or **L5** (Y=OMe, **A=Cl**, R=Ph; pK_D = 7.07 ± 0.22) which lack the 5-cyano group, the presence of the cyano group at 5-position and nitrogen at 6-position in **A17** (Y=OMe, **A=H**, R=Ph; ; pK_D = 8.00 ± 0.32) increased polarity at this part of the ligand and hydrogen bonding interactions with waters positioned between the ligand and TM2 and TM3. In compound **L6** which lacks the 5-cyano group, the hydrogen bonding interactions with waters and consequently the hydrogen bonding interactions with N250$^{6.55}$ are diminished. The much lower residence time of **L6** (RT = 5.55 ± 2.60 min) being ~ 8.5-fold smaller compared to **A17** (RT = 47.23 ± 8.20 min) or ~ 5.8-fold smaller compared to **L5** (RT = 32.05 ± 6.30 min) reflect these ligands' interactions inside the inactive A_3R.

The MD simulations showed that **L9** (A=CH_2NHCH_2Ph; pK_D = 7.0 ± 0.33) or **L8** (CH_2NHCH_2Ph; pK_D = 6.73 ± 0.45) with the increased in length 5-substituent have additional hydrophobic contacts with residues V65$^{2.57}$, L68$^{2.60}$, A69$^{2.61}$, V72$^{2.64}$ extending the ligands' girth from TM6 to TM2, TM1 and TM7. The ligand can form water bridged hydrogen bonds with E19$^{1.39}$ and the pyrazole ring is positioned close to TM5-TM7 so increasing the π-π interactions with F168$^{5.29}$ and forming new hydrogen bonding and π-π interactions with H272$^{7.43}$. While the two ligands **L8** (RT = 5.78 min) and **L9** (RT = 17.85 ± 4.3 min) have similar binding affinity they have residence times that differ by ~ 3.1-fold.

To explore the thermodynamic binding profile of the ligands we applied the MM/GBSA calculations, using an implicit membrane model and considering the waters inside the binding area. [176–178] This protocol is not adequate to rank differences in binding free energy due to subtle changes in substitution of ligands (i.e., SARs) against A_3R and failed also against hA_1R as we previously showed in Chapter 4. Thus, the performance we obtained with MM/GBSA method against hA_3R in ref. [257]with another class of antagonists seemed to be accidental. Such accuracy is possible using the perturbation methods based on statistical mechanics [314,334] as also suggested by studies related to the comparative performance of FEP/MD and MM/PBSA methods for water soluble protein-ligand complexes[314,334] and membrane protein-ligand complexes, e.g., complexes of $hA_{2A}R$. [335]

The alchemical perturbation calculations of relative binding free energies have been used to describe such SARs in membrane protein-ligand complexes, e.g., complexes of $hA_{2A}R$ [156,159–163,335] and hA_1R (see Chapter 4) either with the TI/MD or FEP/MD or using homology models of inactive $hA_{2B}R$ [161] and inactive hA_3R. [112,162,258] We applied the TI/MD method for the calculation of relative binding free energies of our previously identified 3,5-disubstituted-7-(phenylamino)-pyrazolo[3,4-*c*]pyridine antagonists to inactive hA_3R with homology **Models 1, 2, 3** showing a satisfactory performance with a correlation coefficient, r = 0.74, 0.62 or 0.67, respectively, between the calculated and experimental relative binding free energies with mue = 0.96, 1.31 0.81 kcal mol^{-1}, respectively.

To assess the relative RT of compounds within the receptor we applied the τRAMD method, [234,235,293,250] using four selected ligand with different experimental RTs for testing the τRAMD calculations, i.e., **A17** (Y=OMe, A=CN, R=Ph; RT_{exp} = 47.23 ± 8.20 min), **L4** (Y=H, A=CN, R=Ph; RT_{exp} = 46.72 ± 4.50 min), **L5** (Y=OMe, A=Cl, R=Ph; RT_{exp} = 32.05 ± 6.30 min), **L6** (Y=OMe, A=H, R=Ph; RT_{exp} = 5.55 ± 2.60 min). Notably, τRAMD performed well with protein **Models 1** and **2**, effectively distinguishing between short and long RT compounds. The multi-state AF2-based **Model 3** showed in the MD simulations that residue $R173^{5.34}$ in EL2 forms hydrogen bonds through its side chain with methoxy groups of **A17**. Residue $R173^{5.34}$ lying on the top of the binding area can affect egress route of ligands.

To address this and obtain a consistent ranking of the ligands as regards RTs we optimized the AF2-based **Model 3** by rotating side chains of MRM motif to match the orientation of the residues in **Models 1, 2**. In the **optimized Model 3** antagonist **A17** orients its anilino group towards the extracellular water face of the binding pocket and exit the binding site from there. In **Model 3** ligand **A17** forms hydrogen bonds with $R173^{5.34}$ in EL2. It is worth noting that the trimethoxy-anilino group of the ligand **A17** orients towards EL2 in A_1R although this receptor has a glutamic acid instead of valine at position 5.30. We found [89] that when residue $V169^{5.30}$ in hA_3R, which considered to be a selectivity filter for ligands' binding to A_3R orthosteric, was mutated to glutamic acid, the functional activity of agonist **IB-MECA** is increased due to the conformational plasticity of the binding area. With **optimized Model 3** we obtained not only an improved performance with τRAMD method showing a good correlation (r = 0.81) between calculated and experimental RT values but also, we achieved with TI/MD method better performance with a correlation r = 0.84 between calculated and experimental free energies with mue = 0.56 kcal mol^{-1}

Chapter 6.

Conclusions

6. Conclusions

Adenosine receptors, members of the GPCRs family, have garnered significant attention in drug discovery efforts, primarily due to their involvement in various physiological processes and their potential as therapeutic targets. Computational chemistry techniques have emerged as indispensable tools in the quest to design novel drugs targeting ARs. These techniques allow researchers to virtually screen large chemical libraries, predict ligand-receptor interactions, and assess the binding affinities of potential drug candidates.

One particular area of focus in ARs drug design is the development of dual antagonists that can target multiple receptor subtypes simultaneously. Dual antagonists, such as those already published to act on both $hA_1R/hA_{2A}R$ [98–100]. and $hA_{2B}R/hA_3R$ [96] , hold great promise in addressing complex medical conditions considered safer than drug combinations since they have lower toxicities and a lower risk of drug-drug interactions. No pharmacological data on dual hA_1R/hA_3R ligands have yet been published.

In this PhD thesis, we investigated the new 7-aminopyrazolo[3,4-*d*]pyridazine core, as promising scaffold for the development of novel antagonists targeting ARs. A number of derivatives synthesized by the National & Kapodistrian University of Athens revealed that the 1-methyl-3-phenyl-7-benzylaminopyrazolo[3,4-*d*]pyridazine **10b** was a high affinity dual antagonist of the human A_1R (26 nM) and A_3R (7.4 nM). It also displayed weak affinity (>1 μM at the $A_{2B}R$) measured using the NanoBRET method and functional assays. We also determined its kinetics of binding and found that at both the A_1R and A_3R, compound **10a** resides inside the binding pocket for $\geq$ 60 mins. Compound **10b** is placed inside the orthosteric binding area of A_1R interacting with $N^{6.55}$, $H^{7.43}$ and $F^{5.29}$, $W^{6.48}$, $L^{6.51}$, $T^{3.36}$, $H^{6.52}$, $Y^{7.46}$. Interestingly the regio-isomeric derivative **15b** where the methyl group is connected with pyrazole N^2 , lacked affinity due to the steric hindrance for hydrogen bonding interactions with $N^{6.55}$. We performed MD simulations to investigate the binding interaction in the new series as well as the observed regioselectivity in N^1Me (**10b**) compared to N^2Me (**15b**) isomer. The mutagenesis results for **10b** showed that in contrast to previous studies mutation $L250^{6.51}A$ resulted in only a slight reduction of binding affinity for **10b** while $Y271^{7.36}A$ mutation caused a 10-fold reduction in binding affinity. Mutation to alanine of residues $T91^{3.36}$, $H251^{6.52}$ or $S267^{7.32}$, which are deep in the orthosteric binding

affinity, did not affect binding affinity. Thus, **10b** can be used as a useful probe for the investigation of other features in the orthosteric binding area by suitable substitutions of this compound.

We also identified from the re-purposing of *in-house* antiproliferative compounds the novel pyrazolo[3,4-c]pyridine scaffold than can lead to ligands of ARs and improved understanding of SARs of ligands targeting ARs. After testing of pyrazolo[3,4-c]pyridine derivatives against all four AR subtypes we identified binding affinity and antagonistic activity against A_1R and A_3R. We found one series of potent derivatives with phenyl group at 3-position, anilino group at 7-position and cyano group at 5-position and one series with 3-(N-acyl)amino-5-anilino group at 3-position and anilino group at 5-position. Thus, **A17, L4** displayed low nanomolar affinities and **L5, L8, L9** mid-nanomolar affinities to the A_3R. At the A_1R, **A17**, displayed low nanomolar affinity and the five compounds **L4, L6-L9, L12** displayed mid-nanomolar to low nanomolar. Compound **A17** has a K_d = 5.62 nM and RT = 41.33 min measured using a NanoBRET assay for A_1R and K_d = 13.5 nM and RT = 47.23 min for A_3R. The kinetic data showed that compared to not potent congeners, **A17** has similar association but much lower dissociation rate (eg. at A_1R K_{on} = 139.7 $x10^5$ M^{-1} and K_{off} = 0.024 min^{-1}).

We investigated particularly the molecular recognition of the ligands against A_1R for the analogues of the most potent antagonist **A17**, which has a 3-phenyl, 5-cyano and 7-(3,4,5-trimethoxy)anilino substitution pattern, using a combination of MD simulations and accurate binding free energy calculations of the membrane systems using TI/MD method, first applied on a GPCR system, and site-directed mutagenesis. The TI/MD shows a very good agreement between calculated and experimental relative binding free energies for A_1R (r = 0.73). A novel observation from mutagenesis data for drug design purposes is that when the $L250^{6.51}A$ is changed to alanine the binding affinity of **A17** significantly increased at A_1R.

As we showed here, TI/MD is an accurate method to predict the effect of changing a substituent in the structure of **A17** in A_1R and the next step is to design and synthesize analogs of **A17** with improved affinity.

Finally, our study emphasizes the importance of selecting appropriate computational models for the design of antagonists against the unresolved inactive A_3R. The computational model that we suggest, includes a selected homology model in combination with MD simulations and methods that can predict relative binding free energies and relative RTs (TI/MD and τRAMD). The derived computational model can help in the prospective ranking of candidate drugs in a congeneric series prioritizing leads with stronger binding and longer residence times.

Chapter 7.

Bibliography

7. Bibliography

1. Tyndall J, Sandilya R. GPCR Agonists and Antagonists in the Clinic. *Med Chem (Los Angeles)*. 2005;1(4):405-421. doi:10.2174/1573406054368675

2. Lagerström MC, Schiöth HB. Structural diversity of G protein-coupled receptors and significance for drug discovery. *Nat Rev Drug Discov*. 2008;7(4):339-357. doi:10.1038/nrd2518

3. Sriram K, Insel PA. G Protein-Coupled Receptors as Targets for Approved Drugs: How Many Targets and How Many Drugs? *Mol Pharmacol*. 2018;93(4):251-258. doi:10.1124/mol.117.111062

4. Hauser AS, Attwood MM, Rask-Andersen M, Schiöth HB, Gloriam DE. Trends in GPCR drug discovery: new agents, targets and indications. *Nat Rev Drug Discov*. 2017;16(12):829-842. doi:10.1038/nrd.2017.178

5. Katritch V, Kufareva I, Abagyan R. Structure Based Prediction of Subtype-Selectivity for Adenosine Receptor Antagonists. *Neuropharmacology*. 2011;60(1):108. doi:10.1016/J.NEUROPHARM.2010.07.009

6. Janetopoulos C, Jin T, Devreotes P. Receptor-Mediated Activation of Heterotrimeric G-Proteins in Living Cells. *Science (1979)*. 2001;291(5512):2408-2411. doi:10.1126/science.1055835

7. Kristiansen K. Molecular mechanisms of ligand binding, signaling, and regulation within the superfamily of G-protein-coupled receptors: molecular modeling and mutagenesis approaches to receptor structure and function. *Pharmacol Ther*. 2004;103(1):21-80. doi:10.1016/J.PHARMTHERA.2004.05.002

8. Milligan G, Kostenis E. Heterotrimeric G-proteins: a short history. *Br J Pharmacol*. 2006;147 Suppl(Suppl 1):S46-55. doi:10.1038/sj.bjp.0706405

9. Bünemann M, Frank M, Lohse MJ. Gi protein activation in intact cells involves subunit rearrangement rather than dissociation. *Proceedings of the National Academy of Sciences*. 2003;100(26):16077-16082. doi:10.1073/pnas.2536719100

10. Neer EJ, Clapham DE. Roles of G protein subunits in transmembrane signalling. *Nature*. 1988;333(6169):129-134. doi:10.1038/333129a0

11. Sutkeviciute I, Vilardaga JP. Structural insights into emergent signaling modes of G protein-coupled receptors. *J Biol Chem*. 2020;295(33):11626-11642. doi:10.1074/jbc.REV120.009348

12. Smrcka A V. G protein βγ subunits: central mediators of G protein-coupled receptor signaling. *Cell Mol Life Sci*. 2008;65(14):2191-2214. doi:10.1007/s00018-008-8006-5

13. Khan SM, Sleno R, Gora S, et al. The expanding roles of Gβγ subunits in G protein-coupled receptor signaling and drug action. *Pharmacol Rev*. 2013;65(2):545-577. doi:10.1124/pr.111.005603

14. Fredriksson R, Schiöth HB. The Repertoire of G-Protein–Coupled Receptors in Fully Sequenced Genomes. *Mol Pharmacol*. 2005;67(5):1414-1425. doi:10.1124/MOL.104.009001

15. Fredriksson R, Lagerström MC, Lundin LG, Schiöth HB. The G-Protein-Coupled Receptors in the Human Genome Form Five Main Families. Phylogenetic Analysis, Paralogon Groups, and Fingerprints. *Mol Pharmacol*. 2003;63(6):1256-1272. doi:10.1124/mol.63.6.1256

16. Hanson MA, Stevens RC. Discovery of New GPCR Biology: One Receptor Structure at a Time. *Structure*. 2009;17(1):8-14. doi:10.1016/j.str.2008.12.003

17. Watkins HA, Au M, Hay DL. The structure of secretin family GPCR peptide ligands: implications for receptor pharmacology and drug development. *Drug Discov Today*. 2012;17(17):1006-1014. doi:https://doi.org/10.1016/j.drudis.2012.05.005

18. Chun L, Zhang W hua, Liu J feng. Structure and ligand recognition of class C GPCRs. *Acta Pharmacol Sin*. 2012;33(3):312-323. doi:10.1038/aps.2011.186

19. Bessis AS, Rondard P, Gaven F, et al. Closure of the Venus flytrap module of mGlu8 receptor and the activation process: Insights from mutations converting antagonists into agonists. *Proceedings of the National Academy of Sciences*. 2002;99(17):11097-11102. doi:10.1073/pnas.162138699

20. Yang-Snyder J, Miller JR, Brown JD, Lai CJ, Moon RT. A frizzled homolog functions in a vertebrate Wnt signaling pathway. *Current Biology*. 1996;6(10):1302-1306. doi:10.1016/S0960-9822(02)70716-1

21. Nichols AS, Floyd DH, Bruinsma SP, Narzinski K, Baranski TJ. Frizzled receptors signal through G proteins. *Cell Signal*. 2013;25(6):1468-1475. doi:https://doi.org/10.1016/j.cellsig.2013.03.009

22. Shen F, Cheng L, Douglas AE, Riobo NA, Manning DR. Smoothened Is a Fully Competent Activator of the Heterotrimeric G Protein G_i *Mol Pharmacol*. 2013;83(3):691 LP - 697. doi:10.1124/mol.112.082511

23. Krasnoperov VG, Bittner MA, Beavis R, et al. alpha-Latrotoxin stimulates exocytosis by the interaction with a neuronal G-protein-coupled receptor. *Neuron*. 1997;18(6):925-937. doi:10.1016/s0896-6273(00)80332-3

24. Luo R, Jeong SJ, Jin Z, Strokes N, Li S, Piao X. G protein-coupled receptor 56 and collagen III, a receptor-ligand pair, regulates cortical development and lamination. *Proc Natl Acad Sci U S A*. 2011;108(31):12925-12930. doi:10.1073/pnas.1104821108

25. Shonberg J, Kling RC, Gmeiner P, Löber S. GPCR crystal structures: Medicinal chemistry in the pocket. *Bioorg Med Chem*. 2015;23(14):3880-3906. doi:https://doi.org/10.1016/j.bmc.2014.12.034

26. Isberg V, Mordalski S, Munk C, et al. GPCRdb: an information system for G protein-coupled receptors. *Nucleic Acids Res*. 2016;44(D1):D356-64. doi:10.1093/nar/gkv1178

27. Foord SM, Bonner TI, Neubig RR, et al. International Union of Pharmacology. XLVI. G protein-coupled receptor list. *Pharmacol Rev*. 2005;57(2). doi:10.1124/pr.57.2.5

28. Rosenbaum DM, Rasmussen SGF, Kobilka BK. The structure and function of G-protein-coupled receptors. *Nature*. 2009;459(7245):356-363. doi:10.1038/nature08144

29. Lee Y, Basith S, Choi S. Recent Advances in Structure-Based Drug Design Targeting Class A G Protein-Coupled Receptors Utilizing Crystal Structures and Computational Simulations. *J Med Chem*. 2018;61(1):1-46. doi:10.1021/acs.jmedchem.6b01453

30. García-Nafría J, Lee Y, Bai X, Carpenter B, Tate CG. Cryo-EM structure of the adenosine A2A receptor coupled to an engineered heterotrimeric G protein. *Elife*. 2018;7:1-19. doi:10.7554/eLife.35946.001

31. Palczewski K, Kumasaka T, Hori T, et al. Crystal structure of rhodopsin: A G protein-coupled receptor. *Science (1979)*. 2000;289(5480):739-745. doi:10.1126/science.289.5480.739

32. Zhang D, Zhao Q, Wu B. Structural Studies of G Protein-Coupled Receptors. *Mol Cells*. 2015;38(10):836-842. doi:10.14348/molcells.2015.0263

33. Ballesteros JA, Weinstein H. Integrated methods for the construction of three-dimensional models and computational probing of structure-function relations in G protein-coupled receptors. In: *Methods in Neurosciences*. Vol 25. ; 1995:366-428. doi:10.1016/S1043-9471(05)80049-7

34. Jaakola VP, Griffith MT, Hanson MA, et al. The 2.6 angstrom crystal structure of a human A2A adenosine receptor bound to an antagonist. *Science (1979)*. 2008;322(5905):1211-1217. doi:10.1126/science.1164772

35. Rasmussen SGF, Choi HJ, Rosenbaum DM, et al. Crystal structure of the human beta2 adrenergic G-protein-coupled receptor. *Nature*. 2007;450(7168):383-387. doi:10.1038/nature06325

36. Rasmussen SGF, DeVree BT, Zou Y, et al. Crystal structure of the β2 adrenergic receptor–Gs protein complex. *Nature*. 2011;477(7366):549-555. doi:10.1038/nature10361

37. Dunwiddie T V, Masino SA. The role and regulation of adenosine in the central nervous system. *Annu Rev Neurosci*. 2001;24:31-55. doi:10.1146/annurev.neuro.24.1.31

38. Chen JF, Eltzschig HK, Fredholm BB. Adenosine receptors as drug targets—what are the challenges? *Nat Rev Drug Discov*. 2013;12(4):265-286. doi:10.1038/nrd3955

39. Cristóvão-Ferreira S, Navarro G, Brugarolas M, et al. A1R-A2AR heteromers coupled to Gs and G i/0 proteins modulate GABA transport into astrocytes. *Purinergic Signal*. 2013;9(3):433-449. doi:10.1007/s11302-013-9364-5

40. Jacobson KA, Gao ZG. Adenosine receptors as therapeutic targets. *Nat Rev Drug Discov*. 2006;5(3):247-264. doi:10.1038/nrd1983

41. Jacobson KA. Introduction to adenosine receptors as therapeutic targets. In: *Handbook of Experimental Pharmacology*. Vol 193. ; 2009:1-24. doi:10.1007/978-3-540-89615-9_1

42. de Lera Ruiz M, Lim YH, Zheng J. Adenosine A 2A Receptor as a Drug Discovery Target. *J Med Chem*. 2014;57(9):3623-3650. doi:10.1021/jm4011669

43. Madi L, Ochaion A, Rath-Wolfson L, et al. The A3 adenosine receptor is highly expressed in tumor versus normal cells: potential target for tumor growth inhibition. *Clin Cancer Res*. 2004;10(13):4472-4479. doi:10.1158/1078-0432.CCR-03-0651

44. Ji XD, Jacobson KA. Use of the triazolotriazine [3H]ZM 241385 as a radioligand at recombinant human A(2B) adenosine receptors. *Drug Des Discov*. 1999;16(3):217-226.

45. Lebon G, Warne T, Edwards PC, et al. Agonist-bound adenosine A2A receptor structures reveal common features of GPCR activation. *Nature*. 2011;474(7352):521-525. doi:10.1038/nature10136

46. Xu F, Wu H, Katritch V, et al. Structure of an agonist-bound human A2A adenosine receptor. *Science (1979)*. 2011;332(6027):322-327. doi:10.1126/science.1202793

47. Carpenter B, Nehmé R, Warne T, Leslie AGW, Tate CG. Structure of the adenosine A2A receptor bound to an engineered G protein. *Nature*. 2016;536(7614):104-107. doi:10.1038/nature18966

48. White KL, Eddy MT, Gao ZG, et al. Structural Connection between Activation Microswitch and Allosteric Sodium Site in GPCR Signaling. *Structure*. 2018;26(2):259-269.e5. doi:10.1016/j.str.2017.12.013

49. Amelia T, van Veldhoven JPD, Falsini M, et al. Crystal Structure and Subsequent Ligand Design of a Nonriboside Partial Agonist Bound to the Adenosine A 2A Receptor. *J Med Chem*. 2021;64(7):3827-3842. doi:10.1021/acs.jmedchem.0c01856

50. Zhang K, Wu H, Hoppe N, Manglik A, Cheng Y. Fusion protein strategies for cryo-EM study of G protein-coupled receptors. *Nat Commun*. 2022;13(1):4366. doi:10.1038/s41467-022-32125-2

51. Sun B, Bachhawat P, Chu MLH, et al. Crystal structure of the adenosine A 2A receptor bound to an antagonist reveals a potential allosteric pocket. *Proceedings of the National Academy of Sciences*. 2017;114(8):2066–2071. doi:10.1073/pnas.1621423114

52. Congreve M, Andrews SP, Dore AS, et al. Discovery of 1,2,4-Triazine Derivatives as Adenosine A. 2012;55(5):1898-1903.

53. Liu W, Chun E, Thompson AA, et al. Structural basis for allosteric regulation of GPCRS by sodium ions. *Science (1979)*. 2012;337(6091):232-236. doi:10.1126/science.1219218

54. Doré AS, Robertson N, Errey JC, et al. Structure of the adenosine A 2A receptor in complex with ZM241385 and the xanthines XAC and caffeine. *Structure*. 2011;19(9):1283-1293. doi:10.1016/j.str.2011.06.014

55. Glukhova A, Thal DM, Nguyen AT, et al. Structure of the Adenosine A1 Receptor Reveals the Basis for Subtype Selectivity. *Cell*. 2017;168(5):867-877.e13. doi:10.1016/j.cell.2017.01.042

56. Cheng RKY, Segala E, Robertson N, et al. Structures of Human A1and A2AAdenosine Receptors with Xanthines Reveal Determinants of Selectivity. *Structure*. 2017;25(8):1275–1285. doi:10.1016/j.str.2017.06.012

57. Draper-Joyce CJ, Khoshouei M, Thal DM, et al. Structure of the adenosine-bound human adenosine A1 receptor-Gi complex. *Nature*. 2018;558(7711):559-565. doi:10.1038/s41586-018-0236-6

58. Cai H, Xu Y, Guo S, et al. Structures of adenosine receptor A2BR bound to endogenous and synthetic agonists. *Cell Discov*. 2022;8(1):140. doi:10.1038/s41421-022-00503-1

59. Chen Y, Zhang J, Weng Y, et al. Cryo-EM structure of the human adenosine A 2B receptor–G s signaling complex. *Sci Adv*. 2022;8(51):eadd3709. doi:10.1126/sciadv.add3709

60. Massotte D, Kieffer BL. The second extracellular loop: a damper for G protein–coupled receptors? *Nat Struct Mol Biol*. 2005;12(4):287-288. doi:10.1038/nsmb0405-287

61. Nguyen ATN, Vecchio EA, Thomas T, et al. Role of the Second Extracellular Loop of the Adenosine A 1 Receptor on Allosteric Modulator Binding, Signaling, and Cooperativity. *Mol Pharmacol*. 2016;90(6):715-725. doi:10.1124/mol.116.105015

62. Schiedel AC, Hinz S, Thimm D, et al. The four cysteine residues in the second extracellular loop of the human adenosine A 2B receptor: Role in ligand binding and receptor function. *Biochem Pharmacol*. 2011;82(4):389-399. doi:10.1016/j.bcp.2011.05.008

63. Kim HO, Ji X duo, Siddiqi SM, Olah ME, Stiles GL, Jacobson KA. 2-Substitution of N6-benzyladenosine-5'-uronamides enhances selectivity for A3 adenosine receptors. *J Med Chem*. 1994;37(21):3614-3621.

64. Layland J, Carrick D, Lee M, Oldroyd K, Berry C. Adenosine: physiology, pharmacology, and clinical applications. *JACC Cardiovasc Interv*. 2014;7(6):581-591.

65. Deninno MP, Masamune H, Chenard LK, et al. 3 '-Aminoadenosine-5 '-uronamides: discovery of the first highly selective agonist at the human adenosine A3 receptor. *J Med Chem*. 2003;46(3):353-355.

66. Jeong LS, Jin DZ, Kim HO, et al. N6-Substituted D-4'-Thioadenosine-5'-methyluronamides: Potent and Selective Agonists at the Human A3 Adenosine Receptor. *J Med Chem*. 2003;46(18):3775-3777. doi:10.1021/jm034098e

67. Volpini R, Costanzi S, Lambertucci C, et al. N 6-Alkyl-2-alkynyl derivatives of adenosine as potent and selective agonists at the human adenosine A3 receptor and a starting point for searching A2B ligands. *J Med Chem*. 2002;45(15):3271-3279.

68. Melman A, Wang B, Joshi B V, et al. Selective A3 adenosine receptor antagonists derived from nucleosides containing a bicyclo[3.1.0]hexane ring system. *Bioorg Med Chem*. 2008;16(18):8546-8556. doi:10.1016/j.bmc.2008.08.007

69. Tchilibon S, Joshi B V, Kim SK, Duong HT, Gao ZG, Jacobson KA. (N)-Methanocarba 2, N6-disubstituted adenine nucleosides as highly potent and selective A3 adenosine receptor agonists. *J Med Chem*. 2005;48(6):1745-1758. doi:10.1021/jm049580r

70. Fishman P, Bar-Yehuda S, Liang BT, Jacobson KA. Pharmacological and therapeutic effects of A 3 adenosine receptor agonists. *Drug Discov Today*. 2012;17(7-8):359-366. doi:10.1016/j.drudis.2011.10.007

71. Jacobson KA, Tosh DK, Jain S, Gao ZG. Historical and Current Adenosine Receptor Agonists in Preclinical and Clinical Development. *Front Cell Neurosci*. 2019;13:1-17. doi:10.3389/fncel.2019.00124

72. Salvatore CA, Tilley SL, Latour AM, Fletcher DS, Koller BH, Jacobson MA. Disruption of the A 3 Adenosine Receptor Gene in Mice and Its Effect on Stimulated Inflammatory Cells. *Journal of Biological Chemistry*. 2000;275(6):4429-4434. doi:10.1074/jbc.275.6.4429

73. Kreckler LM. Adenosine Inhibits Tumor Necrosis Factor- Release from Mouse Peritoneal Macrophages via A2A and A2B but Not the A3 Adenosine Receptor. *Journal of Pharmacology and Experimental Therapeutics*. 2006;317(1):172-180. doi:10.1124/jpet.105.096016

74. Blackburn MR, Vance CO, Morschl E, Wilson CN. Adenosine receptors and inflammation. In: Wilson C, Mustafa S, eds. *Adenosine Receptors in Health and Disease. Handbook of Experimental Pharmacology*. Springer, Berlin, Heidelberg; 2009:215-269. doi:10.1007/978-3-540-89615-9_8

75. Fredholm BB, IJzerman AP, Jacobson KA, Linden J, Muller CE, Müller CE. International Union of Basic and Clinical Pharmacology . LXXXI . Nomenclature and Classification of

Adenosine Receptors — An Update. *Pharmacol Rev*. 2011;63(1):1-34. doi:10.1124/pr.110.003285.1

76. Chen JFF, Eltzschig HK, Fredholm BB. Adenosine receptors as drug targets-what are the challenges? *Nat Rev Drug Discov*. 2013;12(4):265-286. doi:10.1038/nrd3955

77. Teerlink JR, Iragui VJ, Mohr JP, et al. The Safety of an Adenosine A1-Receptor Antagonist, Rolofylline, in Patients with Acute Heart Failure and Renal Impairment. *Drug Saf*. 2012;35(3):233-244. doi:10.2165/11594680-000000000-00000

78. Pinna A. Adenosine A2A Receptor Antagonists in Parkinson's Disease: Progress in Clinical Trials from the Newly Approved Istradefylline to Drugs in Early Development and Those Already Discontinued. *CNS Drugs*. 2014;28(5):455-474. doi:10.1007/s40263-014-0161-7

79. Salvatore CA, Jacobson MA, Taylor HE, Linden J, Johnson RG. Molecular cloning and characterization of the human A3 adenosine receptor. *Proceedings of the National Academy of Sciences*. 1993;90(21):10365-10369. doi:10.1073/pnas.90.21.10365

80. Jiang J long, van Rhee AM, Chang L, et al. Structure−Activity Relationships of 4-(Phenylethynyl)-6-phenyl-1,4- dihydropyridines as Highly Selective A_3 Adenosine Receptor Antagonists. *J Med Chem*. 1997;40(16):2596-2608. doi:10.1021/jm970091j

81. Ji XD, Lubitz D Von, Olah ME, Stiles GL, Jacobson KA. Species differences in ligand affinity at central A3-adenosine receptors. *Drug Dev Res*. 1994;33(1):51-59. doi:10.1002/ddr.430330109

82. Kim YC, Ji X duo, Jacobson KA. Derivatives of the Triazoloquinazoline Adenosine Antagonist (CGS15943) Are Selective for the Human A3 Receptor Subtype. *J Med Chem*. 1996;39(21):4142-4148. doi:10.1021/jm960482i

83. Li AH, Moro S, Melman N, Ji X duo, Jacobson KA. Structure−Activity Relationships and Molecular Modeling of 3,5-Diacyl-2,4-dialkylpyridine Derivatives as Selective A3 Adenosine Receptor Antagonists. *J Med Chem*. 1998;41(17):3186-3201. doi:10.1021/jm980093j

84. Melman A, Gao ZG, Kumar D, et al. Design of (N)-methanocarba adenosine 5'-uronamides as species-independent A3 receptor-selective agonists. *Bioorg Med Chem Lett*. 2008;18(9):2813-2819. doi:10.1016/j.bmcl.2008.04.001

85. Okamura T, Kurogi Y, Hashimoto K, et al. Structure-activity relationships of adenosine A3 receptor ligands: New potential therapy for the treatment of glaucoma. *Bioorg Med Chem Lett*. 2004;14(14):3775-3779. doi:10.1016/j.bmcl.2004.04.099

86. Gessi S, Merighi S, Varani K, Leung E, Mac Lennan S, Borea PA. The A3 adenosine receptor: An enigmatic player in cell biology. *Pharmacol Ther*. 2008;117(1):123-140. doi:10.1016/j.pharmthera.2007.09.002

87. Lagarias P, Vrontaki E, Lambrinidis G, et al. Discovery of Novel Adenosine Receptor Antagonists through a Combined Structure- and Ligand-Based Approach Followed by Molecular Dynamics Investigation of Ligand Binding Mode. *J Chem Inf Model*. 2018;58(4):794-815. doi:10.1021/acs.jcim.7b00455

88. Lagarias P, Barkan K, Tzortzini E, et al. Insights to the Binding of a Selective Adenosine A3 Receptor Antagonist Using Molecular Dynamic Simulations, MM-PBSA and MM-GBSA Free Energy Calculations, and Mutagenesis. *J Chem Inf Model*. 2019;59(12):5183-5197. doi:10.1021/acs.jcim.9b00751

89. Stamatis D, Lagarias P, Barkan K, Vrontaki E, Ladds G, Kolocouris A. Structural Characterization of Agonist Binding to an A3 Adenosine Receptor through Biomolecular Simulations and Mutagenesis Experiments. *J Med Chem*. 2019;62(19):8831-8846. doi:10.1021/acs.jmedchem.9b01164

90. Barkan K, Lagarias P, Stampelou M, et al. Pharmacological characterisation of novel adenosine A3 receptor antagonists. *Sci Rep*. 2020;10(1):20781. doi:10.1038/s41598-020-74521-y

91. Lindsley CW, Emmitte KA, Hopkins CR, et al. Practical Strategies and Concepts in GPCR Allosteric Modulator Discovery: Recent Advances with Metabotropic Glutamate Receptors. *Chem Rev*. 2016;116(11):6707-6741. doi:10.1021/acs.chemrev.5b00656

92. Congreve M, Oswald C, Marshall FH. Applying Structure-Based Drug Design Approaches to Allosteric Modulators of GPCRs. *Trends Pharmacol Sci*. 2017;38(9):837-847. doi:10.1016/j.tips.2017.05.010

93. Wold EA, Chen J, Cunningham KA, Zhou J. Allosteric Modulation of Class A GPCRs: Targets, Agents, and Emerging Concepts. *J Med Chem*. 2019;62(1):88-127. doi:10.1021/acs.jmedchem.8b00875

94. Yang D, Zhou Q, Labroska V, et al. G protein-coupled receptors: structure- and function-based drug discovery. *Signal Transduct Target Ther*. 2021;6(1):7. doi:10.1038/s41392-020-00435-w

95. Anighoro A, Bajorath J, Rastelli G. Polypharmacology: challenges and opportunities in drug discovery. *J Med Chem*. 2014;57(19):7874-7887. doi:10.1021/jm5006463

96. Press NJ, Taylor RJ, Fullerton JD, et al. A new orally bioavailable dual adenosine A2B/A3 receptor antagonist with therapeutic potential. *Bioorg Med Chem Lett*. Published online 2005. doi:10.1016/j.bmcl.2005.04.021

97. Hou X, Majik MS, Kim K, et al. Structure-activity relationships of truncated C2- or C8-substituted adenosine derivatives as dual acting A 2A and A 3 adenosine receptor ligands. *J Med Chem*. 2012;55(1):342-356. doi:10.1021/jm201229j

98. Mihara T, Mihara K, Yarimizu J, et al. Pharmacological characterization of a novel, potent adenosine A1 and A2A receptor dual antagonist, 5-[5-amino-3-(4-fluorophenyl)pyrazin-2-yl]-1-isopropylpyridine-2(1H)-one (ASP5854), in models of Parkinson's disease and cognition. *J Pharmacol Exp Ther*. 2007;323(2):708-719. doi:10.1124/jpet.107.121962

99. Shook BC, Rassnick S, Wallace N, et al. Design and characterization of optimized adenosine A_2A/A_1 receptor antagonists for the treatment of Parkinson's disease. *J Med Chem*. 2012;55(3):1402-1417. doi:10.1021/jm201640m

100. Sanni O, Terre'Blanche G. Dual A1 and A2A adenosine receptor antagonists, methoxy substituted 2-benzylidene-1-indanone, suppresses intestinal postprandial glucose and attenuates hyperglycaemia in fructose-streptozotocin diabetic rats. *BMC Endocr Disord*. 2023;23(1):97. doi:10.1186/s12902-023-01354-x

101. Müller CE, Jacobson KA. Recent developments in adenosine receptor ligands and their potential as novel drugs. *Biochim Biophys Acta Biomembr*. 2011;1808(5):1290-1308. doi:10.1016/j.bbamem.2010.12.017

102. Brown R a, Spina D, Page CP. Adenosine receptors and asthma. *Br J Pharmacol*. 2008;153 Suppl(December 2007):S446-56. doi:10.1038/bjp.2008.22

103. Dennissen FJA, Anglada-Huguet M, Sydow A, Mandelkow E, Mandelkow EM. Adenosine A 1 receptor antagonist rolofylline alleviates axonopathy caused by human Tau ΔK280. *Proceedings of the National Academy of Sciences*. 2016;113(41):11597-11602. doi:10.1073/pnas.1603119113

104. Li S, Geiger NH, Soliman ML, Hui L, Geiger JD, Chen X. Caffeine, Through Adenosine A3 Receptor-Mediated Actions, Suppresses Amyloid-β Protein Precursor Internalization and Amyloid-β Generation. Agostinho P, ed. *Journal of Alzheimer's Disease*. 2015;47(1):73-83. doi:10.3233/JAD-142223

105. Brunschweiger A, Koch P, Schlenk M, et al. 8-Benzyltetrahydropyrazino[2,1-f]purinediones: water-soluble tricyclic xanthine derivatives as multitarget drugs for neurodegenerative diseases. *ChemMedChem*. 2014;9(8):1704-1724. doi:10.1002/cmdc.201402082

106. Chothia C, Lesk AM. The relation between the divergence of sequence and structure in proteins. *EMBO J*. 1986;5(4):823-826. doi:10.1002/j.1460-2075.1986.tb04288.x

107. Rost B. Twilight zone of protein sequence alignments. *Protein Engineering, Design and Selection*. 1999;12(2):85-94. doi:10.1093/protein/12.2.85

108. Baker D, Sali A. Protein Structure Prediction and Structural Genomics. *Science (1979)*. 2001;294(5540):93-96. doi:10.1126/SCIENCE.1065659

109. Martí-Renom MA, Stuart AC, Fiser A, Sánchez R, Melo F, Šali A. Comparative Protein Structure Modeling of Genes and Genomes. *https://doi.org/101146/annurev.biophys291291*. 2003;29:291-325. doi:10.1146/ANNUREV.BIOPHYS.29.1.291

110. Lee Y, Hou X, Lee JH, et al. Subtle Chemical Changes Cross the Boundary between Agonist and Antagonist: New A3Adenosine Receptor Homology Models and Structural Network Analysis Can Predict This Boundary. *J Med Chem*. 2021;64(17):12525-12536. doi:10.1021/acs.jmedchem.1c00239

111. Ranganathan A, Stoddart LA, Hill SJ, Carlsson J. Fragment-Based Discovery of Subtype-Selective Adenosine Receptor Ligands from Homology Models. *J Med Chem*. 2015;58(24):9578-9590. doi:10.1021/acs.jmedchem.5b01120

112. Yaziji V, Rodríguez D, Gutiérrez-De-Terán H, et al. Pyrimidine derivatives as potent and selective A3 adenosine receptor antagonists. *J Med Chem*. 2011;54(2):457-471. doi:10.1021/jm100843z

113. Berman HM, Westbrook J, Feng Z, et al. The Protein Data Bank. *Nucleic Acids Res*. 2000;28(1):235-242. doi:10.1093/nar/28.1.235

114. Ramachandran GN, Ramakrishnan C, Sasisekharan V. Stereochemistry of polypeptide chain configurations. *J Mol Biol*. 1963;7(1):95-99. doi:10.1016/S0022-2836(63)80023-6

115. Sali A. Comparative protein modeling by satisfaction of spatial restraints. *Mol Med Today*. 1995;1(6):270-277. doi:10.1016/S1357-4310(95)91170-7

116. Waterhouse AM, Procter JB, Martin DMA, Clamp M, Barton GJ. Jalview Version 2—a multiple sequence alignment editor and analysis workbench. *Bioinformatics*. 2009;25(9):1189-1191. doi:10.1093/bioinformatics/btp033

117. Tosh DK, Deflorian F, Phan K, et al. Structure-Guided Design of A 3 Adenosine Receptor-Selective Nucleosides: Combination of 2-Arylethynyl and Bicyclo[3.1.0]hexane Substitutions. *J Med Chem*. 2012;55(10):4847-4860. doi:10.1021/jm300396n

118. Katritch V, Jaakola VP, Lane JR, et al. Structure-based discovery of novel chemotypes for adenosine A2A receptor antagonists. *J Med Chem*. 2010;53(4):1799-1809. doi:10.1021/jm901647p

119. Varadi M, Anyango S, Deshpande M, et al. AlphaFold Protein Structure Database: massively expanding the structural coverage of protein-sequence space with high-accuracy models. *Nucleic Acids Res*. 2022;50(D1):D439-D444. doi:10.1093/NAR/GKAB1061

120. Jumper J, Evans R, Pritzel A, et al. Highly accurate protein structure prediction with AlphaFold. *Nature*. 2021;596(7873):583-589. doi:10.1038/s41586-021-03819-2

121. Baek M, DiMaio F, Anishchenko I, et al. Accurate prediction of protein structures and interactions using a three-track neural network. *Science*. 2021;373(6557):871-876. doi:10.1126/science.abj8754

122. Heo L, Feig M. Multi-state modeling of G-protein coupled receptors at experimental accuracy. *Proteins: Structure, Function, and Bioinformatics*. 2022;90(11):1873-1885. doi:10.1002/PROT.26382

123. Lengauer T, Rarey M. Computational methods for biomolecular docking. *Curr Opin Struct Biol*. 1996;6(3):402-406. doi:10.1016/S0959-440X(96)80061-3

124. Kitchen DB, Decornez H, Furr JR, Bajorath J. Docking and scoring in virtual screening for drug discovery: Methods and applications. *Nat Rev Drug Discov*. 2004;3(11):935-949. doi:10.1038/nrd1549

125. Wei BQ, Weaver LH, Ferrari AM, Matthews BW, Shoichet BK. Testing a Flexible-receptor Docking Algorithm in a Model Binding Site. *J Mol Biol*. 2004;337(5):1161-1182. doi:10.1016/j.jmb.2004.02.015

126. Salmaso V, Moro S. Bridging molecular docking to molecular dynamics in exploring ligand-protein recognition process: An overview. *Front Pharmacol*. 2018;9(AUG). doi:10.3389/fphar.2018.00923

127. Sapundzhi F, Prodanova K, Lazarova M. Survey of the scoring functions for protein-ligand docking. In: *AIP Conference Proceedings*. Vol 2172. ; 2019. doi:10.1063/1.5133601

128. GOLD Suite, version 5.2; Cambridge Crystallographic Data Centre: Cambridge, U.K., 2015. *GOLD Suite, version 52; Cambridge Crystallographic Data Centre: Cambridge, UK, 2015*.

129. Eldridge MD, Murray CW, Auton TR, Paolini G V., Mee RP. Empirical scoring functions: I. The development of a fast empirical scoring function to estimate the binding affinity of ligands in receptor complexes. *J Comput Aided Mol Des*. 1997;11(5):425-445. doi:10.1023/A:1007996124545

130. Sherman W, Day T, Jacobson MP, Friesner RA, Farid R. Novel procedure for modeling ligand/receptor induced fit effects. *J Med Chem*. 2006;49(2). doi:10.1021/jm050540c

131. Friesner RA, Banks JL, Murphy RB, et al. Glide: A New Approach for Rapid, Accurate Docking and Scoring. 1. Method and Assessment of Docking Accuracy. *J Med Chem*. 2004;47(7):1739-1749. doi:10.1021/JM0306430/SUPPL_FILE/JM0306430_S.PDF

132. Allen MP. *Introduction to Molecular Dynamics Simulation Michael*.; 1995. doi:10.1006/cbir.1995.1007

133. Hockney, R.W., Goel, S.P., and Eastwood JW. Quiet high-resolution computer models of a plasma. *J Comput Phys*. 1974;14:148-158.

134. Verlet L. Computer “Experiments” on Classical Fluids. I. Thermodynamical Properties of Lennard-Jones Molecules. *Phys Rev*. 1967;159:98-103.

135. Hess, B., Bekker, H., Berendsen, H.J.C., and Fraaije JGEM. LINCS: A linear constraint solver for molecular simulations. *J Comput Chem*. 1997;18:1463-1472.

136. González MA. Force fields and molecular dynamics simulations. *École thématique de la Société Française de la Neutronique*. 2011;12:169-200. doi:10.1051/SFN/201112009

137. Leach A. *Molecular Modelling: Principles and Applications (2nd Edition).*; 2001.

138. Cornell WD, Cieplak P, Bayly CI, et al. A Second Generation Force Field for the Simulation of Proteins, Nucleic Acids, and Organic Molecules. *J Am Chem Soc*. 1995;117(19):5179-5197. doi:10.1021/ja00124a002

139. MacKerell ADJr, Bashford D, Bellott M, et al. All-Atom Empirical Potential for Molecular Modeling and Dynamics Studies of Proteins. *J Phys Chem B*. 1998;102(18):3586-3616. doi:10.1021/jp973084f

140. Oostenbrink C, Villa A, Mark AE, Van Gunsteren WF. A biomolecular force field based on the free enthalpy of hydration and solvation: The GROMOS force-field parameter sets 53A5 and 53A6. *J Comput Chem*. 2004;25(13):1656-1676. doi:https://doi.org/10.1002/jcc.20090

141. Jorgensen WL, Tirado-Rives J. The OPLS [optimized potentials for liquid simulations] potential functions for proteins, energy minimizations for crystals of cyclic peptides and crambin. *J Am Chem Soc*. 1988;110(6):1657-1666. doi:10.1021/ja00214a001

142. Darden T, York D, Pedersen L. Particle mesh Ewald: An N·log(N) method for Ewald sums in large systems. *J Chem Phys*. 1993;98(12):10089-10092. doi:10.1063/1.464397

143. Hou T, Wang J, Li Y, Wang W. Assessing the performance of the molecular mechanics/Poisson Boltzmann surface area and molecular mechanics/generalized Born surface area methods. II. the accuracy of ranking poses generated from docking. *J Comput Chem*. 2011;32(5):866-877. doi:10.1002/jcc.21666

144. Massova I, Kollman PA. Combined molecular mechanical and continuum solvent approach (MM- PBSA/GBSA) to predict ligand binding. *Perspectives in Drug Discovery and Design*. 2000;18(1):113-135. doi:10.1023/A:1008763014207

145. Åqvist J, Medina C, Samuelsson JE. A new method for predicting binding affinity in computer-aided drug design. *Protein Engineering, Design and Selection*. 1994;7(3):385-391. doi:10.1093/protein/7.3.385

146. Hansson T, Marelius J, Åqvist J. Ligand binding affinity prediction by linear interaction energy methods. *J Comput Aided Mol Des*. 1998;12(1):27-35. doi:10.1023/A:1007930623000

147. Kirkwood JG. Statistical mechanics of fluid mixtures. *J Chem Phys*. 1935;3(5):300-313. doi:10.1063/1.1749657

148. Zwanzig RW. High†ï¿½Temperature Equation of State by a Perturbation Method. I. Nonpolar Gases. *Journal of Chemical Physics*. 1954;22(8):1420-1426. doi:10.1063/1.1740409

149. Izrailev S, Stepaniants S, Isralewitz B, et al. Steered Molecular Dynamics. In: Deuflhard P, Hermans J, Leimkuhler B, Mark AE, Reich S, Skeel RD, eds. *Computational Molecular Dynamics: Challenges, Methods, Ideas*. Springer Berlin Heidelberg; 1999:39-65.

150. Roux B. The calculation of the potential of mean force using computer simulations. *Comput Phys Commun*. 1995;91(1-3). doi:10.1016/0010-4655(95)00053-I

151. Matricon P, Nguyen ATN, Vo DD, et al. Structure-based virtual screening discovers potent and selective adenosine A1 receptor antagonists. *Eur J Med Chem*. 2023;257:115419. doi:10.1016/j.ejmech.2023.115419

152. Carlsson J, Yoo L, Gao ZG, Irwin JJ, Shoichet BK, Jacobson KA. Structure-based discovery of A2A adenosine receptor ligands. *J Med Chem*. 2010;53(9):3748-3755. doi:10.1021/jm100240h

153. Cescon E, Bolcato G, Federico S, et al. Scaffold Repurposing of in-House Chemical Library toward the Identification of New Casein Kinase 1 Inhibitors. *ACS Med Chem Lett*. 2020;11(6):1168-1174. doi:10.1021/acsmedchemlett.0c00028

154. Jazayeri A, Andrews SP, Marshall FH. Structurally Enabled Discovery of Adenosine A 2A Receptor Antagonists. *Chem Rev*. 2016;117(1):21-37. doi:10.1021/acs.chemrev.6b00119

155. Langmead CJ, Andrews SP, Congreve M, et al. Identification of Novel Adenosine A2A Receptor Antagonists by Virtual Screening. *J Med Chem*. 2012;55(5):1904-1909. doi:10.1021/jm201455y

156. Lenselink EB, Beuming T, van Veen C, et al. In search of novel ligands using a structure-based approach: a case study on the adenosine A2A receptor. *J Comput Aided Mol Des*. 2016;30(10):863-874. doi:10.1007/s10822-016-9963-7

157. Tian S, Wang X, Li L, et al. Discovery of Novel and Selective Adenosine A 2A Receptor Antagonists for Treating Parkinson's Disease through Comparative Structure-Based Virtual Screening. *J Chem Inf Model*. 2017;57(6):1474-1487. doi:10.1021/acs.jcim.7b00188

158. Decherchi S, Cavalli A. Thermodynamics and Kinetics of Drug-Target Binding by Molecular Simulation. *Chem Rev*. 2020;120(23):12788-12833. doi:10.1021/acs.chemrev.0c00534

159. Matricon P, Vo DD, Gao ZG, Kihlberg J, Jacobson KA, Carlsson J. Fragment-based design of selective GPCR ligands guided by free energy simulations. *Chemical Communications*. 2021;57(92):12305-12308. doi:10.1039/D1CC03202J

160. Matricon P, Suresh RR, Gao ZG, Panel N, Jacobson KA, Carlsson J. Ligand design by targeting a binding site water. *Chem Sci*. 2021;12(3):960-968. doi:10.1039/D0SC04938G

161. El Maatougui A, Azuaje J, González-Gómez M, et al. Discovery of Potent and Highly Selective A2B Adenosine Receptor Antagonist Chemotypes. *J Med Chem*. 2016;59(5):1967-1983. doi:10.1021/acs.jmedchem.5b01586

162. Azuaje J, Jespers W, Yaziji V, et al. Effect of Nitrogen Atom Substitution in A3 Adenosine Receptor Binding: N-(4,6-Diarylpyridin-2-yl)acetamides as Potent and Selective Antagonists. *J Med Chem*. Published online 2017. doi:10.1021/acs.jmedchem.7b00860

163. Deflorian F, Perez-Benito L, Lenselink EB, et al. Accurate prediction of GPCR ligand binding affinity with free energy perturbation. *J Chem Inf Model*. 2020;60(11):5563-5579. doi:10.1021/acs.jcim.0c00449

164. Nunes-Alves A, Kokh DB, Wade RC. Recent progress in molecular simulation methods for drug binding kinetics. *Curr Opin Struct Biol*. 2020;64. doi:10.1016/j.sbi.2020.06.022

165. Wang L, Wu Y, Deng Y, et al. Accurate and Reliable Prediction of Relative Ligand Binding Potency in Prospective Drug Discovery by Way of a Modern Free-Energy Calculation Protocol and Force Field. *J Am Chem Soc*. 2015;137(7):2695-2703. doi:10.1021/ja512751q

166. Lee TS, Hu Y, Sherborne B, Guo Z, York DM. Toward Fast and Accurate Binding Affinity Prediction with pmemdGTI: An Efficient Implementation of GPU-Accelerated Thermodynamic Integration. *J Chem Theory Comput*. 2017;13(7):3077-3084. doi:10.1021/acs.jctc.7b00102

167. Wang J, Wolf RM, Caldwell JW, Kollman PA, Case DA. Development and testing of a general Amber force field. *J Comput Chem*. 2004;25(9):1157-1174. doi:10.1002/jcc.20035

168. Vanommeslaeghe K, Hatcher E, Acharya C, et al. CHARMM general force field: A force field for drug-like molecules compatible with the CHARMM all-atom additive biological force fields. *J Comput Chem*. 2010;31(4):671-690. doi:https://doi.org/10.1002/jcc.21367

169. Loeffler HH, Michel J, Woods C. FESetup: Automating Setup for Alchemical Free Energy Simulations. *J Chem Inf Model*. 2015;55(12):2485-2490. doi:10.1021/acs.jcim.5b00368

170. Homeyer N, Gohlke H. FEW: A workflow tool for free energy calculations of ligand binding. *J Comput Chem*. 2013;34(11):965-973. doi:10.1002/jcc.23218

171. Straatsma TP, McCammon JA. Computational Alchemy. *Annu Rev Phys Chem*. 1992;43(1):407-435. doi:10.1146/annurev.pc.43.100192.002203

172. Ross Walker, Thomas Steinbrecher, Dwight McGee, Bill Miller III JS. AMBER ADVANCED TUTORIALS. TUTORIAL 3: MM-PBSA. Published 2006. Accessed January 11, 2020. http://ambermd.org/tutorials/advanced/tutorial3/

173. Homeyer N, Gohlke H. Free energy calculations by the Molecular Mechanics Poisson-Boltzmann Surface Area method. *Mol Inform*. 2012;31(2):114-122. doi:10.1002/minf.201100135

174. Constanciel R, Contreras R. Self consistent field theory of solvent effects representation by continuum models: Introduction of desolvation contribution. *Theor Chim Acta*. 1984;65:1–11. doi:10.1007/BF02427575

175. Sun H, Li Y, Tian S, Xu L, Hou T. Assessing the performance of MM/PBSA and MM/GBSA methods. 4. Accuracies of MM/PBSA and MM/GBSA methodologies evaluated by various simulation protocols using PDBbind data set. *Phys Chem Chem Phys*. 2014;16(31):16719-16729. doi:10.1039/C4CP01388C

176. Tan C, Tan YH, Luo R. Implicit Nonpolar Solvent Models. *J Phys Chem B*. 2007;111(42):12263-12274. doi:10.1021/jp073399n

177. Greene D, Qi R, Nguyen R, Qiu T, Luo R. Heterogeneous Dielectric Implicit Membrane Model for the Calculation of MMPBSA Binding Free Energies. *J Chem Inf Model*. 2019;59(6):3041-3056. doi:10.1021/acs.jcim.9b00363

178. Tanizaki S, Feig M. A generalized Born formalism for heterogeneous dielectric environments: Application to the implicit modeling of biological membranes. *Journal of Chemical Physics*. 2005;122(12):124706. doi:10.1063/1.1865992

179. Wong S, Amaro RE, McCammon JA. MM-PBSA Captures Key Role of Intercalating Water Molecules at a Protein−Protein Interface. *J Chem Theory Comput*. 2009;5(2):422-429. doi:10.1021/ct8003707

180. Genheden S, Mikulskis P, Hu L, Kongsted J, Söderhjelm P, Ryde U. Accurate predictions of nonpolar solvation free energies require explicit consideration of binding-site hydration. *J Am Chem Soc*. 2011;133(33):13081-13092. doi:10.1021/ja202972m

181. Mikulskis P, Genheden S, Ryde U. Effect of explicit water molecules on ligand-binding affinities calculated with the MM/GBSA approach. *J Mol Model*. 2014;20(6):2273. doi:10.1007/s00894-014-2273-x

182. Genheden S, Ryde U. The MM/PBSA and MM/GBSA methods to estimate ligand-binding affinities. *Expert Opin Drug Discov*. 2015;10(5):449-461. doi:10.1517/17460441.2015.1032936

183. Cappel D, Sherman W, Beuming T. Calculating Water Thermodynamics in the Binding Site of Proteins – Applications of WaterMap to Drug Discovery. *Curr Top Med Chem*. 2017;17(23):2586-2598. doi:10.2174/1568026617666170414141452

184. Homeyer N, Ioannidis H, Kolarov F, et al. Interpreting Thermodynamic Profiles of Aminoadamantane Compounds Inhibiting the M2 Proton Channel of Influenza A by Free Energy Calculations. *J Chem Inf Model*. 2016;56(1):110-126. doi:10.1021/acs.jcim.5b00467

185. Homeyer N, Stoll F, Hillisch A, Gohlke H. Binding free energy calculations for lead optimization: Assessment of their accuracy in an industrial drug design context. *J Chem Theory Comput*. 2014;10(8):3331-3344. doi:10.1021/ct5000296

186. Miller BR, McGee TD, Swails JM, Homeyer N, Gohlke H, Roitberg AE. MMPBSA.py : An Efficient Program for End-State Free Energy Calculations. *J Chem Theory Comput*. 2012;8(9):3314-3321. doi:10.1021/ct300418h

187. Procacci P. Multiple Bennett acceptance ratio made easy for replica exchange simulations. *J Chem Phys*. 2013;139(12):124105. doi:10.1063/1.4821814

188. Genheden S, Nilsson I, Ryde U. Binding Affinities of Factor Xa Inhibitors Estimated by Thermodynamic Integration and MM/GBSA. *J Chem Inf Model*. 2011;51(4):947-958. doi:10.1021/ci100458f

189. He X, Liu S, Lee TS, et al. Fast, Accurate, and Reliable Protocols for Routine Calculations of Protein-Ligand Binding Affinities in Drug Design Projects Using AMBER GPU-TI with ff14SB/GAFF. *ACS Omega*. 2020;5(9):4611-4619. doi:10.1021/acsomega.9b04233

190. Song LF, Lee TS, Zhu C, York DM, Merz KM. Using AMBER18 for Relative Free Energy Calculations. *J Chem Inf Model*. 2019;59(7):3128-3135. doi:10.1021/acs.jcim.9b00105

191. Lee TS, Allen BK, Giese TJ, et al. Alchemical binding free energy calculations in AMBER20: Advances and best practices for drug discovery. *J Chem Inf Model*. Published online 2020. doi:10.1021/acs.jcim.0c00613

192. Steinbrecher T, Joung I, Case DA. Soft-core potentials in thermodynamic integration: Comparing one- and two-step transformations. *J Comput Chem*. 2011;32(15):3253-3263. doi:10.1002/jcc.21909

193. Paliwal H, Shirts MR. A benchmark test set for alchemical free energy transformations and its use to quantify error in common free energy methods. *J Chem Theory Comput*. Published online 2011. doi:10.1021/ct2003995

194. Tan Z, Gallicchio E, Lapelosa M, Levy RM. Theory of binless multi-state free energy estimation with applications to protein-ligand binding. *Journal of Chemical Physics*. Published online 2012. doi:10.1063/1.3701175

195. Shirts MR, Pande VS. Comparison of efficiency and bias of free energies computed by exponential averaging, the Bennett acceptance ratio, and thermodynamic integration. *Journal of Chemical Physics*. 2005;122(14):144107. doi:10.1063/1.1873592

196. Tonge PJ. Drug–Target Kinetics in Drug Discovery. *ACS Chem Neurosci*. 2018;9(1):29-39. doi:10.1021/acschemneuro.7b00185

197. Schuetz DA, de Witte WEA, Wong YC, et al. Kinetics for Drug Discovery: an industry-driven effort to target drug residence time. *Drug Discov Today*. 2017;22(6):896-911. doi:https://doi.org/10.1016/j.drudis.2017.02.002

198. IJzerman AP, Guo D. Drug–Target Association Kinetics in Drug Discovery. *Trends Biochem Sci*. 2019;44(10):861-871. doi:https://doi.org/10.1016/j.tibs.2019.04.004

199. Varani K, Merighi S, Gessi S, et al. [(3)H]MRE 3008F20: a novel antagonist radioligand for the pharmacological and biochemical characterization of human A(3) adenosine receptors. *Mol Pharmacol*. 2000;57(5):968-975.

200. Müller CE, Diekmann M, Thorand M, Ozola V. [3H]8-Ethyl-4-methyl-2-phenyl-(8R)-4,5,7,8-tetrahydro-1H-imidazo[2,1-i]-purin-5-one ([3H]PSB-11), a Novel High-Affinity Antagonist Radioligand for Human A3 Adenosine Receptors. *Bioorg Med Chem Lett*. 2002;12(3):501-503. doi:10.1016/S0960-894X(01)00785-5

201. Xia L, A. C. Burger W, P. D. van Veldhoven J, et al. Structure–Affinity Relationships and Structure–Kinetics Relationships of Pyrido[2,1-f]purine-2,4-dione Derivatives as Human Adenosine A3 Receptor Antagonists. *J Med Chem*. 2017;60(17):7555-7568. doi:10.1021/acs.jmedchem.7b00950

202. Copeland RA. The drug–target residence time model: a 10-year retrospective. *Nat Rev Drug Discov*. 2016;15(2):87-95. doi:10.1038/nrd.2015.18

203. Stoddart LA, Vernall AJ, Bouzo-Lorenzo M, et al. Development of novel fluorescent histamine H1-receptor antagonists to study ligand-binding kinetics in living cells. *Sci Rep*. 2018;8:1572-. doi:10.1038/s41598-018-19714-2

204. Lee KSS, Yang J, Niu J, et al. Drug-Target Residence Time Affects in Vivo Target Occupancy through Multiple Pathways. *ACS Cent Sci*. 2019;5(9):1614-1624. doi:10.1021/acscentsci.9b00770

205. Guo D, Mulder-Krieger T, IJzerman AP, Heitman LH. Functional efficacy of adenosine A2A receptor agonists is positively correlated to their receptor residence time. *Br J Pharmacol*. 2012;166(6):1846-1859. doi:https://doi.org/10.1111/j.1476-5381.2012.01897.x

206. Pan AC, Borhani DW, Dror RO, Shaw DE. Molecular determinants of drug–receptor binding kinetics. *Drug Discov Today*. 2013;18(13-14):667-673. doi:10.1016/j.drudis.2013.02.007

207. Copeland RA. The drug–target residence time model: a 10-year retrospective. *Nat Rev Drug Discov*. 2016;15(2):87-95. doi:10.1038/nrd.2015.18

208. Schuetz DA, Richter L, Amaral M, et al. Ligand Desolvation Steers On-Rate and Impacts Drug Residence Time of Heat Shock Protein 90 (Hsp90) Inhibitors. *J Med Chem*. 2018;61(10):4397-4411. doi:10.1021/acs.jmedchem.8b00080

209. Strasser A, Wittmann HJ, Seifert R. Binding Kinetics and Pathways of Ligands to GPCRs. *Trends Pharmacol Sci*. 2017;38(8):717-732. doi:10.1016/j.tips.2017.05.005

210. Sykes DA, Stoddart LA, Kilpatrick LE, Hill SJ. Binding kinetics of ligands acting at GPCRs. *Mol Cell Endocrinol*. 2019;485:9-19. doi:10.1016/j.mce.2019.01.018

211. Guo D, Heitman LH, Ijzerman AP. Kinetic aspects of the interaction between ligand and g proteincoupled receptor: The case of the adenosine receptors. *Chem Rev*. 2017;117(1):38-66. doi:10.1021/acs.chemrev.6b00025

212. Auchampach JA, Gizewski ET, Wan TC, de Castro S, Brown GG, Jacobson KA. Synthesis and pharmacological characterization of [125I]MRS5127, a high affinity, selective agonist radioligand for the A3 adenosine receptor. *Biochem Pharmacol*. 2010;79(7):967-973. doi:10.1016/j.bcp.2009.11.009

213. Xia L, Kyrizaki A, Tosh DK, et al. A binding kinetics study of human adenosine A3 receptor agonists. *Biochem Pharmacol*. 2018;153:248-259. doi:10.1016/j.bcp.2017.12.026

214. Mondal J, Ahalawat N, Pandit S, Kay LE, Vallurupalli P. Atomic resolution mechanism of ligand binding to a solvent inaccessible cavity in T4 lysozyme. *PLoS Comput Biol*. 2018;14(5):e1006180-. https://doi.org/10.1371/journal.pcbi.1006180

215. Plattner N, Noé F. Protein conformational plasticity and complex ligand-binding kinetics explored by atomistic simulations and Markov models. *Nat Commun*. 2015;6(1):7653. doi:10.1038/ncomms8653

216. Buch I, Giorgino T, De Fabritiis G. Complete reconstruction of an enzyme-inhibitor binding process by molecular dynamics simulations. *Proceedings of the National Academy of Sciences*. 2011;108(25):10184-10189. doi:10.1073/pnas.1103547108

217. Huber GA, Kim S. Weighted-ensemble Brownian dynamics simulations for protein association reactions. *Biophys J*. 1996;70(1):97-110. doi:10.1016/S0006-3495(96)79552-8

218. Zuckerman DM, Chong LT. Weighted Ensemble Simulation: Review of Methodology, Applications, and Software. *Annu Rev Biophys*. 2017;46(1):43-57. doi:10.1146/annurev-biophys-070816-033834

219. Nunes-Alves A, Zuckerman DM, Arantes GM. Escape of a Small Molecule from Inside T4 Lysozyme by Multiple Pathways. *Biophys J*. 2018;114(5):1058-1066. doi:10.1016/j.bpj.2018.01.014

220. Wang J, Arantes PR, Bhattarai A, et al. Gaussian accelerated molecular dynamics: Principles and applications. *WIREs Computational Molecular Science*. 2021;11(5):e1521. doi:https://doi.org/10.1002/wcms.1521

221. Miao Y, Feher VA, McCammon JA. Gaussian Accelerated Molecular Dynamics: Unconstrained Enhanced Sampling and Free Energy Calculation. *J Chem Theory Comput*. 2015;11(8):3584-3595. doi:10.1021/acs.jctc.5b00436

222. Votapka LW, Jagger BR, Heyneman AL, Amaro RE. SEEKR: Simulation Enabled Estimation of Kinetic Rates, A Computational Tool to Estimate Molecular Kinetics and Its Application to Trypsin–Benzamidine Binding. *J Phys Chem B*. 2017;121(15):3597-3606. doi:10.1021/acs.jpcb.6b09388

223. Votapka LW, Stokely AM, Ojha AA, Amaro RE. SEEKR2: Versatile Multiscale Milestoning Utilizing the OpenMM Molecular Dynamics Engine. *J Chem Inf Model*. 2022;62(13):3253-3262. doi:10.1021/acs.jcim.2c00501

224. Votapka LW, Amaro RE. Multiscale Estimation of Binding Kinetics Using Brownian Dynamics, Molecular Dynamics and Milestoning. *PLoS Comput Biol*. 2015;11(10):e1004381-. https://doi.org/10.1371/journal.pcbi.1004381

225. Jagger BR, Ojha AA, Amaro RE. Predicting Ligand Binding Kinetics Using a Markovian Milestoning with Voronoi Tessellations Multiscale Approach. *J Chem Theory Comput*. 2020;16(8):5348-5357. doi:10.1021/acs.jctc.0c00495

226. Tiwary P, Parrinello M. From Metadynamics to Dynamics. *Phys Rev Lett*. 2013;111(23):230602. doi:10.1103/PhysRevLett.111.230602

227. Limongelli V, Bonomi M, Parrinello M. Funnel metadynamics as accurate binding free-energy method. *Proceedings of the National Academy of Sciences*. 2013;110(16):6358-6363. doi:10.1073/pnas.1303186110

228. Wang Y, Valsson O, Tiwary P, Parrinello M, Lindorff-Larsen K. Frequency adaptive metadynamics for the calculation of rare-event kinetics. *J Chem Phys*. 2018;149(7):072309. doi:10.1063/1.5024679

229. Wang Y, Martins JM, Lindorff-Larsen K. Biomolecular conformational changes and ligand binding: from kinetics to thermodynamics. *Chem Sci*. 2017;8(9):6466-6473. doi:10.1039/C7SC01627A

230. Banerjee P, Bagchi B. Dynamical control by water at a molecular level in protein dimer association and dissociation. *Proceedings of the National Academy of Sciences*. 2020;117(5):2302-2308. doi:10.1073/pnas.1908379117

231. Tiwary P, Limongelli V, Salvalaglio M, Parrinello M. Kinetics of protein–ligand unbinding: Predicting pathways, rates, and rate-limiting steps. *Proceedings of the National Academy of Sciences*. 2015;112(5):E386-E391. doi:10.1073/pnas.1424461112

232. Casasnovas R, Limongelli V, Tiwary P, Carloni P, Parrinello M. Unbinding Kinetics of a p38 MAP Kinase Type II Inhibitor from Metadynamics Simulations. *J Am Chem Soc*. 2017;139(13):4780-4788. doi:10.1021/jacs.6b12950

233. Lamim Ribeiro JM, Provasi D, Filizola M. A combination of machine learning and infrequent metadynamics to efficiently predict kinetic rates, transition states, and molecular determinants of drug dissociation from G protein-coupled receptors. *J Chem Phys*. 2020;153(12):124105. doi:10.1063/5.0019100

234. Nunes-Alves A, Kokh DB, Wade RC. Ligand unbinding mechanisms and kinetics for T4 lysozyme mutants from τRAMD simulations. *Curr Res Struct Biol*. 2021;3:106-111. doi:https://doi.org/10.1016/j.crstbi.2021.04.001

235. Kokh DB, Amaral M, Bomke J, et al. Estimation of Drug-Target Residence Times by τ-Random Acceleration Molecular Dynamics Simulations. *J Chem Theory Comput*. 2018;14(7):3859-3869. doi:10.1021/acs.jctc.8b00230

236. Bianciotto M, Gkeka P, Kokh DB, Wade RC, Minoux H. Contact Map Fingerprints of Protein–Ligand Unbinding Trajectories Reveal Mechanisms Determining Residence Times Computed from Scaled Molecular Dynamics. *J Chem Theory Comput*. 2021;17(10):6522-6535. doi:10.1021/acs.jctc.1c00453

237. Schuetz DA, Bernetti M, Bertazzo M, et al. Predicting Residence Time and Drug Unbinding Pathway through Scaled Molecular Dynamics. *J Chem Inf Model*. 2019;59(1):535-549. doi:10.1021/acs.jcim.8b00614

238. Isralewitz B, Gao M, Schulten K. Steered molecular dynamics and mechanical functions of proteins. *Curr Opin Struct Biol*. 2001;11(2):224-230. doi:https://doi.org/10.1016/S0959-440X(00)00194-9

239. Mollica L, Decherchi S, Zia SR, Gaspari R, Cavalli A, Rocchia W. Kinetics of protein-ligand unbinding via smoothed potential molecular dynamics simulations. *Sci Rep*. 2015;5(1):11539. doi:10.1038/srep11539

240. Souza PCT, Alessandri R, Barnoud J, et al. Martini 3: a general purpose force field for coarse-grained molecular dynamics. *Nat Methods*. 2021;18(4):382-388. doi:10.1038/s41592-021-01098-3

241. Souza PCT, Thallmair S, Conflitti P, et al. Protein–ligand binding with the coarse-grained Martini model. *Nat Commun*. 2020;11(1):3714. doi:10.1038/s41467-020-17437-5

242. Dandekar BR, Mondal J. Capturing Protein–Ligand Recognition Pathways in Coarse-Grained Simulation. *J Phys Chem Lett*. 2020;11(13):5302-5311. doi:10.1021/acs.jpclett.0c01683

243. Bruce NJ, Ganotra GK, Richter S, Wade RC. KBbox: A Toolbox of Computational Methods for Studying the Kinetics of Molecular Binding. *J Chem Inf Model*. 2019;59(9):3630-3634. doi:10.1021/acs.jcim.9b00485

244. Wolf S, Amaral M, Lowinski M, et al. Estimation of Protein–Ligand Unbinding Kinetics Using Non-Equilibrium Targeted Molecular Dynamics Simulations. *J Chem Inf Model*. 2019;59(12):5135-5147. doi:10.1021/acs.jcim.9b00592

245. Ojha AA, Srivastava A, Votapka LW, Amaro RE. Selectivity and ranking of tight-binding JAK-STAT inhibitors using Markovian milestoning with Voronoi tessellations. *bioRxiv*. Published online January 1, 2023:2022.11.10.516058. doi:10.1101/2022.11.10.516058

246. Narayan B, Buchete NV, Elber R. Computer Simulations of the Dissociation Mechanism of Gleevec from Abl Kinase with Milestoning. *J Phys Chem B*. 2021;125(22):5706-5715. doi:10.1021/acs.jpcb.1c00264

247. Gobbo D, Piretti V, Di Martino RMC, et al. Investigating Drug–Target Residence Time in Kinases through Enhanced Sampling Simulations. *J Chem Theory Comput*. 2019;15(8):4646-4659. doi:10.1021/acs.jctc.9b00104

248. Huang Y ming M. Multiscale computational study of ligand binding pathways: Case of p38 MAP kinase and its inhibitors. *Biophys J*. 2021;120(18):3881-3892. doi:10.1016/j.bpj.2021.08.026

249. Dror RO, Pan AC, Arlow DH, et al. Pathway and mechanism of drug binding to G-protein-coupled receptors. *Proc Natl Acad Sci U S A*. 2011;108(32):13118-13123. doi:10.1073/pnas.1104614108

250. Kokh DB, Wade RC. G Protein-Coupled Receptor-Ligand Dissociation Rates and Mechanisms from τRAMD Simulations. *J Chem Theory Comput*. 2021;17(10):6610-6623. doi:10.1021/acs.jctc.1c00641

251. Galvani F, Pala D, Cuzzolin A, et al. Unbinding Kinetics of Muscarinic M3 Receptor Antagonists Explained by Metadynamics Simulations. *J Chem Inf Model*. 2023;63(9):2842-2856. doi:10.1021/acs.jcim.3c00042

252. Bortolato A, Deflorian F, Weiss DR, Mason JS. Decoding the Role of Water Dynamics in Ligand–Protein Unbinding: CRF1R as a Test Case. *J Chem Inf Model*. 2015;55(9):1857-1866. doi:10.1021/acs.jcim.5b00440

253. Lüdemann SK, Lounnas V, Wade RC. How do substrates enter and products exit the buried active site of cytochrome P450cam? 2. Steered molecular dynamics and adiabatic mapping of substrate pathways11Edited by J. Thornton. *J Mol Biol*. 2000;303(5):813-830. doi:https://doi.org/10.1006/jmbi.2000.4155

254. Ballesteros JA, Weinstein H. Analysis and refinement of criteria for predicting the structure and relative orientations of transmembranal helical domains. *Biophys J*. 1992;62(1):107-109. doi:10.1016/S0006-3495(92)81794-0

255. Yaziji V, Rodríguez D, Coelho A, et al. Selective and potent adenosine A3 receptor antagonists by methoxyaryl substitution on the N-(2,6-diarylpyrimidin-4-yl)acetamide scaffold. *Eur J Med Chem*. Published online 2013. doi:10.1016/j.ejmech.2012.11.010

256. Floris M, Sabbadin D, Medda R, Bulfone A, Moro S. Adenosiland: Walking through adenosine receptors landscape. *Eur J Med Chem*. 2012;58:248-257. doi:10.1016/j.ejmech.2012.10.022

257. Lagarias P, Barkan K, Tzortzini E, et al. Insights to the Binding of a Selective Adenosine A3 Receptor Antagonist Using Molecular Dynamic Simulations, MM-PBSA and MM-GBSA Free Energy Calculations, and Mutagenesis. *J Chem Inf Model*. 2019;59(12):5183-5197. doi:10.1021/acs.jcim.9b00751

258. Miranda-Pastoriza D, Bernárdez R, Azuaje J, et al. Exploring Non-orthosteric Interactions with a Series of Potent and Selective A3 Antagonists. *ACS Med Chem Lett*. 2022;13(2):243-249. doi:10.1021/acsmedchemlett.1c00598

259. Margiotta E, Moro S. A Comparison in the Use of the Crystallographic Structure of the Human A1 or the A2A Adenosine Receptors as a Template for the Construction of a Homology Model of the A3 Subtype. *Applied Sciences*. 2019;9(5):821. doi:10.3390/app9050821

260. Pándy-Szekeres G, Munk C, Tsonkov TM, et al. GPCRdb in 2018: adding GPCR structure models and ligands. *Nucleic Acids Res*. 2018;46(D1):D440-D446. doi:10.1093/NAR/GKX1109

261. Sastry GM, Adzhigirey M, Day T, Annabhimoju R, Sherman W. Protein and ligand preparation: parameters, protocols, and influence on virtual screening enrichments. *J Comput Aided Mol Des*. 2013;27(3):221-234.

262. Kaminski GA, Friesner RA, Tirado-Rives J, Jorgensen WL. Evaluation and reparametrization of the OPLS-AA force field for proteins via comparison with accurate quantum chemical calculations on peptides. *Journal of Physical Chemistry B*. 2001;105(28):6474-6487. doi:10.1021/jp003919d

263. Shivakumar D, Williams J, Wu YJ, Damm W, Shelley J, Sherman W. Prediction of Absolute Solvation Free Energies using Molecular Dynamics Free Energy Perturbation and the OPLS Force Field. *J Chem Theory Comput*. 2010;6(5):1509-1519. doi:10.1021/ct900587b

264. Mohamadi F, Richards NGJ, Guida WC, et al. Macromodel?an integrated software system for modeling organic and bioorganic molecules using molecular mechanics. *J Comput Chem*. 1990;11(4):440-467. doi:10.1002/jcc.540110405

265. Halgren TTA. Merck molecular force field. I. Basis, form, scope, parameterization, and performance of MMFF94. *J Comput Chem*. 1996;17(5-6):490-519. doi:10.1002/(SICI)1096-987X(199604)17:5/6<490::AID-JCC1>3.0.CO;2-P

266. Shelley JC, Cholleti A, Frye LL, Greenwood JR, Timlin MR, Uchimaya M. Epik: a software program for pK a prediction and protonation state generation for drug-like molecules. *J Comput Aided Mol Des*. 2007;21(12):681-691.

267. Jones G, Willett P, Glen RC, Leach AR, Taylor R. Development and validation of a genetic algorithm for flexible docking. *J Mol Biol*. 1997;267(3):727-748. doi:10.1006/jmbi.1996.0897

268. Lomize MA, Pogozheva ID, Joo H, Mosberg HI, Lomize AL. OPM database and PPM web server: resources for positioning of proteins in membranes. *Nucleic Acids Res*. 2012;40(D1):D370-D376. doi:10.1093/nar/gkr703

269. Jorgensen WL, Chandrasekhar J, Madura JD, Impey RW, Klein ML. Comparison of simple potential functions for simulating liquid water. *J Chem Phys*. 1983;79(2):926-935. doi:10.1063/1.445869

270. Wang J, Cieplak P, Kollman PA. How Well Does a Restrained Electrostatic Potential (RESP) Model Perform in Calculating Conformational Energies of Organic and Biological

Molecules? *J Comput Chem*. 2000;21(12):1049-1074. doi:10.1002/1096-987X(200009)21:12<1049::AID-JCC3>3.0.CO;2-F

271. Hornak V, Abel R, Okur A, Strockbine B, Roitberg A, Simmerling C. Comparison of multiple amber force fields and development of improved protein backbone parameters. *Proteins: Structure, Function and Genetics*. 2006;65(3):712-725. doi:10.1002/prot.21123

272. Bayly CI, Cieplak P, Cornell WD, Kollman PA. A well-behaved electrostatic potential based method using charge restraints for deriving atomic charges: The RESP model. *Journal of Physical Chemistry*. 1993;97(40):10269-10280. doi:10.1021/j100142a004

273. risch, M. J.; Trucks, G. W.; Schlegel, H. B.; Scuseria, G. E.; Robb, M. A.; Cheeseman, J. R.; Montgomery, J. A., Jr.; Vreven, T.; Kudin, K. N.; Burant, J. C.; Millam, J. M.; Iyengar, S. S.; Tomasi, J.; Barone, V.; Mennucci, B.; Cossi, M.; Scalmani, G.; Re JA. Gaussian 03. Published online 2007.

274. Davidson ER, Feller D. Basis Set Selection for Molecular Calculations. *Chem Rev*. 1986;86(4):681-696. doi:10.1021/cr00074a002

275. D.A. Case, I.Y. Ben-Shalom, S.R. Brozell, et al. *AMBER 2018, University of California*.; 2018.

276. Bowers KJ, Chow E, Xu H, et al. Scalable algorithms for molecular dynamics simulations on commodity clusters. In: *Proceedings of the 2006 ACM/IEEE Conference on Supercomputing, SC'06*. ACM Press; 2006:84. doi:10.1145/1188455.1188544

277. Koynova R, Caffrey M. Phases and phase transitions of the phosphatidylcholines. *Biochimica et Biophysica Acta (BBA) - Reviews on Biomembranes*. 1998;1376(1):91-145. doi:10.1016/S0304-4157(98)00006-9

278. Ryckaert JP, Ciccotti G, Berendsen HJC. Numerical integration of the cartesian equations of motion of a system with constraints: molecular dynamics of n-alkanes. *J Comput Phys*. 1977;23(3):327-341. doi:10.1016/0021-9991(77)90098-5

279. Balusek C, Hwang H, Lau CH, et al. Accelerating Membrane Simulations with Hydrogen Mass Repartitioning. *J Chem Theory Comput*. 2019;15(8):4673-4686. doi:10.1021/acs.jctc.9b00160

280. Martyna GJ, Klein ML, Tuckerman M. Nosé–Hoover chains: The canonical ensemble via continuous dynamics. *J Chem Phys*. 1992;97(4):2635-2643.

281. Martyna GJ, Tobias DJ, Klein ML. Constant pressure molecular dynamics algorithms. *J Chem Phys*. 1994;101(5):4177-4189. doi:10.1063/1.467468

282. Humphreys DD, Friesner RA, Berne BJ. A Multiple-Time-Step Molecular Dynamics Algorithm for Macromolecules. *J Phys Chem*. 1994;98(27):6885-6892. doi:10.1021/j100078a035

283. Delano WL. The PyMOL Molecular Graphics System. *CCP4 Newsletter on protein crystallography*. 2002;40(1).

284. Maffucci I, Contini A. Explicit Ligand Hydration Shells Improve the Correlation between MM-PB/GBSA Binding Energies and Experimental Activities. *J Chem Theory Comput*. 2013;9(6):2706-2717. doi:10.1021/ct400045d

285. Michaud-Agrawal N, Denning EJ, Woolf TB, Beckstein O. MDAnalysis: A toolkit for the analysis of molecular dynamics simulations. *J Comput Chem*. 2011;32(10):2319-2327. doi:10.1002/jcc.21787

286. Jo S, Kim T, Iyer VG, Im W. CHARMM-GUI: A web-based graphical user interface for CHARMM. *J Comput Chem*. 2008;29(11):1859-1865. doi:10.1002/jcc.20945

287. Maier JA, Martinez C, Kasavajhala K, Wickstrom L, Hauser KE, Simmerling C. ff14SB: Improving the Accuracy of Protein Side Chain and Backbone Parameters from ff99SB. *J Chem Theory Comput*. 2015;11(8):3696-3713. doi:10.1021/acs.jctc.5b00255

288. Frisch M, Trucks G, Schlegel H, Scuseria G. Gaussian 03, revision C. 02; Gaussian, Inc.: Wallingford, CT, 2004. *There is no corresponding*. Published online 2013.

289. Feller SE, Zhang Y, Pastor RW, Brooks BR. Constant pressure molecular dynamics simulation: The Langevin piston method. *J Chem Phys*. 1995;103(11):4613-4621. doi:10.1063/1.470648

290. Salomon-Ferrer R, Case DA, Walker RC. An overview of the Amber biomolecular simulation package. *Wiley Interdiscip Rev Comput Mol Sci*. 2013;3(2):198-210. doi:10.1002/wcms.1121

291. Berendsen HJC, Postma JPM, Van Gunsteren WF, Dinola A, Haak JR. Molecular dynamics with coupling to an external bath. *J Chem Phys*. 1984;81(8):3684-3690. doi:10.1063/1.448118

292. Su PC, Johnson ME. Evaluating thermodynamic integration performance of the new amber molecular dynamics package and assess potential halogen bonds of enoyl-ACP reductase (FabI) benzimidazole inhibitors. *J Comput Chem*. 2016;37(9):836-847. doi:10.1002/jcc.24274

293. Kokh DB, Doser B, Richter S, Ormersbach F, Cheng X, Wade RC. A workflow for exploring ligand dissociation from a macromolecule: Efficient random acceleration molecular dynamics simulation and interaction fingerprint analysis of ligand trajectories. *Journal of Chemical Physics*. 2020;153(12):125102. doi:10.1063/5.0019088/1062851

294. D.A. Case, K. Belfon, I.Y. Ben-Shalom, S.R. Brozell, D.S. Cerutti, T.E. Cheatham, III VWDC, T.A. Darden, R.E. Duke, G. Giambasu, M.K. Gilson, H. Gohlke, A.W. Goetz, R Harris, S. Izadi, S.A. Izmailov, K. Kasavajhala, A. Kovalenko, R. Krasny, T. Kurtzman, T.S. Lee, S. LeGrand, P. Li, C. Lin JL, T. Luchko, R. Luo, V. Man, K.M. Merz, Y. Miao, O. Mikhailovskii, G. Monard, H. Nguyen, A. Onufriev F, Pan, S. Pantano, R. Qi, D.R. Roe, A. Roitberg, C. Sagui, S. Schott-Verdugo, J. Shen, C.L. Simmerling NR, Skrynnikov, J. Smith, J. Swails, R.C. Walker, J. Wang, L. Wilson, R.M. Wolf, X. Wu, Y. Xiong YX, Kollman DMY and PA. *AMBER 2020, University of California*. University of California; 2020.

295. Tian C, Kasavajhala K, Belfon KAA, et al. Ff19SB: Amino-Acid-Specific Protein Backbone Parameters Trained against Quantum Mechanics Energy Surfaces in Solution. *J Chem Theory Comput*. 2020;16(1). doi:10.1021/acs.jctc.9b00591

296. Swails J. ParmEd Parameter/topology editor and molecular simulator. Published 2020. https://github.com/ParmEd/ParmEd

297. Humphrey W, Dalke A, Schulten K. VMD: Visual molecular dynamics. *J Mol Graph*. 1996;14(1):28-33. doi:10.1016/0263-7855(96)00018-5

298. Tuccinardi T, Zizzari AT, Brullo C, et al. Substituted pyrazolo[3,4-b]pyridines as human A 1 adenosine antagonists: Developments in understanding the receptor stereoselectivity. *Org Biomol Chem*. 2011;9(12):4448-4455. doi:10.1039/c0ob01064b

299. Catarzi D, Colotta V, Varano F, et al. Pyrazolo[1,5-c]quinazoline derivatives and their simplified analogues as adenosine receptor antagonists: synthesis, structure-affinity relationships and molecular modeling studies. *Bioorg Med Chem*. 2013;21(1):283-294. doi:10.1016/j.bmc.2012.10.031

300. Squarcialupi L, Catarzi D, Varano F, et al. Structural refinement of pyrazolo[4,3-d]pyrimidine derivatives to obtain highly potent and selective antagonists for the human A3 adenosine receptor. *Eur J Med Chem*. 2016;108:117-133. doi:10.1016/j.ejmech.2015.11.015

301. Suchankova A, Stampelou M, Koutsouki K, et al. Discovery of a High Affinity Adenosine A1/A3Receptor Antagonist with a Novel 7-Amino-pyrazolo[3,4- d]pyridazine Scaffold. *ACS Med Chem Lett*. 2022;13(6):923-934. doi:10.1021/acsmedchemlett.2c00052

302. Bento AP, Gaulton A, Hersey A, et al. The ChEMBL bioactivity database: an update. *Nucleic Acids Res*. 2014;42(D1):D1083-D1090. doi:10.1093/nar/gkt1031

303. Gaulton A, Bellis LJ, Bento AP, et al. ChEMBL: A large-scale bioactivity database for drug discovery. *Nucleic Acids Res*. 2012;40(D1):D1100-7. doi:10.1093/nar/gkr777

304. Hawkins PCD, Skillman AG, Nicholls A. Comparison of shape-matching and docking as virtual screening tools. *J Med Chem*. 2007;50(1):74-82. doi:10.1021/jm0603365

305. Cheong SL, Venkatesan G, Paira P, et al. Pyrazolo Derivatives as Potent Adenosine Receptor Antagonists: An Overview on the Structure-Activity Relationships. *Int J Med Chem*. 2011;2011:1-15. doi:10.1155/2011/480652

306. Duan J, Dixon SL, Lowrie JF, Sherman W. Analysis and comparison of 2D fingerprints: Insights into database screening performance using eight fingerprint methods. *J Mol Graph Model*. 2010;29(2):157-170. doi:10.1016/j.jmgm.2010.05.008

307. Stampelou M, Suchankova A, Tzortzini E, et al. Dual A1/A3 Adenosine Receptor Antagonists: Binding Kinetics and Structure-Activity Relationship Studies Using Mutagenesis and Alchemical Binding Free Energy Calculations. *J Med Chem*. 2022;65(19):13305-13327. doi:10.1021/acs.jmedchem.2c01123

308. Hilser A. *Drug Discovery at Class A and Class B GPCRs*. 2022.

309. Stoddart LA, Vernall AJ, Denman JL, Briddon SJ, Kellam B, Hill SJ. Fragment screening at adenosine-A3 receptors in living cells using a fluorescence-based binding assay. *Chem Biol*. 2012;19(9):1105-1115. doi:10.1016/j.chembiol.2012.07.014

310. Stoddart LA, Johnstone EKM, Wheal AJ, et al. Application of BRET to monitor ligand binding to GPCRs. *Nat Methods*. 2015;12(7):661-663. doi:10.1038/nmeth.3398

311. Ravula S, Bobbala RR, Kolli B. Synthesis of novel isoxazole functionalized pyrazolo[3,4-b]pyridine derivatives; their anticancer activity. *J Heterocycl Chem*. 2020;57(6):2535-2538. doi:10.1002/jhet.3968

312. Wang E, Sun H, Wang J, et al. End-Point Binding Free Energy Calculation with MM/PBSA and MM/GBSA: Strategies and Applications in Drug Design. *Chem Rev*. 2019;119(16):9478-9508. doi:10.1021/acs.chemrev.9b00055

313. Papastathopoulos A, Lougiakis N, Kostakis IK, et al. New bioactive 5-arylcarboximidamidopyrazolo[3,4-c]pyridines: Synthesis, cytotoxic activity, mechanistic investigation and structure-activity relationships. *Eur J Med Chem*. 2021;218:113387. doi:10.1016/j.ejmech.2021.113387

314. Aldeghi M, Bodkin MJ, Knapp S, Biggin PC. Statistical Analysis on the Performance of Molecular Mechanics Poisson–Boltzmann Surface Area versus Absolute Binding Free Energy Calculations: Bromodomains as a Case Study. *J Chem Inf Model*. 2017;57(9):2203-2221. doi:10.1021/acs.jcim.7b00347

315. Kim Y, de Castro S, Gao ZG, IJzerman AP, Jacobson KA. Novel 2- and 4-Substituted 1 H -Imidazo[4,5- c]quinolin-4-amine Derivatives as Allosteric Modulators of the A 3 Adenosine Receptor. *J Med Chem*. 2009;52(7):2098-2108. doi:10.1021/jm801659w

316. Heitman LH, Göblyös A, Zweemer AM, et al. A Series of 2,4-Disubstituted Quinolines as a New Class of Allosteric Enhancers of the Adenosine A 3 Receptor. *J Med Chem*. 2009;52(4):926-931. doi:10.1021/jm8014052

317. Slee DH, Chen Y, Zhang X, et al. 2-Amino- N -pyrimidin-4-ylacetamides as A 2A Receptor Antagonists: 1. Structure−Activity Relationships and Optimization of Heterocyclic Substituents. *J Med Chem*. 2008;51(6):1719-1729. doi:10.1021/jm701185v

318. Francis JE, Webb RL, Ghai GR, et al. Highly selective adenosine A2 receptor agonists in a series of N-alkylated 2-aminoadenosines. *J Med Chem*. 1991;34(8):2570-2579. doi:10.1021/jm00112a035

319. Siddiqi SM, Jacobson KA, Esker JL, et al. Search for New Purine- and Ribose-Modified Adenosine Analogs as Selective Agonists and Antagonists at Adenosine Receptors. *J Med Chem*. 1995;38(7):1174-1188. doi:10.1021/jm00007a014

320. Roelen H, Veldman N, Spek AL, von Frijtag Drabbe Künzel J, Mathôt RAA, IJzerman AP. N 6 ,C8-Disubstituted Adenosine Derivatives as Partial Agonists for Adenosine A 1 Receptors. *J Med Chem*. 1996;39(7):1463-1471. doi:10.1021/jm950267m

321. Weston C, Poyner D, Patel V, Dowell S, Ladds G. Investigating G protein signalling bias at the glucagon-like peptide-1 receptor in yeast. *Br J Pharmacol*. 2014;171(15):3651-3665. doi:10.1111/bph.12716

322. Knight A, Hemmings JL, Winfield I, et al. Discovery of Novel Adenosine Receptor Agonists That Exhibit Subtype Selectivity. *J Med Chem*. 2016;59(3):947-964. doi:10.1021/acs.jmedchem.5b01402

323. Tallarida RJ, Murray RB. *Manual of Pharmacologic Calculations*. Springer New York; 1986. doi:10.1007/978-1-4612-4974-0

324. Vauquelin G. Effects of target binding kinetics on in vivo drug efficacy: koff , kon and rebinding. *Br J Pharmacol*. 2016;173:2319-2934. doi:10.1111/bph.13504

325. Jespers W, Schiedel AC, Heitman LH, et al. Structural Mapping of Adenosine Receptor Mutations: Ligand Binding and Signaling Mechanisms. *Trends Pharmacol Sci*. 2018;39(1):75-89. doi:10.1016/j.tips.2017.11.001

326. Jiang Q, Van Rhee AM, Kim J, Yehle S, Wess J, Jacobson KA. Hydrophilic side chains in the third and seventh transmembrane helical domains of human A(2A) adenosine receptors are required for ligand recognition. *Mol Pharmacol*. 1996;50(3):512-521.

327. Gao ZGG, Chen A, Barak D, Kim S kyung K, Müller CE, Jacobson KA. Identification by Site-directed Mutagenesis of Residues Involved in Ligand Recognition and Activation of the Human A 3 Adenosine Receptor. *Journal of Biological Chemistry*. 2002;277(21):19056-19063. doi:10.1074/jbc.M110960200

328. Lane JR, Herenbrink CK, Van Westen GJP, Spoorendonk JA, Hoffmann C, IJzerman AP. A novel nonribose agonist, LUF5834, engages residues that are distinct from those of adenosine-like ligands to activate the adenosine A 2a receptor. *Mol Pharmacol*. 2012;81(3):475-487. doi:10.1124/mol.111.075937

329. Kim J, Wess J, van Rhee AMM, Schöneberg T, Jacobson KAKAKA. Site-directed Mutagenesis Identifies Residues Involved in Ligand Recognition in the Human A Adenosine Receptor. *Journal of Biological Chemistry*. 1995;270(23):13987-13997. doi:10.1074/jbc.270.23.13987

330. Pohorille A, Jarzynski C, Chipot C. Good practices in free-energy calculations. *Journal of Physical Chemistry B*. 2010;114(32):10235-10253. doi:10.1021/jp102971x

331. Matricon P, Ranganathan A, Warnick E, et al. Fragment optimization for GPCRs by molecular dynamics free energy calculations: Probing druggable subpockets of the A 2A adenosine receptor binding site. *Sci Rep*. 2017;7(1):6398. doi:10.1038/s41598-017-04905-0

332. Keränen H, Åqvist J, Gutiérrez-De-Terán H. Free energy calculations of A2A adenosine receptor mutation effects on agonist binding. *Chemical Communications*. 2015;51(17):3522-3525. doi:10.1039/c4cc09517k

333. Pearlman DA, Charifson PS. Are free energy calculations useful in practice? A comparison with rapid scoring functions for the p38 MAP kinase protein system. *J Med Chem*. 2001;44(21):3417-3423. doi:10.1021/jm0100279

334. Wan S, Bhati AP, Zasada SJ, et al. Rapid and Reliable Binding Affinity Prediction of Bromodomain Inhibitors: A Computational Study. *J Chem Theory Comput*. 2017;13(2):784-795. doi:10.1021/acs.jctc.6b00794

335. Wan S, Potterton A, Husseini FS, et al. Hit-to-lead and lead optimization binding free energy calculations for G protein-coupled receptors. *Interface Focus*. 2020;10(6):20190128. doi:10.1098/rsfs.2019.0128

336. Xia L, Burger WAC, Van Veldhoven JPD, et al. Structure-Affinity Relationships and Structure-Kinetics Relationships of Pyrido[2,1-f]purine-2,4-dione Derivatives as Human Adenosine A3 Receptor Antagonists. *J Med Chem*. 2017;60(17):7555-7568. doi:10.1021/acs.jmedchem.7b00950

337. Hoare SRJ, Fleck BA, Williams JP, Grigoriadis DE. The importance of target binding kinetics for measuring target binding affinity in drug discovery: a case study from a CRF1 receptor antagonist program. *Drug Discov Today*. 2020;25(1):7-14. doi:10.1016/j.drudis.2019.09.011

338. Dawson ES, Wells JN. Determination of amino acid residues that are accessible from the ligand binding crevice in the seventh transmembrane-spanning region of the human A1 adenosine receptor. *Mol Pharmacol*. 2001;59(5):1187-1195. doi:10.1124/mol.59.5.1187

339. Salmaso V, Jacobson KA. In Silico Drug Design for Purinergic GPCRs: Overview on Molecular Dynamics Applied to Adenosine and P2Y Receptors. *Biomolecules*. 2020;10(6):812. doi:10.3390/biom10060812

340. Kiss DJ, Pándy-Szekeres G, Keserű GM. Computational Medicinal Chemistry to Target GPCRs. In: *Comprehensive Pharmacology*. Elsevier; 2022:84-114. doi:10.1016/B978-0-12-820472-6.00208-5

341. Wang J, Do HN, Koirala K, Miao Y. Predicting Biomolecular Binding Kinetics: A Review. *J Chem Theory Comput*. 2023;19(8):2135-2148. doi:10.1021/acs.jctc.2c01085

342. Bruce NJ, Ganotra GK, Kokh DB, Sadiq SK, Wade RC. New approaches for computing ligand–receptor binding kinetics. *Curr Opin Struct Biol*. 2018;49:1-10. doi:10.1016/j.sbi.2017.10.001

343. Wolf S. Predicting Protein–Ligand Binding and Unbinding Kinetics with Biased MD Simulations and Coarse-Graining of Dynamics: Current State and Challenges. *J Chem Inf Model*. 2023;63(10):2902-2910. doi:10.1021/acs.jcim.3c00151

344. Bernetti M, Cavalli A, Mollica L. Protein–ligand (un)binding kinetics as a new paradigm for drug discovery at the crossroad between experiments and modelling. *Medchemcomm*. 2017;8(3):534-550. doi:10.1039/C6MD00581K

345. Sohraby F, Nunes-Alves A. Advances in computational methods for ligand binding kinetics. *Trends Biochem Sci*. 2023;48(5):437-449. doi:10.1016/j.tibs.2022.11.003

346. Kolb P, Phan K, Gao ZG, Marko AC, Sali A, Jacobson KA. Limits of Ligand Selectivity from Docking to Models: In Silico Screening for A1 Adenosine Receptor Antagonists. *PLoS One*. 2012;7(11):e49910. doi:10.1371/JOURNAL.PONE.0049910

347. Ivanov AA, Barak D, Jacobson KA. Evaluation of Homology Modeling of G-Protein-Coupled Receptors in Light of the A_{2A} Adenosine Receptor Crystallographic Structure. *J Med Chem*. 2009;52(10):3284-3292. doi:10.1021/jm801533x

348. Mallo-Abreu A, Prieto-Díaz R, Jespers W, et al. Nitrogen-Walk Approach to Explore Bioisosteric Replacements in a Series of Potent A2B Adenosine Receptor Antagonists. *J Med Chem*. 2020;63(14):7721-7739. doi:10.1021/acs.jmedchem.0c00564

349. Dal Ben D, Buccioni M, Lambertucci C, et al. Different efficacy of adenosine and NECA derivatives at the human A3 adenosine receptor: Insight into the receptor activation switch. *Biochem Pharmacol*. 2014;87(2):321-331. doi:10.1016/J.BCP.2013.10.011

350. Deganutti G, Cuzzolin A, Ciancetta A, Moro S. Understanding allosteric interactions in G protein-coupled receptors using Supervised Molecular Dynamics: A prototype study analysing the human A3 adenosine receptor positive allosteric modulator LUF6000. *Bioorg Med Chem*. 2015;23(14):4065-4071. doi:10.1016/J.BMC.2015.03.039

351. Kim SK, Riley L, Abrol R, Jacobson KA, Goddard WA. Predicted structures of agonist and antagonist bound complexes of adenosine A3 receptor. *Proteins: Structure, Function, and Bioinformatics*. 2011;79(6):1878-1897. doi:10.1002/PROT.23012

352. Cappel D, Hall ML, Lenselink EB, et al. Relative Binding Free Energy Calculations Applied to Protein Homology Models. *J Chem Inf Model*. 2016;56(12):2388-2400. doi:10.1021/acs.jcim.6b00362

353. Woolley MJ, Conner AC. Understanding the common themes and diverse roles of the second extracellular loop (ECL2) of the GPCR super-family. *Mol Cell Endocrinol*. 2017;449:3-11. doi:10.1016/J.MCE.2016.11.023

354. Nicoli A, Dunkel A, Giorgino T, De Graaf C, Di Pizio A. Classification Model for the Second Extracellular Loop of Class A GPCRs. *J Chem Inf Model*. 2022;62(3):511-522. doi:10.1021/ACS.JCIM.1C01056/ASSET/IMAGES/LARGE/CI1C01056_0007.JPEG

355. Argyros O, Lougiakis N, Kouvari E, et al. Design and synthesis of novel 7-aminosubstituted pyrido[2,3-b]pyrazines exhibiting anti-breast cancer activity. *Eur J Med Chem*. 2017;126:954-968. doi:10.1016/j.ejmech.2016.12.025

356. Giannouli V, Lougiakis N, Kostakis IK, et al. The discovery of new cytotoxic pyrazolopyridine derivatives. *Bioorg Med Chem Lett*. 2016;26(21):5229-5233. doi:10.1016/j.bmcl.2016.09.056

357. Giannouli V, Lougiakis N, Kostakis IK, et al. Design and Synthesis of New Substituted Pyrazolopyridines with Potent Antiproliferative Activity. *Med Chem (Los Angeles)*. Published online 2019. doi:10.2174/1573406415666190222130225

358. Sklepari M, Lougiakis N, Papastathopoulos A, et al. Synthesis, Docking Study and Kinase Inhibitory Activity of a Number of New Substituted Pyrazolo[3,4-*c*]pyridines. *Chem Pharm Bull (Tokyo)*. 2017;65(1):66-81. doi:10.1248/cpb.c16-00704

359. Evangelou K, Lougiakis N, Rizou S V., et al. Robust, universal biomarker assay to detect senescent cells in biological specimens. *Aging Cell*. 2017;16(1):192-197. doi:10.1111/acel.12545

360. Papastathopoulos A, Lougiakis N, Kostakis IK, et al. New bioactive 5-arylcarboximidamidopyrazolo[3,4-c]pyridines: Synthesis, cytotoxic activity, mechanistic investigation and structure-activity relationships. *Eur J Med Chem*. 2021;218:113387. doi:10.1016/j.ejmech.2021.113387

361. Gerasi M, Frakolaki E, Papadakis G, et al. Design, synthesis and anti-HBV activity evaluation of new substituted imidazo[4,5-b]pyridines. *Bioorg Chem*. 2020;98:103580. doi:10.1016/j.bioorg.2020.103580

362. Lougiakis N, Marakos P, Pouli N, Fragopoulou E, Tenta R. Synthesis of new nebularine analogues and their inhibitory activity against adenosine deaminase. *Chem Pharm Bull (Tokyo)*. 2015;63(2):134-142. doi:10.1248/cpb.c14-00731

363. Papadakis G, Gerasi M, Snoeck R, et al. Synthesis of new imidazopyridine nucleoside derivatives designed as maribavir analogues. *Molecules*. 2020;25(19):4531. doi:10.3390/molecules25194531

364. Lougiakis N, Frakolaki E, Karmou P, et al. Novel nucleoside analogues targeting HCV replication through an NS5A-dependent inhibition mechanism. *Chem Biol Drug Des*. 2017;90(3):352-367. doi:10.1111/cbdd.12966

Appendix

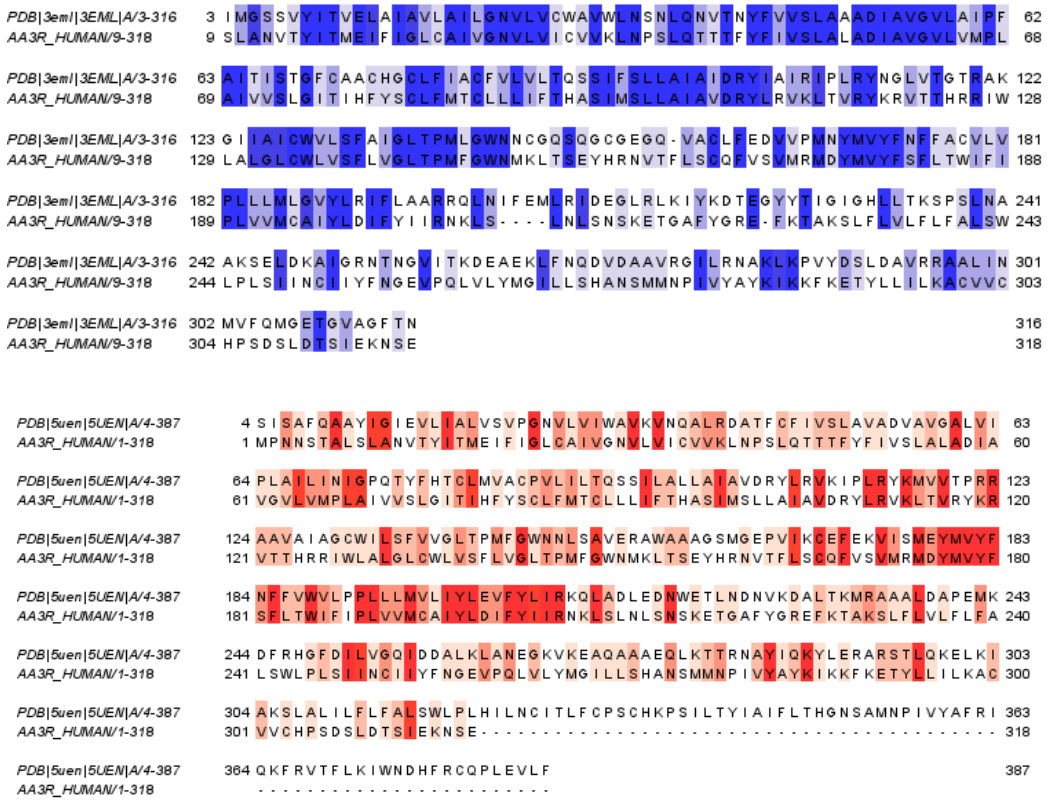

***Figure S4**: Pairwise sequence alignments (A) Pairwise sequence alignment of hA_{2A} crystal structure (PDB ID 3EML [34]) that was used as template for the homology modelling of A_3R (Uniprot ID P0DMS8) showing the identical (blue), the strongly conserved (purple), and the weakly conserved (light-purple) residues. (B) Pairwise sequence alignment of hA_1 crystal structure (PDB ID 5UEN [55]) that was used as template for the homology modelling of A_3R (Uniprot ID P0DMS8) showing the identical (red), the strongly conserved (orange), and the weakly conserved (light-orange) residues. This figure was made with Jalview 2.11.2.6. [116]*

Table S1: Antagonistic potencies (pEC50 in presence of NECAa) of 7-amino-pyrazolo[3,4-d]pyridazines 10a-c, 15a-c against $A_{2A}R$ and $A_{2B}R$.

	$A_{2A}R$ (10 µm)	$A_{2B}R$ (10 µm)	
COMPOUND	**pEC_{50} of NECA in presence of compound[a]**	**pEC_{50} of NECA in presence of compound[a]**	**pK_d[b]**
10a	5.64 ± 0.38	7.01 ± 0.10	4.79± 0.15
10b	5.82 ± 0.33	6.39 ± 0.07*	5.76± 0.14
10c	5.60 ± 0.52	7.23 ± 0.10	N.B.
15a	6.17 ± 0.47	6.87 ± 0.09	5.09± 0.15
15b	5.71 ± 0.46	7.22 ± 0.13	N.B.
15c	5.84 ± 0.46	7.24 ± 0.10	N.B.
vehicle	6.42 ± 0.17	7.22 ± 0.12	-

[a]Mean ± SEM; Functional activities of at least 3 independent repeats, conducted in duplicate.

Statistical significance compared to NECA was determined, at $p< 0.05$, through One-Way ANOVA with Dunnett's post-test (*, $p< 0.05$).

[b]Mean ± SEM; Equilibrium binding affinities of the ligands measured with NanoBRET against WT $A_{2B}R$; NECA was used as positive control.

Adapted from the Doctoral Thesis of Dr Anna Hilser [308] and ref [307] .

Table S2: Chemical structures of 53 compounds from our *in-house* library.

NO	CODE	STRUCTURE	REF	COMPOUND CLASS
A9	NL666	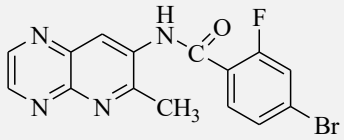	[355]	pyrido[2,3-*b*]pyrazine
A10	NL660	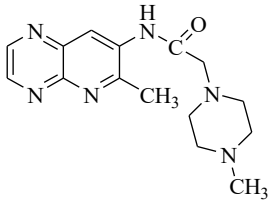	[355]	pyrido[2,3-*b*]pyrazine
A11	NL681	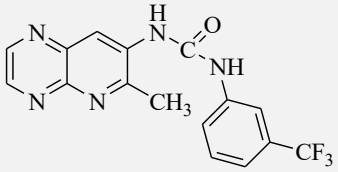	[355]	pyrido[2,3-*b*]pyrazine
A12	NL605	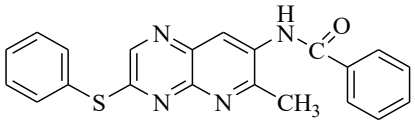	[355]	pyrido[2,3-*b*]pyrazine
A13	NL757	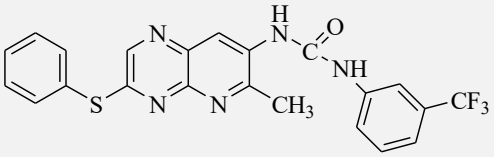	[355]	pyrido[2,3-*b*]pyrazine
A14	MVN196	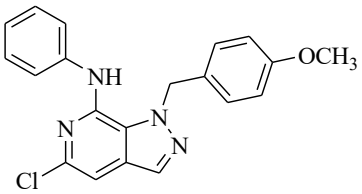	[356]	pyrazolo[3,4-*c*]pyridine
A15	MVN377	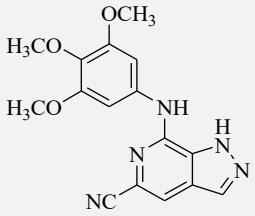	[356]	pyrazolo[3,4-*c*]pyridine

A16	MVN445	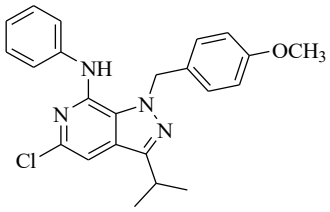	356	pyrazolo[3,4-*c*]pyridine
A17	MVN492	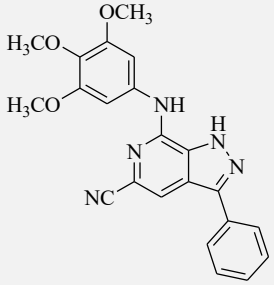	357	pyrazolo[3,4-*c*]pyridine
A18	MVN281	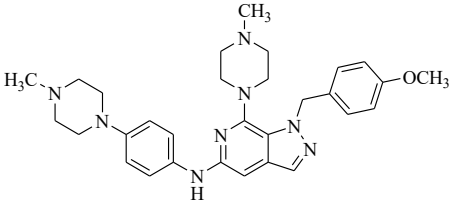	358	pyrazolo[3,4-*c*]pyridine
L1	Mvn450	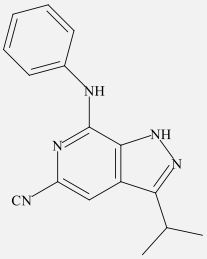	357	pyrazolo[3,4-*c*]pyridine
L2	Mvn468	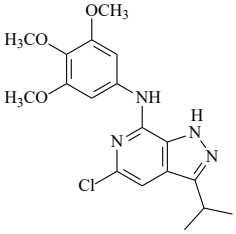	356	pyrazolo[3,4-*c*]pyridine
L3	Mvn451	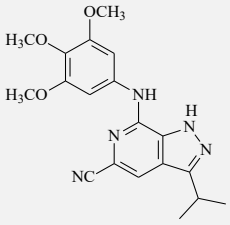	356	pyrazolo[3,4-*c*]pyridine
L4	Mvn489	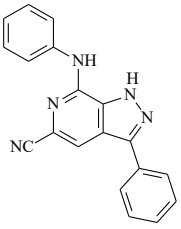	357	pyrazolo[3,4-*c*]pyridine

L5	Mvn411	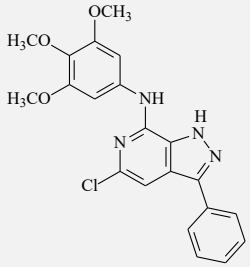	356	pyrazolo[3,4-*c*]pyridine
L6	Mvn474	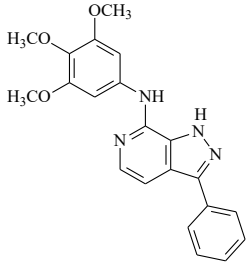	356	pyrazolo[3,4-*c*]pyridine
L7	Mvn494	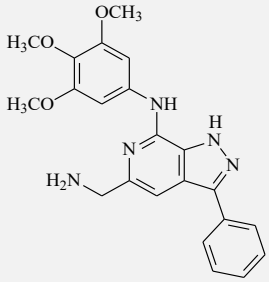	357	pyrazolo[3,4-*c*]pyridine
L8	Mvn 497	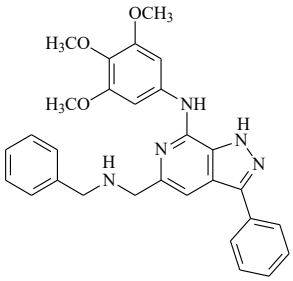	357	pyrazolo[3,4-*c*]pyridine
L9	Mvn498	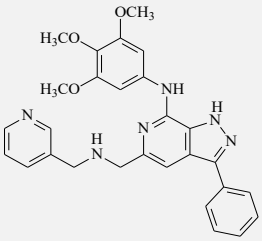	357	pyrazolo[3,4-*c*]pyridine
L10	Mvn496	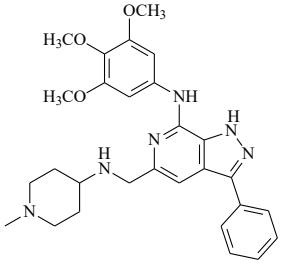	357	pyrazolo[3,4-*c*]pyridine

L11	Mvn487	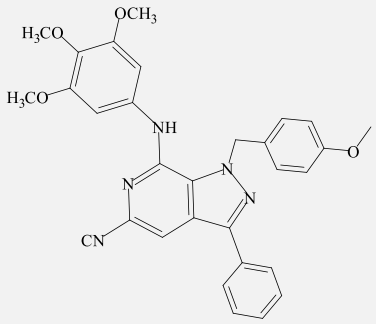	357	pyrazolo[3,4-*c*]pyridine
A20	NLG35	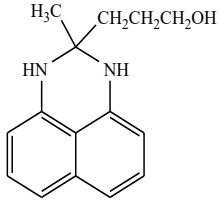	359	perimidine
A25	MER142	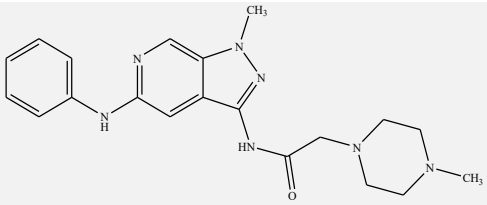	360	pyrazolo[3,4-*c*]pyridine
A26	MER143	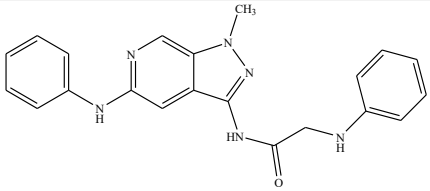	360	pyrazolo[3,4-*c*]pyridine
A27	MER191	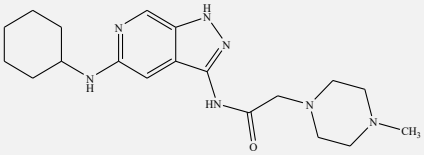	360	pyrazolo[3,4-*c*]pyridine
L12	MER148rn	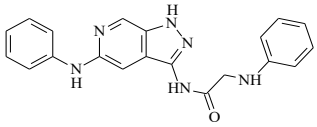	360	pyrazolo[3,4-*c*]pyridine
L13	MER117	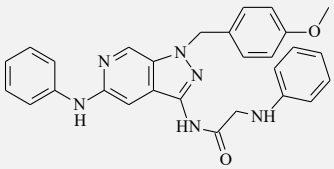	360	pyrazolo[3,4-*c*]pyridine
L14	MER140	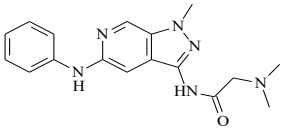	360	pyrazolo[3,4-*c*]pyridine
L15	MER139	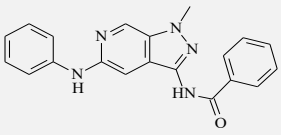	360	pyrazolo[3,4-*c*]pyridine

L16	MER194	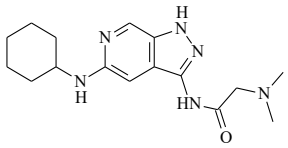	360	pyrazolo[3,4-*c*]pyridine
L17	MER196r	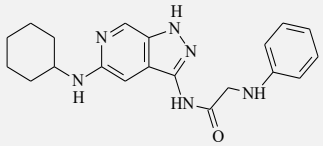	360	pyrazolo[3,4-*c*]pyridine
L18	MER195r	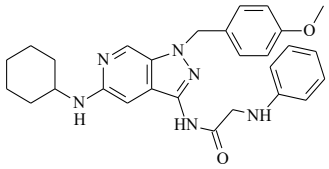	360	pyrazolo[3,4-*c*]pyridine
L19	MER172t	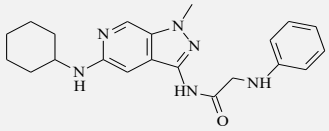	360	pyrazolo[3,4-*c*]pyridine
L20	TP 29	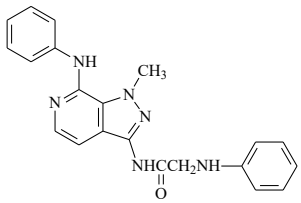	360	pyrazolo[3,4-*c*]pyridine
L21	TP 59	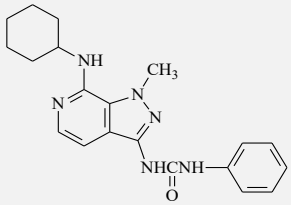	360	pyrazolo[3,4-*c*]pyridine
L22	TP 64	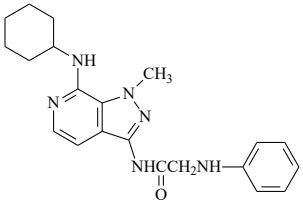	360	pyrazolo[3,4-*c*]pyridine
A28	TP27	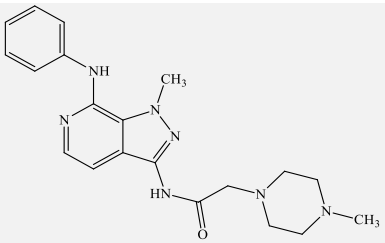	360	pyrazolo[3,4-*c*]pyridine

A29	TP102	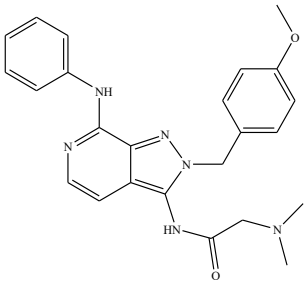	360	pyrazolo[3,4-*c*]pyridine
A32	TP265	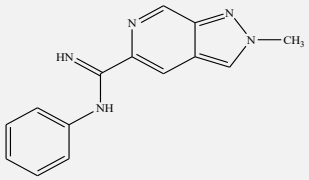	360	pyrazolo[3,4-*c*]pyridine
A33	TP325D	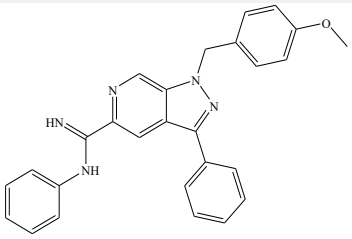	360	pyrazolo[3,4-*c*]pyridine
A34	TP383	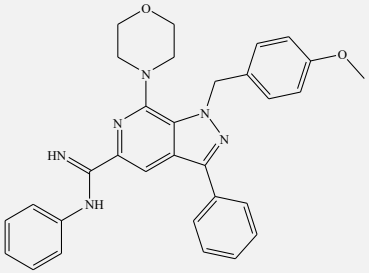	360	pyrazolo[3,4-*c*]pyridine
A35	GP239	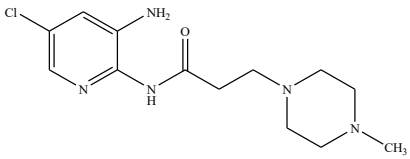	361	pyridine
A36	GP327B	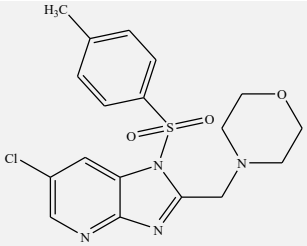	361	imidazo[4,5-*b*]pyridine
A37	NL647	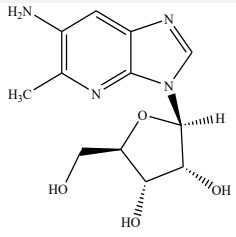	362	imidazo[4,5-*b*]pyridine

A38	NL639	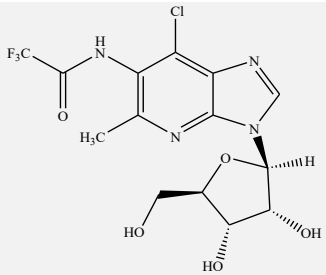	362	imidazo[4,5-*b*]pyridine
A39	NL642	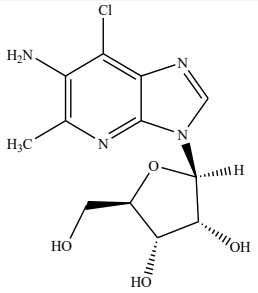	362	imidazo[4,5-*b*]pyridine
A40	NL566	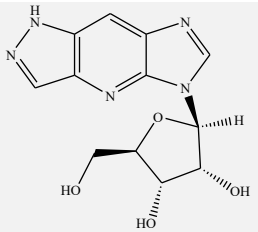	362	imidazo[4,5-*b*]pyrazolo[3,4-*e*]pyridine
A41	GP126	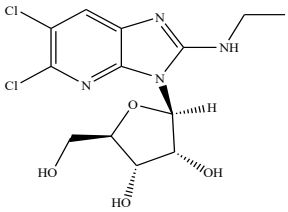	363	imidazo[4,5-*b*]pyridine
A42	GP174	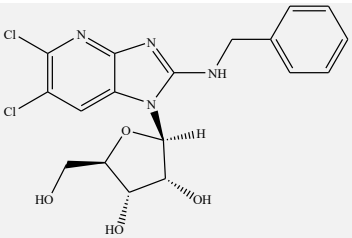	363	imidazo[4,5-*b*]pyridine
A43	GP172	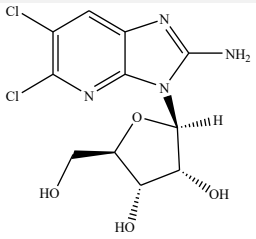	363	imidazo[4,5-*b*]pyridine

A44	PK288	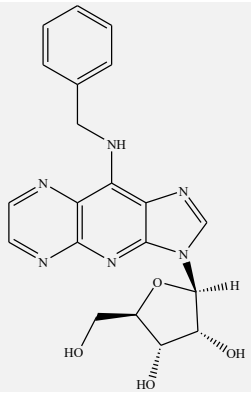	[364]	imidazo[4',5':5,6]pyrido[2,3-*b*]pyrazine
A45	PK285	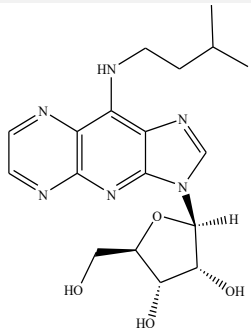	[364]	imidazo[4',5':5,6]pyrido[2,3-*b*]pyrazine

Table S3: Functional activities for A15, A17 and A26 against $A_{2A}R$ and $A_{2B}R$.

COMPOUND	$A_{2A}R$		$A_{2B}R$	
	pIC_{50} in presence of NECA [a]	pK_d [b]	pIC_{50} in presence of NECA [a]	pK_d [b]
DMSO	5.94 ± 0.18	-	7.22 ± 0.12	-
A15	5.79 ± 0.24	-	7.07 ± 0.09	-
A17	5.94 ± 0.2	-	6.62 ± 0.07*	5.50 ± 0.12
A26	6.12 ± 0.43	-	7.21 ± 0.09	-

[a] pIC_{50} values are reported as mean ± standard error of the mean (SEM) of at least 3 independent repeats, conducted in duplicate.

[b] Dissociation constant (pK_d) of the ligands as mean ± standard error of the mean (SEM) of at least 3 independent repeats, conducted in duplicate as determined using the Schild analysis (Equation 1).

Statistical significance (* $p < 0.05$) determined using ANOVA and Dunnett' s post-test.

Adapted from the Doctoral Thesis of Dr Anna Hilser [308] and ref [307] .

Table S4: Functional activities for L2-L10, and L12, L15, L21 against $A_{2A}R$ and $A_{2B}R$.

COMPOUND	$A_{2A}R$		$A_{2B}R$	
	pEC_{50} in presence of NECA [a]	pK_d [b]	pEC_{50} in presence of NECA [a]	pK_d [b]
DMSO	5.94 ± 0.18	-	7.22 ± 0.12	-
L2	5.33 ± 0.28	-	7.20 ± 0.07	-
L3	6.35 ± 0.22	-	7.33 ± 0.09	-
L4	5.58 ± 0.22	-	6.60 ± 0.09*	5.77 ± 0.12
L5	6.09 ± 0.22	-	6.82 ± 0.09	-
L6	5.31 ± 0.19	-	6.64 ± 0.10	-
L7	5.73 ± 0.22	-	6.99 ± 0.09	-
L8	5.80 ± 0.19	-	6.82 ± 0.07	-
L9	5.46 ± 0.3	-	6.92 ± 0.08	-
L10	6.15 ± 0.30	-	7.15 ± 0.08	-
L12	5.68 ± 0.25	-	6.97 ± 0.10	-
L15	6.56 ± 0.30	-	7.16 ± 0.12	-
L21	6.18 ± 0.32	-	7.03 ± 0.11	-

[a] Functional activities (pIC_{50} values in presence of NECA) for the ligands as mean ± standard error of the mean (SEM) of at least 3 independent repeats, conducted in duplicate.

Statistical significance (* $p < 0.05$) determined using ANOVA and Dunnett' s post-test.

Adapted from the Doctoral Thesis of Dr Anna Hilser [308] and ref [307] .

Table S5: pIC_{50} of NECA in the presence of DMSO and in the presence of each potential antagonist, in A_3R Flp-In™ CHO cells.

	A_3R		A_1R	
COMPOUND	pIC_{50} of NECA[a]	Mean difference from DMSO[b]	pIC_{50} of NECA[a]	Mean difference from DMSO[b]
DMSO	9.03 ± 0.1	-	8.95 ± 0.1	-
A17	7.27 ± 0.1***	-1.72	6.70 ± 0.1***	-2.25
L2	6.57 ± 0.39***	-2.46	6.85 ± 0.1***	-2.15
L3	8.42 ±0.19*	-0.61	8.49 ±0.17	-0.46
L4	7.40 ± 0.1***	-1.60	7.04 ± 0.1**	-1.55
L5	7.91 ± 0.1**	-1.09	8.54 ± 0.1	-0.41
L6	8.29 ± 0.1*	-0.74	8.72 ± 0.23	-0.23
L7	8.31 ± 0.21*	-0.72	7.64 ± 0.14**	-1.31
L8	8.14 ± 0.1*	-0.89	8.41 ± 0.22	-0.51
L9	8.05 ± 0.1**	-0.95	7.92 ± 0.11**	-1.03
L10	8.56 ± 0.2	-0.47	8.33 ± 0.15*	-0.62
A26	7.86 ± 0.1**	-1.14	8.58 ± 0.1	-0.37
L12	8.52 ± 0.21	-0.51	8.16 ± 0.09*	-0.89
L15	8.17 ± 0.2*	-0.86	8.30 ± 0.14*	-0.65
L21	8.78 ± 0.1	-0.22	8.85 ± 0.12	-0.1

[a] pIC_{50} values are reported as mean ± standard error of the mean (SEM) of at least 3 independent repeats, conducted in duplicate. [b] Difference in pIC_{50} between DMSO and each potential antagonist. Statistical significance (* $p < 0.05$, ** $p < 0.01$, *** $p < 0.001$) determined using ANOVA and Dunnett' s post-test.

Adapted from the Doctoral Thesis of Dr Anna Hilser [308] and ref [307] .

Table S6: Binding affinities for A26 measured using NanoBRET against WT and mutant A_1Rs.

Mutation	K_d *(nM)* [a]	pK_d
	CA200645	**A26**
WT	76.37 ± 9.37	6.30 ± 0.07
$T91^{3.36}A$	166.35 ± 17.36	6.10 ± 0.07
$E172^{5.30}A$	116.04 ± 12.22	5.98 ± 0.06
$L250^{6.51}A$	158.28 ± 17.37	6.15 ± 0.09
$H251^{6.52}A$	145.19 ± 19.13	7.15 ± 0.08**
$S267^{7.32}A$	70.99 ± 7.03	5.97 ± 0.17
$Y271^{7.36}A$	71.10 ± 7.68	6.33 ± 0.07

[a] Affinity constant for CA200645 binding to mutant A_1R receptors.

[b] n.b. NECA was unable to displace CA200645 at the mutant receptor

Statistical significance (* $p < 0.05$, ** $p < 0.01$,) determined using ANOVA and Dunnett' s post-test.

Adapted from the Doctoral Thesis of Dr Anna Hilser [308] and ref [307] .

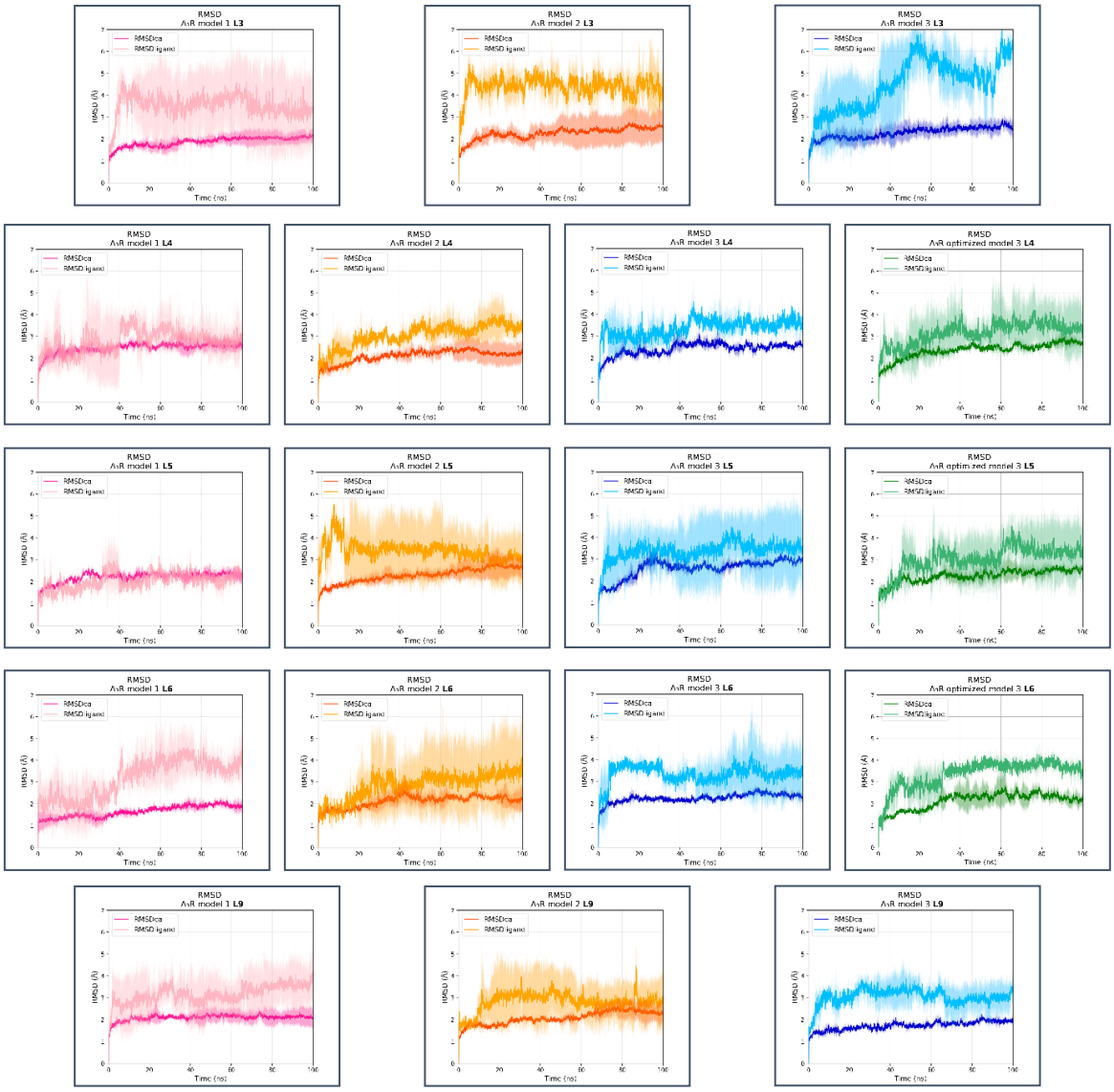

***Figure S25**: RMSD plots from 100 ns MD simulations with amber99sb of Inactive A_3R - A17, L3, L4, L5, L6, L9 complexes embedded in phospholipid bilayers. Pink plots were used for Model 1, orange for Model 2 and blue for Model 3 and green for optimized Model 3.*

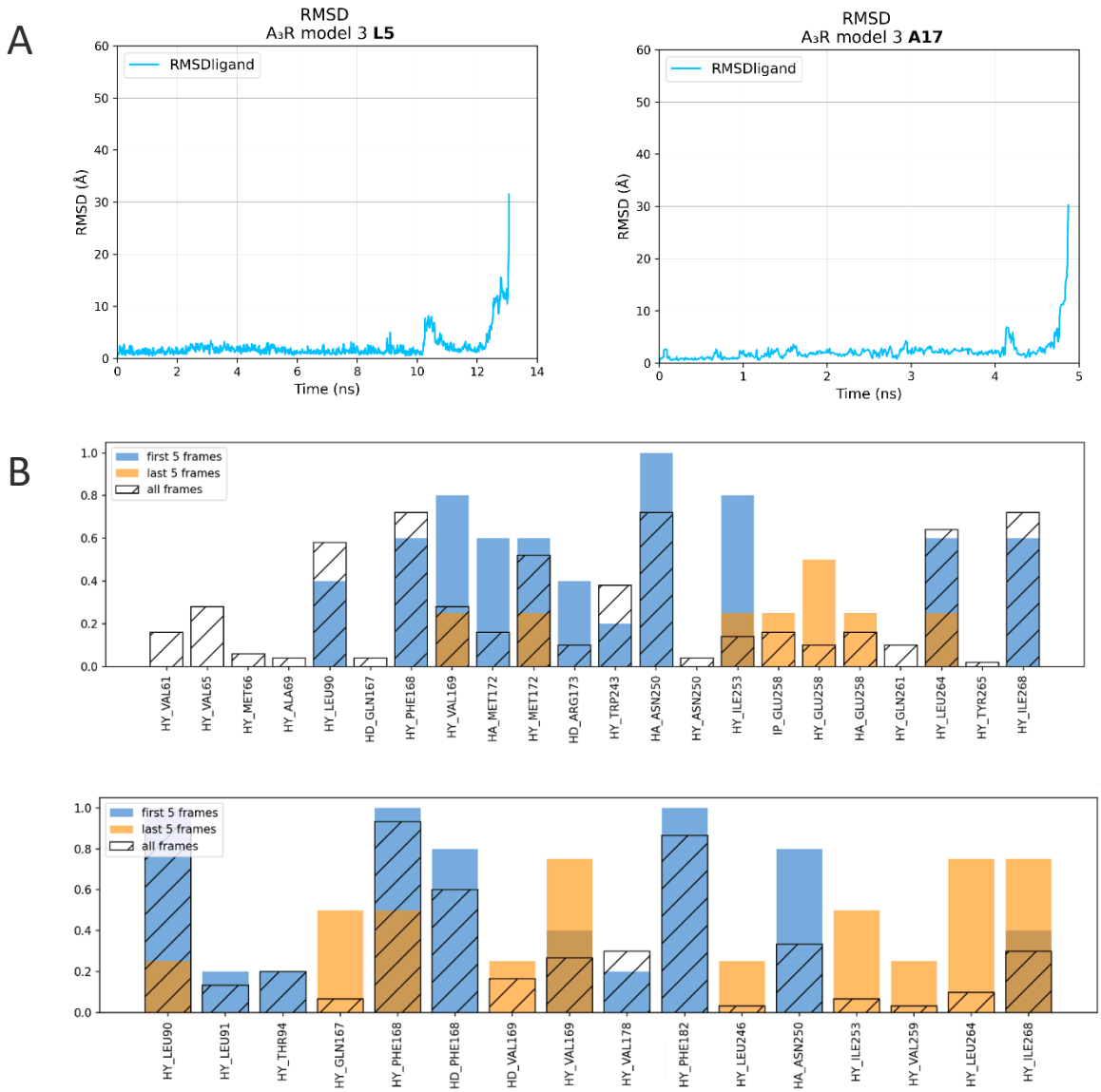

***Figure S3**: MD simulations with τRAMD. (A) RMSD plots of the ligand from MD simulations showing the egress of ligands L5 and A17. (B) Protein-ligand interactions during the suggested egress route of A17 showing the 5/100 MD simulation snapshots (blue color) and the last 5/100 MD simulation snapshots snapshots (light brown color) for Model 3 (up) and optimized Model 3 (bottom); HY: hydrophobic, HD H-bond donor, HA H-bond acceptor interactions.*

Table S7: Experimental dissociation constants, ΔG_{eff} calculated from the MD simulations using amber99sb and the MM-GBSA method using OPLS2005 force field with an implicit membrane model and considering the waters inside the binding area, for A15, L2-L6, L8, L9, A17 against inactive A_3R using homology Model 1.

Compound	pK_d [a]	ΔG_{eff} [b]
A15	5.91± 0.19	-94.31 ± 8.62
A17	8.00 ±0.32	-116.06 ± 7.74
L2	6.26 ± 0.18	n.d.
L3	6.45 ± 0.23	-119.03 ±6.28
L4	7.58 ± 0.33	-102.16 ± 5.44
L5	7.07 ± 0.22	-141.44 ± 5.62
L6	7.13 ± 0.55	-98.55 ± 8.02
L8	6.73 ± 0.45	-127.39 ± 8.87
L9	6.89 ± 0.2	-143.08 ± 7.68

[a] See also **Table 5-1**.

[b] Mean ± SEM; Calculated effective binding free energy (kcal mol^{-1}) between ligand and receptor. ΔG_{eff} is calculated from the last 20 ns of the trajectories using 40 ps intervals (ie. 500 frames per trajectory) using the MM/GBSA model that considers the membrane as hydrophobic slab. Mean from three 20ns-MD simulations.

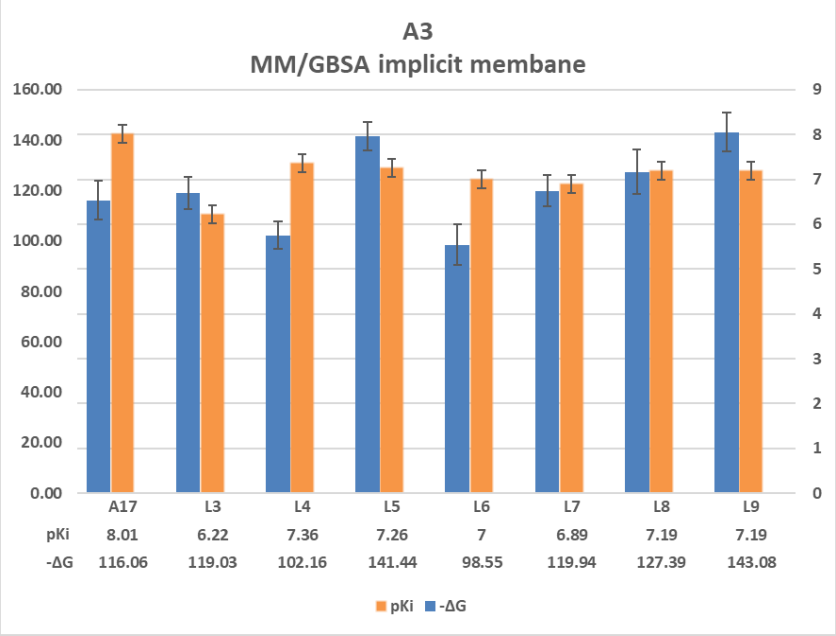

***Figure S4**: ΔG_{eff} values from MM/GBSA calculations and experimental binding affinities pKi for for inactive A_3R.* MM/GBSA calculations using a model that is taking into account the membrane as hydrophobic slab (blue bars) and pKi values measured using BRET (blue bars). *Homology Model 1 of inactive A_3R was used used for the MM/GBSA calculations.*

"As I close this chapter of my life, I'm reminded of Oscar Wilde: 'I'm not young enough to know everything.' I now embrace the journey ahead, eager to keep learning and growing."